THE UNIVERSITY
of EDINBURGH

This thesis has been submitted in fulfilment of the requirements for a postgraduate degree (e.g. PhD, MPhil, DClinPsychol) at the University of Edinburgh. Please note the following terms and conditions of use:

This work is protected by copyright and other intellectual property rights, which are retained by the thesis author, unless otherwise stated.
A copy can be downloaded for personal non-commercial research or study, without prior permission or charge.
This thesis cannot be reproduced or quoted extensively from without first obtaining permission in writing from the author.
The content must not be changed in any way or sold commercially in any format or medium without the formal permission of the author.
When referring to this work, full bibliographic details including the author, title, awarding institution and date of the thesis must be given.

Towards Environmentally Friendly Electrodeposition: Using Citrate Based Electrolytes to Deposit Nickel and Nickel-Iron

THE UNIVERSITY
of EDINBURGH

Richard Perry

2015

Abstract

The production of magnetic materials is of great interest for use in the micro-fabrication industry. In particular, Permalloy ($Ni_{80}Fe_{20}$) is used in the production of micro-electromechanical systems (MEMS) due to its favourable magnetic properties (high relative permeability, low coercivity and high magnetic saturation). This leads to applications in devices such as inductors, transformers and micro-actuators. The electrodeposition of NiFe is also of fundamental electrochemical interest, as there is anomalous thermodynamic behavior, with the less noble (iron) metal depositing preferentially to the more noble (nickel) metal.

To enable consistent alloy deposition nickel and nickel-iron baths are currently almost exclusively based on boric acid. Boric acid has an important role in the deposition of NiFe films but its role(s) in the electrodeposition mechanism is (are) not wholly understood. Recently (2011) boric acid has been identified as a "substance of very high concern" based on the criteria established by EU chemical regulation, REACH. In anticipation of increased regulation an alternative was sought to provide a benign alternative to boric acid in the NiFe plating bath suitable for use in micro-fabrication.

Initial work was performed to benchmark the performance of existing boric acid based electrodeposition baths. Cyclic voltammetry was performed, which demonstrated the deposition of nickel and nickel-iron from boric acid baths. Coulombic efficiencies up to 93 % were measured for the deposition of nickel using the electrochemical quartz crystal microbalance (EQCM) on platinum electrodes. For nickel-iron deposition control of the film composition was demonstrated on copper electrodes through varying the iron (II) concentration, current density and temperature. A citrate bath for the deposition of nickel-iron was then developed and characterised. Cyclic voltammetry was performed in these citrate baths demonstrating the deposition of nickel and nickel-iron. Optimal conditions for depositing $Ni_{80}Fe_{20}$ were demonstrated to be an elevated temperature (60 °C) with a current density of 20 mA cm^{-2} and a pH of 3.

Using the EQCM the efficiency for nickel deposition was measured to be > 80 %. The effects of sodium saccharin and sodium dodecyl sulfate as additives were investigated; these were shown to influence morphology but not the coulombic efficiency. Decreasing the pH was shown to lower the efficiency of nickel deposition from the citrate bath.

Comparisons of key properties were made between NiFe films deposited from a boric acid bath and the citrate bath developed in this work. Test structures were used to compare the strain in the films; no significant difference was found. For 2.2 µm thick $Ni_{80}Fe_{20}$ films the sheet resistance was measured using Greek cross structures as 0.078 ± 0.004 Ω/square for films deposited from the boric acid bath and 0.090 ± 0.006 Ω/square from the citrate bath. The magnetic saturation, M_s, was measured as 895 ± 66 emu cm^{-3} for deposits from the boric acid bath and 923 ± 111 emu cm^{-3} from the citrate bath. These again show no significant difference in these values within experimental error. Coercivities for these films were measured to be between 20 and 120 A m^{-1}. In combination, this work demonstrates the development and characterisation of a new citrate based electrodeposition bath for nickel and nickel-iron. Similar chemical, electrical, mechanical and magnetic properties were found from films deposited from both baths, thus demonstrating the suitability of the citrate bath for the deposition of nickel-iron films in microfabrication.

Lay Summary

Electrodeposition is a useful, potentially green and low carbon process which enables the extraction of metals from a solution onto a surface using an electric current. Electrodeposition is commonly used as decorative process, for example in the plating of gold and silver, but can also be used to produce layers of material which exhibit certain functional properties. This thesis concerns the electrodeposition of the useful magnetic alloy, Permalloy. Permalloy is an alloy of 80 % nickel and 20 % iron and is used extensively in electronic devices.

The solution or bath which is currently used to deposit Permalloy contains a number of chemicals which improve the quality of the deposited metal. One of these additives is a chemical called boric acid. Evidence suggests that boric acid may be harmful to fertility and the unborn child. For this reason there is a desire to remove and replace this chemical in the bath. Additionally, the deposition of nickel-iron alloys is of fundamental interest as the deposition of iron is disproportionally favoured when compared to nickel. This results in the iron content in the metal being unexpectedly high and hard to control.

In this thesis experiments were performed on an established boric acid-containing plating bath to examine and identify key parameters required for the electrodeposition of the nickel-iron alloy. There have been numerous suggestions for the role of boric acid in these baths. The identification for the primary roles of boric acid was important and proved useful in the identification of a replacement in the nickel-iron plating bath.

Citric acid and sodium citrate, which are both environmentally benign, have previously been identified as potential alternatives to boric acid in nickel plating baths. However there is very limited literature on the viability of their use in nickel-iron plating baths. In this work a boric acid-free nickel-iron bath was developed using sodium citrate. Conditions were sought to optimise

the performance of the new electroplating bath and to make the deposits comparable to existing baths.

The fundamental electrochemistry of citrate plating baths was examined for both the deposition of nickel and nickel-iron with comparisons made between the new citrate bath and the existing boric acid bath. For example, measurements for the efficiency of deposition were made to provide insight into the effects of temperature, current density and pH. This enabled the selection of optimal plating conditions for the desired Permalloy.

Comparisons were also made for the properties of deposits made from the existing boric acid bath and the new citrate bath. One important property is the stress present in the film. High levels of stress may cause the failure of the final device. Measurements were made showing the stress in the films from the new citrate bath were comparable to that from the boric bath. Electrical measurements were made to measure the resistance in the films. It was found that films made from the citrate bath had a slightly higher resistance than those made from the boric acid bath. The magnetic properties of the films were also compared. In general the magnetic properties displayed by the two sets of films were shown to be comparable demonstrating the suitability for citrate to be used as a replacement for boric acid in the deposition of nickel-iron films.

Declaration

I hereby declare that the work presented in this thesis is my own unless otherwise credited and that the work has not been submitted for any other degree or professional qualification.

Richard Perry

Acknowledgements

The author of this work wishes to thank the following people for their assistance and advice during this work. Firstly I must thank my supervisors Professor Andy Mount and Professor Anthony Walton whose insight and direction during this work were invaluable. I must thank those in Mount group and those based in the Scottish Microelectronics Center throughout my time here. Particular mention goes to those involved in the magnetics and inductors group: Dr Jeremy Murray, Dr Giuseppe Schiavone, Dr Ross Walker and Dr Evgeny Sirotkin as well as Dr Jonathan Terry and Dr Nathan Brockie.

For their electrochemical insight and patience Dr Damion Corrigan and Dr John Henry.

Those who have traveled through this journey with me: Kate Fisher, David French, Erik Rowbotham, Simon Wood, Dr Ilka Schmueser, Dr Miriam Kaatz, Andrew Relf, Ewen Blair, Andrew Piper, Justin Elliot, Simon Reeves, Dr Patrick Thomson, Dr Martin Ward.

To those I love, my family, Charlotte.

To the future. Dr Charlotte Brady will you marry me?

Contents

List of Abbreviations

CE	coulombic efficiency
CV	cyclic voltammetry
DI	de-ionised
EIS	electrochemical impedance spectroscopy
EQCM	electrochemical quartz crystal microbalance
GPES	general purpose electrochemical software
HER	hydrogen evolution reaction
IC	integrated circuit
LSV	linear sweep voltammetry
MEMS	micro electromechanical systems
OCP	open circuit potential
PECVD	plasma enhanced chemical vapour deposition
PVD	physical vapour deposition
RDE	rotating disc electrode
RDS	Rate Determining Step
RE	reference electrode
REACH	Registration, Evaluation, Authorisation & restriction of CHemicals
RRDE	rotating ring disc electrode
Sac	saccharin or sodium saccharin
SCE	saturated calomel electrode
SDS	sodium dodecyl sulfate
SEM	scanning electron microscopy
WE	working electrode
XRD	X-ray diffraction
XRF	X-ray fluorescence

Chapter 1

Introduction

1.1 Motivation

1.1.1 Integrated Circuits and Micro-Electromechanical Systems

The industries of integrated circuits (ICs) and micro electromechanical systems (MEMS) are closely related through their dependance on microfabrication technologies. The basic microfabrication processes of etching, patterning, doping and layer deposition are employed to fabricate devices in both disciplines. A fundamental difference between IC and MEMS is that MEMS devices can contain physically moveable elements alongside any electrical parts and are typically made with dimensions between 1 and 100 µm.

In Richard Feynman's 1959 lecture "There's Plenty of Room at the Bottom" he envisioned the miniaturisation of the computer and the ability to construct small machines [1]. With the advent of microfabrication technologies this vision has been realised. Today MEMS devices enable a mechanical element to sense (*eg.* movement) and in turn provide an electrical function (*eg.* switching). Typical applications of MEMS devices include accelerometers [2, 3], gyroscopes [4, 5] and pressure sensors [6, 7].

Fundamental to MEMS are the materials used during fabrication. Metallic conductors, semiconductors and insulators are employed in microfabrication and are fundamental for constructing wires, capacitors, resistors, inductors, beams, mirrors, and so forth. Different materials, of course, exhibit different properties which can be exploited appropriately. Copper, due to its excellent conductivity,

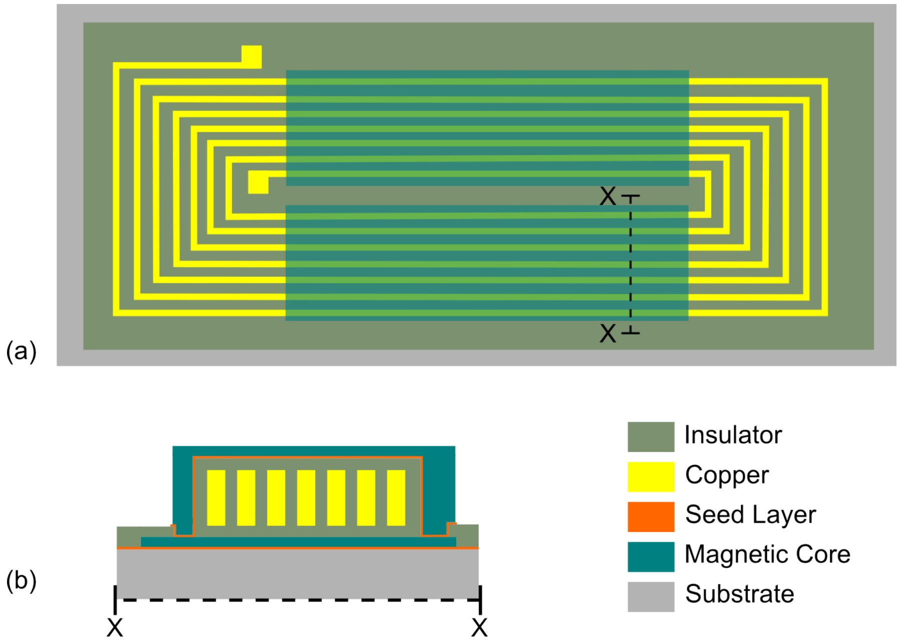

Figure 1.1: Schematic for a simple planar coil micro-inductor design. (a) Top view. (b) Cross section through plane X–X.

is commonly used as an interconnect. Titanium and chromium are used as adhesion layers for noble metals such as gold or platinum. Transparent conductors, such as indium tin oxide (ITO), are critical in the production of displays or LEDs. Equally, materials may be chosen for their favorable magnetic properties.

Principally, this thesis concerns the deposition of conducting magnetic materials for use in power applications (inductors) and in MEMS devices (switches, actuators). Figure 1.1 shows a design for a simple micro-inductor. A typical micro-inductor consists of copper coils which are encapsulated within a suitable magnetic material [8, 9, 10, 11]. In this type of design the deposition of magnetic films ranging in thickness from 1 to 10's μm is required. To this end, the copper coils and conducting magnetic cores are typically deposited using electrochemical methods.

1.1.2 Ferromagnetic Materials and Applications

Ferromagnetic materials are the most technologically important magnetic materials, with wide ranging applications in motors, transformers, inductors, actuators, magnetic tape recording, electromagnets, compasses and data storage [12].

The characteristic feature of a ferromagnetic material is spontaneous magnetisation below its Curie temperature, T_c. This occurs due to the the alignment of the material's magnetic moments when at its lowest energy state. Heating above the Curie point leads to a collapse of this ferromagnetic behavior. Out of the entire periodic table only four elements display ferromagnetic behavior at (or close to) room temperature; these are iron (T_c = 1043 K), cobalt (T_c = 1390 K), nickel (T_c = 629 K) and gadolinium (T_c = 292 K) [13]. Luckily, one of the best ferromagnets, iron, is readily available in the Earth's crust (at 5 % by weight). Nickel and cobalt are available in smaller quantities, (80 ppm and 23 ppm) [14]. It is from this pool of elements that the majority of functional ferromagnetic material is drawn.

There are a plethora of magnetic materials available with many specialised uses depending on the properties of any given material. This thesis concerns soft ferromagnetic materials which are desired as inductor core materials for use in the microfabrication industry, specifically nickel-iron alloys.

The ideal soft magnetic material displays the greatest possible permeability, minimal hysteresis and low magnetostriction. The permeability of a material, μ, is the degree to which a material is magnetised in response to an applied magnetic filed. Given appropriate geometry where demagnetising effects are negligible and in a suitable range, the magnetic flux density, $\boldsymbol{B}$, is proportional to the applied magnetic field, $\boldsymbol{H}$.

$$\boldsymbol{B} = \mu_0 \mu_r \boldsymbol{H} \tag{1.1}$$

where the relative permeability of the material is $\mu_r = \mu/\mu_0$, and μ_0 is the permeability of free space.

Hysteresis is characteristic of ferromagnetic materials and is epitomised by the irreversible response of the magnetisation of a material, $\boldsymbol{M}$, to an applied magnetic field. Soft ferromagnets display a small coercive force, H_c, compared to hard ferromagents as shown in Figure 1.2. The area within the hysteresis loop is proportional to the work required to cycle between the two fully magnetised states. It follows that to minimise energy losses in an inductor core a soft material with a small coercive force is desired.

Magnetostriction is where a material changes its dimensions when undergoing magnetisation. This phenomena is responsible for the heating-up and humming noise heard from transformers.

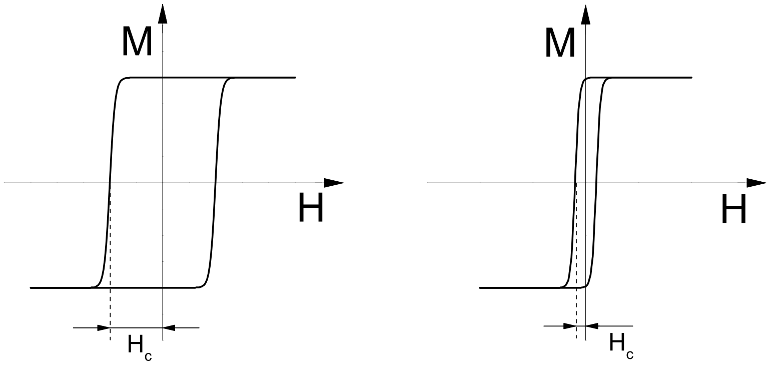

Figure 1.2: Typical M-H loops for a hard (left) and soft (right) ferromagnetic material.

Frequency	Materials	Applications
<1 Hz	Soft iron, Fe-Co (permendur), Ni-Fe (Permalloy)	Electromagnets, relays
1 Hz - 1kHz	Si Steel, Permalloy, finmet, magnetic glasses	Transformers, motors, generators
100 Hz - 100 kHz	Permalloy foils, finmet, magnetic glasses, Fe-Si-Al powder, Mn-Zn ferrite	Inductors, transformers
0.1-1000 MHz	Mn-Zn ferrite, Ni-Zn ferrite, YIG, Li ferrite	Microwave isolators, circulators, phase shifters, filters

Table 1.1: Soft magnetic materials and their applications (from reference [13]).

Given the range of applications a summary of the most commonly used soft magnetic materials and their applications is shown in Table 1.1.

Nickel-Iron Alloys

Nickel-iron alloys have been extensively used as a magnetic material. In particular the Permalloy composition of 80 % wt. nickel and 20 % wt. iron ($Ni_{80}Fe_{20}$) is of great technological significance. First discovered in 1914 by Gustav Elmen at Bell Laboratories [15] it has been widely used as an inductor core material [13], for magnetic shielding [16, 17] and in patterned magnetic recording media [18, 19].

Permalloy's attractive properties include a high relative permeability and low coercivity. Figure 1.3 shows the variation in the initial permeability across the range of nickel-iron alloy compositions, which demonstrates the benefit of the Permalloy composition.

A fundamental issue regarding the deposition of nickel-iron in microfabrication is the intrinsic stress. Intrinsic stress can be compressive or tensile and occurs *via* numerous mechanisms including void formation and the incorporation of foreign atoms [21, 22, 23]. High levels of stress can cause delimitation and the failure of MEMS device. This has led to various methods to assess and reduce stress in the Permalloy films. Methods for the determination of stress include wafer bow measurements [24, 25], the use of quartz resonators [26], cantilever measurements [27, 28], and Raman spectroscopy [29]. Within The University of Edinburgh, methods for the rapid spatial mapping of deposited films using cantilever test structures have been developed and were available for this work [30, 31, 32].

1.1.3 Deposition Methods

In the context of microfabrication there are two methods available for the deposition of nickel-iron alloys: sputtering and electrodeposition (either electroless or electrodeposition). Nickel-iron films can be deposited as blanket films or as patterned structures by combining these methods with lithographic techniques.

1.1.3.1 Sputtering

Sputtering is one of the most widely used physical vapour deposition (PVD) methods. Typically argon ions (Ar^+) are used to bombard a metal target which ejects target atoms. These atoms then travel to the substrate in a vacuum and coat the wafer. For the deposition of alloys a target quantitatively enriched in the metal which gives a lower sputtering yield, is used to produce a film with the desired composition.

Sputtering is typically suitable for the deposition of films in the 10 to 1000 nm range. This is due to the practical limitation of the deposition rate, which is typically up to 100 nm/min [23]. For the deposition of thicker films liquid phase methods (electroless or electrochemical deposition) are typically used.

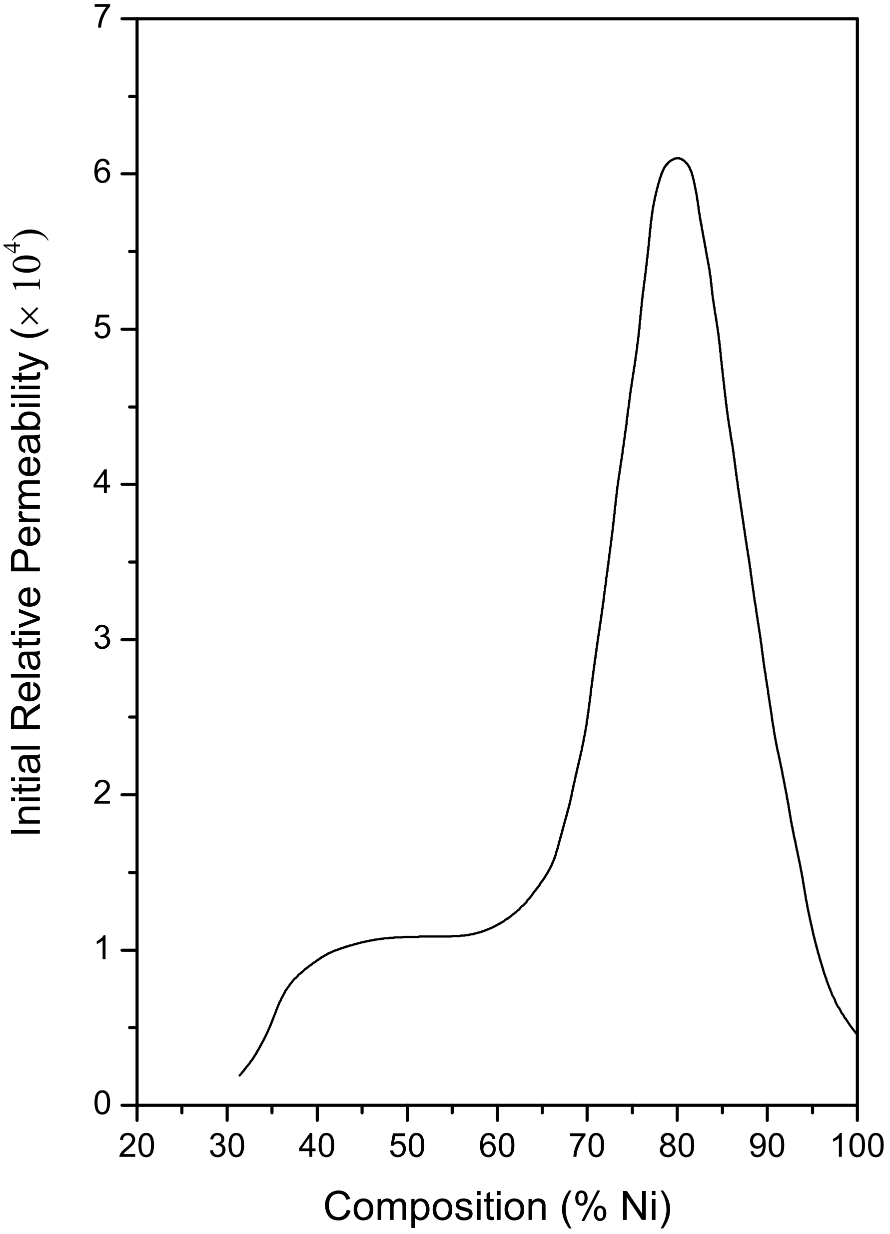

Figure 1.3: Initial relative permeability ($\mu_r = \mu/\mu_0$) of nickel-iron alloys as a function of composition. Adapted from reference [20].

1.1.3.2 Electrodeposition

A commonly used approach for the deposition of nickel-iron films is electrodeposition. Electrodeposition is the deposition of a material (in this case a metal or metal alloy) onto a substrate *via* the reduction of (metal) ions from an electrolyte. The reduction can be achieved by two different methods: 1) Electroless deposition, where the electrons required to reduce a species are provided by a reducing agent. 2) Electrochemical deposition, where the necessary electrons are provided through an electrically connected cathode driven by an external power supply.

Electrodeposition can be an excellent method of deposition due to the ability to rapidly deposit thick films (up to 100's µm). Using this method deposition rates vary widely but rates of up to 10 µm/min can be achieved [33]. Electrodeposition methods also enable the bottom-up filling of trenches during the fabrication process.

1.1.4 Regulation

REACH is a European Union regulation concerning the registration, evaluation, authorisation and restriction of chemicals. This legislation originally came into force on the 1st of June 2007. Among other objectives it aims:

> "To provide a high level of protection of human health and the environment from the use of chemicals."

As part of this legislation the SIN (Substitute It Now) list was compiled by The International Chemical Secretariat (ChemSec), Sweden, to identify substances of very high concern with the aim to reduce the use of harmful chemicals [34].

Existing electrodeposition baths for nickel, nickel-iron and other nickel alloys contain the additive boric acid (H_3BO_3, Figure 1.4). Following numerous toxicology studies and assessments [35, 36, 37, 38, 39, 40] boric acid currently appears on the candidate list for REACH status as it "may impair fertility" and "may cause harm to the unborn child" [41]. For this reason it has been encouraged that a suitable replacement for boric acid be sought in nickel and nickel-iron electrodeposition electrolytes.

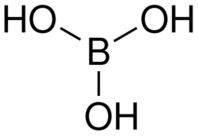

Figure 1.4: Boric acid

1.1.5 Fundamental Electrochemistry

In addition to the practical applications of electrodepositing nickel-iron films there are some aspects which are of interest to fundamental electrochemistry. The nickel-iron system exhibits a phenomena known as anomalous deposition. This is where the less noble metal, iron, deposits preferentially compared to the more noble nickel. Thermodynamically this is not expected as is discussed further in Section 1.3.2.

To enable the rapid deposition of smooth and level films, additives are required in electrodeposition baths. The function of these additives in the bath is of interest, particularly if there is a requirement to replace them with benign alternatives. There are numerous postulated roles for boric acid in these baths deposition bath which are discussed in Section 1.2.2.

If the fundamental role of additives and the deposition mechanisms are known then this enables the identification of potential alternatives to boric acid as an additive in the electrolyte. With the identification of an alternative a new deposition process can be then be designed and optimised to give deposits with the desired physical properties.

The remainder of this chapter gives an overview of the electrochemical literature regarding the deposition of nickel and nickel-iron alloys.

1.2 Electrodeposition of Nickel

The electrodeposition of nickel is used to give nickel films for a wide range of applications which are usually based upon its non-corrosive or heat resistant properties. Significant use of nickel occurs in the automotive industry, in the production of turbines and in the chemical industries. The world wide production of nickel is approximately 2 400 000 tonnes *p.a.,* with electrodeposition accounting for approximately 150 000 tonnes *p.a.* [42]. Due to the technological importance of nickel electrodeposition it has been widely studied in the literature.

1.2.1 History of the Introduction of Boric Acid

One of the earliest recorded instances for the deposition of nickel was in 1837 by G. Bird [43]. He claimed to have deposited a crust of nickel on a platinum cathode from chloride and sulfate salts over the course of "some hours". Soon after, in 1843, the first commercial electrolyte was developed by Bottger consisting of an aqueous solution of nickel and ammonium sulfates [44]. This remained in use for around 70 years. In 1869 Dr. Issac Adams Jr. patented a nickel electrodeposition bath that involved deposition from nickel ammonium sulfate [45] which resulted in the first commercialisation of nickel plating in the United States.

The next major advancement in the electrodeposition of nickel was the use of boric acid to aid rapid nickel plating. In 1916 Oliver Watts first used boric acid to overcome excessive hydrogen evolution on the cathode and found it led to "superior quality and adherence to ordinary nickel plate" [46]. The Watts bath consisted of nickel chloride, nickel sulfate and boric acid and to this day these components remain the foundation of most modern Ni electroplating baths.

Watts type electrolytes remain popular for decorative plating, generally with the addition of organic additives. With the addition of these additives, modern baths result in the deposition of bright deposits with good leveling properties and low internal stress over a range of current densities [33]. The nature of these additives and mechanism by which they function is discussed in Section 1.2.5.

Further types of nickel plating baths have been developed, most notably sulfamate containing electrolytes [47]. Although not used for decorative plating, sulfamate baths are used for functional plating and electroreforming [48].

For the purposes of rapid deposition there are advantages associated with an all-chloride bath. All-chloride baths have been demonstrated to display different morphological properties [49, 50]. In addition, they have been shown to have improved throwing power (the ability to deposit a uniform thickness over an irregularly shaped cathode) [51]. Deposits from all-chloride baths tend to withstand the use of high current densities and have a finer grain size, be harder and be stronger than deposits from the Watts bath. However, these deposits tend to result in higher stressed films [33].

1.2.2 The Role of Boric Acid

Since boric acid was introduced in the Watts bath its role has been studied and debated. There have been numerous suggestions for the role of boric acid. With a view to replacing boric acid in the electrodeposition bath the major roles suggested in the literature are now reviewed and assessed.

1.2.2.1 Action as a buffering agent

One of the suggestions for the role of boric acid is to act as a buffering agent [52]. This would reduce the extent of hydrogen evolution by minimising the pH rise at the electrode surface [52]. However, the bulk pH for a nickel bath is maintained at approximately 4.0 where boric acid does not make an effective buffer. The speciation diagram for boric acid is shown in Figure 1.5 which demonstrates the lack of buffering capacity at the lower pH range. This is due to the dominant reaction, $H_3BO_3 \rightleftharpoons H_2BO_3^-$, having a $\mathrm{pK_a}$ of 9.23. Therefore, all the boric acid would be present as $\mathrm{H_3BO_3}$.

To explain this discrepancy, the presence of a weakly bound nickel-borate complex has been postulated [53]. Among other similar systems, it has been demonstrated that the buffering capacity of a $\mathrm{NiSO_4 + H_3BO_3 + Na_2SO_4}$ solution is greater than that for $\mathrm{H_3BO_3 + Na_2SO_4}$ alone. From the pH titration data Tilak suggests the presence of the species $\mathrm{Ni(H_2BO_3)_2}$ with a $\log K$ between 3.8 and 4.9. Despite its suggested presence from pH titration data there is no additional experimental evidence for the presence of such a species.

Furthermore, a species ability to buffer at an electrode surface is dependent on kinetics. The dissociation of the acid must be able to take place quickly enough for protons to be available at the electrode surface where there is a high pH. Horkans' data [54] suggests that boric acid dissociates too slowly to provide significant buffering effects at the electrode.

1.2.2.2 Action as a Catalyst

It has been claimed that boric acid acts as a homogeneous catalyst for nickel deposition [56, 57]. Hoare reported that the rate of nickel deposition, when compared to the hydrogen evolution reaction, was directly proportional to the concentration of boric acid between 0.1 and 0.25 M concentrations. He states that boric acid reduces the overpotential required to deposit nickel to

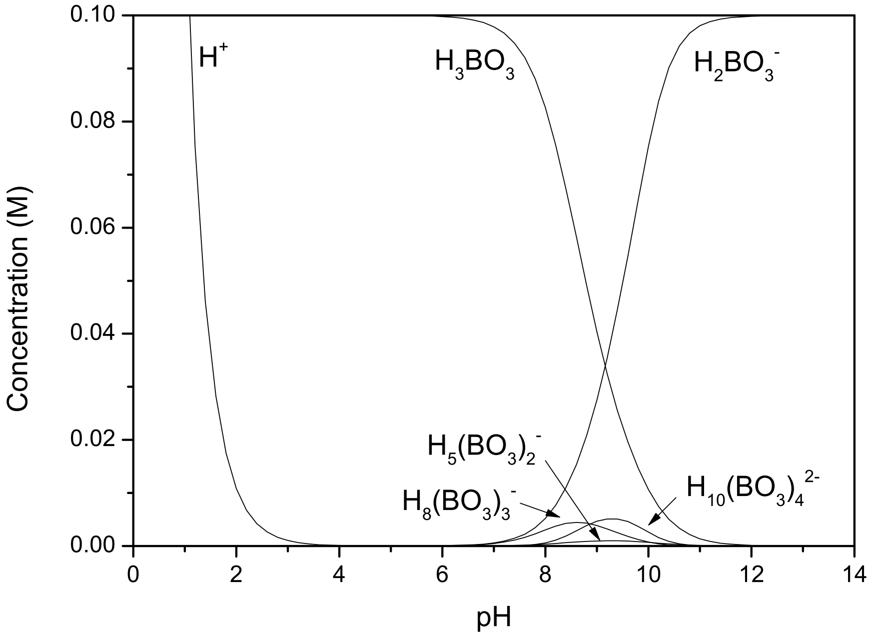

Figure 1.5: Speciation diagram for 0.1 M boric acid. $\log K$ values from reference [55].

the extent that nickel is deposited instead of hydrogen. However, this could instead be due to the suppression of the HER (see Section 1.2.2.3).

1.2.2.3 Suppression of the Hydrogen Evolution Reaction (HER)

It has been demonstrated that boric acid reduces the extent of the hydrogen evolution reaction during deposition. The presence of boric acid has been shown to increase the coulombic efficiency for the deposition of nickel [58].

Horkans claims that boric acid could be co-adsorbed onto the electrode surface which reduces the effective area of the electrode [54]. In this study a comparison of boric acid's effects on the HER in sodium chloride and sodium sulfate solutions was made. In chloride solutions it was postulated that boric acid must compete for sites on the electrode, whereas for the sulfate solution there is little competition. Linear sweep voltammetry on a RDE showed that for the sulfate solution the limiting current was reduced and there was a decrease in the slope suggesting the adsorption of boric acid on the electrode.

1.2.2.4 Reduction of Passive Film Formation (*i.e.* hydroxides)

The formation of hydroxides on the electrode is a significant issue during electrodeposition. The formation of nickel hydroxide is due to an increase in the surface pH at the electrode which results in the precipitation of $Ni(OH)_2$. Yin claims boric acid adsorbs on certain active sites and stabilises the nickel ion preventing passivation of the electrode [59]. In the absence of boric acid, deposits on the electrodes were examined and shown to be nickel hydroxide [60]. However, the formation of hydroxides may also be achieved by the reduction of the pH change through H^+ donation from H_3BO_3.

1.2.3 Nickel Deposition Mechanisms

The generally accepted mechanism for the deposition of nickel is two consecutive one-electron transfers involving an adsorbed complex [61, 62, 63]. The general form of this mechanism is

$$Ni^{2+} + X^- \rightarrow NiX^+ \tag{1.2}$$

$$NiX^+ + e^- \rightarrow NiX_{ads} \tag{1.3}$$

$$NiX_{ads} + e^- \rightarrow Ni + X^- \tag{1.4}$$

where the species X^- has been suggested to be OH^-, SO_4^{2-} or Cl^-. In the Watts bath it has been demonstrated that the X^- anion is Cl^- and the rate determining step is the first electron transfer (Equation 1.3) [64].

Oriňáková *et al.* examined electrochemical deposition from the Watts bath on paraffin impregnated graphite electrodes (PIGE) [65], by using cyclic voltammetry, elimination voltammetry and chronoamperometry. They concluded that in a sulfate electrolyte the hydrogen evolution reaction enabled an increase in pH, the accumulation of OH^- and the formation of the $NiOH^+$ electroactive species. For a chloride electrolyte the mechanism involved $NiCl^+$ as the charge transfer species.

There have been a number of studies of nickel deposition from unbuffered solutions [62, 66]. From cyclic voltammetry it was shown there are two successive reduction reactions which take place. In this case the deposition mechanism (Equations 1.5–1.8) is suggested to occur *via* a $Ni(OH)^+$ (or chloride containing) species.

$$Ni^{2+} + H_2O \rightleftharpoons Ni(OH)^+ + H^+ \tag{1.5}$$

$$Ni(OH)^+ + e^- \rightarrow Ni(OH)_{ads} \tag{1.6}$$

$$Ni(OH)_{ads} + Ni^{2+} + 2e^- \rightarrow Ni + Ni(OH)_{ads} \tag{1.7}$$

$$Ni(OH)_{ads} + e^- \rightarrow Ni + OH^- \tag{1.8}$$

In the presence of oxygen there is the precipitation of Ni(OH)$_2$ brought about by an enhanced local pH change due to oxygen reduction ($O_2 + 4e^- + 2H_2O \rightarrow 4(OH^-)$). The formation of nickel hydroxide reduces the adsorption of the reactive intermediate, Ni(OH)$^+$ and therefore suppresses reaction 1.6.

Epoelboin and Wiart have studied the mechanism for nickel deposition by applying electrochemical impedance spectroscopy (EIS) [62, 61]. In these works they demonstrate that the electrode kinetics are highly sensitive to the type of anion (either chloride or sulfate). In the chloride electrolyte there was little dependance of the kinetics on the pH. An inductive loop at low frequencies indicated that nickel deposition was slowly activated with an increase in potential. For the sulfate electrolyte the kinetics were shown to be dependent on an interaction with hydrogen evolution. From this work they mechanistically suggested the following reactions.

$$2(H^+ + e^-) \rightarrow H_2 \tag{1.9}$$

$$Ni^{2+} + e^- \rightarrow Ni^+_{ads} \tag{1.10}$$

$$Ni^+_{ads} + e^- \rightarrow Ni \tag{1.11}$$

$$Ni^+_{ads} + H^+ + e^- \rightarrow Ni^+_{ads} + H^*_{ads} \tag{1.12}$$

$$2H^*_{ads} \rightarrow H_2 \tag{1.13}$$

$$Ni^+_{ads} + H^*_{ads} + e^- \rightarrow Ni + H_{incl} \tag{1.14}$$

They proposed the generation of a strongly adsorbed form of hydrogen, H^*_{ads}, through the slow reaction 1.12. The slow rate of this reaction essentially makes it act as an inhibitor for hydrogen evolution. H^*_{ads} can then be consumed through hydrogen evolution (Equation 1.13) or be included into the deposit (Equation 1.14).

Gómez *et al.* have studied the initial stages of nickel deposition on vitreous carbon [67] and then on platinum, nickel and iron substrates [67, 68] using cyclic voltammetry and potential step methods. In these studies, differing morphologies of nickel were found depending on the deposition potential. In explanation they proposed two types of mechanisms resulting in the differing deposits. At low overpotentials the first steps would involve the reduction of Ni^{2+} to Ni^{+} followed by further reactions leading to nickel deposition. This mechanism was suggested to lead to the compact, uniform deposits. At higher overpotentials a disproportion mechanism was proposed. The initial reduction of Ni^{2+} would occur as previously and then disproportion could occur simultaneously with reaction 1.17, which results in hydrogen evolution.

$$Ni^{2+} + e^- \rightarrow Ni^+ \tag{1.15}$$

$$Ni^+ + Ni^+ \rightarrow Ni + Ni^{2+} \tag{1.16}$$

$$Ni^+ + H_2O \rightarrow NiOH^+ + H \tag{1.17}$$

In their later study [68] it was concluded that the hydrogen evolution reaction in blank electrolytes was mass transfer controlled. It was demonstrated that hydrogen atoms adsorbed strongly on the electrodeposited nickel and that different metallic substrates influence the morphology over short deposition times. Inhibition due to adsorbed hydrogen occurred across the range of potentials they applied (-650 to -800 mV *vs.* Ag/AgCl). With sufficient pH change, hydrogen evolution and nickel hydroxide precipitation was apparent forming black, non-adherent deposits.

There have been attempts to model the electrode response and validate the model against experimental data (steady-state polarisation curves and EIS). Santana and coworkers [69] derived their kinetic model by considering two distinct species, $[\mathrm{Ni(OH)}]^{+}{}_{\mathrm{ads}}$ and $[\mathrm{Ni(OH)}]_{\mathrm{ads}}$, as described by Equations 1.18–1.21.

$$Ni^{2+} + H_2O + e^- \rightleftharpoons Ni(OH)^+_{ads} + H \tag{1.18}$$

$$Ni(OH)^+_{ads} + Ni^{2+} + 2e^- \rightarrow Ni(OH)^+_{ads} + Ni \tag{1.19}$$

$$Ni(OH)^+_{ads} + e^- \rightleftharpoons Ni(OH)_{ads} \tag{1.20}$$

$$Ni(OH)_{ads} + Ni^{2+} + 2e^- \rightarrow Ni(OH)_{ads} + Ni \tag{1.21}$$

Using various assumptions such as electrochemical reactions follow Tafel's law and the Langmuir isotherm applies for adsorbed species their model matched well with experimental data in the pH range 4 to 6. Above this pH range the model was seen to break down which they attributed to the precipitation of hydroxides at the electrode which introduces additional kinetic factors.

In a separate study, by Vazquez-Arenas and Pritzker, a model was proposed based on reactions 1.22-1.25 [70].

$$Ni^{2+} + e^- \rightarrow Ni^+_{ads} \tag{1.22}$$

$$Ni^+_{ads} + e^- \rightarrow Ni \tag{1.23}$$

$$H^+ + e^- \rightarrow H_{ads} \tag{1.24}$$

$$2H_{ads} \rightarrow H_2 \tag{1.25}$$

In this model it was assumed that nickel reduction occurred through consecutive reductions (1.22 and 1.23) without defining the rate determining step. The HER was assumed to proceed *via* the Volmer-Tafel mechanism (Equations 1.24 and 1.25). The adsorption and desorption of boric acid was taken into consideration where boric acid blocked the formation of H_{ads} but not $Ni^+{}_{ads}$.

This model was applied to the electrode response on an RDE and to EIS. Through comparison with experimental data it was concluded that this model supported a mechanism of consecutive one electron nickel reduction steps with the first reduction being the rate determining step. Additionally the presence of boric acid was shown to have minimal effect on the electrode response for nickel deposition and the HER. In their EIS model they fitted the rate constants and charge transfer coefficients reactions 1.22 to 1.25. The sensitivity of each parameter was examined by changing it's

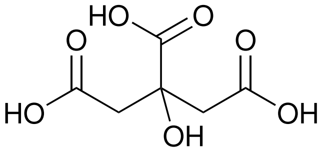

Figure 1.6: Citric acid

value by 5 % with the remaining variables fixed. It was found the model was highly sensitive to the rate constant and charge transfer coefficient for the the first electron transfer of nickel (reaction 1.22). This implies that for nickel reduction the rate determining step is the the first electron transfer.

1.2.4 Studies of Citric Acid Electrodeposition Baths

With a view to eliminating the use of boric acid from the nickel-iron electrodeposition bath benign alternatives must be sought. An important limitation is that the bath must be stable in the presence of iron (II). For example, there are a number of studies using acetate baths for the deposition of nickel [71, 72, 73]; however, iron (II) acetate is insoluble in water. One possible alternative is citric acid (Figure 1.6). The use of citric acid in electrodeposition of nickel and its alloys can be split into two distinct classes. The first is where citric acid or sodium citrate has been added to a bath which still contains boric acid [74, 75, 76, 77]. In these cases it has generally been added as an additional complexing agent to stabilise the bath (*i.e.* to prevent the precipitation of non-soluble species). The other case is where nickel has been deposited in a bath not containing boric acid. This is of course more relevant to our purposes.

Citric acid is a tri-protic acid. Each successive deprotonation (Equations 1.26–1.28) has $\mathrm{pK_a}$ values of 3.13, 4.76 and 6.39. Citric acid is then ideally placed to buffer around the pH of 3 where nickel-iron baths are typically used due to the multiple species found present at this pH (as shown in Figure 1.7).

$$H_3Cit \rightleftharpoons H_2Cit^- + H^+ \qquad pK_a = 3.13 \tag{1.26}$$

$$H_2Cit^- \rightleftharpoons HCit^{2-} + H^+ \qquad pK_a = 4.76 \tag{1.27}$$

$$HCit^{2-} \rightleftharpoons Cit^{3-} + H^+ \qquad pK_a = 6.39 \tag{1.28}$$

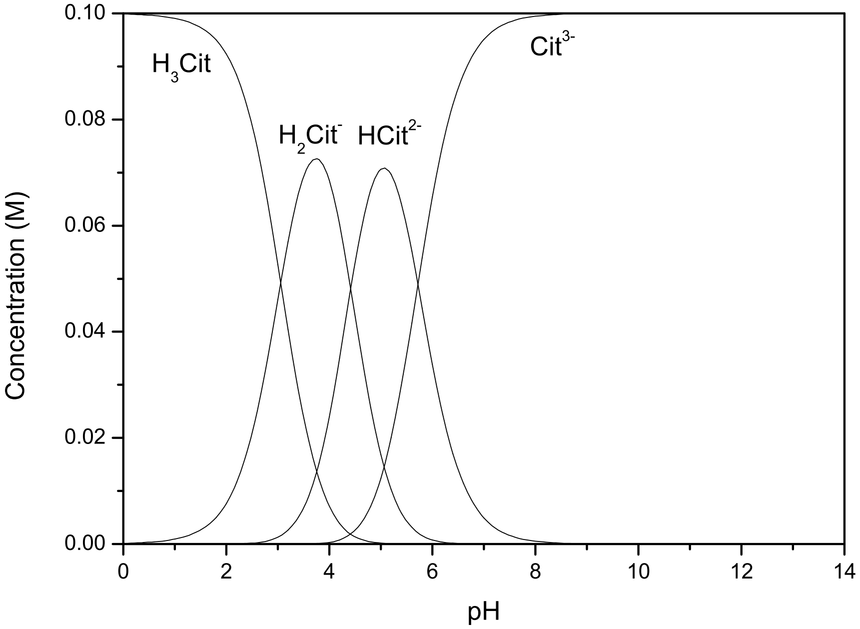

Figure 1.7: Speciation diagram for 0.1 M citric acid. $\log K$ values from reference [55].

There have been studies of the behavior of citric acid or the citrate anion at electrode surfaces. One area of focus is the electrochemical decomposition of citric acid. UV-spectral analysis demonstrated the decomposition of citric acid during prolonged oxidative electrolysis [78]. Trettenhahn and Köberl studied the anodic decomposition of citric acid on gold and stainless steel electrodes and detected the formation of carbon dioxide using FTIR-spectroscopy [79].

In the study of Berkh *et al.* they performed electrolysis at potentials between 0 and -1.4 V *vs.* SCE. By using high resolution X-ray photoelectron spectroscopy (HR-XPS) to examine the electrodeposited films produced at the electrode they found evidence for the formation of hydrocarbons, esters, alcohols, ketones and carbonate groups [80]. Even under open circuit conditions they suggested citrate underwent a catalytic reaction on a Pt electrode.

$$Citrate \rightarrow Acetone - 1,3 - dicarboxylate + CO_2 + 2e^- \tag{1.29}$$

They concluded that citric acid not only acts as a complexing agent, but can form many, potentially polymeric, species. By using time of flight mass spectroscopy (TOF-MS) they found evidence for higher mass species ($C_{17}H_5O_{10}$, $C_{15}H_6O_{10}Na$, $C_{19}H_6O_7Na$) which may partially block the electrode surface during electrodeposition. This blocking of the electrode may lead to reduce the rate of hydrogen evolution.

There are a number of examples where boric acid free, citric baths have been investigated. Doi *et al.* demonstrated the deposition of nickel from a citric bath and compared the effects of additives on the deposits [81]. In this work, they demonstrated the brightening effects of saccharin and butynediol (separate and in combination) which showed a marked decrease in roughness when using the butynediol additive. With the addition of additives they measured a decrease in efficiency of the bath as well as changes in stress and hardness of the films.

In a second study Doi *et al.* examined the effects of pH on an additive free citric bath [82]. The efficiency of deposition was demonstrated to decrease as the pH was lowered, particularly below pH 4. The deposit hardness was also shown to decrease at pH 4, although the hardness of the deposit was always greater than that for the citric acid-free bath. A change in surface morphology and crystallographic orientation favouring Ni <100> was also observed below pH 4.

The work of Li *et al.* compares the behavior and deposits of a citric bath to a traditional Watts bath [83]. In this work they measure the coulombic efficiency against a number of parameters including pH, $NiSO_4$ concentration, sodium citrate concentration and temperature. The efficiencies were generally high, above 95 %. Lower pH (<4) was shown to decrease the efficiency. They measured the efficiency for deposits made between 15 and 65 °C. Between 25 and 65 °C similar efficiencies were measured whereas at 15 °C there was a sharp decrease in the efficiency.

Using linear sweep voltammetrey the polarization curves for different baths were compared. Their buffer-free bath (containing no citric or boric acid) was shown to require the lowest overpotential to deposit nickel. A more negative overpotential was required for the boric and citric baths, with larger still required for a bath containing both boric acid and sodium citrate. The authors explained this in terms of increased blocking of the electrode. Using XRD the dominant peak was shown to be due to the Ni(111) orientation. SEM images showed large grain sizes in the region of 1 μm.

There are even fewer examples where nickel-iron alloys have been deposited from a citric bath. Shimokawa and coworkers investigated the structural and magnetic properties of NiFe films deposited from a citric bath [84]. They deposited films onto copper plate at a current density of 200 mA cm^{-2}. The films they deposited exhibited acceptable magnetic properties with coercivities below 50 A/m. However, the coulombic efficiency for the deposits was between 20 % (for $Ni_{80}Fe_{20}$)

and 50 % (for $Ni_{50}Fe_{50}$). With this quantity of hydrogen evolution the bath is unsuitable for use in microfabrication.

1.2.5 The Role of Additional Additives

Further additives, in addition to boric acid, are added to nickel deposition baths to improve the properties of deposited films and are commonly referred to as brighteners, levelers or carriers. The use of these chemicals enables the deposition of bright, reflective and level films [85]. In addition they can provide good leveling or scratch filling characteristics. Additives can be roughly categorised (although not exclusively) according to their chemical nature, mechanism of adsorption at the cathode, or effect on the deposit.

One classification of additives is species which display rapid adsorption and desorption on the electrode, and are known as carriers or class I brighteners or control agents. The primary role of a carrier is to reduce the grain size of the deposits, which commonly leads to them being referred to as grain refiners. Reducing the grain size leads to increased lustre but does not provide mirror-bright deposits on its own [86]. Carriers are typically aromatic organic compounds which adsorb on the electrode. Examples include saccharin (Figure 1.8) [87, 88, 24, 89, 90], 2-butane-1,4-diol [91] and *p*-toluene sulfonamide [92]. Additional benefits of carriers include stress relief, which is of acute importance for MEMS device fabrication. The stress relieving properties of saccharin are widely known [24, 93]. The main drawback from the use of carriers is co-deposition which is the principle source of sulfur in deposits. Sulfur containing deposits lead to increased reactivity of the metal and lessened corrosion resistance [94]. A study using sodium allyl sulfonate containing a radioactive isotope S-35 demonstrated that the additive was preferentially incorporated into the deposit at high points on an irregular surface [95]. This implies the mechanism involves the preferential adsorption of the additive on peaks preventing deposition of the metal on these sites and is a mechanism by which larger grain growth can be inhibited.

A second classification is additives which display specific adsorption to the electrode surface and are known as levelers or class II brighteners or polarizers. These leveling agents help produce bright deposits with good ductility. In addition they enhance the leveling ability over a wide range of current densities. Examples include the use of thiourea [96] and coumarin [97]. Brighteners tend to result in increased internal stress in films and also make them more brittle [33].

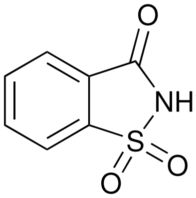

Figure 1.8: Saccharin

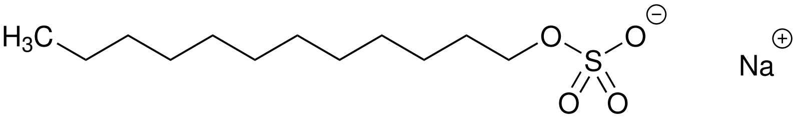

Figure 1.9: Sodium Dodecyl Sulfate (SDS)

Surfactants are often used as additives in electroplating baths. Commonly also known as wetting agents, surfactants reduce the surface tension and help to prevent bubble formation on the electrode surface. Surfactants also display specific adsorption on the electrode surface which enhances their leveling properties. A commonly used surfactant in nickel plating is sodium dodecyl sulfate (SDS, Figure 1.9).

1.3 Electrodeposition of Nickel-Iron

The electrodeposition of alloys enables the production of deposits with superior properties compared to single metals. Alloyed deposits can be harder, more corrosion resistant, denser or have enhanced magnetic properties. There are, of course, a huge number of possible alloys for deposition and for this reason there is a large range of literature on the subject. In this section an introduction to the principles of alloy deposition is made before an examination of the literature on anomalous deposition with respect to nickel-iron.

1.3.1 Principles of Alloy Deposition

The deposition of an alloy requires a minimum of two metals to be deposited on the electrode. At its simplest this can be envisioned through the potentiostatic codeposition of two metals (A and B). Metals A and B both have their own polarisation curves where, if a potential, V, is applied, then the current densities at which the metals deposit are i_A and i_B. Provided the metals deposit independently of each other they deposit in the compositional ratio $i_A n_B / i_B n_A$ where n

is the number of electrons. If a different composition is required the deposition potential and/or concentration can be changed and the ratio i_A/i_B changes. It is important to note that due to the difference in polarisation curves the species A and B in solution are consumed at different rates and replenishment of the faster depositing species through mass transport is required to avoid depletion at the electrode and thus maintain a uniform deposit.

The deposition of alloys can be further complicated by hydrogen evolution. Careful selection of the deposition parameters (*eg.* potential) are required to avoid significant hydrogen evolution and reduction in deposition efficiency.

Despite these complications the deposition of alloys (and indeed single metals) can be considered to occur through three main steps:

1. **Metal ion transport** - The hydrated ion in the electrolyte must be transported to the electrode. This can occur *via* diffusion due to a concentration gradient at the electrode or convection.
2. **Electron transfer** - The hydrated ion reaches the cathode and is adsorbed.
3. **Incorporation** - The adsorbed ad-atom is physisorbed and traverses the surface of the cathode until it encounters a stable chemical site and is incorporated into the growing lattice.

1.3.2 Anomalous Deposition

A number of alloy deposition systems display anomalous behavior, that is where a thermodynamically less noble metal (with a lower reduction potential) is unexpectedly deposited preferentially to a more noble metal (with a higher reduction potential). This behavior is most commonly observed in the iron group (Fe, Co, Ni) alloys *eg.* Co-Fe, Zn-Co, Zn-Ni, Ni-Fe, Zn-Ni-Co, Ni-Fe-Mo and Fe-Ni-Co [98, 71, 74, 99, 75, 100, 101].

Dahms and Croll proposed an early model for the anomalous deposition of nickel-iron [102]. Their model was based upon the suppression of nickel deposition caused by hydroxide formation. The explanation for anomalous deposition was based upon the observation that this only occurred when the surface pH was increased enough for the formation of hydroxides and the suppression of nickel deposition only occurred in the presence of iron. From this they attributed the suppression of nickel deposition to the presence of $Fe(OH)_2$ which preferentially absorbed on the electrode and blocked the deposition of nickel.

Later work demonstrated anomalous behavior in systems with a lower surface pH than that required by the model of Dahms and Croll [103]. Due to this, Hessami and Tobias constructed a mathematical model to explain their experimental results on rotating disc electrodes [104]. This model was based upon mass transport and interfacial kinetics determining the surface concentrations of metal ion, metal hydroxide ions and the surface pH. The model considered the following homogenous reactions:

$$H_2O \rightleftharpoons H^+ + OH^- \tag{1.30}$$

$$FeOH^+ \rightleftharpoons Fe^{2+} + OH^- \tag{1.31}$$

$$NiOH^+ \rightleftharpoons Ni^{2+} + OH^- \tag{1.32}$$

with the metal atoms then being reductively deposited from the free (hydrated) metal ion or the ion complex.

$$FeOH^+ + 2e^- \rightleftharpoons Fe + OH^- \tag{1.33}$$

$$Fe^{2+} + e^- \rightleftharpoons Fe \tag{1.34}$$

$$NiOH^+ + 2e^- \rightleftharpoons Ni + OH^- \tag{1.35}$$

$$Ni^{2+} + e^- \rightleftharpoons Ni \tag{1.36}$$

Additionally, the hydrogen reaction was postulated as occurring by the reduction of a proton or the splitting of water.

$$H^+ + e^- \rightleftharpoons \frac{1}{2}H_2 \tag{1.37}$$

$$H_2O + e^- \rightleftharpoons \frac{1}{2}H_2 + OH^- \tag{1.38}$$

The results of this model were compared to the observed effects of varying RDE rotation speed and solution pH. With respect to agitation the model was in qualitative agreement with experimental data; however, the effect on alloy composition appeared more complex. Increasing agitation at low potentials decreased the iron content of the deposits, whereas at more negative potentials it enriched the iron content. At low potentials they attributed this to the build-up of $FeOH^+$ while maintaining the Fe^{2+} concentration. Increasing the agitation reduced the buildup of hydroxide and hence lowered the Fe content in the deposit. At more negative potentials both Fe^{2+} and $FeOH^+$ became depleted. Increased agitation reduced the extent of depletion and resulted in a higher Fe content.

An alternative model based upon competitive adsorption, as opposed to physical blocking on the surface, was proposed by Matlosz [105]. Their mechanism was based around the two step irreversible reduction of the metals:

$$M(II) + e^- \rightarrow M(I)_{ads} \tag{1.39}$$

$$M(I)_{ads} + e^- \rightarrow M(s) \tag{1.40}$$

During codeposition of metals they proposed a mechanism based upon competitive rate of formation of the adsorbed intermediate ion $M(I)_{ads}$. The free surface coverage, θ_o during deposition is then

$$\theta_o = 1 - \theta_{Ni} - \theta_{Fe} \tag{1.41}$$

The free surface coverage is the same for both metals and therefore the ratio of the deposition rates is independent of the surface coverage.

$$\frac{r_{Ni}}{r_{Fe}} = \frac{k_{1,Ni} c_{Ni(II)}}{k_{1,Fe} c_{Fe(II)}} \tag{1.42}$$

$$= \frac{k^\circ_{1,Ni} c_{Ni(II)}}{k^\circ_{1,Fe} c_{Fe(II)}} \exp[(b_{1,Ni} - b_{1,Fe})V] \tag{1.43}$$

where $k_{1,M}$ is the potential dependent rate constant and $b_{1,M}$ is the Tafel slope for the reaction 1.39. Therefore, if $b_{1,Fe} > b_{1,Ni}$ the rate of nickel formation can decrease relative to iron resulting in anomalous deposition.

Following this, they considered the effect of surface pH taking into account the formation of the hydroxide complexes $FeOH^+$ and $NiOH^+$. They concluded that changes in surface pH had minimal effect on the iron composition and the difference in Tafel slope between nickel and iron deposition was the dominate effect.

They then extended the model to include transport effects for comparison with RDE data [106]. They calculated the efficiencies and composition for deposits made on a RDE at different potentials and rotation speeds. They calculated that the efficiency should increase with an increased current density and there would be an increase in the iron composition at low current densities followed by a slow decline at higher current densities. They also calculated that there would be an increase in the iron content with increased agitation. These conclusions agreed with the experimental data.

The work of Zech and Podlaha built upon the model of Matlosz by including both inhibiting and enhancing effects [107, 108]. Their experimental work has demonstrated that along with the known decrease in reaction rate for the more noble metal there was an increase in reaction rate for the less noble metal. To allow for this enhancing effect further catalytic reactions (1.44 and 1.45) were included to improve the model.

$$M_2(II) + M_1(II) + e^- \rightarrow [M_2M_1(III)]_{ads} \tag{1.44}$$

$$[M_2M_1(III)]_{ads} + e^- \rightarrow M_2(s) + M_1(II) \tag{1.45}$$

Vaes *et al.* assessed the hydroxide model of Hessami and Tobias against the inhibition model of Matlsoz (then built upon by Zech and Podlaha) [109]. With comparisons to polarisation curves they determined that the hydroxide model was based upon two key characteristics: the Tafel parameters were chosen to favour iron reduction and that hydroxide formation could take place to any extent. The hydroxide model was therefore considered unrealistic. Additionally, they suggested that the intermediate species were not hydroxides and the inhibiting role of iron hydroxide was widely overstated.

In 2007 these models were examined again by Larson [110]. He wanted to investigate some of the key assumptions made in these models. The first of these commonly held assumptions is that the reactions taking place in solution occur infinitely fast compared to those on the deposition surface stating that as increased potentials are applied the reaction rates at the surface are not slow compared to that in solution. To test this approximation he repeated the calculations to include a full kinetic treatment of the homogeneous chemistry. In the bath examined (sulfate based containing boric acid and sodium sulfate) this included the presence of 17 distinct species.

The second assumption to be addressed was the possibility of metal hydroxide formation. Where hydrogen evolution leads to a increase in pH at the electrode surface it has generally been assumed that this pH rise is insignificant or the buffering action negates any substantial pH change and hence the precipitation of hydroxides has been largely ignored. Where hydroxides have been taken into account (Dahms and Croll's hydroxide model) it is only at the electrode surface itself.

Larson's work focuses on the assumption of homogeneous equilibrium. From this it was put forward that by applying finite-rate homogeneous kinetics the surface concentration of Ni^{2+} would be reduced and $NiOH^{+}$ concentration would be further enhanced contradicting the conclusions of Vaes *et al.*

These models present viable mechanisms to explain anomalous deposition. However some predictive aspects of the models require further improvement. Quantitative prediction of the alloy composition currently remains out of reach. Further critical evaluation for the deposition mechanisms for the single metals with changing pH and solution composition is still required. It is also apparent that a definitive evaluation for the role of the metal hydroxide species in anomalous deposition is yet to be established.

In this thesis the mechanisms for anomalous deposition is not addressed directly. However, it is appropriate to compare the implications of these models to the behavior of the new boric acid free bath developed herein. The similarities and differences between deposits made in a boric bath and a citric bath may pave the way to evaluate and validate the role of boric acid in anomalous deposition.

1.4 Summary

Nickel and nickel-iron are functional materials with a wide range of uses across a large range of industries. Electrodeposition currently provides an efficient method for the deposition of these materials in a reliable manner. However, with the addition of boric acid on the candidate list for REACH status alternative methods to deposit films of these materials must be sought. The primary aim of this thesis is to develop an alternative electrodeposition bath to deposit nickel and nickel-iron which contains an environmentally benign alternative to boric acid.

In order to develop an alternative bath an understanding of the primary roles of boric acid should be made. In this chapter some of the suggested roles of boric acid have been highlighted and discussed. These roles include action as a buffer, action as a catalyst, suppressing the HER and reducing film passivation. Given these key roles, citric acid has been identified as an alternative to boric acid. However, a suitable bath for the production of high quantity nickel-iron films for use in MEMS production has remained elusive.

In this thesis a new bath based upon citric acid as an alternative to boric acid was pursued. Initially an existing boric acid bath can be used as a benchmark to enable the evaluation of any new plating bath. With understanding of the properties of the boric acid bath a new bath can then be developed and optimised.

Following the development of a new citric acid based bath to deposit nickel-iron investigation of the electrochemical behavior of this bath can be pursued. In addition, the properties of the deposited films should be characterised and compared to determine the suitability of the new bath as a direct replacement for existing, industrial, boric acid based baths.

Chapter 2

Theoretical Aspects

The following chapter outlines the background theory for measurement techniques used within this thesis. Initial focus is based on electrochemical methods. This is followed by a brief description of the electrochemical quartz crystal microbalance (EQCM). With the desire to deposit magnetic materials in this work there is finally a description of magnetic hysteresis in the context of ferromagnetic materials.

2.1 Electrochemistry

2.1.1 Electrolysis

An electrode can be induced to pass a current by the application of a potential (*e.g.* by applying a voltage or potential difference between the electrode and a reference electrode of constant potential). The current is a measure of the rate of exchange of electrons between the electrode and species in solution. This transfer of electrons can be either from the electrode to the species in solution (reduction) or from the species in solution to the electrode (oxidation). This is termed electrolysis. The total charge, Q, passed during electrolysis can then be measured by integrating the current, i, with respect to time according to Faraday's law.

$$Q = \int i dt \tag{2.1}$$

Assuming 100 % efficiency the mass, m, of species reacting at the electrode can then be calculated as

$$m = \left(\frac{Q}{F}\right)\left(\frac{M_w}{n}\right) \tag{2.2}$$

where F is Faraday's constant (96485 C mol^{-1}), M_w is the molecular weight of the species reacting at the electrode and n is the number of electrons required to convert the reactant to the product.

In the case where the reaction is not 100 % efficient due to an additional current (*e.g.* the HER) the coulombic efficiency (CE) for the reaction(s) of interest can be calculated. In the case of metal deposition the CE is simply obtained as a percentage from the ratio of mass deposited, m_{dep}, *vs.* the theoretically calculated value through Faraday's Law, m.

$$\text{Coulombic Efficiency} = \frac{m_{dep}}{m} \times 100 \tag{2.3}$$

2.1.2 Electrode Potentials

2.1.2.1 Equilibrium Potential

In this section the thermodynamics and kinetics of a general electron transfer reaction are considered.

$$O + ne^- \rightleftharpoons R \tag{2.4}$$

At thermodynamic equilibrium (where there is no overall current passing) the equilibrium potential, E, can be determined from the Nernst equation

$$E = E^{\ominus} + \frac{RT}{nF} \ln \frac{a_O}{a_R} \tag{2.5}$$

where $E^{\ominus}$ is the standard potential and $a_O$and a_R are the activities for the oxidised and reduced species. The activity of a species in solution is $a_i = \gamma_i c_i / c^{\ominus}$ where γ_i is the activity coefficient, c_i is the concentration of the species in solution and $c^{\ominus}$ is the standard concentration (1 mol dm^{-3}).

Alternatively the potential can be described using the formal potential, $E^{\circ\prime}$, as

$$E = E^{\circ\prime} + \frac{RT}{nF} \ln \frac{[O]}{[R]} \tag{2.6}$$

where

$$E^{\circ\prime} = E^{\ominus} + \frac{RT}{nF} \ln \frac{\gamma_O}{\gamma_R} \tag{2.7}$$

$[O]$ and $[R]$ are the concentrations of the oxidised and reduced species. Most notably for the deposition of a metal,

$$M^{n+} + ne^- \rightleftharpoons M \tag{2.8}$$

the Nernst equation can be simplified to

$$E = E^{\circ\prime} + \frac{RT}{nF} \ln[M^{n+}] \tag{2.9}$$

as the activity of the deposited metal is, by definition, unity.

2.1.2.2 Non-Equilibrium Potentials

For a reversible (rapid) electron transfer and if a potential is applied to the electrode, E, the system will locally seek to achieve a new equilibrium where the concentration of the oxidised and reduced species are changed at the electrode to fulfill the Nernst equation for the applied potential. Thermodynamically this means that an increase in the potential from $E^{\circ\prime}$ results in an anodic (positive) current as $R \to O$ and a decrease results in a cathodic (negative) current as $O \to R$.

If the reaction is under kinetic control (e.g. for an electrochemically irreversible reaction) there is a limitation on the rate of reaction for oxidation/reduction. The rate of electron transfer (in moles cm^{-2} s^{-1}) is then determined as a product of the electrochemical rate constant, $k_{a/c}$, and the concentration at the electrode surface, $(c_{O/R})_{x=0}$.

$$\begin{aligned} Rate\,of\,oxidation &= k_a(c_R)_{x=0} && (2.10)\\ Rate\,of\,reduction &= k_c(c_O)_{x=0} && (2.11) \end{aligned}$$

These rate constants each have a dependance on the electrode potential, generally of the form

$$\begin{aligned} k_a &= k^\circ \exp \frac{\alpha_a nF(E-E^\ominus)}{RT} && (2.12)\\ k_c &= k^\circ \exp \frac{-\alpha_c nF(E-E^\ominus)}{RT} && (2.13) \end{aligned}$$

where α_a and α_c are the anodic and cathodic transfer coefficients, where $0 < \alpha < 1$ and k° is the standard rate constant and E is the applied potential [111].

To obtain the current density the rate of reaction can be multiplied by nF (to obtain A cm^{-2}). An expression for the overall current density, j, at any potential can then be determined by combining the anodic and cathodic current densities (note that j_c is negative by convention).

$$\begin{aligned} j &= j_a + j_c \\ &= nFk_a^\circ c_R \exp \frac{\alpha_a nFE}{RT} - nFk_c^\circ c_O \exp \frac{-\alpha_c nFE}{RT} && (2.14) \end{aligned}$$

Defining the overpotential as $\eta = E - E_e$ the exchange current density at equilibrium j_0 can be defined where the overall current density is zero (at $\eta = 0$).

$$j_0 = nFk^\circ c_R \exp \frac{\alpha_a nF(E_e - E^\ominus)}{RT} = -nFk^\circ c_O \exp \frac{-\alpha_c nF(E_e - E^\ominus)}{RT} \qquad (2.15)$$

Equations 2.14 and 2.15 lead to the Butler-Volmer equation [111].

$$j = j_0 \left(\exp\left[\frac{\alpha_a nF\eta}{RT}\right] - \exp\left[-\frac{\alpha_c nF\eta}{RT}\right]\right) \qquad (2.16)$$

In the case where $j_a \gg j_c$, as found at positive overpotentials the Butler-Volmer equation becomes

$$j = j_a = j_0 \exp\left[\frac{\alpha_a nF\eta}{RT}\right] \tag{2.17}$$

Taking the logarithm of this equation results in the Tafel equation

$$\ln j = \ln j_0 + \frac{\alpha_a nF}{RT}\eta \tag{2.18}$$

$$= \ln j_0 + \frac{\alpha_a nF}{RT}E + \frac{\alpha_a nF}{RT}E_e \tag{2.19}$$

Therefore a plot of $\ln|j|$ *vs.* η or E should provide a linear slope with gradient $\alpha_a nF/RT$ for oxidation and $-\alpha_a nF/RT$ for reduction.

In the case where $j_a \ll j_c$, as found at negative overpotentials the Tafel equation becomes

$$\ln(-j) = \ln j_0 + \frac{-\alpha_c nF}{RT}\eta \tag{2.20}$$

$$= \ln j_0 + \frac{-\alpha_c nF}{RT}E + \frac{-\alpha_c nF}{RT}E_e \tag{2.21}$$

and hence a plot of $\ln|j|$ *vs.* η or E should provide a linear slope with gradient $-\alpha_c nF/RT$ for reduction.

2.1.3 Mass Transport

In general there are three different forms of mass transport to an electrode. These methods are diffusion, convection and migration.

2.1.3.1 Diffusion

The transport of a species caused by a concentration gradient is called diffusion. Under diffusion only conditions the simplest model is linear diffusion to a planar electrode. The rate of diffusion, or flux, is described by Fick's first law:

$$Flux = -D\frac{\mathrm{d}c}{\mathrm{d}x} \tag{2.22}$$

where D is the diffusion coefficient (cm^2 s^{-1}) and x is the distance normal to the working electrode. Fick's second law (2.23) describes the changing diffusion profile with time.

$$\frac{\partial c}{\partial t} = \frac{\partial^2 c}{\partial x^2} \tag{2.23}$$

Applying Fick's law to a reaction at the electrode surface an expression for the current density is obtained.

$$j = nFD_R\left(\frac{\partial c_R}{\partial x}\right)_{x=0} = -nFD_O\left(\frac{\partial c_O}{\partial x}\right)_{x=0} \tag{2.24}$$

2.1.3.2 Convection

The mass transport of species to an electrode can be increased with the introduction of convection. The rotating disc electrode provides a forced-convection system where the hydrodynamics can be described precisely. Figure 2.1 shows a representation of the solution flow at the electrode. The model used for mass transport to the electrode is the Nernst diffusion model. In this model the solution can be seen to consist of two regions (see Figure 2.2). The bulk solution is strongly mixed by stirring and maintains a constant, uniform bulk concentration. There is then a boundary layer (the Nernst diffusion layer) where the solution is essentially stagnant in the x-direction and diffusion is the only means of mass transport in this direction. This second layer has a thickness, δ.

The boundary layer thickness is dependent on the rotation frequency of the disc, W in Hz. The mathematical model predicts the thickness of the boundary layer to be:

$$\delta = \frac{0.61\nu^{1/6}D^{1/3}}{W^{1/2}} \tag{2.25}$$

where ν is the kinematic viscosity (viscosity/density) of the solution in cm^2 s^{-1} and D is the diffusion coefficient in cm^2 s^{-1}.

At a steady state the concentration gradient in the diffusion layer is considered linear across thickness δ and therefore the current density is written as

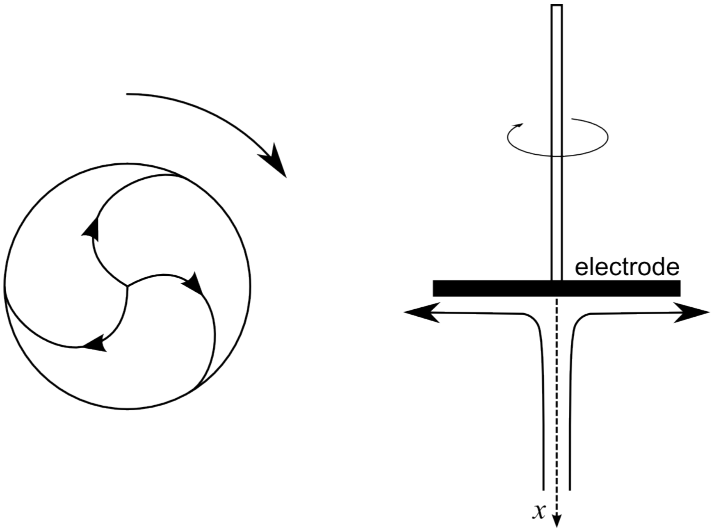

Figure 2.1: Solution flow at a rotating disc electrode (RDE). Left: a view from below showing the rotational movement of the solution at the electrode. Right: side view showing the flow approaching the electrode. Adapted from Reference [111].

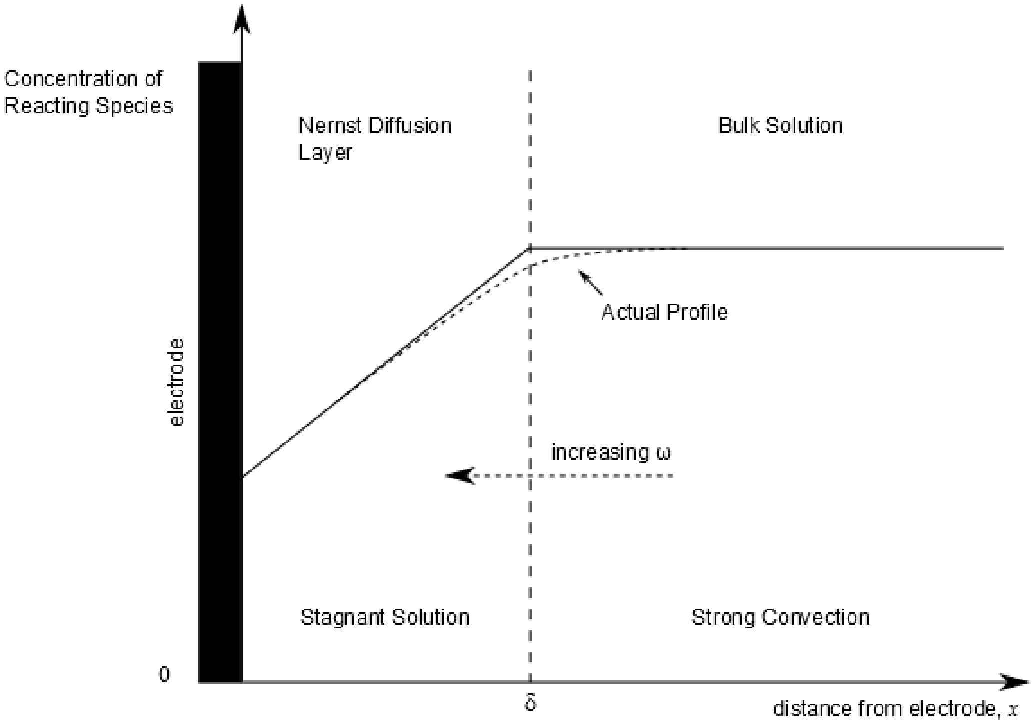

Figure 2.2: Nernst diffusion model for the oxidation of R where there is no O in bulk solution at a RDE.

$$\begin{aligned} j &= nFD_R \left(\frac{\mathrm{d}c_R}{\mathrm{d}x} \right)_{x=0} \\ &= nFD \frac{c_R - (c_R)_{x=0}}{\delta} \end{aligned} \tag{2.26}$$

At high enough overpotentials the surface concentration of the reacting species, $(c_R)_{x=0}$, becomes zero at the electrode. Any further increase in potential cannot decrease the surface concentration further and the mass transport limiting current density then becomes

$$j_{lim} = \frac{nFDc_R}{\delta} \tag{2.27}$$

Substituting Equation 2.25 in 2.27 one obtains the Levich equation [111].

$$j_{lim} = \frac{1.554nFD_R^{2/3}c_R W^{1/2}}{\nu^{1/6}} \tag{2.28}$$

This demonstrates that the current density is proportional to the square root of the rotational frequency.

2.1.3.3 Migration

Migration occurs due to the presence of charged species in a potential field. Migration is an electrostatic phenomena and in many cases is not an important form of mass transport if there is a large excess of inert electrolyte which effectively screens the electrode and provides little penetration of the electric field from the electrode surface. If the reactant is present in high concentrations, as occurs in an industrial electrolysis cell, then the effects of migration may become apparent.

2.1.4 Potentiostatic Methods

In this section we consider the current-time transient for a reaction at a planar electrode under diffusion only conditions. In this example we consider a potential step from a value where the current density is zero to a potential far away from the equilibrium value where either oxidation or reduction occurs.

Initially there is a large step in potential, this effectively causes the electrode to change the ratio of c_R/c_O so that essentially only O or R is present. For a reduction the electrode rapidly converts O to R resulting in a large and negative current density and the concentration of O drops (almost to zero) at the electrode surface. Over time diffusion will result in the minimising of the concentration differences throughout the solution. This results in the flux (and hence current) of O to the electrode surface decreasing over time and the thickness of the zone depleted through diffusion increasing as the experiment continues.

From Fick's first and second laws the shape of the current-time transient can be determined and is known as the Cottrell equation. The current density at a time, t, is

$$j = \frac{nFD^{1/2}(c_{bulk} - c_{x=0})}{\pi^{1/2}t^{1/2}} \tag{2.29}$$

for an electrode at a fixed potential.

2.1.5 Galvanostatic Methods

Galvanostatic methods are similar to a potential step method except in this case the current is stepped from zero to an oxidative or reductive value. Under diffusion controlled conditions the resulting potential-time transients can be explained as follows.

For current to flow a reaction must be taking place at the electrode. The electrode will therefore apply the minimum potential required to pass the constant current required. If there is a redox species present which will oxidise or reduce easier than the solvent then the potential will be driven to its appropriate redox potential. As the concentration of this species is reduced towards zero the potential will change, reflecting the change from the Nernst equation or the Butler-Volmer equation, until the concentration of this redox species is such that it can no longer maintain the required current density. Then the potential will move to the potential for the next, available reaction that can maintain this current.

The transition time between the start of the experiment and this change in potential is predicted by the Sand equation [112].

$$\tau = \frac{\pi^{1/2}c_{bulk}nFAD^{1/2}}{2i} \tag{2.30}$$

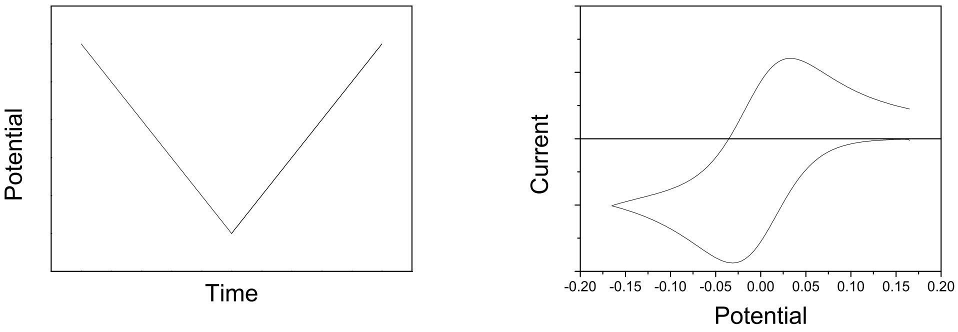

Figure 2.3: Triangular waveform used in cyclic voltammetry (left) and response for a one electron reversible redox couple (right)

2.1.6 Cyclic Voltammetry

Cyclic Voltammetry (CV) is a technique extensively used to study electrochemical systems. In a CV experiment a potential applied to a working electrode is changed linearly with time (at a constant potential sweep rate). At a given potential limit, the direction of the potential scan is reversed, whilst maintaining the sweep rate. This is the first cycle of a cyclic voltammogram. During the experiment there is a linear relationship between the applied potential and time. The response (current) is recorded and plotted against the applied potential. A typical wave form and response is shown in Figure 2.3.

Important factors in the design of the experiment include:

- the starting potential
- the potential limit at which the scan is reversed
- the sweep rate
- the number of cycles.

For CV analysis, typically only the first cycle is used, as there can be assumed to be no reaction before the onset of the scan. The shape of the CV curve can be explained in terms of the changing state of diffusion to the electrode. Considering a linear sweep for the reaction $O \rightarrow R$. If $E \gg E^{\ominus}$ there is no reaction. As the potential is swept to more reducing potentials the reduction of O to R begins and a (negative) current begins to pass. This increases exponentially as implied by Equation 2.13. During this initial part of a CV the diffusion is rapid and the reaction remains under electrochemical control. As the sweep progresses the surface concentration of the redox species becomes zero and the concentration profile extends further into solution. The rising current due to the increasing electrochemical reaction rate is then counterbalanced by a fall in current due to the decreasing rate of diffusion to the electrode. Hence the current peaks, then falls in magnitude as the reaction becomes diffusion controlled. Beyond this potential the current is under mass transport control and decays toward the steady state limiting current density due to the small amount of convective flow in an experimental measurement.

The potential is then swept in the reverse direction. At potentials far negative of the equilibrium potential for the O/R couple the surface concentration of O is unaffected and remains zero. The current continues to fall toward the steady state limiting current density. As the equilibrium potential for the O/R couple is approached the presence of both O and R is required to fulfill the Nernst equation for a reversible redox reaction. Therefore O is generated from R at the electrode surface and the current density passes through the axis and changes sign. The response again peaks as the oxidation reaction becomes diffusion controlled. Similarly to the forward scan, beyond this potential the current density is under mass transport control and decays toward the steady state limiting current.

During voltammetry for reactions involving phase formation (as for metal deposition) the shape is significantly different. During the cathodic sweep the scan is a similar shape to before and peaks as the reaction becomes diffusion controlled. On the reverse scan there may be the presence of a nucleation loop (Figure 2.4). This occurs when it is difficult to form stable nuclei on the electrode substrate and hence nucleation requires an increased overpotential. On the reverse scan the metal phase being deposited already exists and deposition is more favourable, resulting in a nucleation loop. Also in the reverse scan is a characteristic, sharp, stripping peak as there is no diffusion to the electrode required for the reaction to occur. The charge for metal stripping is limited by the amount of metal deposited on the electrode.

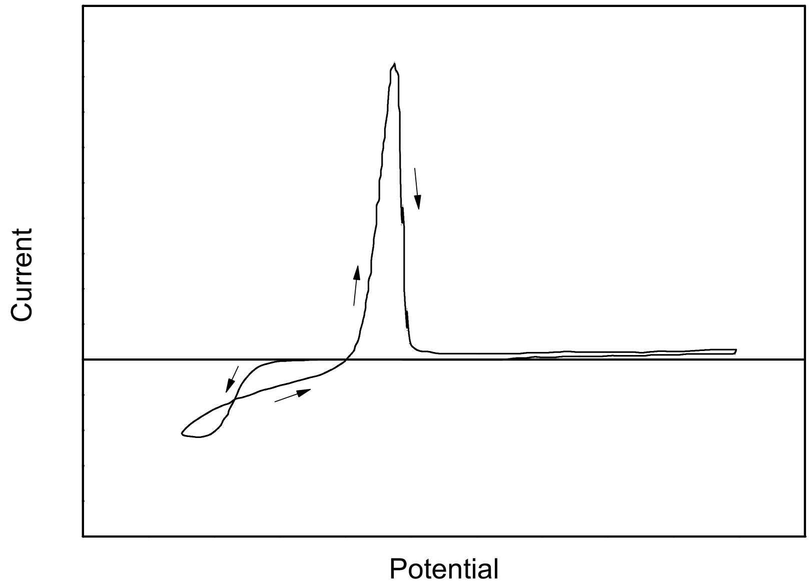

Figure 2.4: Metal deposition/stripping CV showing a nucleation loop (adapted from [113])

2.2 EQCM

The electrochemical quartz crystal microbalance (EQCM) is an excellent tool for the measurement of small mass changes at an electrode surface. The operation of a EQCM is described by the Sauerbrey equation [114, 115].

$$\Delta f = -C_f \times \Delta m \tag{2.31}$$

where Δf is the change in frequency, C_f is the sensitivity factor for the crystal and Δm is the change in mass per unit area. The Sauerbrey equation assumes any additional mass added to the crystal has the same acousto-elastic properties as quartz. This assumption is reasonable for a uniformly deposited, rigid, thin film.

The sensitivity factor (or Sauerbrey coefficient) is a fundamental property of the quartz crystal,

$$C_f = \frac{2n \times f^2}{\sqrt{\rho_{quartz} \times \mu_{quartz}}} \tag{2.32}$$

where f is the resonant frequency of the quartz crystal (Hz), ρ_{quartz} is the density of quartz (2.648 g cm^{-3}) and μ_{quartz} is the shear modulus of quartz (2.947×10^{11} g cm^{-1} s^{-2}). Combining Equations 2.31 and 2.32 gives

$$\Delta m = \frac{-\Delta f}{C_f} = \frac{(f_q - f)\sqrt{\rho_{quartz} \times \mu_{quartz}}}{2n \times f^2} \tag{2.33}$$

A 5 MHz crystal, as used in this study, has a calculated sensitivity coefficient of $C_f = 0.0566$ Hz ng^{-1} cm^2.

Up to this point the EQCM has been considered as a true mass sensor. In reality the overall frequency response of the EQCM is not solely dictated by the mass deposited on the surface but is a combination of many effects [116, 111].

Viscosity effects, where additional loading of the crystal is present due to immersion in a viscous medium, result in a decrease in the resonant frequency of the crystal. During typical electrochemical experiments the viscosity of the solution remains constant and is a negligible effect [111].

The resonant frequency has been shown to increase linearly with pressure at pressures up to 50 MPa [117]. During electrochemical experiments the pressure generally remains constant so this is a negligible effect.

The resonant frequency of the quartz crystal is dependent on the temperature. The change in frequency due to variation in temperature is commonly reduced by the use of AT-cut quartz which has a turn around point (or a point of inflection in the temperature *vs.* frequency plot) at 25 °C and therefore has good thermal stability around this temperature. In addition, if the experiment is performed at a constant temperature there should be minimal contribution to the frequency change [118].

Surface stress can have an influence on the crystal response. The effects of stress in a thin surface film have been discussed in literature [26, 119] and been shown to decrease the resonant frequency according to the equation $\Delta f_s = -K(f_0/d)\Delta\gamma$ where $\Delta\gamma$ is the change in surface tension, K is a constant dependent only on the crystal properties, f_0 is the fundamental frequency and d is the crystal thickness.

The surface roughness can drastically affect the frequency response [120]. Liquid can be incorporated into voids or trenches and become vibrationally coupled with the surface. If the surface roughness remains constant this effect is removed or can be minimised using calibration [121].

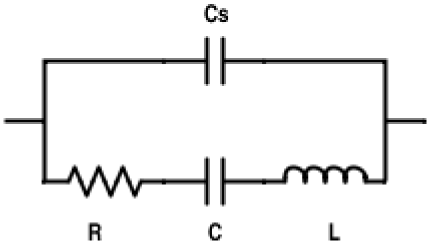

Figure 2.5: Equivalent circuit for a quartz crystal

Given that the frequency response of the EQCM can be dictated by a range of factors, a better representation of the overall frequency response is therefore

$$\Delta f = \Delta f_m + \Delta f_v + \Delta f_p + \Delta f_T + \Delta f_s + \Delta f_r \tag{2.34}$$

Where Δf_m is the mass response as described by the Sauerbrey equations, Δf_v is the viscosity effect, Δf_p the pressure effect, Δf_T the temperature effect, Δf_s the stress effect and Δf_r the roughness effect. Under certain conditions, as described previously, these effects can be minimised and the EQCM can be considered a true mass sensor, however careful consideration must be made when interpreting the frequency response.

Figure 2.5 shows the equivalent circuit for a quartz crystal. There are two branches to the circuit. The shunt branch contains a single Cs element and represents the shunt capacitance in addition to any capacitance from cables and fixtures. The motional branch contains R, C and L elements. It is the motional branch which varies with loading of the quartz crystal.

2.3 Magnetism

2.3.1 Magnetic Hysteresis

Magnetic hysteresis is where the magnetisation of a ferromagnetic material is dependent not only on the applied magnetic field but on the history of the magnet. This occurs when the dipoles in the ferromagnetic material become aligned in an applied magnetic field. Once this field is removed the dipoles remain aligned and the material remains magnetised. To demagnetise the material a magnetic field can be applied in the opposite direction. The behavior of a magnetic material can be represented by a plot of the magnetic induction, $\boldsymbol{B}$, against the applied field strength, $\boldsymbol{H}$.

Alternatively the magnetisation, $\boldsymbol{M}$, can be plotted against $\boldsymbol{H}$ (Figure 2.6). Each of these curves present the same information as a hysteresis curve can be represented by the general formula

$$\boldsymbol{B} = \mu_0(\boldsymbol{H} + \boldsymbol{M}) \tag{2.35}$$

For a soft ferromagnetic material the applied field,$\boldsymbol{H}$, is much smaller than the corresponding magnetisation values. Therefore $\boldsymbol{B} \cong \mu_0\boldsymbol{M}$ and plotting $\boldsymbol{B}(\boldsymbol{H})$ or $\boldsymbol{M}(\boldsymbol{H})$ makes negligible difference [122].

Figure 2.6 shows a typical hysteresis loop for a ferromagnetic material. If the material were initially demagnetised and a magnetic field applied gradually the magnetisation, $\boldsymbol{M}$, will follow the initial magnetisation curve (dashed line). As the field increases the magnetisation will asymptotically approach magnetic saturation, $\mathrm{M_s}$. When the field is reversed the magnetisation follows a different curve. On the return curve the point at which there is zero applied magnetic field is called the remanence. The reverse field, applied to return the material to zero magnetisation, is the coercivity, $\mathrm{H_c}$. If the field is further strengthened then saturation magnetisation is achieved again in the reverse direction.

Another important property of a ferromagnet is the permeability. The permeability of a material can be described as the ease in which a material can be magnetised. As a characteristic property, the permeability of a ferromagnet is not overly useful, as the permeability can be measured at any point on the hysteresis curve and a wide range of values obtained. The differential permeability $\mu' = \mathrm{d}\boldsymbol{B}/\mathrm{d}\boldsymbol{H}$ can be used however there is a dependance on the applied magnetic field. The most appropriate quantity to characterise the material is the maximum differential permeability, μ'_{max}, which usually occurs at the coercive points, $\mathrm{H} = \mathrm{H_c}$ and $\mathrm{H} = \mathrm{-H_c}$. The relative permeability is a dimensionless quantity which relates the permeability to the permeability of free space , μ_0.

$$\mu_r = \mu/\mu_0 \tag{2.36}$$

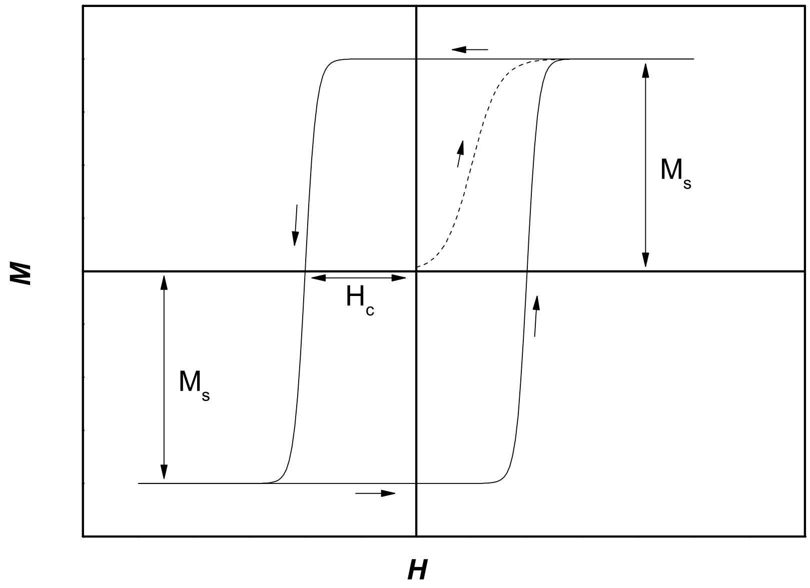

Figure 2.6: Example hysteresis loop for a ferromagnetic material. The dashed line indicates the initial magnetisation curve.

2.3.2 Magnetic Anisotropy

Another important feature is the directional dependance of magnetic properties. This is referred to as the magnetic anisotropy. Different types of magnetic anisotropy include:

- Magnetocrystalline anisotropy (due to crystal structure)
- Shape anisotropy (due to grain and sample geometry)
- Magnetoelastic anisotropy (due to stress)
- Induced anisotropy (due to process treatments)

Magnetocrystalline anisotropy leads to the presence of "easy" and "hard" directions of magnetisation. The energetically favourable direction for spontaneous magnetic alignment is the "easy axis". It is therefore easier to magnetise the sample in this direction compared to the "hard axis". If there is no preferential direction of magnetisation (unless under the influence of a magnetic field), the material is anisotropic and will not display hysteresis.

2.3.3 Magnetic Flux

The magnetic flux, Φ, is the product of the average magnetic field, $\boldsymbol{B}$, and the area perpendicular to which it penetrates, A.

$$\text{Magnetic Flux} = \Phi = \boldsymbol{B}A \tag{2.37}$$

In a B-H loop measurement, the magnetic flux can be measured at a pick-up coil. The magnetic flux measured at this coil is termed the “pick-up flux”.

Chapter 3

Experimental Materials and Methods

This chapter details the materials and methods used in this thesis. This includes a description of the electrodes used in this work and, when applicable, their fabrication methods and procedures for electrode cleaning.

Calibration experiments are presented for various techniques and electrodes. EQCM calibration was performed to ensure data obtained can be interpreted quantitatively. The collection efficiency for the rotating ring disc electrode was also performed using ferricyanide for use in further experiments. Various methods to determine coulombic efficiency were examined including dynamic measurements on the EQCM and thickness measurements.

Methods to characterise the deposited films are discussed. Test structures can be used to evaluate the strain in electrodeposited films and Greek cross test structure enable the measurement of the sheet resistance. X-ray fluorescence is discussed as a method for the evaluation of film composition and thickness.

3.1 Materials (chemicals)

The chemicals used in this thesis were provided from the following sources:

Sigma Aldrich: iron chloride ($FeCl_2.4H_2O$, ≥99.0 %), copper sulfate ($CuSO_4.5H_2O$, 99 %), lead acetate ($PbC_4H_6O_4$, 99 %), ammonium persulfate ($(NH_4)_2S_2O_8$, 98 %), potassium nitrate (KNO_3, 99+ %), sodium acetate ($C_2H_3NaO_2.3H_2O$, ≥99.0 %), sodium hydroxide ($NaOH$, ≥98.0 %), silver nitrate ($AgNO_3$, 99+ %), sodium nitrate ($NaNO_3$, ≥99 %), sodium saccharin hydrate ($C_7H_4NNaO_3S.xH_2O$, ≥98.0 %).

Fisher Scientific: boric acid (H_3BO_3), citric acid ($C_6H_8O_7$, 100.25 % assay), tri-sodium citrate ($Na_3C_6H_5O_7.2H_2O$, 99.0-101.0 % assay), sodium chloride (NaCl, ≥99.5 %), nitric acid (HNO_3, analytical reagent grade, s.g. 1.42).

Acros Organics: potassium ferricyanide ($K_3Fe(CN)_6$, 99 %).

VWR: sulfuric acid (H_2SO_4, 98 %).

BDH Chemicals: sodium dodecyl sulfate ($C_{12}H_{25}SO_4Na$).

Rohm and Haas Electronic Materials (DOW): Intervia™ CU 8540 Carrier, Intervia™ CU 8540 Additive.

3.2 Electrodes

Several types of working electrodes were used throughout this work. Platinum electrodes were purchased whereas copper electrodes were fabricated in-house. This section details the fabrication of the electrodes (if applicable) and cleaning methods prior to use.

3.2.1 Platinum Disc Electrodes

Platinum rotating disc electrodes (RDE) were sourced from Oxford Electrodes Ltd. The disc electrodes had an area of 0.387 cm^2. Rotating ring disc electrodes (RRDE) (Oxford Electrodes Ltd) with the same disc area were also used when appropriate. The collection efficiency for the ring was measured as 0.203 ± 0.002 as described in Section 3.3.1.2.

For cleaning, electrodes were polished mechanically with alumina paste of decreasing particle size from 1 µm to 0.3 µm (Bruker). The electrodes were cleaned electrochemically prior to use in 0.1 M H_2SO_4 using cyclic voltammetry. The potential was swept between -0.32 V and 1.40 V *vs.* SCE (see Section 2.1.6 on voltammetry) at a scan rate of 100 mV s^{-1}. A diagnostic voltammogram of a clean electrode is shown in Figure 3.1. Peaks for the oxidation and reduction of adsorbed hydrogen [111] are clearly visible at potentials of -0.08 V and -0.18 V for reduction and -0.17 V, -0.09 V and -0.05 V. The electrodes were deemed to be clean when sequential scans coincided and gave this diagnostic response.

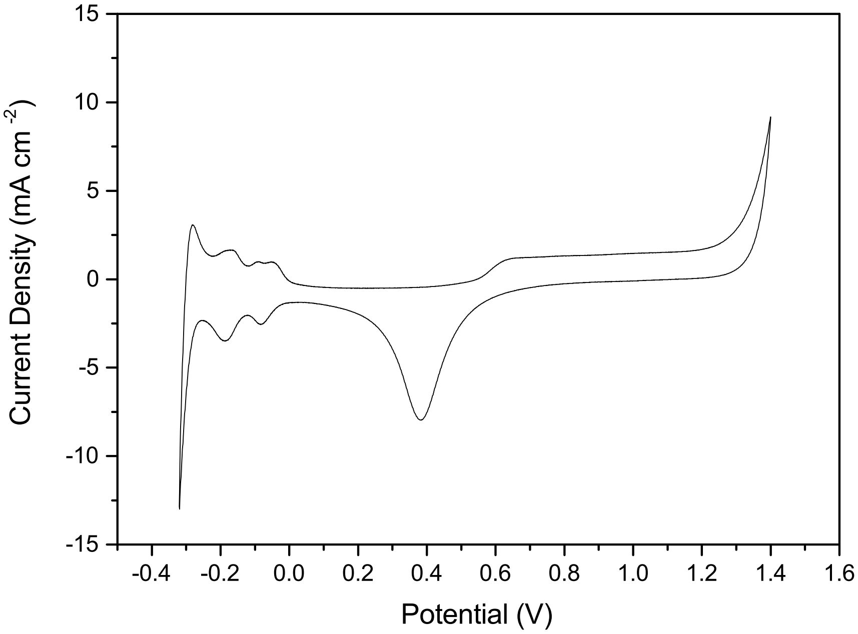

Figure 3.1: Cyclic voltammogram of a clean Pt electrode in 0.1 M H_2SO_4. The potential was swept between -0.32 and 1.4 V *vs.* SCE at a scan rate of 100 mV s^{-1}.

3.2.2 Platinum EQCM Electrodes

Platinum electrodes for use in the EQCM were sourced from Maxtek. This work uses AT-cut, 5 MHz, 1-inch diameter crystals. The AT-cut gives increased thermal stability due to the turn around point (or point of inflection) for the temperature coefficient at 25 °C. The electrode configuration is shown in Figure 3.2. The electrode material was platinum with a titanium adhesion layer. The exposed, working electrode, has an area of 1.37 cm^2. The sensitivity factor, C_f, for this crystal was calculated from the Sauerbrey equations (2.2) as 0.056 Hz ng^{-1} cm^2.

The electrodes were cleaned electrochemically prior to use in 0.1 M H_2SO_4 by cyclic voltammetry. The potential was swept between -0.38 V and 1.4 V at a scan rate of 100 mV s^{-1}. On the EQCM the change in frequency can be measured to determine when the electrode is clean in addition to the voltammetry. Figure 3.3 shows the change in frequency across sequential scans during the cleaning on an unused electrode measured at 1.4 V. The change in frequency during the voltammetry shows the oxide formation and oxide reduction as the frequency decreases and increases respectively. During sequential scans there was an overall increase in the frequency as mass is lost from the

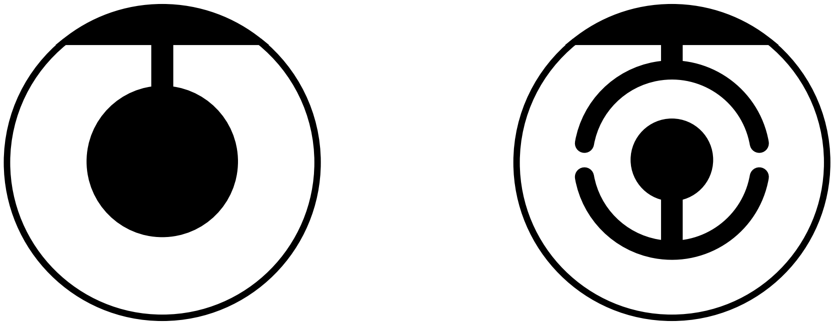

Figure 3.2: EQCM electrode configuration. Left: front side working electrode. Right: back side contact electrode. Adapted from [123].

EQCM. Cleaning was performed for a limited time (25 - 50 scans) until the frequency change was minimal.

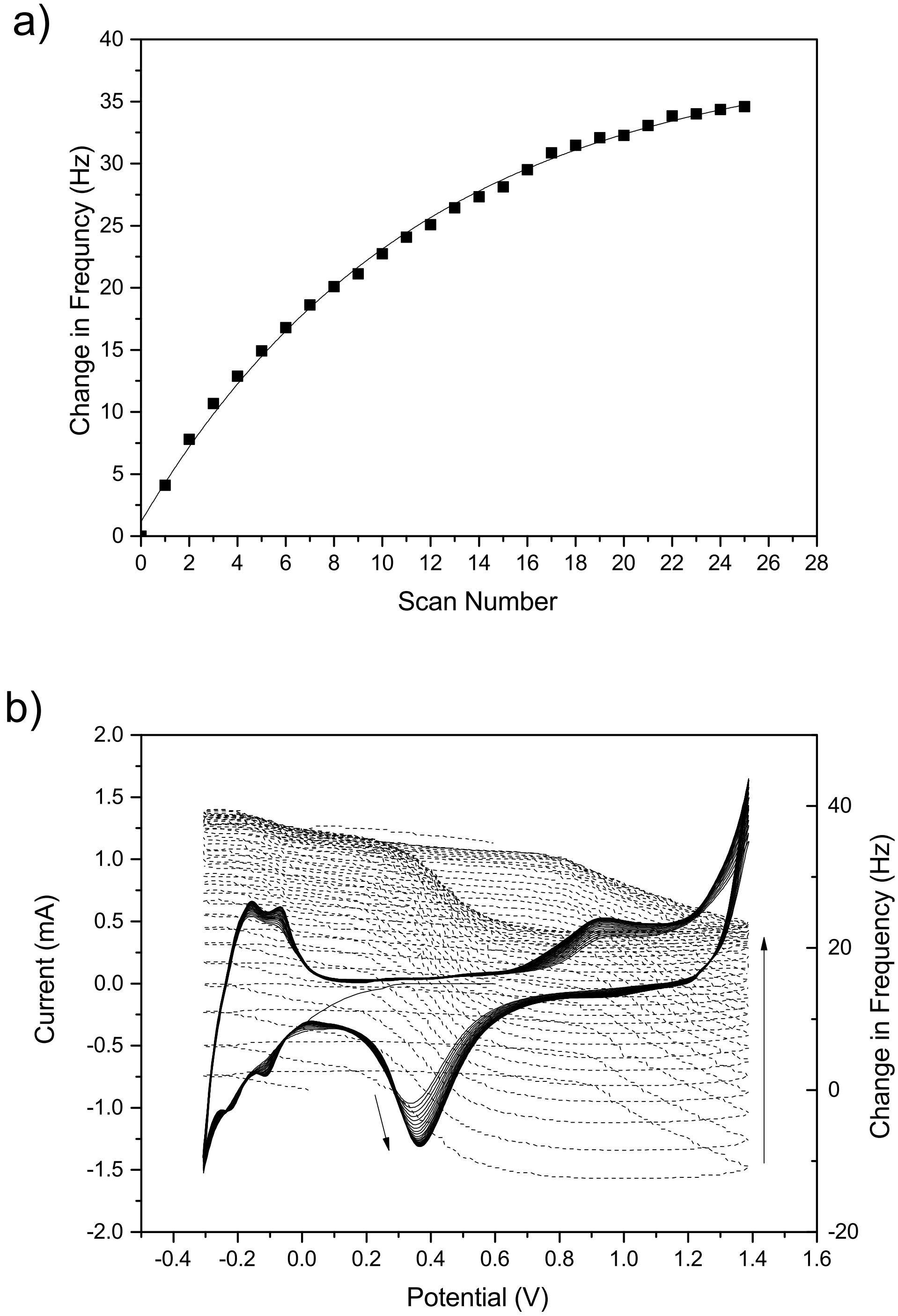

Figure 3.3: a) The net change in frequency from each CV cycle during the cleaning of a Pt EQCM electrode in 0.1 M H_2SO_4. b) The change in frequency (dashed) during electrochemical cleaning by cyclic voltammetry (solid) on the EQCM. The potential was swept between -0.38 and 1.4 V *vs.* SCE at a scan rate of 100 mV s^{-1}.

3.2.3 Fabrication of Copper Square Electrodes

Copper 1 cm × 1 cm square electrodes were fabricated using lithographic techniques. Fabrication was performed on 3 inch or 100 mm n-type <100> silicon wafers (IDB Technologies).

Isolation of the silicon carrier wafer was performed by depositing SiO_2 using a Surface Technology Systems (STS) plasma enhanced chemical vapor deposition (PECVD) tool. The deposition time was 15 minutes which resulted in a layer of approximately 0.7 µm as measured by reflectometry.

The following steps were used to deposit the Ti-Cu-Ti layers (collectively referred to hereafter as the seed layer) *via* sputtering using an OPT Plasmalab 400 magnetron sputtering system (Oxford Instruments). For some devices the final protective layer of titanium was omitted. An Argon mill was first performed for 10 minutes. Titanium was then deposited for 10 minutes (1 kW, 3 mTorr) followed by copper deposition for 30 minutes (1 kW, 3 mTorr) and then titanium deposition for 10 minutes (1 kW, 3 mTorr). These deposition times result in 30 nm layers of titanium and 300 nm layers of copper.

The wafer was then patterned using photo-lithographic techniques. Hexamethyl disilazane (HMDS) was used as a primer to promote adhesion of the photoresist to the metal surface. The photoresist, SPR-220-7 (MicroChem, Chestech), was then spin coated onto the wafer to obtain a layer of 6 to 10 µm thickness and then soft baked on a hot plate for 90 s. Using the appropriate mask, the wafer was then exposed using a MA-BA8 mask aligner (Karl Suss). The photoresist was then developed in MF-26 A developer (MicroChem) to reveal the electrode design. The wafer was then diced to obtain individual electrodes.

The mask design for copper square electrodes is shown in Figure 3.4. A single wafer produces a total of 10 electrodes. A 1 cm × 1 cm square at the bottom of the device is the working electrode area. At the top of the device is a smaller square for the bond pad to which a crocodile clip can be attached. Between the working electrode area and the bond pad is the insulating photoresist.

The top titanium layer was removed using a bath of 1 % HF to expose the copper electrode upon which deposition can be performed. Immediately prior to use the copper electrode was immersed in 10 % H_2SO_4 to remove the surface oxide and then rinsed with deionised water. A cross section of the final layers of the device is shown in Figure 3.5.

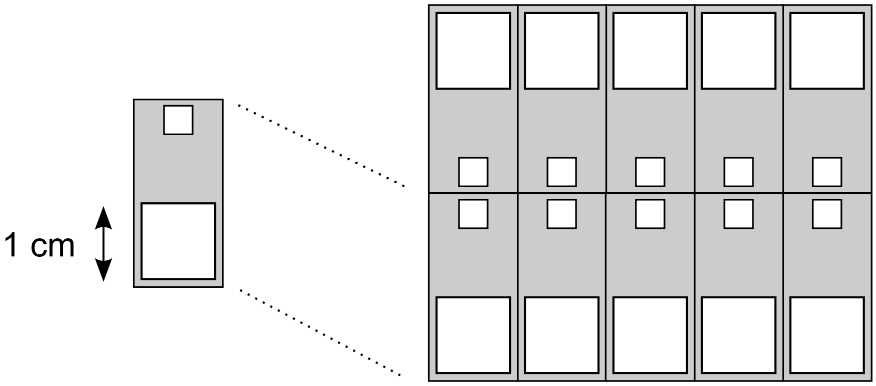

Figure 3.4: Mask design used for fabrication of 1 cm × 1 cm square electrodes. The white squares show the exposed area to make the bond pad (at the top of the electrode) and the 1 cm × 1 cm electrode area (at the bottom of the electrode) The grey area indicates the area covered by photoresist in the final device.

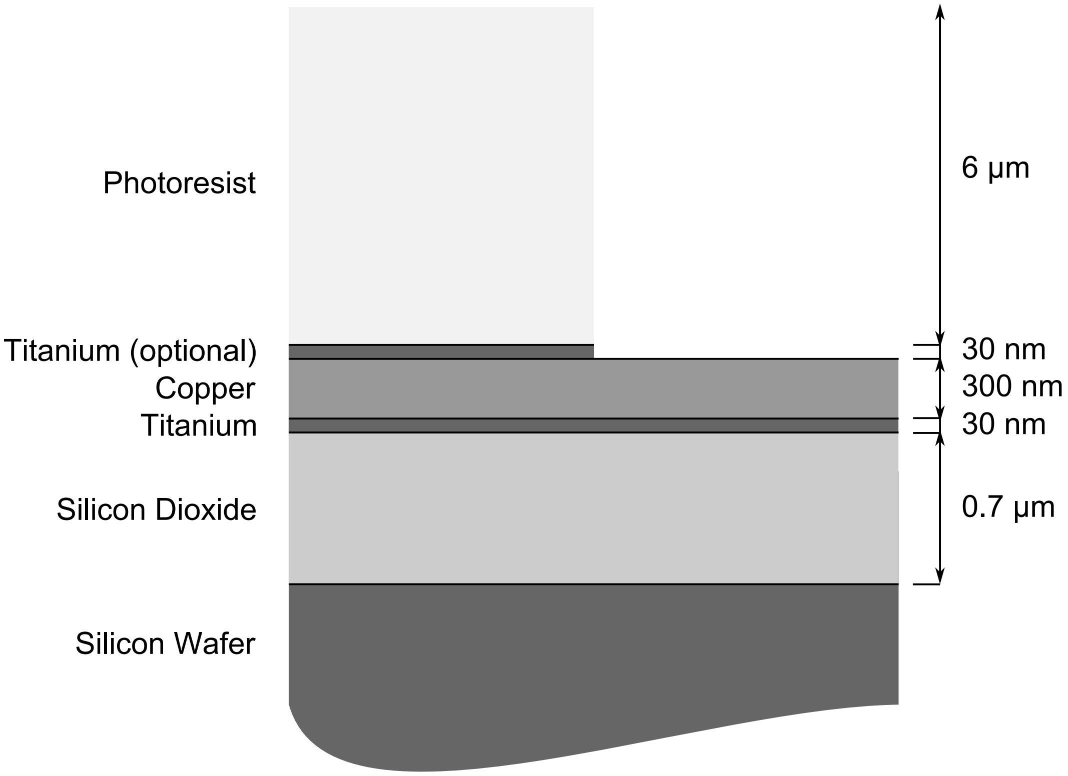

Figure 3.5: Cross-sectional representation illustrating the layers in fabricated copper electrodes (not to scale).

3.2.4 Fabrication of Copper Test Structure Chips

The fabrication process for copper test structure chips was designed to replicate the fabrication of MEMS structures but on a smaller, beaker scale. This is described in more detail in reference [124]. A brief description of this fabrication procedure follows.

The chips were fabricated using a similar process as in Section 3.2.3 but on a 200 mm wafer. Multiple lithography steps were used to pattern the chips using a combination of soda-lime glass and laser printed acetate masks. The patterning of the test structure was performed from the soda-lime mask. The acetate mask was then used to expose alternate rows of the test structures. Each die (Figure 3.6) contained two types of test structure: 36 linewidth test structures for electrical measurements and 64 rotating arm test structures (Figure 3.7) to indicate the strain in the film. Of these 64 rotating arm structures, the geometry was varied so that the ratio of the beam width to the beam offset, $\Delta Y/W$, was 1.75 for 32 structures, 1.5 for 16 structures and 2.0 for 16 structures. When diced, a single 200 mm wafer resulted in approximately 190 electrodes of dimensions 13 × 17 mm . The exposed electrode area for each chip was 0.765 cm^2.

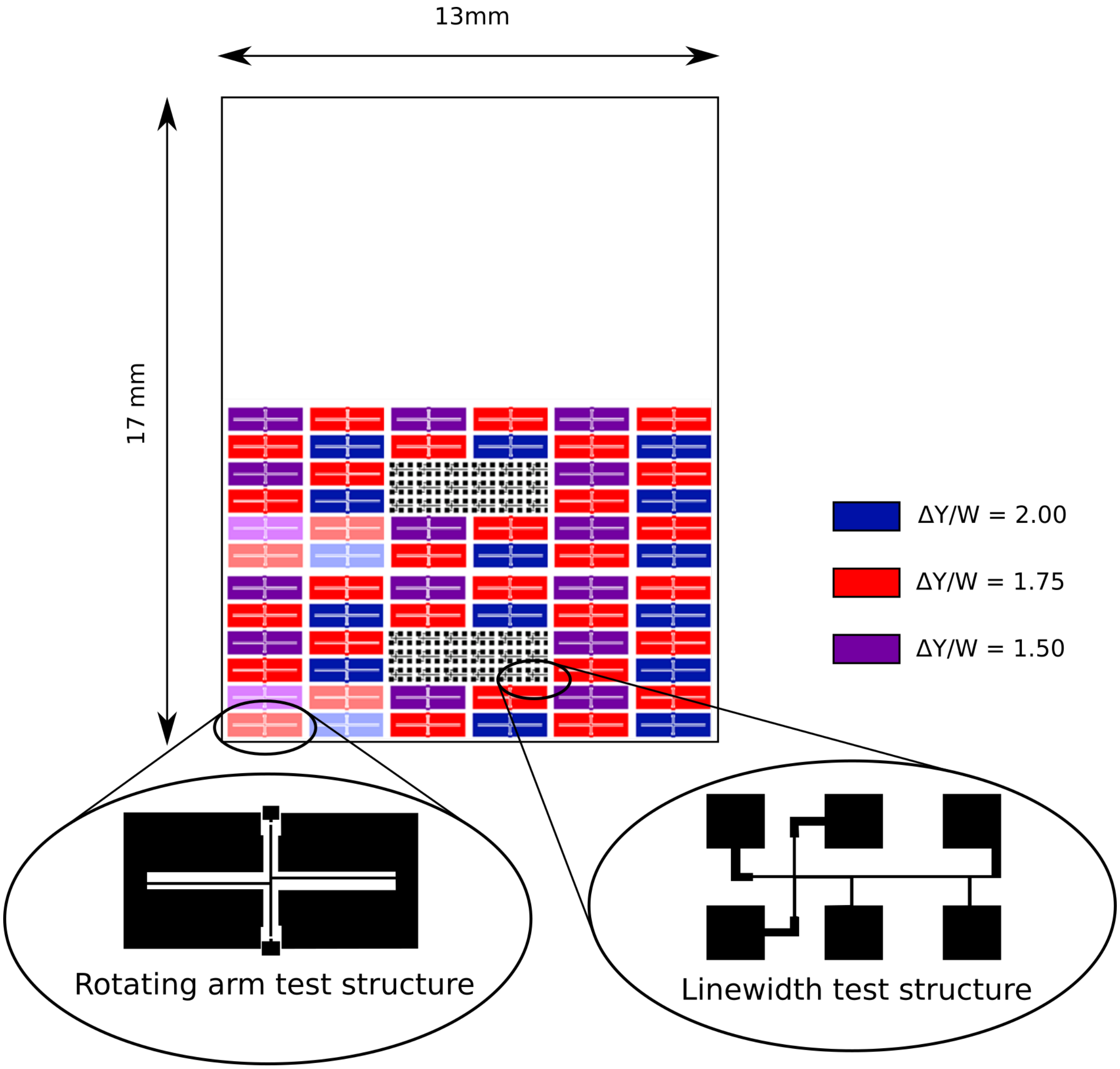

Figure 3.6: Layout for the test structure chip. The chip contains 64 rotating arms test structures with varying beam offset ($\Delta Y/W$) and 36 linewidth test structures Detailed layouts for the two test structures are shown in Figure 3.7.

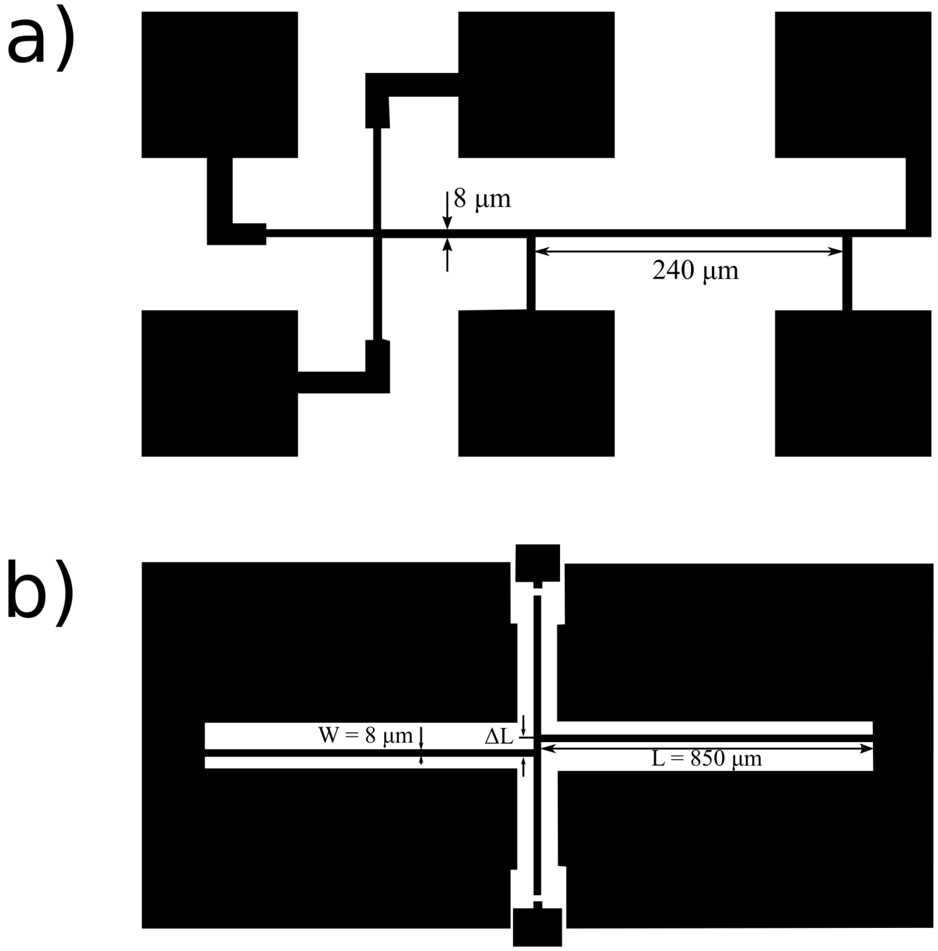

Figure 3.7: Detail of a) linewidth and b) rotating arm test structures showing the critical dimensions.

3.2.5 Fabrication of Circular Electrodes

For magnetic measurements of electrodeposited films circular electrodes were fabricated to reduce the effects of shape anisotropy. Electrodes were made using the same method as in Section 3.2.3 on 100 mm wafers with no top, protective, titanium layer. The mask used produced 14 chips from a single wafer as shown in Figure 3.8. On each chip there were 4 exposed circles, of diameter 5 mm. This enabled the production of four equivalent circles during electrodeposition. After electrodeposition, and the removal of the remaining photoresist, the chips were then diced to give four equivalent circular deposits as shown in Figure 3.8.

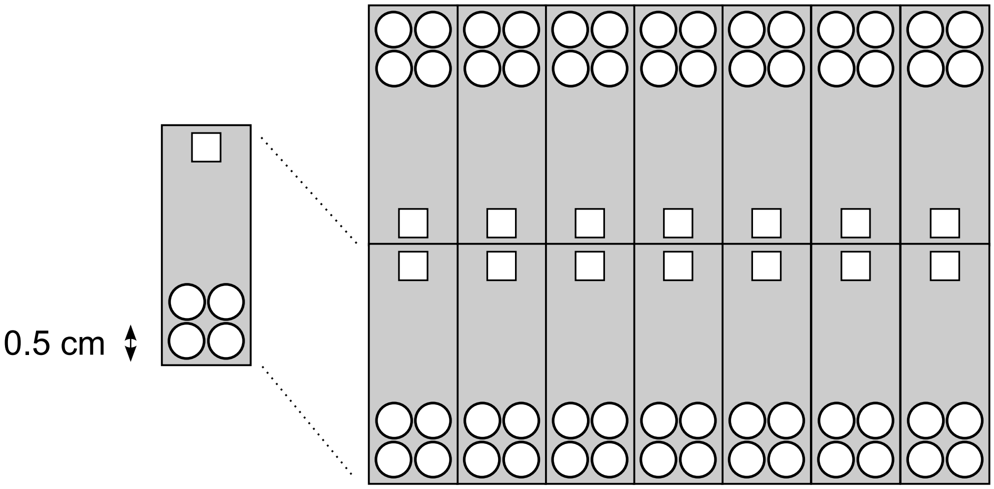

Figure 3.8: Mask design used for the fabrication of the circular electrodes. 14 equivalent chips were produced following dicing, each with 4 equivalent circular electrodes.

3.2.6 Copper Seed Layer Etching

After electrodeposition of nickel or nickel-iron it was sometimes necessary to remove the copper seed layer from the electrode. Some common copper etching solutions include ammonium persulfate, $FeCl_3$ or HNO_3. Etching solutions using solely these chemicals also attack the deposited NiFe films. An etching solution which selectively removed copper without damage to the electrodeposited NiFe film was required. A copper etch based on ammonium persulfate was developed. The etch was made with a high pH (> 12) solution to protect the NiFe film and a complexing agent was added to prevent the redeposition of copper from the solution. The etch solution composition is shown in Table 3.1.

Chemical	Concentration / g L^{-1}
$(NH_4)_2S_2O_8$	20
$Na_3Cit.2H_2O$	20
NaOH	20 (to obtain pH >12)

Table 3.1: Copper seed layer etching solution compatible with nickel and nickel-iron films.

The chemistry of the etch can be described through Equations 3.1-3.4. The persulfate anion oxidises the copper film, producing soluble copper ions (Equation 3.1). The free copper cation is then free to complex with ammonia (Equation 3.2). With citrate as a complexing agent in the bath a ligand exchange reaction can occur to give a copper citrate complex (Equation 3.3). This reaction resulted in the release of ammonia gas seen as bubbles during the etch. Alternatively the copper (II) cation may directly bind with the citrate anion (Equation 3.4). The surface of Ni or NiFe film is likely to oxidised due to the high pH which in turn prevents it from being attacked.

$$Cu_{(s)} + S_2O_8^{2-} \longrightarrow Cu^{2+} + 2(SO_4)^{2-} \tag{3.1}$$

$$Cu^{2+} + 4NH_3 \longrightarrow Cu(NH_3)_4^{2+} \tag{3.2}$$

$$Cu(NH_3)_4^{2+} + Cit^{3-} \longrightarrow (CuCit)^{-} + 4NH_{3(g)} \tag{3.3}$$

$$Cu^{2+} + Cit^{3-} \longrightarrow (CuCit)^{-} \tag{3.4}$$

A fresh solution of the copper etch was found to remove the 300 nm seed layer in approximately 5 minutes.

3.3 Electrochemistry

Throughout this work a three electrode system (Figure 3.9) was used to make electrochemical measurements. This set up consists of a working electrode (WE), reference electrode (RE), and a counter electrode (CE). A saturated calomel electrode (SCE) (Scientific Laboratory Supplies) was used as a reference electrode unless otherwise stated. When required a Ag/AgCl double junction reference electrode with 3 M KCl inner solution was used. Platinum gauze (Alfa Aesar, VWR) was

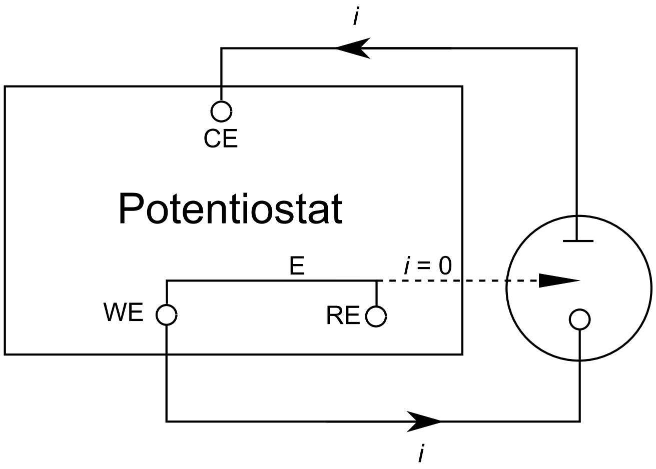

Figure 3.9: Schematic of 3-electrode system.

used as a counter electrode and was flame cleaned prior to use. The working electrodes used in this thesis have been described previously (Section 3.2).

Electrochemical experiments were performed using a computer controlled electrochemical measurement system, the Autolab PGSTAT12 or PGSTAT30 (Eco Chemie). RRDE measurements required use of the bipotentiostat module.

3.3.1 Rotating Disc and Rotating Ring Disc Methods

3.3.1.1 Experimental Set-up

Rotating disc experiments were performed using the Autolab PGSTAT12 system in conjunction with a rotator and motor controller (Oxford Electrodes Ltd). A schematic of the system is shown in Figure 3.10.

3.3.1.2 Collection Efficiency of the RRDE

The collection efficiency, $N_\circ$, for the ring of a RRDE can be defined as

$$|i_{ring}| = N_\circ |i_{disc}| \tag{3.5}$$

when there are the same number of electrons transferred in the disc and ring reaction. This is appropriate as the ring electrode is often set to detect by performing the reverse reactions to the disc. In addition both reaction must be under mass transfer control.

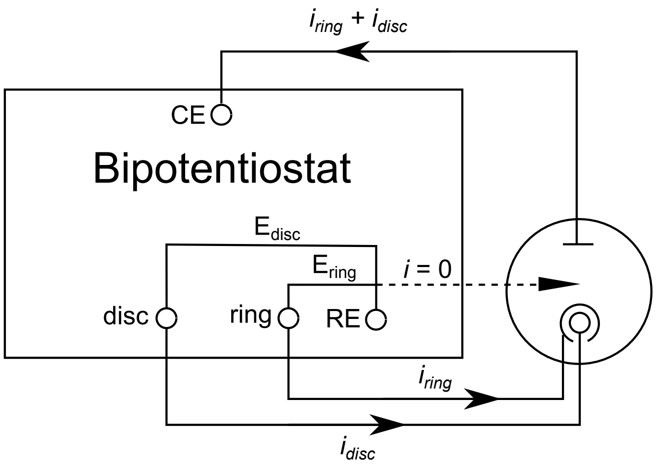

Figure 3.10: Schematic of RRDE electrochemical set-up.

The collection efficiency at the ring was determined using 10 mM $K_3Fe(CN)_6$ in 1 M KNO_3. The solution was degassed with argon first. The potential at the ring was held at 0.5 V to reoxidise $Fe(CN)_6^{4-}$ under mass transport control and linear sweep voltammetry (LSV) performed on the disc electrode at a scan rate of 10 mV s^{-1}. This was performed and repeated at rotation frequencies of 1, 2, 4 and 9 Hz.

An example of the measured currents on the disc and ring during LSV are shown in Figure 3.11. The disc current displays a limiting current (measured at E_{disc} = -0.1 V) proportional to the square root of the rotation frequency according the Levich equation (Equation 2.28). The limiting currents were extracted from these data and the collection efficiencies calculated. Across all the rotation frequencies the collection efficiency (i_{ring}/i_{disc}) was calculated to be 0.203 ± 0.002.

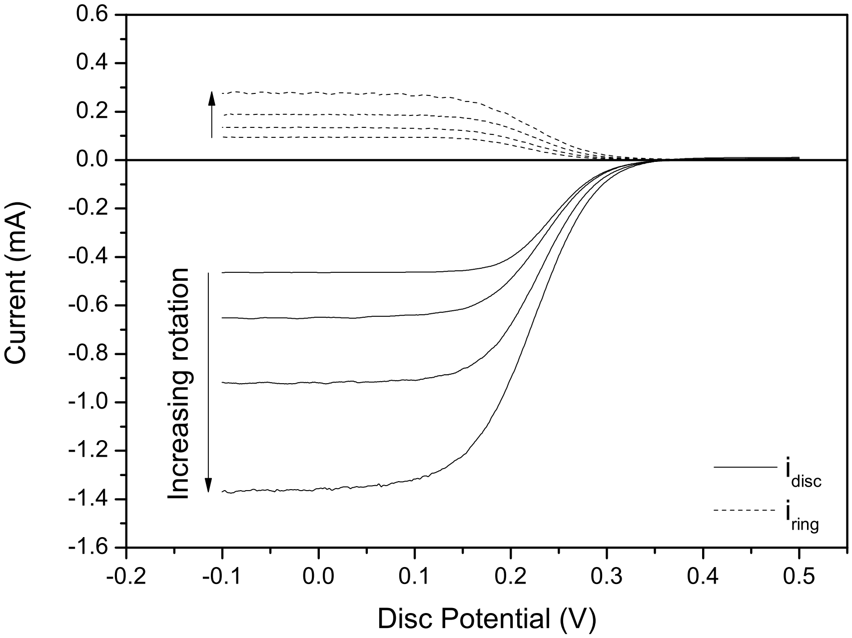

Figure 3.11: Typical disc and ring currents measured on a RRDE during LSV at the disc electrode *vs.* SCE. The ring potential, E_{ring}, was 0.5 V. The disc was swept between 0.5 V and -0.1 V at a scan rate of 10 mV s^{-1}. Varying rotation speeds are shown. The direction of the arrow indicates increasing rotation speed.

3.3.2 EQCM

3.3.2.1 Experimental Set-Up

EQCM experiments were performed using a Research Quartz Crystal Microbalance (Maxtek) in conjunction with an Autolab PGSTAT30 (Eco Chemie). Experiments were performed either at room temperature or in a water bath. The temperature was monitored and recorded using a K-type thermocouple to ensure there were minimal temperature fluctuations during experiments thereby minimizing the effects of changing temperature on the frequency response. Electrochemical control of the cell was performed through the GPES software. EQCM data acquisition was performed through the RQCM software and simultaneous electrochemical logging was performed by using the data acquisition card and analog inputs into the RQCM from the outputs of the Autolab potentiostat. (see Figure 3.12).

The EQCM electrode (Figure 3.2) was mounted in a crystal holder (Maxtek CHC-100). The holder provided electrical contact to the wrap around electrodes using spring loaded pin connectors and

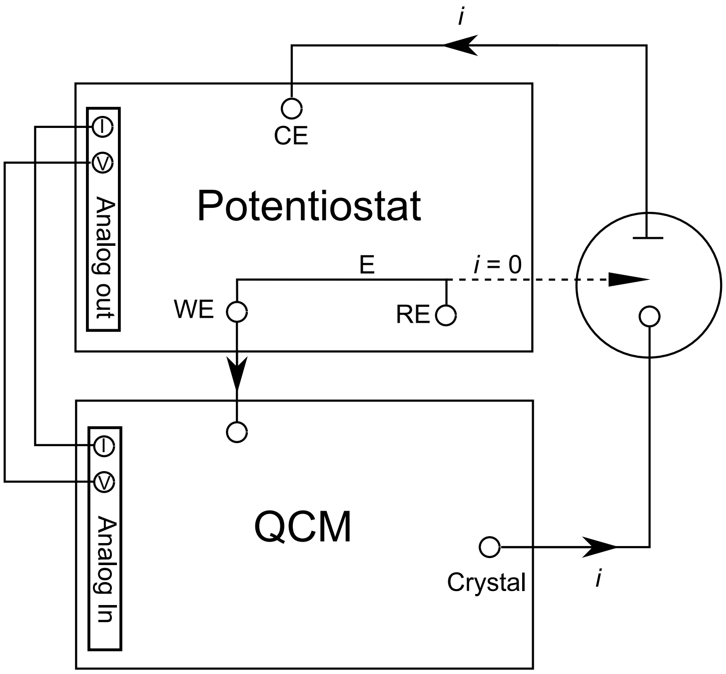

Figure 3.12: Schematic of EQCM set-up.

ensured the backside of the electrode was in contact with air in the cavity of the holder. The electrode, held in the holder, was immersed into the electrochemical cell (see Figure 3.13) ensuring no leaking of the electrolyte into the inner chamber. Before measurements were recorded the electrode was held in the solution to stabilise for approximately 30 minutes.

3.3.2.2 Calibration of the EQCM

More commonly in EQCM the electrodeposition of thin films containing up to 100's of monolayers is studied. In this work the deposition of thick films is of interest as is deposition on to a foreign substrate, therefore the response under these conditions require calibration.

Quantitative interpretation of EQCM data was made after calibration. As discussed in Section 2.2 the Sauerbrey equation linearly relates the change in frequency to the mass per unit area. In this work the EQCM response to thick metal films is of interest. To determine the constant, C_f, a rigid film of metal was deposited on the surface by electrodeposition and the change in frequency measured. A well behaved electrochemical reaction was required to calibrate the EQCM. Typically used reactions for calibration are the deposition of silver, copper or lead [125, 119, 116, 126, 127].

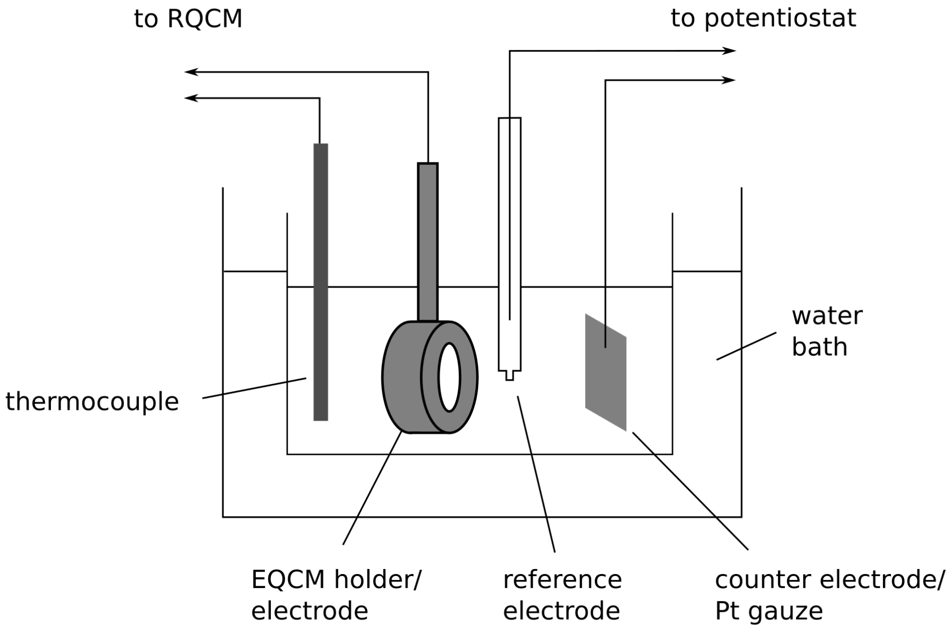

Figure 3.13: Set-up of the electrochemical cell for use with the EQCM.

For calibration the reaction is required to deposit with 100 % coulombic efficiency and deposit uniformly in a rigid film.

In this section calibration of the EQCM was performed experimentally to determine the best calibration system and hence determine the Sauerbrey constant and compare it to the value derived from Equation 3.6 (0.056 Hz ng^{-1} cm^{2}). In addition, the effects of increasing temperature on the EQCM and calibration was studied with experiments performed at different temperatures.

$$C_f = -\frac{\Delta f}{Q}\frac{nFA}{M_w} = -\frac{df}{dt} \times \frac{1}{i} \times \frac{nFA}{M_w} \tag{3.6}$$

Deposition of Ag Using CV

Calibration of the EQCM was performed using cyclic voltammetry. Using a silver nitrate solution, 50 mM $AgNO_3$ in 0.5 M HNO_3, voltammetry was performed across a range of scan rates (2 to 50 mV s^{-1}) between 0.65 and 0.4 V *vs.* the Ag/AgCl double junction reference electrode with 3 M KNO_3 in the outer chamber to prevent AgCl precipitation. Each scan rate was repeated for three scans. A typical response for the change in frequency against the charge passed during a single

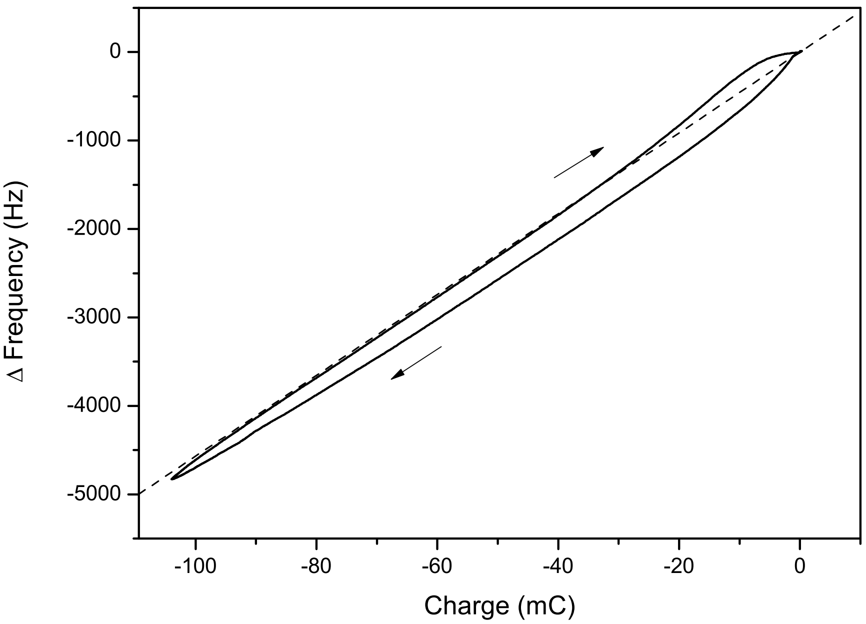

Figure 3.14: Typical example for the change in frequency *vs.* charge passed during silver deposition and stripping using cyclic voltammetry (between 0.65 and 0.4 V *vs.* Ag/AgCl) for a silver nitrate solution (50 mM $AgNO_3$ in 0.5 M HNO_3). Dashed line: theoretically calculated gradient for $C_f = 0.056$ Hz ng^{-1} cm^2.

CV is shown in Figure 3.14. This plot clearly shows the frequency returns to the initial value at the end of the scan indicating that all the silver is removed during stripping. In general the plot matches the gradient expected from the Sauerbrey equation. Deviations from this gradient were observed during the initial and final parts of the scan where the frequency response may be affected by changes in surface roughness or changes in stress.

To obtain an experimentally derived Sauerbrey constant the total change in frequency and the charge passed was extracted from these data across the range of scan rates applied and is plotted in Figure 3.15. From the best fit line the gradient was 46.1 ± 0.3 Hz mC^{-1}. Using Equation 3.6, C_f was calculated to be 0.0559 ± 0.0005 Hz ng^{-1} cm^2 in remarkably good agreement with the Sauerbrey equation. This demonstrates that the EQCM can be applied as a mass sensor for use in cyclic voltammetry experiments although careful interpretation of the data is required as the morphological properties of the film changes.

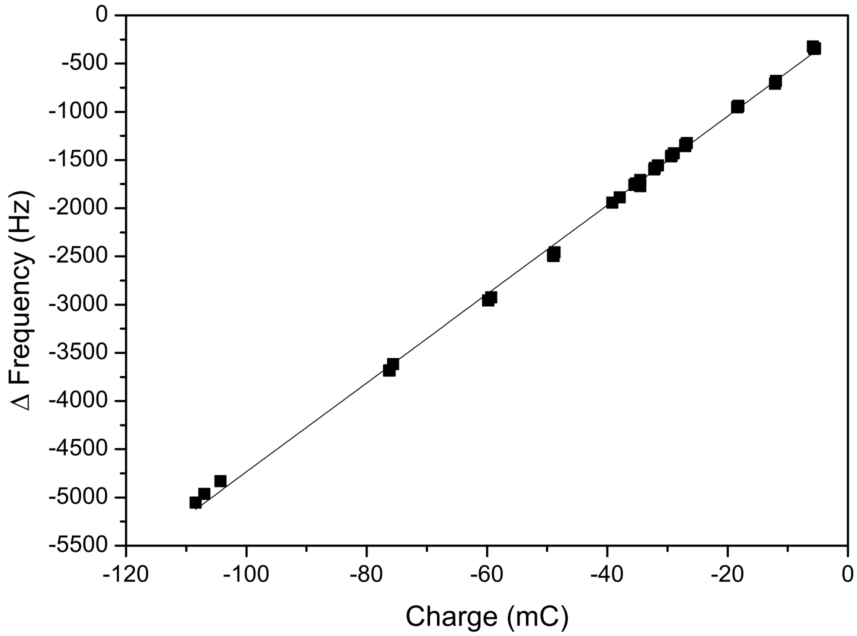

Figure 3.15: Maximum change in frequency and charge passed for Ag deposition *via* cyclic voltammetry. Points were determined from scan rates between 2 and 50 mV s^{-1}. Each scan rate was repeated 3 times. The best fit line is shown and has a gradient of 46.1 ± 0.3 Hz mC^{-1}.

Deposition of Ag at Constant Current

An alternative technique for the calibration of the EQCM is galvanostatic deposition. Silver was deposited from a solution of 50 mM $AgNO_3$ in 0.5 M HNO_3 at currents between 100 and 5000 µA at the electrode for 60 s. Deposits were made on the bare platinum electrode with the deposit removed and cleaned electrochemically in H_2SO_4 using the procedure in Section 3.3 before the next deposit.

From a plot of the frequency change against time the gradient, df/dt, was calculated using linear regression. The values for the Sauerbrey constant at each current applied was calculated using Equation 3.6. A plot of $C_{f,measured}/C_{f,theory}$ against the applied current is shown in Figure 3.16(a). At lower currents the magnitude of C_f was found to be large. The measured C_f value was seen to asymptotically approach the calculated value of 0.056 Hz ng^{-1} cm^2. This deviation from the value obtained from the Sauerbrey equation may arise from the effects of stress and surface roughness as previously described.

Separating the effects of changing surface roughness and stress is not trivial, however both may be eliminated. To test whether these effects caused the over-estimation of C_f, a layer of silver was pre-depositied on the electrode to nullify the effects of a changing substrate. An initial deposit of silver was plated on to the Pt electrode at a current of 3 mA for 100 s (a current where prior experiments appeared to show the expected value for C_f). This initial film was intended to give a layer, with many nucleation points, from which further deposits could be made with no stress or surface roughness effects due to the deposits being silver on silver. Silver was then deposited on this layer at currents of 0.25 to 5 mA for 60 s with each current being applied sequentially to deposit layers on top of each other.

Values for C_f were calculated as previously described and are compared to the theoretical value as shown in Figure 3.16(b). It was found that across the varying currents the measured value gave a consistent response. The measured value for this electrode was found to be 0.0514 ± 0.0006 Hz ng^{-1} cm^{2}. This varies from the previous experiments, however this calibration experiment was performed on a different electrode as the previous electrode had failed and a different value can be expected.

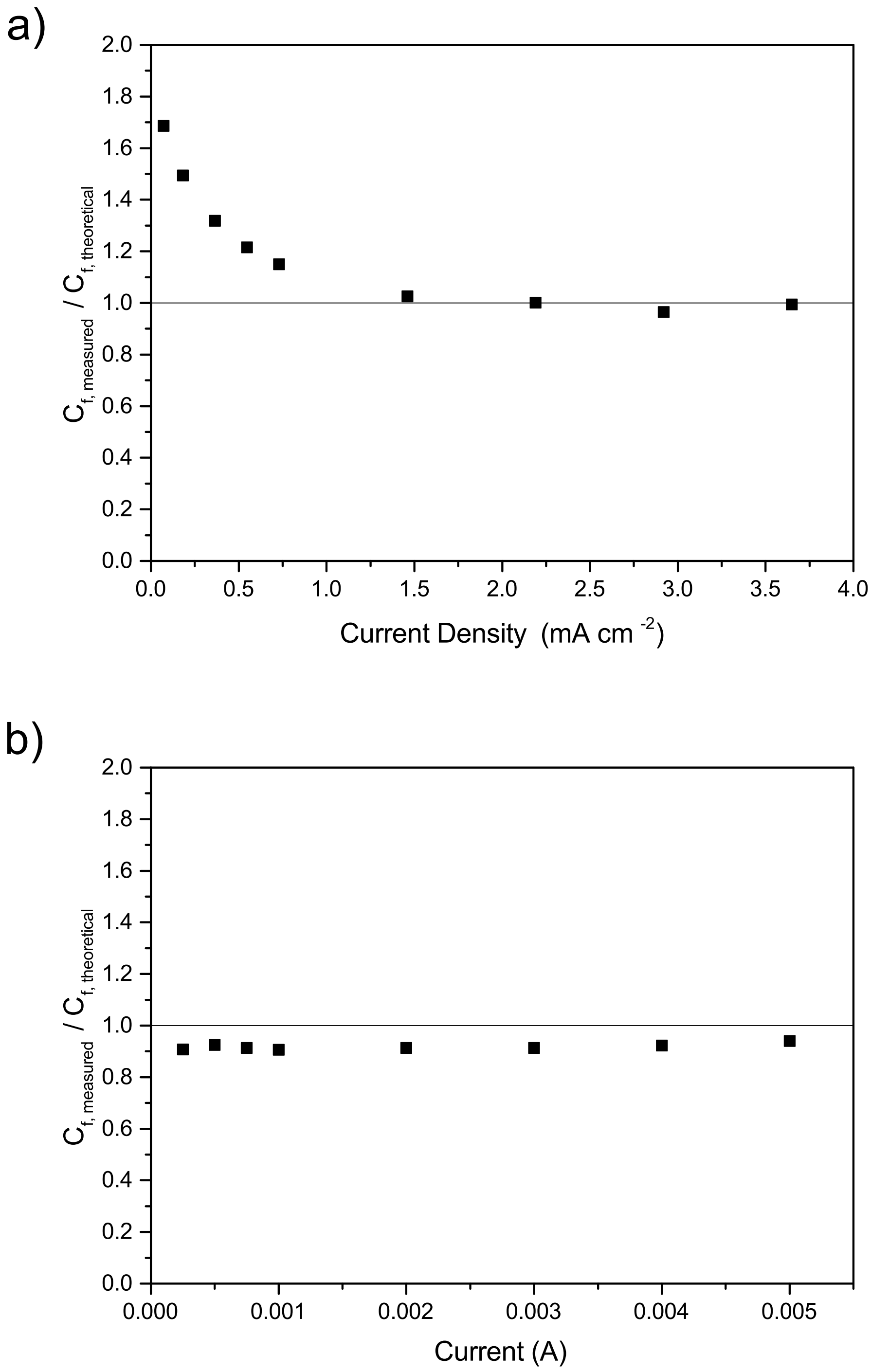

Figure 3.16: Ratios for the measured value of C_f against the applied current during deposition. a) Deposition on a clean Pt electrode. b) Deposition on a pre-depositied layer of silver (on a different electrode).

Calibration Using Alternative Metals

Calibration of the EQCM was also attempted using the potentiostatic deposition of copper and lead onto the bare platinum electrode. Figure 3.17 shows the ratio of the measured calibration constants against that calculated from the Sauerbrey equation.

The deposition of lead, from a solution of 8 mM lead acetate in 0.1 M sodium acetate, was performed on the EQCM. Deposits were made galvanostatically on the working electrode of the EQCM at currents between 50 and 1000 µA over 400 s. It was observed that the frequency change during the deposition of lead was not always linear. Dendrite growth of lead was visually observed for deposition at 1000 µA. As dendrite growth continued the deposited metal film was less rigid and the frequency response became increasingly non-linear. Figure 3.17 shows that the calculated values for the Sauerbrey constant at applied currents less than 1000 µA are considerably smaller than expected. It was therefore concluded that this solution was not suitable for the calibration of thick film deposits on the EQCM.

The galvanostatic deposition of copper, from 0.5 M $CuSO_4$ and 0.5 M H_2SO_4, showed a similar response to the deposition of silver. When the applied current was increased the measured Sauerbrey constant approached the value calculated from Equation 3.6. However, from cyclic voltammetry, the reaction was demonstrated not to be 100 % efficient. This was apparent due to the measured charge during deposition being consistently greater than that required for stripping.

From these measurements silver was found to provide the most reliable calibration from the EQCM. Furthermore, the simplest technique for monitoring the deposition of metals requires the deposition of the metal onto a pre-deposited layer of the same metal to minimise the effects of changing surface roughness or stress. Alternative experimental methods (*eg.* CV or deposition onto a foreign substrate) may provide insight into stress, surface roughness, solution-metal interactions or other potential dependent effects.

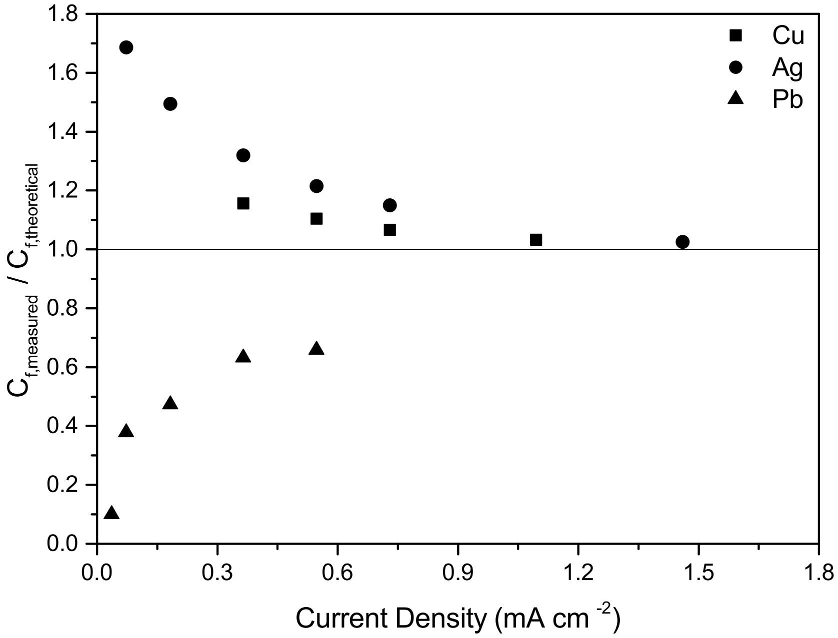

Figure 3.17: Ratios of the measured apparent C_f against the theoretically calculated values for Pb, Ag and Cu. Deposits were made at a constant current onto platinum electrodes

EQCM Calibration at Elevated Temperatures

The frequency response of the EQCM is temperature dependent. The effects of temperature can be reduced by using a crystal with a “turn around point” close to the working temperature. This minimises any effect of temperature variations on the frequency response. In this work AT-cut quartz was used for the electrodes which has a turn around point at 25 °C. In air this is usually modeled by a cubic function of the form $\triangle f_T = a_3T^3 + a_2T^2 + a_1T + a_0$, where T is the temperature and a_0 to a_3 are the temperature coefficients [118, 128]. The overall response of the EQCM is the result of numerous effects (see Equation 2.34) of which changing viscosity is also important. It is therefore difficult to entirely predict the response of the EQCM due to increasing temperature. The majority of EQCM experiments were performed at room temperature where there is little temperature dependance on the frequency due to the AT-cut of the quartz used. However it was also of interest to perform work at elevated temperatures up to 60 °C. Therefore it is best to determine the extent of these effects experimentally.

To determine the change in the resonance frequency of the quartz crystal when immersed in solution

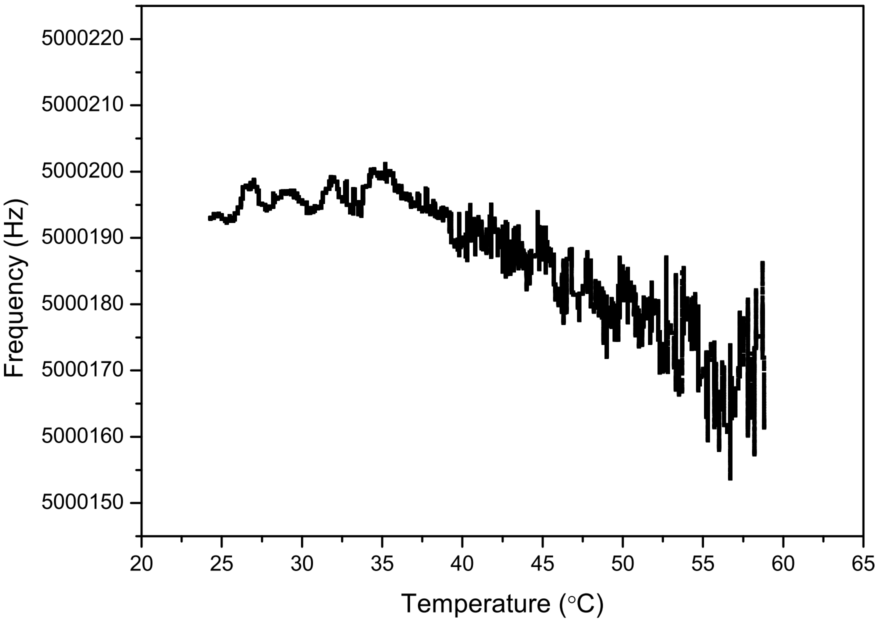

Figure 3.18: Variation in frequency across a range of temperatures for an AT-cut quartz crystal in D.I. water.

the frequency of a bare crystal was monitored as it was cooled from 60 °C. The crystal was immersed in DI water (resistivity > 18.2 MΩ.cm) and was allowed to cool to ambient temperature over 150 minutes.

Figure 3.18 shows the measured frequency during cooling across the temperature range. The frequency was seen to increase as the water temperature cooled. There is greatest noise in the measurement at high temperatures. The effects of convection currents in the solution would be greatest at the higher temperatures which could give rise to the greater noise observed. The overall frequency change is roughly 20 Hz (the equivalent of 4 ppm). This change is small enough to have minimal effects for the deposition of thick films on the EQCM.

To ensure there are no significant temperature related effects during the deposition of films, deposits of silver were made between 17 and 60 °C. Silver was deposited galvanostatically for 100 s at 3 mA. For each temperature the deposition was repeated 3 times.

Figure 3.19 shows the calculated calibration constant, C_f, for each temperature. It can be seen that as the temperature was increased the variation (noise) increased significantly. This is not

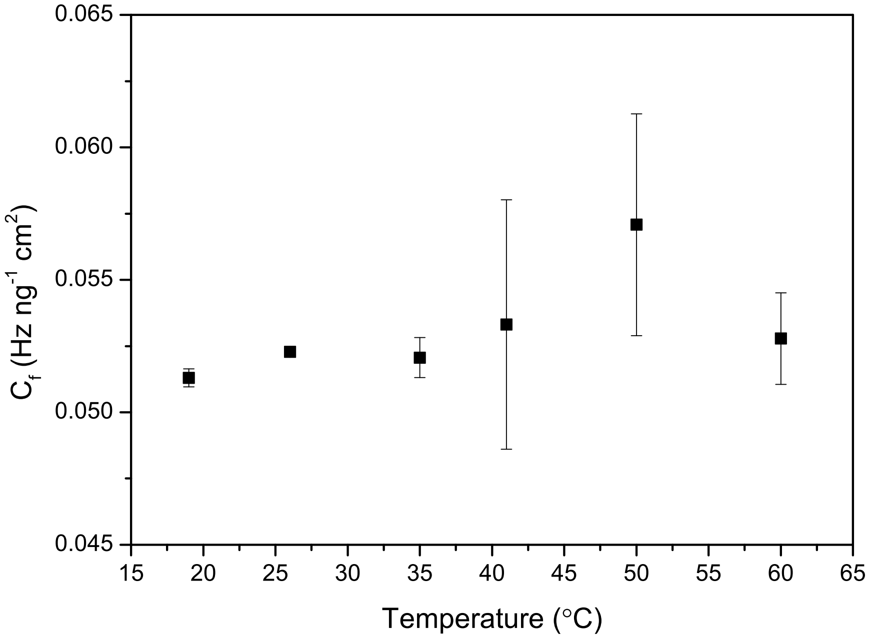

Figure 3.19: Variation of experimentally measured calibration constant, C_f, with temperature from the deposition of silver. Silver was deposited at 3 mA for 100 s

unexpected for the reasons stated previously. For use as a microbalance it is reassuring that across these temperatures C_f remains effectively constant within experimental error.

3.3.3 Methods to Measure Efficiency

3.3.3.1 Measuring Efficiency Using Film Thickness

A method to approximate coulombic efficiency (Equation 2.3) is to measure the thickness of the deposit. The thickness of deposits in this thesis was measured using a Dektak surface profiler (Veeco) or *via* X-ray fluorescence (XRF) (Thermo Electron Corporation, Micro XR).

A theoretical thickness, T, for 100 % efficient deposition can be calculated from the charge passed using the equation

$$T = \frac{itM_w}{\rho nFA} \tag{3.7}$$

where M_w is the atomic mass of the metal or in the case of an alloy the average mass based upon the fractional content of the metals (*e.g.* for $Ni_{80}Fe_{20}$ $M_w = 0.8M_{Ni} + 0.2M_{Fe}$). The density, ρ, used for nickel was 8.90 g cm^{-3} [129] for copper 8.96 g cm^{-3} [129] and for $Ni_{80}Fe_{20}$ 8.447 g cm^{-3} [130].

The coulombic efficiency was then calculated as a percentage given the measured thickness, t.

$$C.E. = \frac{t}{T} \times 100 \tag{3.8}$$

An efficiency measured from a thickness can only be as accurate as the thickness measurement itself. Practical difficulties include non-uniform deposits where the thickness varies across the film. Additionally variations in the composition change the deposit density and hence influence the efficiency measurement. Further still, the bulk density values may not be appropriate if a porous film is deposited.

Care must also be taken when interpreting thickness derived from XRF measurements. A comparison of thickness measurements made from surface profile measurements and XRF is shown for nickel films of various thickness in Figure 3.20. There is a clear discrepancy between the two measurements for thicker films as shown by deviation from the line of unity and zero intercept. A fitted line for the data collected for films less than 6 µm thick has a slope of 0.79 ± 0.2. At larger thicknesses the linear type relationship breaks down.

This is due to the limitation of the penetration depth for X-rays where electron scattering within the material reduces the measurable signal. For example the penetration depth can be approximated from the Beer-Lambert law,

$$I = I_0 \exp(-\mu x) \tag{3.9}$$

where I is the intensity at distance x in cm, I_0 is the intensity at $x = 0$ and μ is the mass attenuation coefficient. For the fluorescence of the K series in nickel $\mu/\rho = 3.294 \times 10^2$ [131]. Given the density of nickel (8.90 g cm^{-3}) the $1/e$ penetration depth (where the signal falls to $1/e \approx 37\,\%$) is 3.4 µm. Likewise at greater depths the signal from fluoresced X-rays is reduced further and become more difficult to detect. These results indicate that for thickness measurements the surface profile measurements should be used in preference to the XRF results.

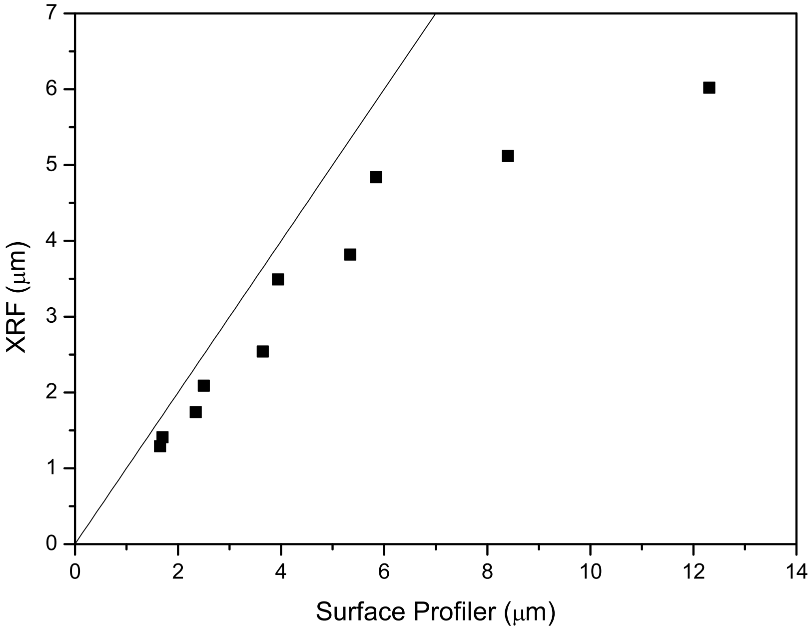

Figure 3.20: Thickness comparison measurements between surface profile measurements and XRF measurements for nickel films. The solid line has a gradient of unity and passes through the origin.

3.3.3.2 Measuring Efficiency Using Deposit Mass

Another technique to measure the efficiency of deposition is through the mass of the deposit. Assuming 100 % efficiency, the expected mass, M, of a deposit for a given amount of charge can be calculated as

$$M = \frac{itM_w}{nF} \tag{3.10}$$

where M_w is the atomic mass of the metal. This calculated mass can be compared to the measured mass, m, to obtain the efficiency as a percentage.

$$C.E. = \frac{m}{M} \times 100 \tag{3.11}$$

One advantage of this technique is that it is insensitive to the film morphology.

This method was applied dynamically to the EQCM. Assuming the EQCM behaves as a true mass balance with the Sauerbrey constant, C_f, the change in frequency was used to measure the mass of the deposit. For the EQCM the rate of change for the frequency, df/dt, is directly proportional to the rate of change of mass, dm/dt, and was used to calculate the efficiency. For 100 % efficient deposition the rate of change in frequency was calculated as

$$\left(\frac{df}{dt}\right)_{100\%} = i \times \frac{-C_f M_w}{nFA} \tag{3.12}$$

The instantaneous coulombic efficiency can then be calculated as a percentage using the measured rate of change of frequency.

$$C.E. = \frac{\left(\frac{df}{dt}\right)_{measured}}{\left(\frac{df}{dt}\right)_{100\%}} \times 100 \tag{3.13}$$

3.4 Test Structures Analysis

3.4.1 Copper Deposits on Test Structure Chips

To examine the uniformity of deposition across the test structure chips copper was deposited from a commercial plating solution (see Table 3.2). Deposits were made with a current density of 5 mA cm^{-2} for 20 min. Under these conditions a film thickness of 2.20 µm was expected for 100 % efficient deposition. Figure 3.21 shows the measured thickness of the deposits across different points of the test structure electrode. The average thickness measured was 2.11 ± 0.15 µm. Thicker deposits were found at the electrode edges where a higher current density resulted which may be expected due to enhanced mass transport at the edge of the device. Optically the copper formed a bright and uniform layer across the electrode as shown in Figure 3.22.

Chemical	Concentration
$CuSO_4.5H_2O$	120 g L^{-1}
H_2SO_4	190 g L^{-1}
NaCl	50 mg L^{-1}
8540 Additive	5 mL/L
8540 Carrier	5 mL/L

Table 3.2: Contents of copper deposition bath

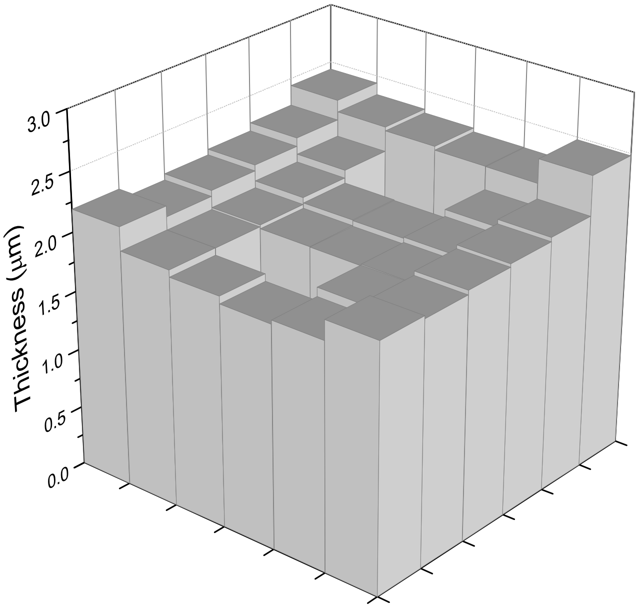

Figure 3.21: Variation in deposit thickness across a test structure electrode. The copper film was deposited at 5 mA cm^{-2} for 20 minutes from a commercial Cu plating bath. Each square represents the measured film thickness for the pointer arm test structure at that location.

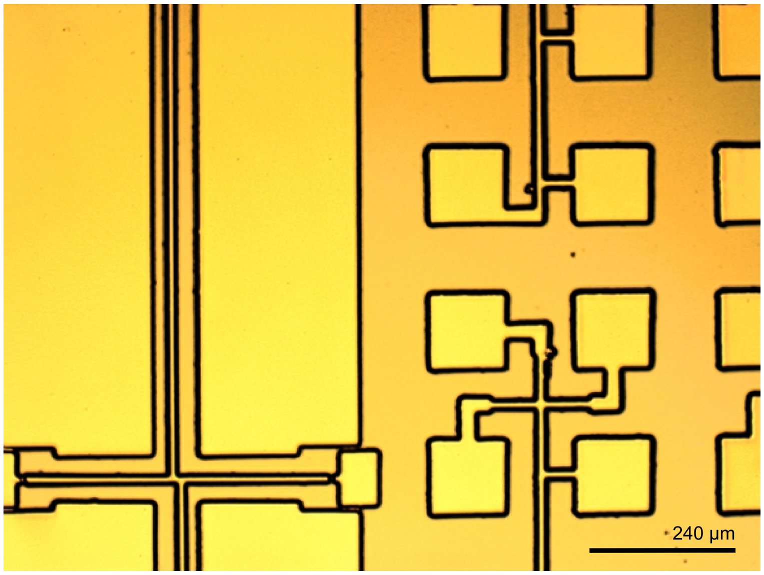

Figure 3.22: Optical image of copper deposited onto the test structure electrodes showing bright, uniform and flat deposits.

Element	$K_{\alpha 1}$	$K_{\alpha 2}$	$K_{\beta 1}$
Ni	7.48	7.46	8.26
Fe	6.40	6.39	7.06
Cu	8.05	8.03	8.91
Ti	4.51	4.50	4.93

Table 3.3: Energies for XRF K series lines for selected elements (keV)

3.4.2 Composition of NiFe Films Measured Using XRF

The composition of NiFe films was measured using X-ray Fluorescence (Thermo Electron Corporation, Micro XR). An example spectra measured for a nickel-iron sample deposited onto a copper test structure electrode is shown in Figure 3.23. The major peaks are labeled on the spectra. The K-series energies for elements used in the electrodes and for nickel and iron are shown in Table 3.3. The composition of the film was calculated by the built-in software.

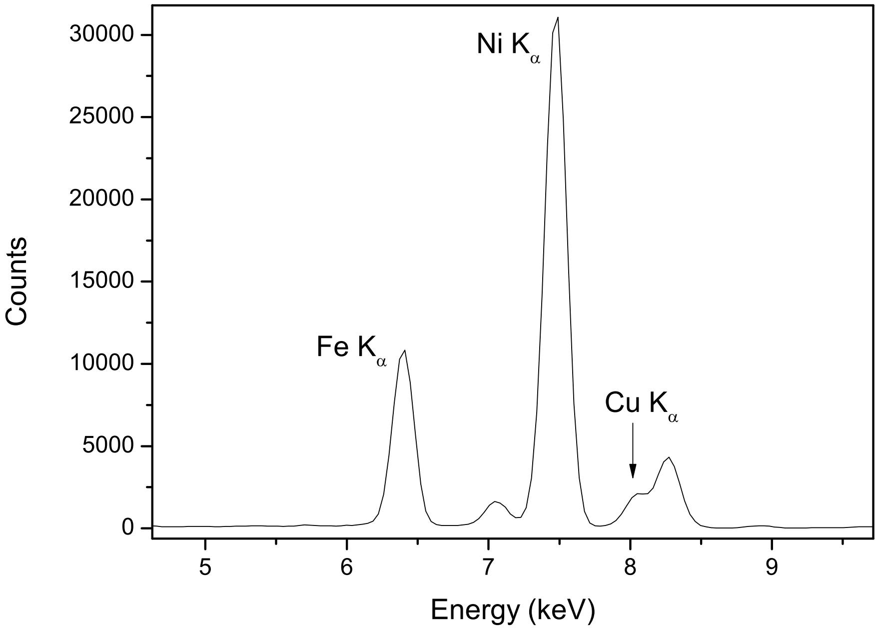

Figure 3.23: XRF spectra collected for 120 s for NiFe film on test structure electrode.

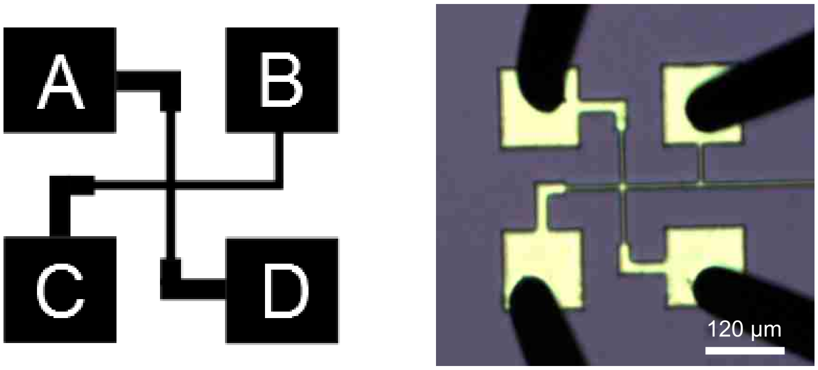

Figure 3.24: Greek cross test structure. Left: showing pad notation. Right: showing actual measurement.

3.4.3 Pointer Arm and Electrical Test Structures

Measurements of the electrical and rotating-arm test structures were performed using a semi-automatic probing system developed by Jeremy Murray [124].

3.4.3.1 Sheet Resistance

The sheet resistances of the deposited films were measured using Greek cross structures (Figure 3.24) [132, 133]. These structures were fabricated on the test structure chips as part of the line-width test structure using lithographic techniques (Section 3.2.4). Each chip contained 32 test structures. Resistance measurements were made by forcing a current of 10 mA chosen so not to heat the structure significantly. Electrical measurements to obtain the sheet resistance were made using a 4-point prober on the line-width test structures which systematically measures each test structure [30, 124].

The sheet resistance, R_s, was be calculated from 4-point resistance measurements on a Greek cross structure using Equation 3.14 [134].

$$R_s = f(\pi R(\pm I))/(\ln 2) \tag{3.14}$$

For these structures it has been shown that no correction factor is required, *i.e.* $f = 1$ [135, 133]. $R(\pm I)$ is the average value for the resistance taking into account current direction and the different orientations current can be passed in the test structure. The resistance is measured by passing a current from pads A to B, I_{AB}, and the voltage is measured between pads C and D, V_{CD}. This is then repeated in the reverse direction so a current is forced from pad B to pad A, I_{BA}, and voltage measured between pads D and C, V_{DC}. A value for R_0 can then be calculated using Equation 3.15. This process is repeated at a 90° orientation to obtain R_{90} (Equation 3.16).

$$R_0 = \frac{|V_{DC}| + |V_{CD}|}{|I_{AB}| + |I_{BA}|} \tag{3.15}$$

$$R_{90} = \frac{|V_{AD}| + |V_{DA}|}{|I_{BC}| + |I_{CB}|} \tag{3.16}$$

An average value by combining both orientations, $R(\pm I)$, can then be calculated using Equation 3.17.

$$R(\pm I) = (R_0 + R_{90})/2 \tag{3.17}$$

3.4.3.2 Pointer Arm Rotation

To measure the strain in the electrodeposited films rotating arm test structures were used. Films were first deposited onto the test structure chip. Following deposition, the photoresist and the sacrificial layer below the structure were removed, shown schematically in Figure 3.25. The removal of the layer underneath the expansion and pointer arms results in their suspension and are then free to rotate. For the test structure chips, the copper seed layer was removed as the sacrificial layer, using the copper etch detailed in Section 3.2.6. Figure 3.26 shows an SEM of a released structure, using the wet etch, where the suspension of the structure is clearly visible. Once the rotating arm structure is released the expansion arms can contract or expand depending on the intrinsic stress in the film. Due to the offset of the two expansion arms this causes rotation of the pointer arm.

In the configuration shown in Figure 3.27, and because of the expansion arm offset, if the film is under compressive stress the arms will rotate clockwise. If under tensile stress the pointer arm will rotate anti-clockwise. Microscope images were then taken of the structure and pattern recognition software was used to measure the angle of rotation, θ. A more detailed description of this system can be found in reference [124].

Figure 3.27 shows a simple schematic for the pointer arm structures. The strain, ϵ, can be defined as

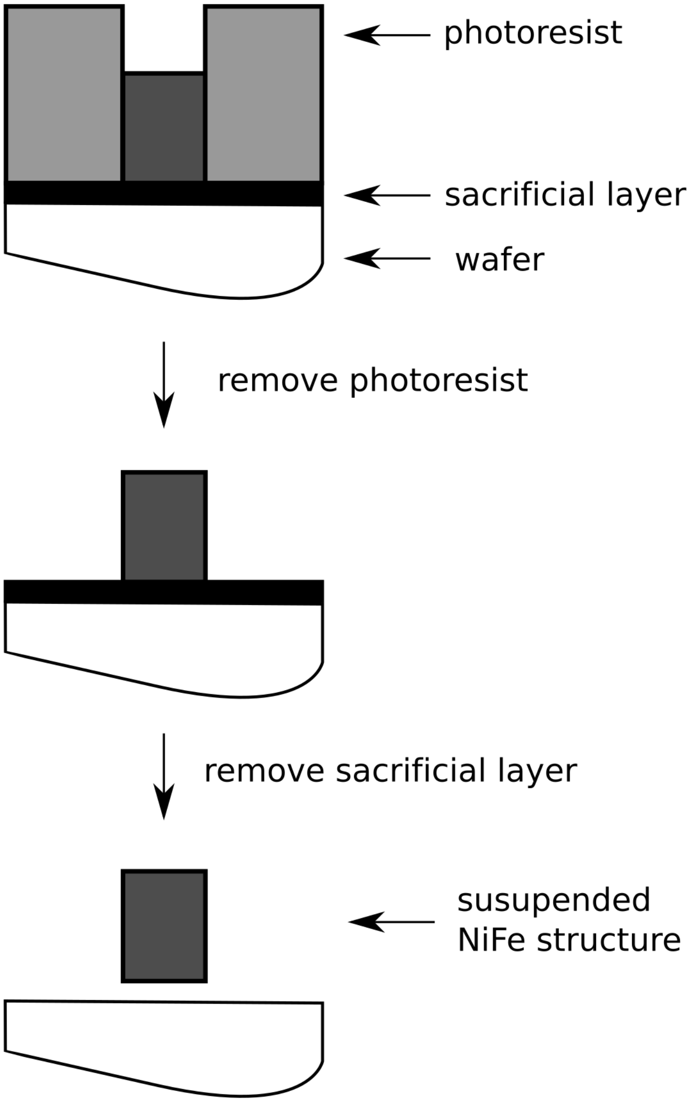

Figure 3.25: X-sectional representation of the fabrication process to release the rotating arm test structures. After deposition the photoresist in removed using acetone then the sacrificial layer (copper seed layer) is removed using a copper etch to release the structure.

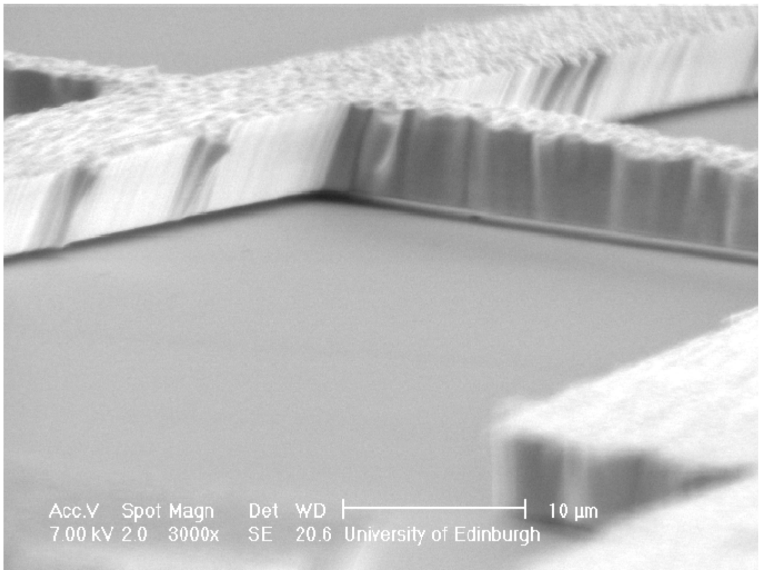

Figure 3.26: SEM of a released rotating arm test structure.

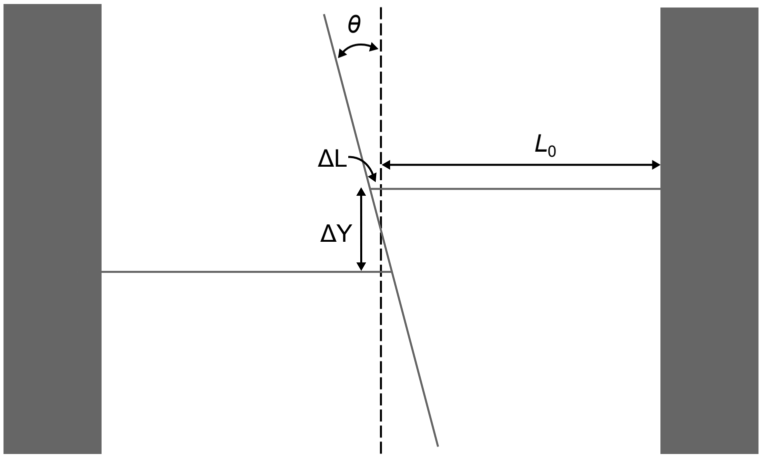

Figure 3.27: Schematic for the geometry of a rotating arm test structure

$$\epsilon = \frac{\Delta L}{L_0} \tag{3.18}$$

Assuming the structure remains rigid and there is no out of plane twisting, basic geometry can then be applied to give Equation 3.19. For small angles of rotation (<10°) the small angle approximation can be applied ($\tan\theta \approx \theta$) and given that $\Delta L \ll L_0$ the angle of rotation is proportional to the strain according to Equation 3.20.

$$\begin{aligned} \theta &= \tan^{-1}\left[\frac{2\Delta L}{\Delta Y}\right] && (3.19) \\ &\approx \epsilon\frac{L_0}{\Delta Y} && (3.20) \end{aligned}$$

The strain, ε, can then be related to the stress, σ, through the Young's modulus of the material, E.

$$\sigma = E \times \epsilon \tag{3.21}$$

3.5 Magnetic Analysis

Magnetic measurements were performed on films deposited onto the circle electrodes (Section 3.2.5). Each device was diced to separate the four circular electrodes and provide a single circular sample on a 5 mm square substrate.

Magnetic saturation experiments were performed on a super conducting quantum interface detector (SQUID) magnetometer (Quantum Design MPMS-XL, USA) at 300 K. Fields of 10, 25, 75, 100, 200 and 300 Oe were applied to ensure magnetic saturation of the sample had occurred.

B-H loop measurements were performed on a B-H looper (Shb Instruments Inc., California) at Glasgow University. In-plane measurements were made at room temperature using a frequency of 10 Hz. Samples were placed in a custom mount to ensure reproducibility in positioning. To ensure there was minimal magnetic effect from the substrate (or mount) B-H loops were also performed on a blank electrode. No detectable magnetic response was observed as shown in Figure 3.28 compared to sample measurements (see Section 8.5).

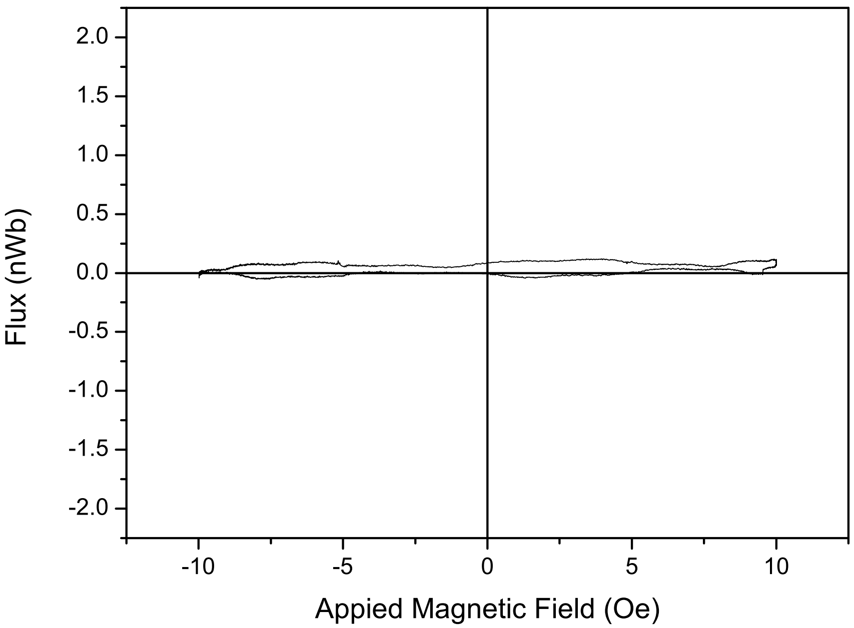

Figure 3.28: B-H response measured for a blank electrode on the custom holder. The loop was measured at a frequency of 10 Hz. The response did not change with the angle of the substrate.

3.6 Summary

This chapter has described some of the methods used through the remainder of this thesis. The fabrication and use of test structure electrodes has been presented as a method to evaluate the electrical properties of deposited films and the strain in electrodeposited films. Similarly the fabrication of circular electrodes was presented to enable magnetic measurements using a B-H looper or SQUID magnetometer. The fabrication of simple 1 cm square electrodes was also described for use in depositing blanket films on a copper seed layer.

Calibration experiments were performed using the deposition of silver on the EQCM and compared with the calibration constant calculated from the Sauerbrey equation. In general the measured value for C_f agreed well with the Sauerbrey equation (0.0514 ± 0.0006 Hz ng^{-1} cm^2 from galvanostatic measurements). The EQCM was additionally tested at increased temperatures (up to 60 °C) where despite increased variability consistent measurements can still be made provided the temperature remains constant.

Methods for measuring deposit thickness and hence the coulombic efficiency were evaluated. It was demonstrated that XRF measurements for thickness were not reliable, particularly for thicker ($>$ 4 µm) films. In preference surface profile measurements can be used to measure the film thickness.

Chapter 4

Electrodeposition of Ni and NiFe from a Boric Acid Bath

4.1 Motivation

Currently nickel and nickel-iron are generally deposited from boric acid based electrolytes either from a Watt's type bath or variations upon this such as chloride, sulfate, or sulfamate baths [33, 62, 136, 137, 138, 139]. For the reasons detailed earlier in this thesis (Chapter 1) the development of a boric acid free electrodeposition bath for nickel-iron is required. In order to benchmark any replacement used the functions of boric acid in the bath should be assessed.

There are many possible suggested roles attributed to boric acid in the electrodeposition bath. These include:

- suppressing the hydrogen evolution reaction (HER)
- acting as a buffering agent or a source of protons
- reducing passive film formation (*i.e.* hydroxides)
- acting as a catalyst
- being a co-adsorbate on the cathode
- accelerating deposit growth rates

These roles are discussed previously in Section 1.2.2. This chapter sets out to attempt to define the most important roles of boric acid in the nickel and nickel iron deposition bath and therefore determine the properties required for a viable alternative. The development of a new electrodeposition bath can then be guided by this information and improved upon to optimise conditions for the electrodeposition of nickel-iron films.

4.2 Deposition of Nickel from a Boric Acid Bath

Boric acid is used extensively in the electrodeposition of nickel and nickel-iron films. In this section nickel is first deposited from a boric acid based bath from chloride salts to avoid the complications of alloy formation. This bath is based upon the nickel-iron plating bath as used by industrial partners and in the microfabrication of MEMS devices [30, 31, 32] where the iron content has been removed. The contents of this bath are shown in Table 4.1. The pH of the bath was adjusted to 2.8 using 10 % v/v. HCl. This is not the ideal solution for the deposition of nickel on its own due to its low pH but is more relevant when applied to the nickel-iron bath. At a lower pH the hydrogen evolution becomes more favoured and the coulombic efficiency of deposition is reduced [140]. However, for the deposition of nickel-iron this lower pH is required to stabilise $FeCl_2$. At higher pH the bath is unstable as iron (II) hydroxide may form and precipitate from the bath.

4.2.1 Cyclic Voltammetry on Pt Disc Electrode

The electrochemical processes which occur in a boric acid based nickel electrodeposition bath were examined using cyclic voltammetry. Using the bath as described in Table 4.1, cyclic voltammetry was performed on a Pt disc electrode in a stagnant solution. Figure 4.1 shows the typical voltammetry of nickel deposition and stripping.

Chemical	Concentration (g L^{-1})
$NiCl_2.6H_2O$	110
H_3BO_3	25
sodium saccharin	2
SDS	0.1

Table 4.1: Contents of boric acid based nickel plating bath used in this work.

As well as the deposition and stripping of nickel metal, in the cathodic sweep there are two additional peaks observed at approximately -0.62 V and -0.88 V. Hoare associates these additional peaks with hydrogen evolution on the platinum surface [57]. A significant difficulty in the deposition of nickel arises from the fact that nickel reduces at a lower potential than hydrogen evolution. A suggested role of boric acid is that it suppresses the reduction of hydrogen [58, 54]. Nickel reduction then becomes the favoured reaction but now occurs simultaneously with hydrogen evolution. If boric acid does suppress the HER then it is not clear that these peaks are indeed due to the reduction of hydrogen. The assignment of these peaks is not possible solely from this information; however, experiments on the EQCM (in Section 4.2.2) can determine whether a gaseous or solid material is evolved during this part of the scan.

An indication of the coulombic efficiency of nickel deposition in this bath can be obtained from the charges passed. For example at a scan rate of 100 mV s^{-1}, the charge passed in the negative part of the scan, Q^{-}, is 96.6 mC, whereas the charge passed in the positive part of the scan, Q^{+}, is 87.9 mC. If the positive charge passed in the scan were assumed only to be due to nickel stripping then the efficiency of deposition can be calculated to be 91.0 %. Using this technique information was gained about the efficiency over the whole CV cycle but it does not give information about how the efficiency changes with potential or with the current applied. The effects of current density on the deposition of nickel are further discussed in Section 4.2.2.

To aid identification of the initial peaks in the outward scan additional voltammetry was performed in a narrower potential range between 1.00 and -1.00 V. This provides a potential window for the voltammetry in which there is less nickel deposited at the electrode. Figure 4.2 shows successive voltammogram cycles where nickel deposition no longer dominates the voltammetry. These scans show oxidation peaks which progressively reduce in size with each scan.

In this potential window the cathodic charge far outweighs the anodic charge passed. This implies that the material being produced at the electrode is either entirely stable and therefore cannot be removed from the electrode or that a species is evolved which shows no reverse reaction (due to further chemical reactions or escaping the system as a gas). Given the evolution of hydrogen in this system there are a number of reactions which may occur on the reverse scan. The oxidation of adsorbed hydrogen on a nickel surface, the oxidation of adsorbed hydrogen on a platinum surface and nickel stripping [56]. Additionally there may be the formation of $NiOH_2$ caused by an increase

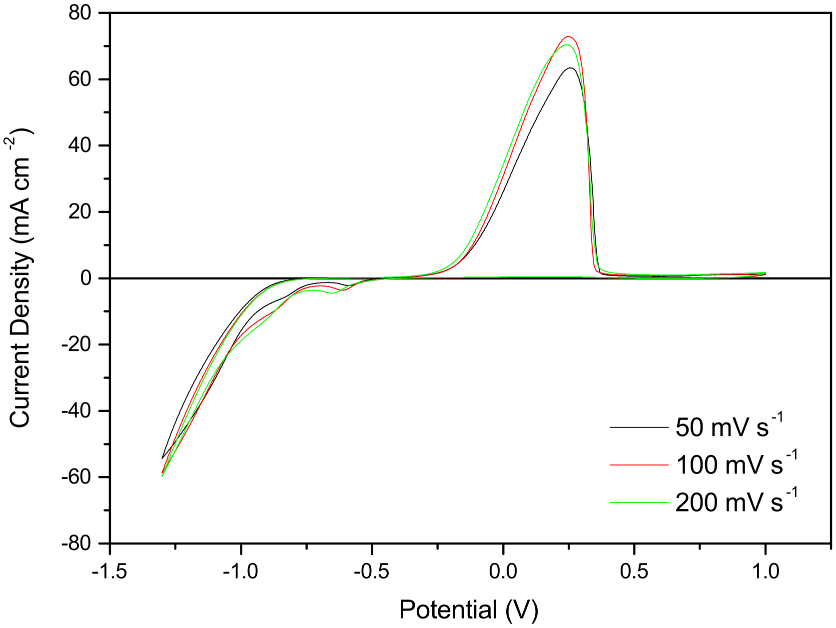

Figure 4.1: Cyclic Voltammetry of nickel deposition and stripping in the boric acid based bath described in Table 4.1 Voltammetry was performed on a Pt electrode using a SCE reference. The potential was swept from 1.0 V to -1.3 V at room temperature. The scan was started at 1.0 V and the 5th scan is shown.

in pH due to hydrogen evolution [141]. Formation of hydroxide species would result in the electrode becoming inert over time and decrease the stripping current observed.

For comparison, cyclic voltammetry of boric acid on a the platinum disc electrode was performed in the potential range between 1.00 and -1.00 V. Five sequential scans were made under the same conditions as Figure 4.2 and are shown in Figure 4.3. As expected, the current densities measured in these scan were lower, as no metal deposition can occur. PtO formation was observed in the cathodic scan at a potential of 0.14 V. The rate of the HER reaction increases rapidly form a potential around -0.55 V. This is a potential similar to that seen for the HER from the nickel plating bath. In the return scan the x-axis is intercepted at -0.4 V. Using the Nernst equation, and for a pH of 2.8, the equilibrium potential for the HER is calculated as E = -0.41 V *vs.* SCE. These background scans demonstrate hydrogen evolution occurs in boric acid at a potential similar to that for the first cathodic peak (at -0.62 V in Figure 4.1) in nickel plating bath. Furthermore,

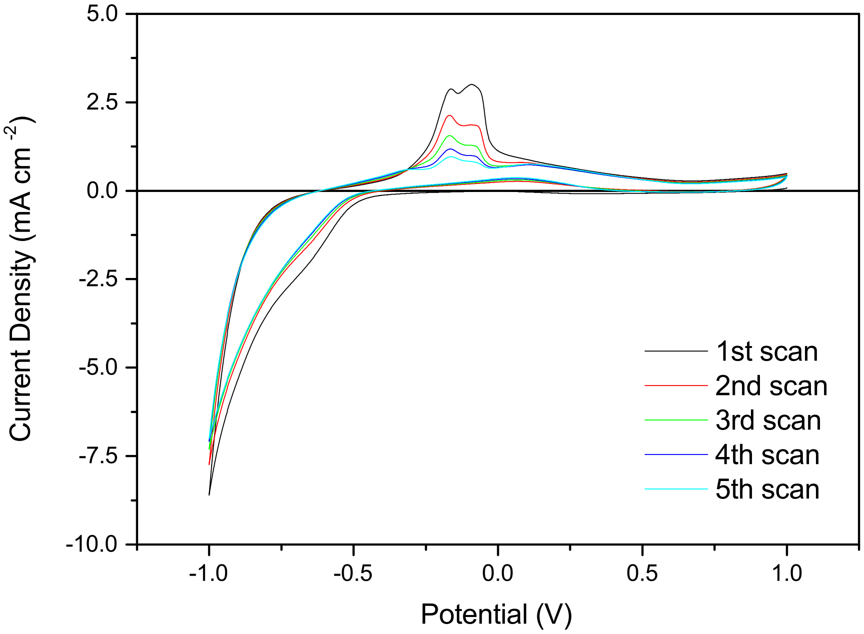

Figure 4.2: Series of cyclic voltammograms obtained from the boric acid based nickel electroplating bath with a restricted potential window compared to Figure 4.1. Voltammetry was performed on a platinum electrode at room temperature using a SCE reference.

the addition of SDS and saccharin to the bath is not expected to significantly shift the potentials for hydrogen evolution.

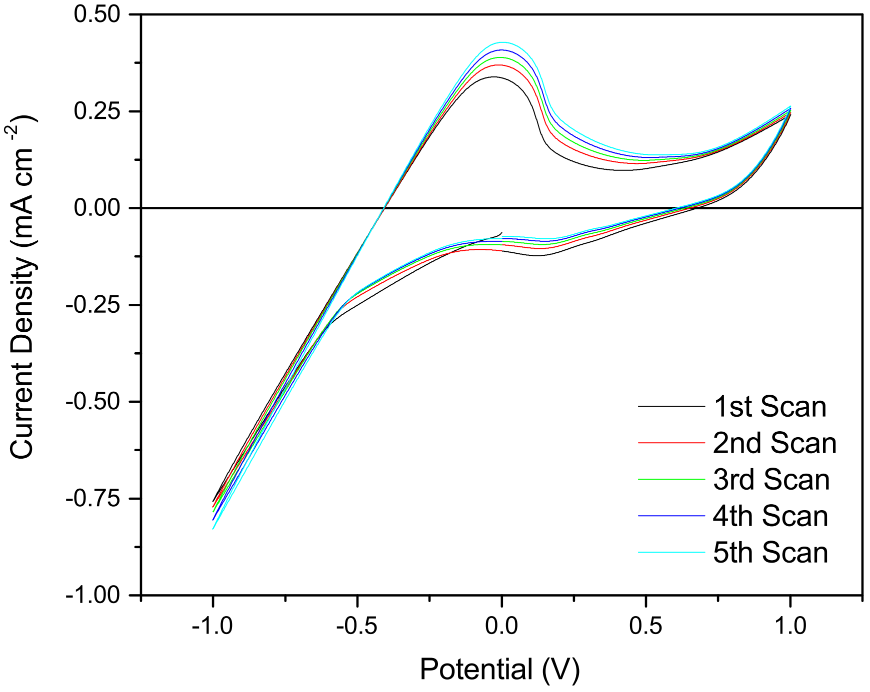

Figure 4.3: Series of cyclic voltammograms obtained from boric acid (25 g L^{-1}) at pH 2.8. Cyclic voltammetry with a scan rate of 100 mV s^{-1} was performed on a platinum electrode at room temperature using the SCE as a reference.

4.2.2 Electrochemical Quartz Crystal Microbalance (EQCM)

Using the EQCM more detailed information about the nickel deposition process can be obtained. The EQCM can determine what potential is required for material to be deposited on the electrode, and distinguishing which peaks in the voltammetry lead to the deposition of solid material on the electrode. The EQCM can also determine the efficiency and deposition rate of material on to the electrode providing insight into the deposition mechanism.

Cyclic Voltammetry on the EQCM

A series of cyclic voltammograms with measured, associated frequency changes are shown in Figure 4.4. At slower scan rates more material is deposited resulting in the larger overall frequency change. It's interesting that the frequency does not return to its initial value after the scan taken at 50 mV s^{-1}. This implies that some material remains on the electrode. For a slower scan rate there is a longer time for the deposited metal, Ni, to form the more stable bulk material. It therefore becomes more difficult to strip the metal from the electrode. This is reflected in the CV as a change of shape of the stripping peak. During the outward scan the currents are larger than for the return scan. In the outward scan there are contributions to the current from nickel and hydrogen which are under diffusion control resulting in the increased current with scan rate. The reverse scan is more representative of the nickel kinetics.

Using this data an increase of mass on the electrode can be determined. To obtain the rate of solid material being deposited on the electrode the derivative of the frequency was taken and then compared to the current being passed. The derivative of the frequency w.r.t. potential is shown in Figure 4.5 at a scan rate of 50 mV s^{-1}. The outward scan shows that material is being deposited on the electrode from a potential of -0.41 V and initially matches well with the current. The efficiency is highest during the initial stages of deposition. This shows that there was solid material being deposited on the electrode and no significant region where hydrogen is evolved on its own.

On the reverse scan material stops being deposited at a potential of -0.70 V. During stripping the current and rate of change of frequency were in good agreement indicating that no measurable additional oxidative processes occur at these scan rates.

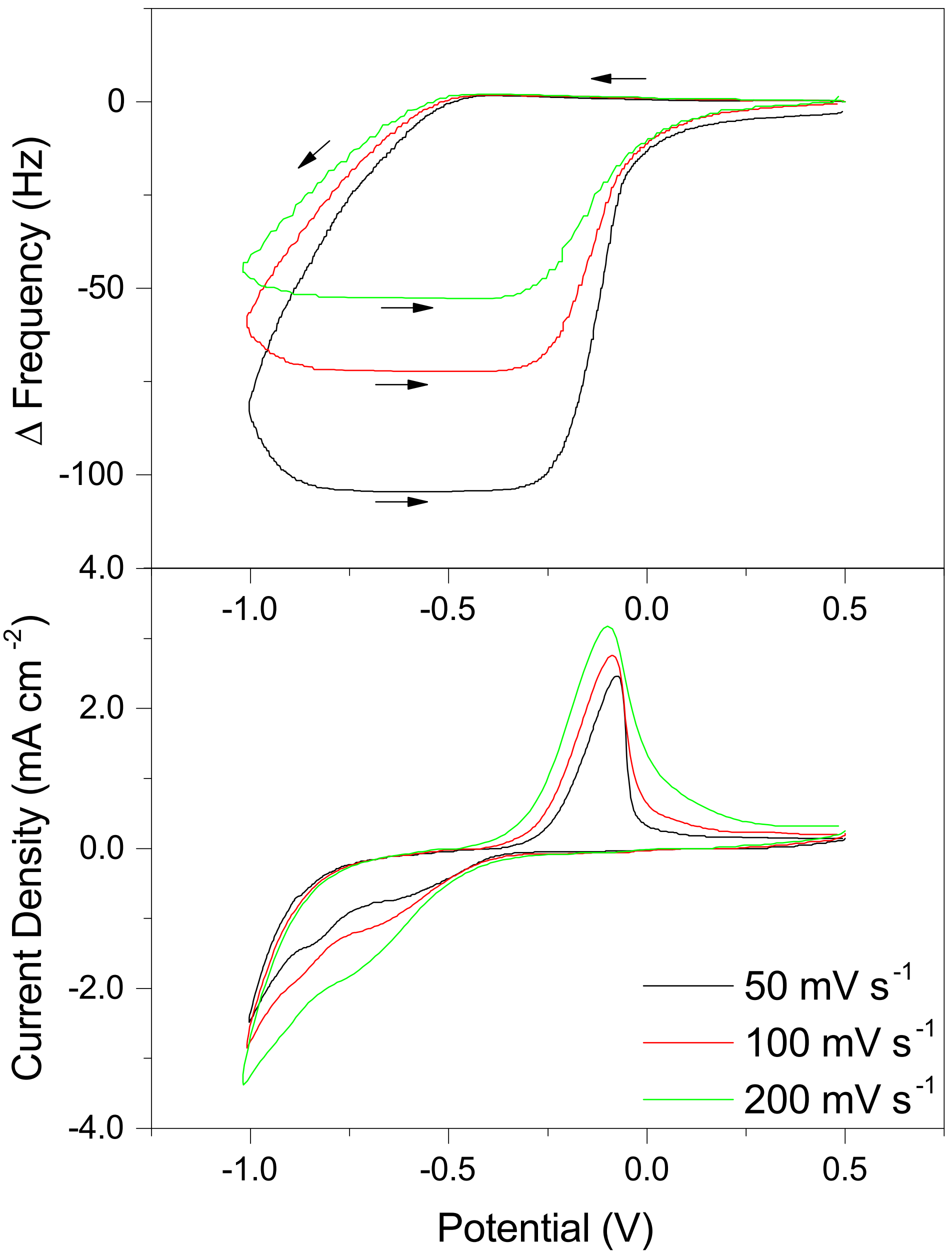

Figure 4.4: Cyclic voltammetry of the boric acid based nickel plating bath and change in frequency response measured on the EQCM. Scans were performed at room temperature, on a Pt electrode and using a SCE reference. The responses shown are the 5th scan at each scan rate.

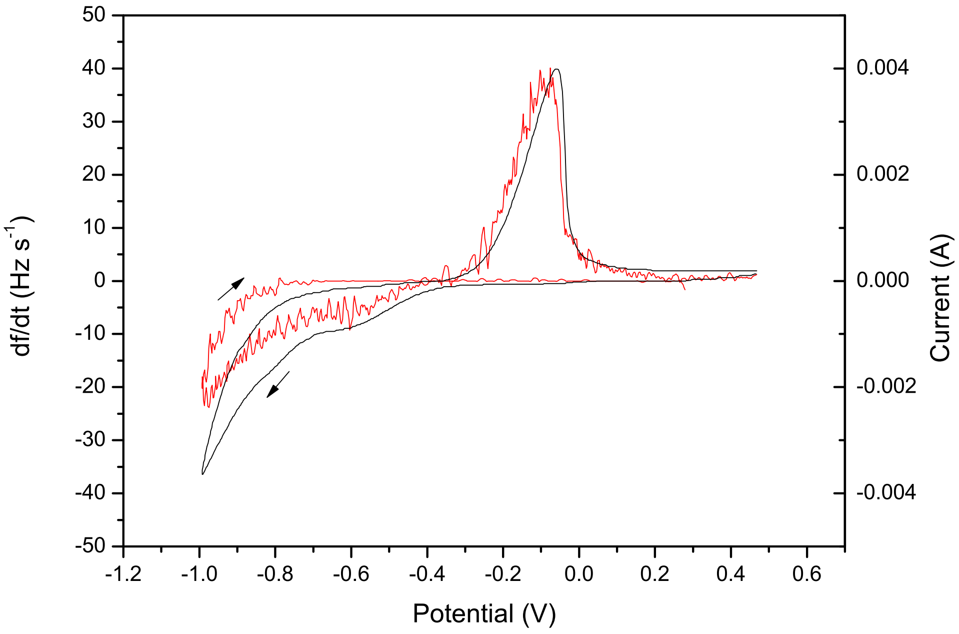

Figure 4.5: The rate of change of frequency w.r.t. time (*df/dt*, red) during the cyclic voltammogram in Figure 4.4 (black) at 50 mV s^{-1}.

The efficiencies in the potential window +1 to -1 V were measured to be low, less than 50 %. To deposit more nickel on the electrode and better represent the bulk deposition of nickel further experiments were performed extending the potential window and lowering the scan rate. Cyclic voltammetry was performed between 0.5 and -1.2 V on the EQCM to deposit and strip nickel at scan rates between 2 and 50 mV s^{-1}. An typical example for the voltammetry and frequency response (*df/dt*) measured is shown in Figure 4.6.

There are some significant differences when comparing the voltammetry and frequency response in the narrower potential window. At potentials further negative than -1.0 V there is a greater efficiency and for the reverse scan the frequency response follows the current. Initially the stripping peak follows the current. However, as more of the film is removed *df/dt* deviates from the current before spiking rapidly as the last of the film is removed. It is possible that this could be caused by an increase in the amount of intrinsic stress of the early deposit. The HER is more prevalent during the initial stages of deposition and its increased incorporation into the film may result in a higher stress resulting in the frequency response observed.

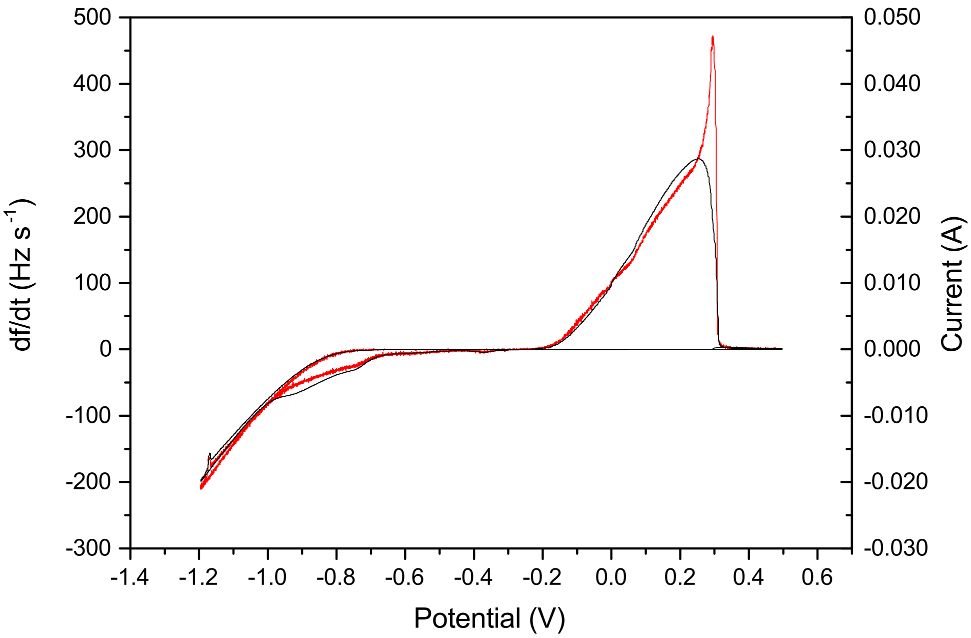

Figure 4.6: The rate of change of frequency w.r.t. time (df/dt, red) during the cyclic voltammogram (black) for an extended potential window of 0.5 V to -1.2 V. The scan shown is the 3rd scan performed at 5 mV s^{-1}.

To measure the overall efficiency across the potential window the charge passed for plating and stripping was measured for each scan from integration of the current and plotted against the frequency change for each scan (Figure 4.7). From this plot the gradient was obtained and an overall efficiency across the potential window can be calculated. For deposition the gradient was found to be 10.356 ± 0.026 Hz mC^{-1} and 11.038 ± 0.032 Hz mC^{-1} for the stripping portion. For a C_f of 0.056 Hz ng^{-1} cm^2 (see EQCM calibration, Section 3.3.2.2) this results in overall efficiencies for deposition and stripping of 83.9 ± 0.2 % and 88.8 ± 0.3 % respectively.

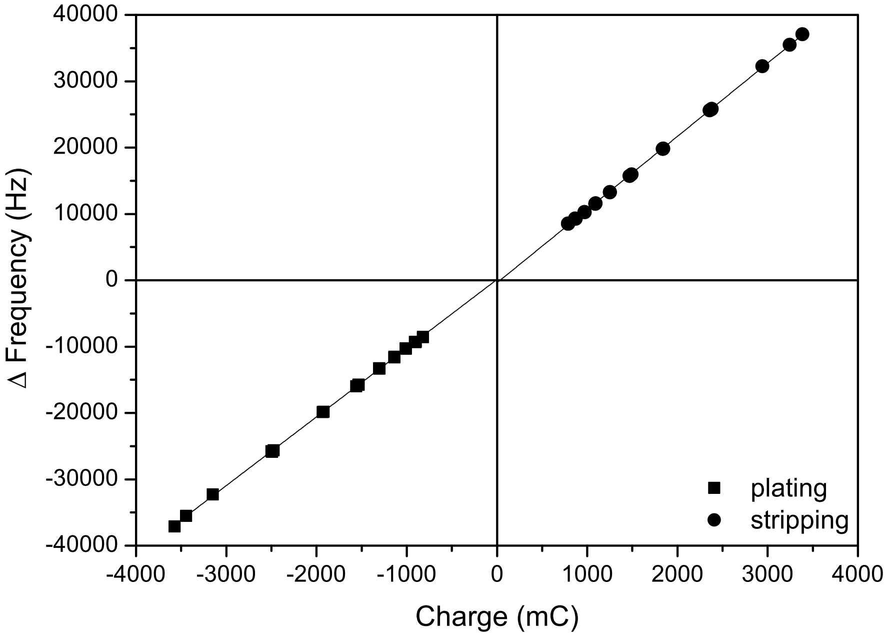

Figure 4.7: Total plating and stripping current against change in frequency for the deposition of nickel over scan rates of 2-50 mV s^{-1}in the potential window 0.5 to -1.2 V. Three scans were performed at each scan rate (2, 3, 4, 5, 6, 7, 8, 9, 10, 15, 25 and 50 mV s^{-1})

Galvanostatic Deposition on the EQCM

It is easiest to interpret EQCM data once steady state conditions have been achieved [115]. In galvanostatic experiments a steady-state (or close to) can be seen to be achieved when the potential remains constant and there are no further changes in the concentration profile.To this end the galvanostatic deposition of nickel was performed on the EQCM. From these experiments the efficiency of nickel deposition can be measured across a range of currents once a steady potential and hence frequency response has been achieved.

In the previous section it is demonstrated that the deposition of nickel onto platinum differs from the deposition of nickel on to itself. To remove the effects of platinum an initial layer of nickel was electrochemically deposited from the nickel bath (room temperature, pH 3.0) at a current of 20 mA for 100 s. Subsequently deposits were made over 60 s at currents ranging from 0.5 to 25 mA. The change in frequency was measured. The slope of the frequency-time plots was determined from a linear regression. The fit of these linear plots was very good with R^2 values of 0.997 or better. The

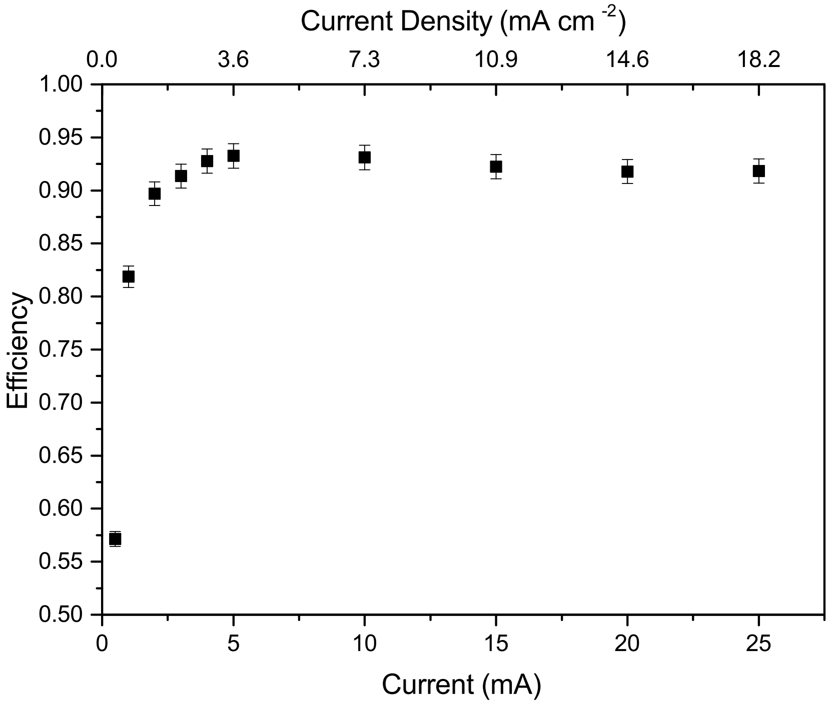

Figure 4.8: Measured efficiency for Ni deposition on to a nickel electrode from a boric bath using galvanostatic methods.

efficiency at each current density was determined from the Sauerbrey equation using the previously measured Sauerbrey constant for the crystal (0.0514 ± 0.0006 Hz ng^{-1} cm^{2}).

Figure 4.8 shows the measured coulombic efficiency of deposition over the range of current densities. At low currents the efficiency is at its lowest indicating increased hydrogen evolution. The efficiency then peaks at approximately 5 mA at an efficiency of 93%. As the current is increased further the efficiency begins to gradually decrease to approximately 90 %. When low currents ($<$ 2 mA) were applied the efficiency of deposition reduced significantly. When the current is increased the HER cannot provide the necessary flux to the electrode and an increased proportion of nickel is then deposited.

Galvanostatic experiments were also performed on the bare Pt electrode. Figure 4.9 shows the change in frequency (a) and potential (c) over time for deposition performed at 10 mA. In addition a calculated plot for the change in frequency expected for 85 % efficient deposition has been added as a guide for the eye (b) where the gradient is 105.7 Hz s^{-1}. This was the efficiency measured from the later stages of the experiment where the increase in frequency remains linear.

There are three identifiable regions of the EQCM response during deposition. Initially there is a linear increase in the frequency with time (or charge) and then, after approximately 3 s or a frequency decrease of 290 Hz, the response deviates from linear. In this region the gradient is -101 Hz s^{-1} which corresponds to an efficiency of 81 %. A frequency change of -290 Hz corresponds to approximately 30 layers of nickel deposition onto the platinum electrode (given the mass of a monolayer of nickel is approximately 158 ng cm^{-2}). In this early phase of the experiment the response can be associated with deposition of nickel with properties greatly influenced by the underlying platinum electrode.

In the second region the frequency response was found to be slower until 250 mC of charge has been passed after which the frequency response again becomes linear. This also aligns with the leveling off of the deposition potential. As the thin film grows into a bulk film changes in the stress and surface roughness can result in a shift of the frequency response. Once the film has grown further the deposition of nickel occurs on a bulk nickel electrode the film properties no longer change and a linear response is observed once again and gives a coulombic efficiency of 85 %.

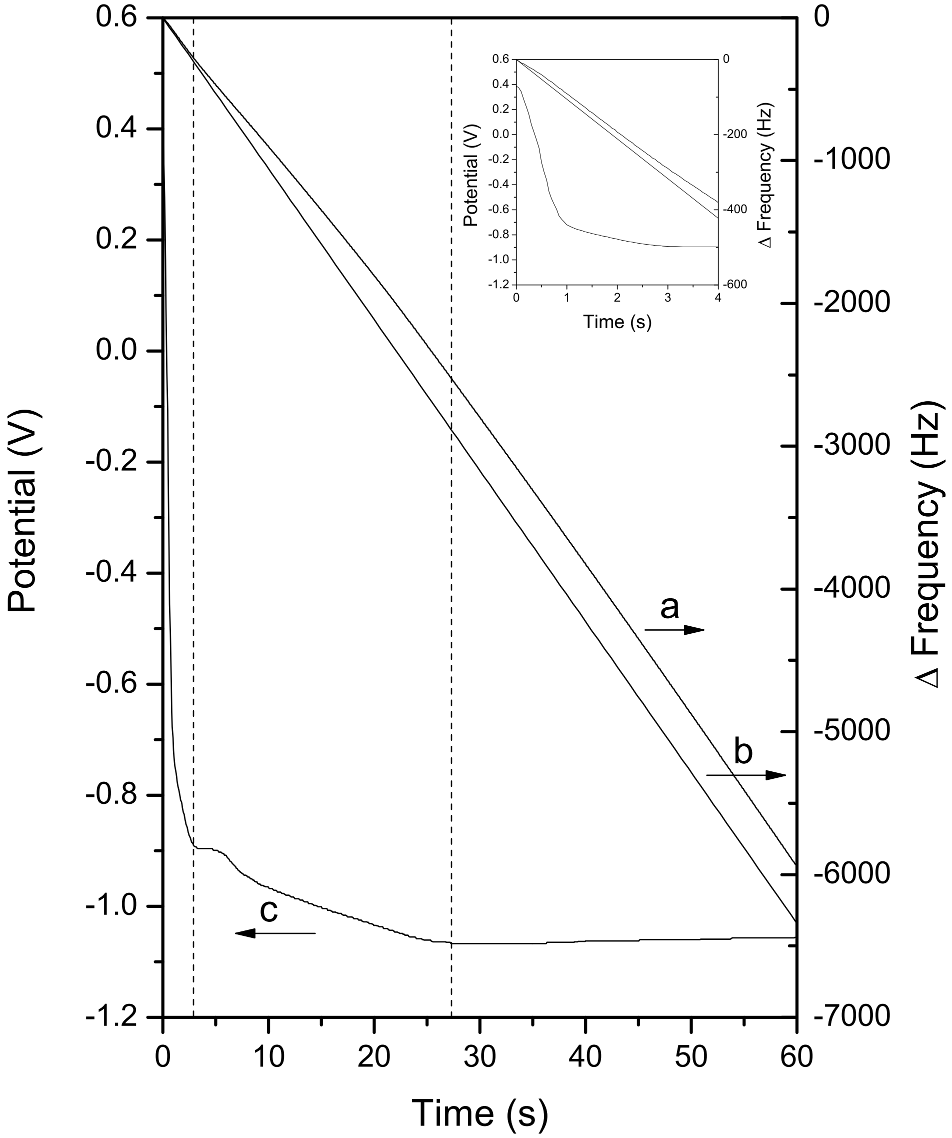

Figure 4.9: Deposition of nickel from the boric acid bath on to a platinum electrode at a current of 10 mA over 60 s showing: a) the change in frequency measured experimentally; b) the calculated change in frequency expected for 85 % efficient deposition; c) the electrode potential. Inset: Initial 4 seconds.

In summary this section has examined nickel deposition on to platinum disc electrodes and the EQCM. It was shown that, in the boric acid bath, hydrogen is co-evolved with the deposition of nickel. The extent of the HER can be lowered compared to nickel deposition by applying an optimal current density. The influence of the substrate and potential changes must also be considered in the interpretation of EQCM data.

4.3 Deposition of Nickel-Iron from a Boric Acid Bath

The introduction of iron to deposit a nickel-iron alloy further complicates the electrodeposition mechanism. As discussed previously in Section 1.3.2 the nickel-iron system exhibits anomalous behavior where the less noble metal, iron, deposits preferentially to the more noble metal, nickel. This behavior makes the nickel-iron system of fundamental electrochemical interest. In this section a boric acid based nickel-iron bath, as detailed in Table 4.2, was used to investigate the effects of iron during deposition. This bath is based upon the nickel-iron plating bath as used by industrial partners and in the microfabrication of MEMS devices [30, 31, 32]. Deposits were made at room temperature and the bath adjusted to a pH of 2.8 with HCl prior to deposition. The electrochemical behavior of the boric acid based nickel-iron bath would provide useful information for comparisons with any new bath which is developed. The similarities and differences between baths may also provide insight towards the deposition mechanism and provide a better understanding of the anomalous behavior displayed in this system.

Chemical	Concentration (g L^{-1})
$NiCl_2.6H_2O$	110
$FeCl_2.4H_2O$	6
H_3BO_3	25
sodium saccharin	2
SDS	0.1

Table 4.2: Contents of the boric acid based nickel-iron plating bath.

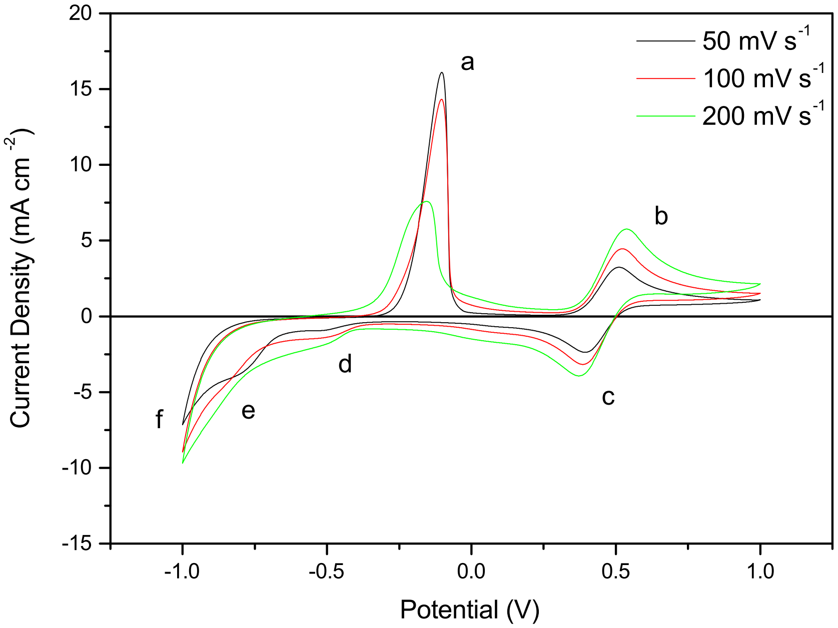

Figure 4.10: Cyclic voltammetry of nickel-iron boric acid electrodeposition bath. Voltammetry was performed at room temperature, on a Pt electrode using a SCE reference. The scan was performed from a stating potential of 1.0 V and swept negative to -1.0 V then positive to return to 1.0 V. The 5th cycle is shown for each scan rate.

4.3.1 Cyclic Voltammetry on Pt electrodes

Using the boric acid based nickel-iron electrodeposition bath cyclic voltammetry was performed on platinum electrodes. Figure 4.10 shows voltammetry between +1.0 and -1.0 V performed at scan rates of 50, 100 and 200 mV s^{-1}.

Compared to the voltammetry of the nickel only bath (Figure 4.1) there are a number of additional features observed due to the addition of $FeCl_2$. Fe(II) / Fe(III) redox chemistry is observed (peaks b and c) centered around $E_{1/2} = 0.45$ V.

At slow scan rates a single nickel-iron stripping peak (a) is found on the reverse scan. However, at faster scan rates this peak changes shape as additional processes occur. The changing nature of the peak (a) may be associated with hydrogen or the deposited film becoming more stable over a longer period of time. The currents for peaks (d) and (e) are seen to increase in magnitude with scan rate (more clearly seen at an extended potential window in Figure 4.11) although have little effect on the stripping peak.

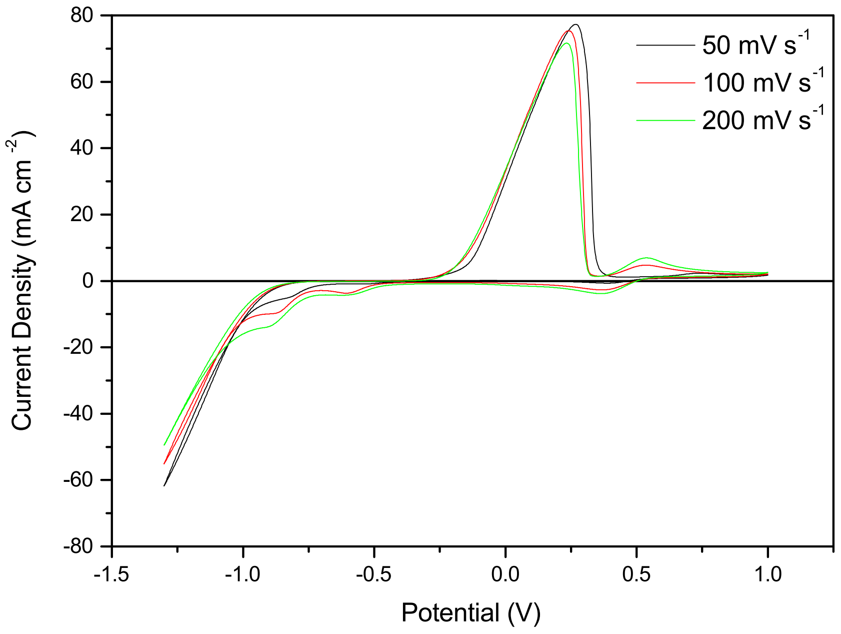

Figure 4.11: Cyclic voltammetry of the nickel-iron boric acid electrodeposition bath with an extended potential window of -1.3 V to 1.0 V. Voltammetry was performed at room temperature, on a Pt electrode using a SCE reference.

With a wider potential window (Figure 4.11) nickel plating and stripping dominates the voltammetry. Interestingly, the currents during nickel deposition were found to be larger at a slower scan rate. This may be due to larger bubbles of hydrogen being generated decreasing the overall area of the electrode and hence the current. Durning stripping of the metal alloy it is interesting that the it is removed in a single peak. Other alloy systems (Cu-Zn, Cu-Au, Au-Ag) have demonstrated the removal of the less nobel metal prior to the more nobel metal [142, 143, 144]. Addtionally, electrochemical dealloying of Ni-Cu films was demonstrated to produce nanopourous nickel due to the formation of a passive oxide film on the nickel [145]. No similar effects for the nickel-iron system were found in the literature. In this case the stripping potential for both components are similar and, in practical terms appear to strip simultaneously as a single peak.

4.3.2 Blanket Films on Cu Electrodes

4.3.2.1 Galvanostatic Deposition

Galvanostatic deposition is widely used to deposit films of metal in commercial applications. It requires simpler circuitry than potentiostatic deposition to deposit in this manner since no feed back is required from the reference electrode and it is therefore used widely in industrial processing [111]. To be commercially viable deposition must occur at a reasonable rate. For many systems current densities upward of 100 mA cm^{-2} can be used; however, NiFe deposition is usually performed at current densities between 10 and 40 mA cm^{-2} [33]. To determine the concentration of iron chloride required to give the ideal composition ($Ni_{80}Fe_{20}$) deposits were made from baths with varying nickel compositions. Square copper electrodes were used to replicate deposition onto a copper seed layer.

The plots in Figure 4.12 shows the potential during deposition of films at 20 mA cm^{-1} under agitation from a magnetic stirrer at 750 rpm. The deposition potential was found to become more negative as the concentration of Fe^{2+} was increased. It has been suggested that iron species inhibit nickel deposition [102, 100, 109]. The addition of Fe^{2+} would then require a larger potential to drive the reaction at a given rate provided that the concentration of Fe^{2+} is such that it cannot provide the necessary current on its own.

The OCP was measured before and after deposition. It was found that prior to deposition, on the copper electrode, the OCP was more positive with a higher concentration of Fe^{2+}. After deposition the OCP was more negative with an increasing Fe^{2+} concentration. This change in order is due to the electrode material changing from copper at the start of the experiment to Ni or NiFe after deposition.

For the experiment where there is no iron in the bath, $[Fe^{2+}] = 0$ g L^{-1}, the OCP after deposition can be analysed according to the Nernst equation (2.6). A number of reactions may determine the OCP. If the reduction and oxidation of nickel (reaction 4.1) determined the OCP after deposition the potential can be calculated.

$$Ni \rightleftharpoons Ni^{2+} + 2e^- \qquad E^0 = -0.499\,\mathrm{V\ vs.\,SCE} \tag{4.1}$$

$$\begin{aligned} E &= E^0 + \frac{RT}{nF} ln[Ni^{2+}] \\ &= -0.499 + \frac{RT}{2F} ln[0.5] \\ &= -0.51\,\mathrm{V}\ vs.\,\mathrm{SCE} \end{aligned}$$

This shows for a concentration of 0.5 M Ni^{2+} the OCP would be -0.51 V vs. SCE. Experimentally the OCP is -0.2 V this implies that a different reaction is determining the open circuit potential. Alternatively the OCP may be determined from the hydrogen evolution reaction (4.2). For a pH of 2.8 the concentration $[H^+] = 10^{-2.8}$ from this the potential can be calculated.

$$H^+ + e^- \rightleftharpoons {}^1\!/_2 H_2 \qquad E^0 = -0.242\,\mathrm{V\,vs.\,SCE} \tag{4.2}$$

$$\begin{aligned} E &= E^0 + \frac{RT}{nF} ln[H^+] \\ &= -0.242 + \frac{RT}{F} ln[10^{-2.8}] \\ &= -0.41\,\mathrm{V}\ vs.\,\mathrm{SCE} \end{aligned}$$

These calculations do not satisfactorily explain the measured OCP but they do not take into account use of additives in the plating solution. These additives, be it boric acid, saccharin or SDS, adsorb on the electrode surface (see Sections 1.2.2 and 1.2.5) and therefore may have a role in determining the open circuit potential. Indeed it is most likely a combination of these factors determine the observed OCP.

The fraction of iron in these NiFe deposits was measured using XRF and was found to increase linearly with the concentration of Fe^{2+} in the bath (Figure 4.13). Further deposits were made at an increased temperature of 60 °C. When the temperature of the bath was increased the iron content in the film still increased in a linear manner; however, the proportion of iron in the film was found to be less than that at lower temperatures. If the deposition of iron is mass transport limited then a change in temperature should not increase the rate of deposition and hence the composition. From

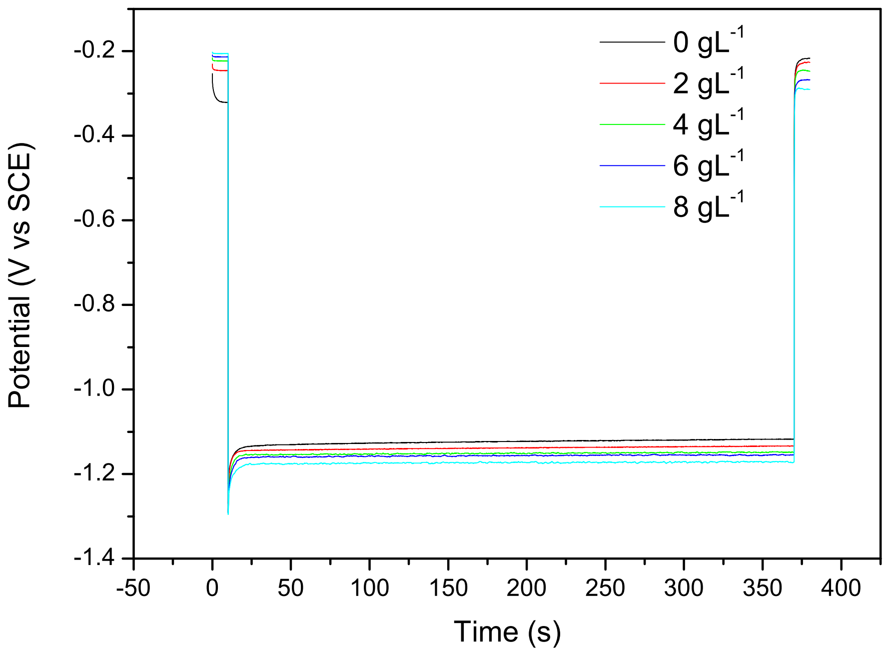

Figure 4.12: Potential-time plots for deposition of NiFe from the boric acid bath varying the iron concentration. A current density of 20 $mAcm^{-2}$ was applied to deposit on copper square electrodes. Deposition was performed under agitation from a magnetic stirrer at 750 rpm at room temperature.

this it is inferred that the change in composition is due to an increased rate of nickel deposition which is not under mass transport control.

4.3.2.2 Varying Current Density

To examine the effects of current density on the deposition of nickel-iron from the boric acid bath blanket films of nickel iron were deposited on square copper electrodes. Deposition was performed with mild agitation (750 rpm) *via* a magnetic stirrer. The charge passed during deposition remained constant at 7.2 C and the current was varied from 10 to 50 mA.

The potential-time transients are shown in Figure 4.14. A steady state response is achieved for all current densities. The transition to this steady state is seen to take a longer time at the lower currents. It can be expected that it takes longer to achieve a steady state diffusion regime at lower currents. When compared to the voltammetry the potentials at low current are comparable to

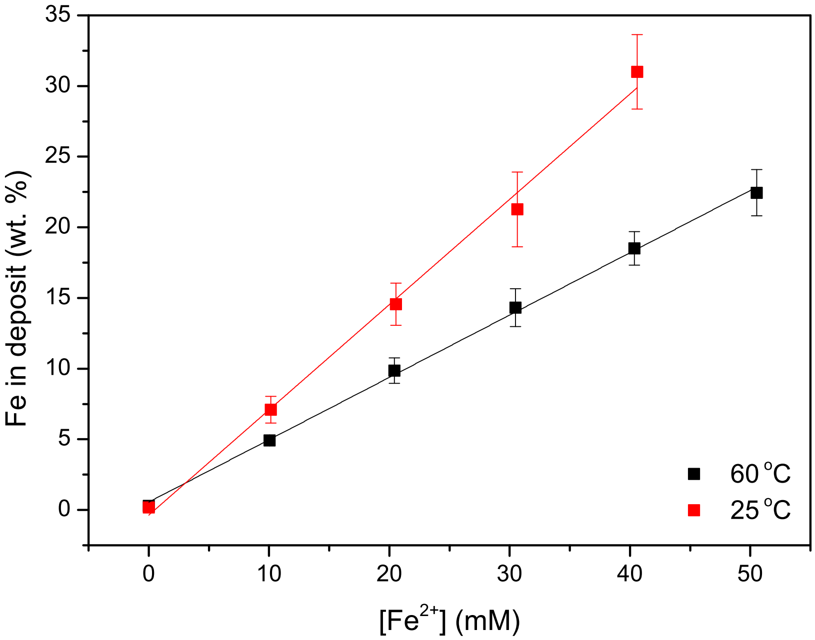

Figure 4.13: Measured film composition using XRF against the iron concentration in solution for deposits made on to copper square electrodes at 20 mA cm^{-2} with agitation from a magnetic stirrer.

that of the hydrogen reduction peaks. The species required for this reaction may have to become depleted before nickel deposition becomes the dominant process.

Scanning electron micrographs (SEMs) were taken of films deposited from the boric acid bath at 50 mA cm^{-2} and are shown in Figure 4.15. In these images the electrodeposited nickel iron film is shown on the right hand side with the sputtered titanium layer shown on the left. High magnification is required to see the surface texture on the film. In general the films appear smooth and flat.

The composition of the films deposited at different current densities from the same bath was measured using XRF and is shown in Figure 4.16. The composition was shown to vary with current density. The error bars indicate the variation in composition across the electrode. A maximum iron content was seen for a current density of 30 mA cm^{-2}. A greater variation in composition was found at increased current densities.

From the deposition of nickel only it was shown that the efficiency of nickel deposition is lowest

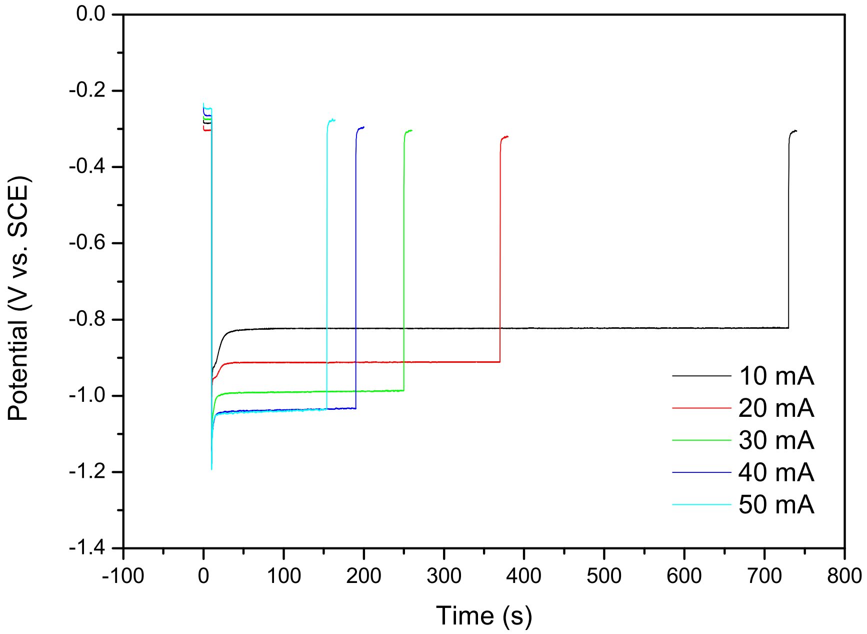

Figure 4.14: Potential-time plots for NiFe deposition at varying current densities from boric acid bath as described in Table 4.2. Deposits were made on to copper square electrodes at room temperature under agitation from a magnetic stirrer.

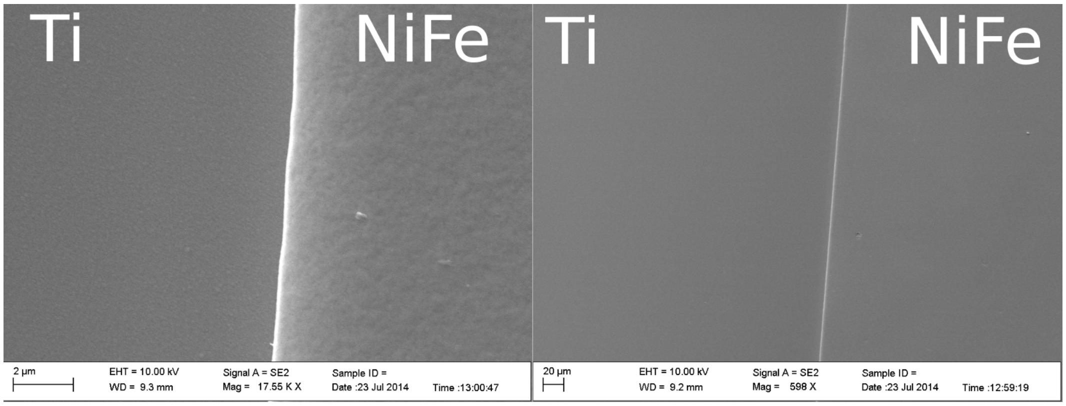

Figure 4.15: SEMs of a NiFe film deposited form the boric acid bath (50 $mAcm^{-2}$) left: high magnification (17.55 K ×) Right: low magnification (598 ×).

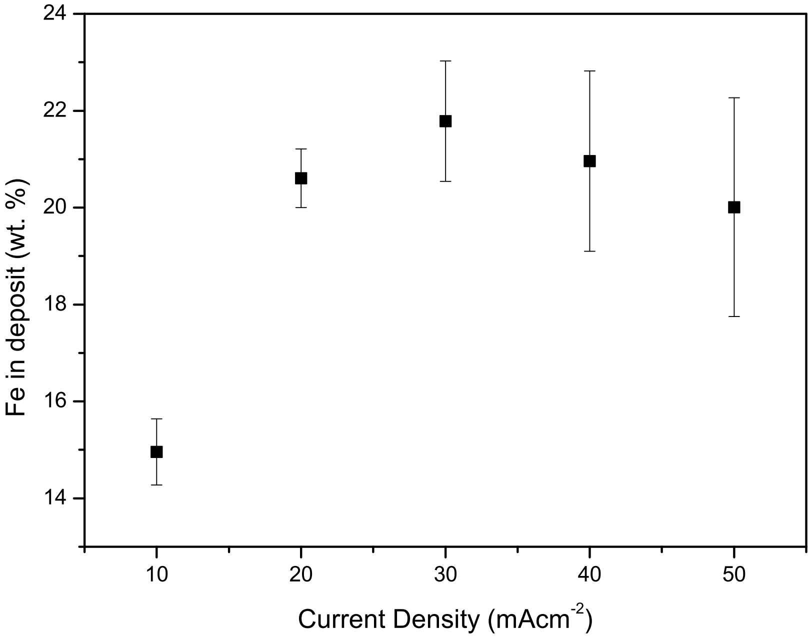

Figure 4.16: Composition of NiFe films measure using XRF deposited from the boric acid bath (Table 4.2). Deposits were made on to copper square electrodes at room temperature under agitation from a magnetic stirrer.

at low currents. For the deposition of the nickel-iron alloy it is shown that the film has a larger proportion of nickel at these same low currents.

4.3.2.3 Controlling Film Thickness

Nickel iron films of varying thickness may be required for the fabrication of MEMS devices. It is important to ensure that the deposition bath can reliably deposit films of varying thickness according to the charge passed. Faraday's law (Equation 4.3) dictates a linear relationship between mass (and therefore thickness) and the charge passed. To ensure there was a linear type response for nickel iron on the copper electrodes deposits were made at a current density of 20 mA cm^{-2} over increasing time periods to deposit different quantities of nickel film. After deposition the photoresist on the electrode was removed to measure the film thickness at the edge of the electrode using surface profilometry.

$$m = \left(\frac{it}{F}\right)\left(\frac{M}{z}\right) \tag{4.3}$$

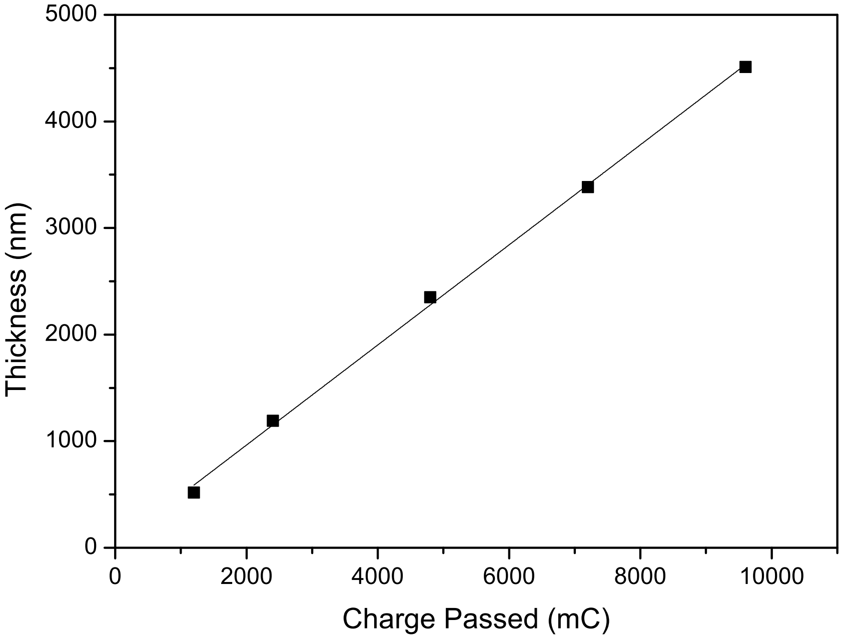

Figure 4.17: Measured film thicknesses from surface profilometry for nickel-iron films. Deposits were made at a current density of 20 mA cm^{-2} for varying lengths of time between 60 and 480 s onto copper square electrodes. Experiments were performed at room temperature, under agitation from a magnetic stirrer (750 rpm).

A plot of the thickness of the deposit against charge passed, Figure 4.17, gives a linear plot with a deposition rate of 470 ± 9 nm C^{-1} or 564 ± 11 nm min^{-1}. The anticipated deposition rate of a $Ni_{80}Fe_{20}$ film is expected to be 357 nm C^{-1} (100 % efficiency, $\rho = 8.447$ g cm^{-3} [130]). The measured deposition rate is 1.3 times larger that expected. There are two reasons for which this may occur. The density of the polycrystalline film deposited may be less that for the bulk metal due to a microporous structure. It is also known that a larger proportion of the current passes at the edge of the electrodes where the thickness was measured. With an increase in the proportion of the current passing at the edge a thicker film would be deposited. Therefore, although the measured deposition rate appears too high, the linear relation indicates the electrodeposition of NiFe films follows Faraday's law.

4.4 Conclusions

Using the boric acid based bath the deposition of nickel and nickel-iron has been examined. Using cyclic voltammetry on platinum electrodes and on the EQCM the significance of the hydrogen evolution reaction was emphasised particularly during the initial stages of deposition where an increase in HER may increase the stress of the film. Additionally, at low currents of overpotentials the HER is more prevalent.

As a benchmark for further work nickel-iron was deposited using galvanostatic techniques onto fabricated copper electrodes and then characterised. The effects of key parameters (current density, iron concentration, temperature, deposition time) in the nickel-iron deposition process were evaluated using these electrodes.

For the development of a new deposition bath there are a number of key lessons which can be applied.

- The hydrogen evolution reaction displays a significant role in the deposition of nickel and nickel-iron.
- During deposition the formation of hydroxide species can occur. The formation of these species is not desired and deposition conditions should be modified to avoid this.
- The composition of NiFe can be controlled using a range of techniques including the current density, temperature and the iron concentration however the effects on the coulombic efficiency must be taken into account.

With the general behavior of this existing boric acid based bath examined work to develop a new bath could be initiated.

Chapter 5

Development of the Nickel-Iron Citric Bath

5.1 Motivation

The desire to develop a new bath for the deposition of nickel-iron is driven from concern about the potential health impact of boric acid. Deposition of nickel and nickel-iron from boric acid based baths have been widely studied in the literature due to commercial relevance and in an attempt to fundamentally understand the processes behind anomalous deposition. In addition to this, information obtained in the previous chapter gives an indication of the behavior to be expected from nickel and nickel-iron plating baths. In the development of a new plating bath these characteristics can guide and influence the process to produce an alternative bath.

Others have identified the citrate anion as a potential alternative to boric acid in the nickel deposition bath. Fundamentally it has been suggested that citrate and its associated additional polymeric species may partially block the electrode to act as an inhibitor for the HER [80, 146]. This can, in turn, lead to more uniform deposits. The electrodeposition of nickel itself from a citric bath has been demonstrated [81, 83, 82]; however, citrate has been more widely used as a stabilising or complexing agent in addition to boric acid in electrodeposition baths [76, 77, 147, 74, 148].

The deposition of nickel-iron presents a larger challenge than the deposition of nickel alone due to the requirement of dissolved iron (II) stability in the bath. The deposits must also be of suitable quality (uniformity, composition, etc.) for use in MEMS devices. It is also favourable if the new bath could be used as a direct replacement for the boric acid bath, hence requiring minimal changes in deposition equipment.

This chapter shows the development of a citric acid based nickel-iron electrodeposition bath suitable for the replacement of existing boric acid based electrolytes. Investigations into the composition of the electrolyte, the variation of current density, the effects of temperature, etc. were used to guide the process of development. These also gave some insight into the fundamental mechanisms of nickel-iron electrodeposition.

5.2 Initial Bath

The initial citric bath used was based around the existing boric acid based plating solution as detailed in Table 4.2 of the previous chapter. Nickel (II) chloride was used as the source of nickel in the bath. It is generally accepted that chloride salts have improved throwing power (for example over the sulfate salt) as desired when filling trenches [33]. For a commercial plating bath a reasonable deposition rate is required (20 mA cm^{-2}). In order to avoid the electrochemical reaction from becoming mass transport limited due to concentration depletion, a high concentration of nickel salt is desired. A high salt concentration also gives the advantage that during deposition there is minimal effect from concentration changes over prolonged periods of plating. Similarly to boric acid studies, iron (II) chloride was used to provide iron content. The concentration of Fe (II) among other parameters is critical in achieving the desired film composition. Iron is required in smaller quantities than nickel and even less than thermodynamically expected due to anomalous deposition (see Section 1.3.2).

To prevent the formation of insoluble iron oxide in the bath, a low pH is required. Initially, to maintain this low pH, a sodium citrate / citric acid buffer system was applied in this new bath. The ratio of the salt and acid required to give a pH of 2.8 was approximated from the Henderson-Hasselbalch equation (5.1) and then refined experimentally to give the required value. The Henderson-Hasselbalch equation does not strictly apply to a tri-protic acid like citric acid due to the small separation of it's pK_a values but the resulting value remains close enough as an initial approximation therefore it is not surprising that the actual measured pH was lower than the predicted value. This could be due to a variety of reasons including activity effects,

Chemical	Concentration / g L^{-1}
$NiCl_2.6H_2O$	110
$FeCl_2.4H_2O$	8
$Na_3Cit.2H_2O$	15.69
$H_3Cit.H_2O$	3.75
sodium saccharin	2
SDS	0.01

Table 5.1: Contents of the initially proposed citric acid based NiFe plating bath.

high concentrations of salts (resulting in a high ionic strength) or hydrolysis caused by the high concentrations of nickel (and iron) salts.

$$pH = pK_a + \log\left(\frac{[A^-]}{[HA]}\right) \tag{5.1}$$

The additives sodium saccharin and SDS were initially maintained at the same concentration as for the boric bath. Saccharin (sodium salt) acts as a leveler and brightener enabling smooth flat deposits and SDS is used to improve wetting at the electrode (Section 1.2.5). The initial composition of the bath is shown in Table 5.1. pH is an important parameter during deposition and was further decreased using HCl (10 % vol). Increasing the pH is more difficult, as the local addition of NaOH in high concentrations causes a high local pH change which then precipitates nickel and iron hydroxide species as in Equations 5.2 and 5.3. The precipitation of these species is not desired and should be avoided.

$$NiCl_{2\,(aq)} + 2NaOH_{(aq)} \longrightarrow NiOH_{2\,(s)} + 2NaCl_{(aq)} \tag{5.2}$$

$$FeCl_{2\,(aq)} + 2NaOH_{(aq)} \longrightarrow FeOH_{2\,(s)} + 2NaCl_{(aq)} \tag{5.3}$$

5.3 Citrate Concentration

An important parameter in the composition of the bath is the concentration of the citrate anion. Initial studies to determine a suitable concentration of total citrate content at a fixed pH of 3.0 were performed to determine an optimal citrate concentration.

Galvanostatic deposition was performed at 20 mA cm^{-2} onto test structure electrodes for 360 s to assess the performance of varying citrate concentration. Solutions contained citric acid and tri-sodium citrate in a molar ratio of 1:3 to obtain a pH of 3.0 ± 0.1 at 25 °C. The total citrate concentration in the solutions studied was 0.0714, 0.10, 0.15, 0.20 and 0.40 M with the remaining bath contents as detailed in Table 5.1. Solutions were degassed with argon prior to deposition and plating was carried out in a stagnant solution.

During deposition of the NiFe films hydrogen evolution was observed at the working electrode for all concentrations of citrate, to varying degrees. The potential-time transients, shown in Figure 5.1, show that when the concentration of citrate was 0.20 M and above 'run away' hydrogen evolution occurred and the electrode potential decreased to that diagnostic of the hydrogen evolving regime. At lower citrate concentrations (0.07 to 0.15 M) a steady state potential was reached but bubbles on the electrode were still observed. In this range increasing the citrate concentration was found to decrease to more negative potentials to pass the applied current. When the citrate concentration was increased further the HER became more favoured over nickel and iron deposition. At citrate concentration of 0.4 M, there was visible excessive H_2 production and films with a thickness of only 0.2 µm were produced. The films also appeared dark in colour, consistent with an increase in surface roughness. This clearly suggests an upper limit of citrate concentration for use in this bath.

At lower concentrations of citrate, 0.07 to 0.15 M, patterned dark lines and regions were seen on both the pointer arm and electrical test structures (Figure 5.2). Despite this, the deposited test structures were generally bright and reflective in appearance indicating an improved surface roughness. An example of the surface profile across two rotating arm test structures with local film composition is shown in Figure 5.3. These surface profile measurements show a variation in height for the bulk film between approximately 500 and 2500 nm. The pointer arms for the test structure were measured to have a thickness of 250 nm The target thickness for a $Ni_{80}Fe_{20}$ film deposited at 20 mA cm^{-2} for 360 s was 2.6 µm, similar to the thickness measured for the upper regions of the

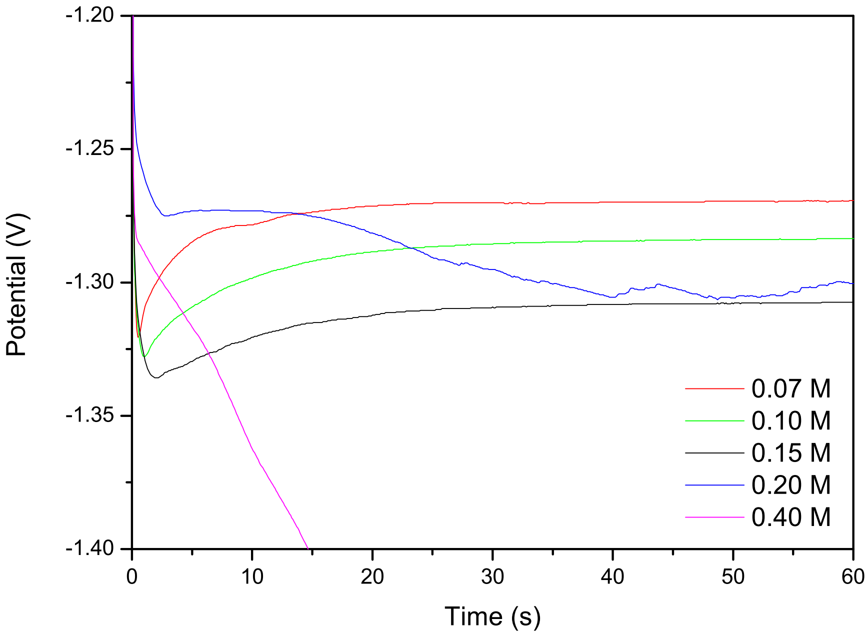

Figure 5.1: Potential-time plot for the first 60 s of NiFe deposition on test structure electrodes at 20 mA cm^{-2} while varying citrate concentration.

electrode. The thicker portion of the film remained at the upper edge of the electrode, regardless of orientation, indicating a gravitational effect on the plating.

The variation in the composition of the test structure follows the film thickness. At thinner, and hence less efficient, regions the nickel content is reduced from approximately 85 % to 60 %. This may indicate that in these regions the nickel deposition reaction was less favorable and the rate of the HER increases. It is apparent the the prevention of the formation and growth of bubbles on the electrode is essential in forming a uniform and flat film.

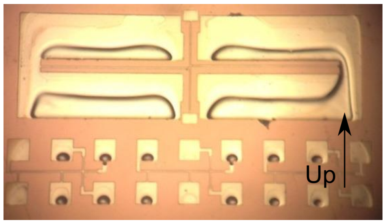

Figure 5.2: Images of the nickel-iron deposits on a test structure electrode showing patterned dark lines and regions. The 'up' arrow indicates the orientation at which the test structure chip was held when deposition occurred, *i.e.* the chip was held vertically.

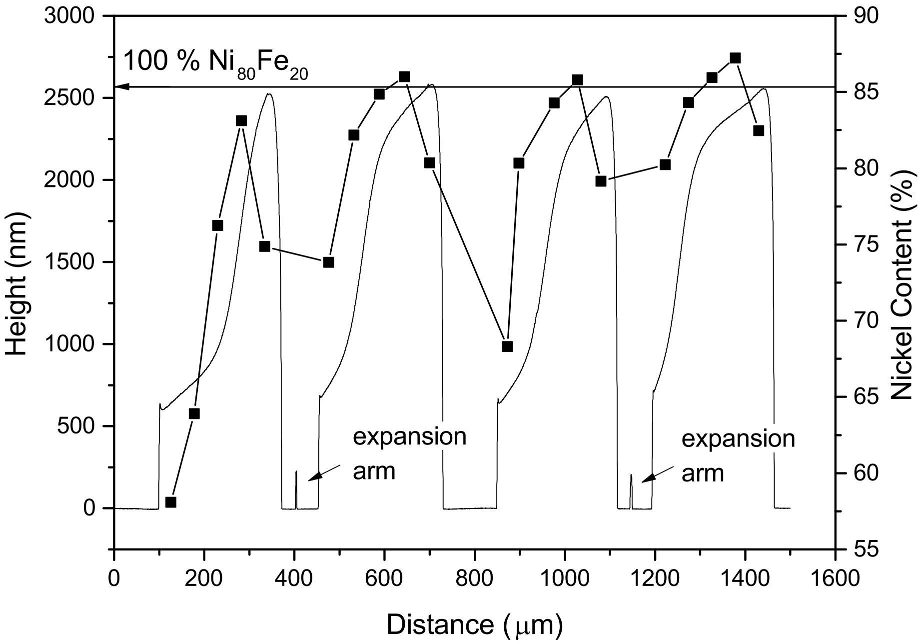

Figure 5.3: Surface profile (line) of rotating arm test structures, as shown in Figure 5.2, with local composition (points) measured from XRF. Distances are measured from the bottom of the electrode. The horizontal solid line indicates the predicted thickness for a film of composition $Ni_{80}Fe_{20}$ deposited for 360 s at 20 mA cm^{-2}.

The concentration of citrate in the nickel-iron plating bath has a significant effect on the nature of the deposits. Too much citrate increases the overpotential required to deposit nickel-iron to the extent that hydrogen evolution is the preferred process at the electrode. Variation of citrate concentration by itself does not provide the desired uniformity of deposition but its presence does enable the deposition of bright and reflective films with a composition spanning across the desired target range.

5.4 Temperature

Temperature can have wide ranging effects on the nature of electrodeposited films including effects on morphology and grain size. [149, 88, 150, 139] A major hurdle in obtaining an adequate citric bath, as shown in the previous section, is the generation of bubbles at the electrode. With regards to temperature two approaches may be taken to tackle the issue of bubbles. The first, and ideal, approach to this is to prevent the generation of any gaseous species at the working electrode. This would result in a highly efficient process where the build up of bubbles can not occur. Unfortunately, in the case of nickel deposition separating hydrogen evolution and the nickel deposition reaction at low pH is difficult. It may be possible however to reduce the rate of the HER compared to nickel and iron deposition sufficiently to allow time for the diffusion of these species away from the electrode surface.

An alternative approach may be to accept the production of at least some hydrogen but make the conditions less favorable to significant bubble formation. Considering the following equilibrium:

$$A_{(aq)} \rightleftharpoons A_{(g)} \tag{5.4}$$

The Gibbs free energy, ΔG, for this reaction is related to the enthalpy and entropy through the equation $\Delta G = \Delta H - T\Delta S$. For the forward reaction the change in entropy, ΔS, is positive (aqueous to gas) and if the change in the enthalpy, ΔH, is relatively insensitive to temperature then increasing the temperature would make ΔG increasingly negative. With a more negative ΔG the equilibrium of the reaction will be shifted towards the right producing more of the gaseous species *i.e.* as temperature is increased the species “A” is less stable in solution. It may then be beneficial to reduce the temperature of the plating bath to reduce bubble formation.

Alternatively, the kinetics of the reactions may play a more important role than the thermodynamics. If the temperature is increased there could be increased transport of hydrogen away from the electrode. The build up of hydrogen at the electrode could be reduced as bubbles can diffuse away and do not build up to a critical concentration.

Furthermore, the kinetics of the metal deposition reactions can be considered. The different reactions at the electrode may have a different response to the changing temperature. The films are deposited at a overall fixed current. The proportion of this current resulting in nickel (or iron) deposition will increase if these deposition reactions becomes more kinetically favored due to the increase in temperature.

Therefore, an investigation to determine if varying the temperature could improve the deposit properties was carried out with the bath described in Table 5.1. To vary the temperature the cell was placed in an ice bath or in a water bath heated by a hotplate. Initially experiments were performed with no agitation with the pH maintained at 2.8 ± 0.1. Images typical of the resulting

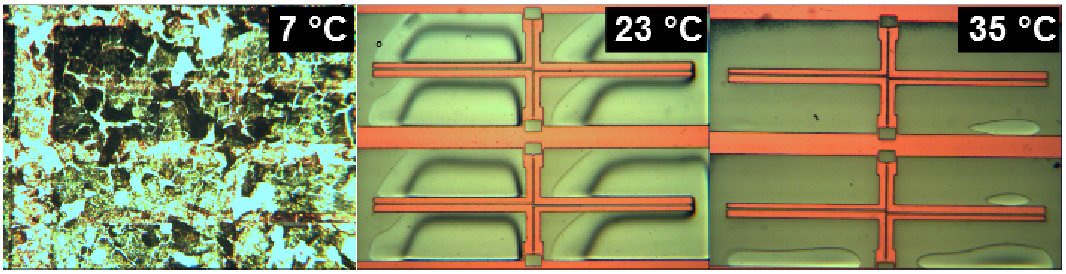

Figure 5.4: Micrographs of deposits made on test structures at three different temperatures.

deposits are shown in Figure 5.4. The potential-time transients measured at a current density of 20 mA cm^{-2} are shown in Figure 5.5.

At temperatures of 7 or 8 °C the electrode potential was found to be significantly more negative than at higher temperatures (around -1.6 V) and this varied erratically. As well as the evolution of hydrogen it was observed that a white organic-like material was being deposited onto and around the electrode in addition to any metal (see Figure 5.4). Deposits of this nature were clearly not desired.

At 23 °C similar wave like deposits were seen on the film as described previously. The potential was seen to reach and maintain a steady state at approximately -1.2 V performing similarly to the bath in Section 5.3.

At 35 °C and above a metal film was deposited. The surface appeared darker (a possible indication of increased surface roughness) but the film thickness was measured to be less variable. The deposition potential was found to become increasingly less negative with increasing temperature. Visually the uniformity of the deposits improved with an increase in temperature.

Further deposits were then made with agitation and at increased temperatures to determine any improvement in film uniformity, for example from a bath at 60 °C and with agitation at 750 rpm. Under these conditions a dull, rough looking film was deposited. Surface profile measurements confirm the rough nature of this type of film (Figure 5.6). The composition of the film was measured to be 33–38 % Fe. The film thickness was measured to be 1300 nm indicating a low efficiency. For 100 % efficient nickel deposition a film approximately 2700 nm thick would be expected. Deposits made under these condition have a low efficiency, in the region of 50 %, and a high iron content. It is reasonable to think therefore that iron species may accelerate the HER or inhibit the nickel deposition reaction as discussed in Section 1.3.2.

The temperature of the electrodeposition bath has wide ranging effects on the deposits. For this

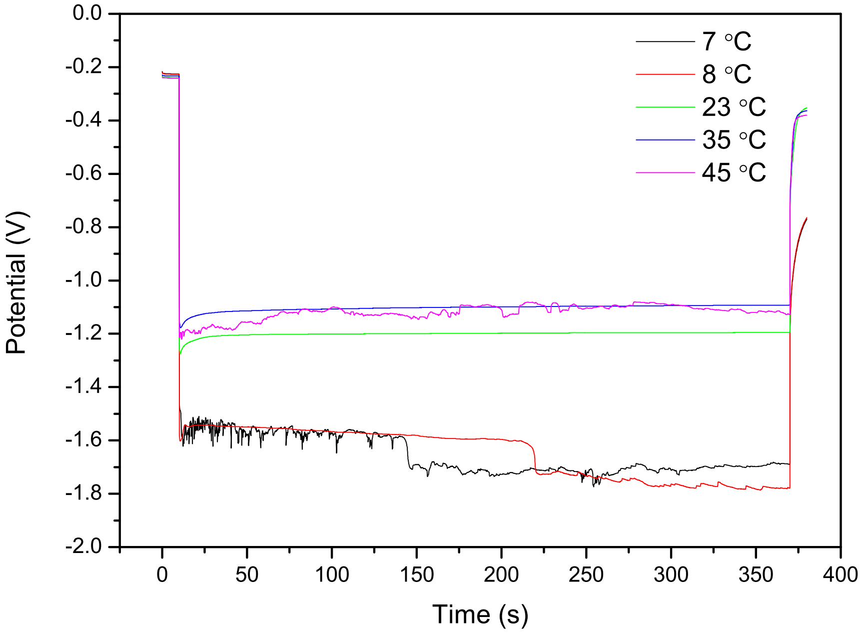

Figure 5.5: Potential time transients for deposition from a nickel-iron bath at 20 mA cm^{-2} at varying temperatures.

citric bath it appeared that a decrease from room temperature was not beneficial. An increase in temperature has potentially beneficial effects on the deposits as the variation in film thickness and composition is reduced. Apparent drawbacks include an increased surface roughness and loss of coulombic efficiency. The composition of the films at higher temperatures was seen to favour iron which itself may cause an increase in the rate of the HER. Therefore further work was pursued maintaining the bath temperature at 60 °C while varying the iron concentration to achieve the required film composition.

5.5 Iron Concentration

It has been suggested that various iron species inhibit the deposition of nickel [105]. In an attempt to enhance the deposition of nickel and reduce the iron composition of these deposited films the concentration of Fe (II) was varied. Using the bath described in Table 5.1, but varying the iron chloride concentration, deposits were made at a current density of 20 mA cm^{-2} on test structure electrodes at a temperature of 60 °C.

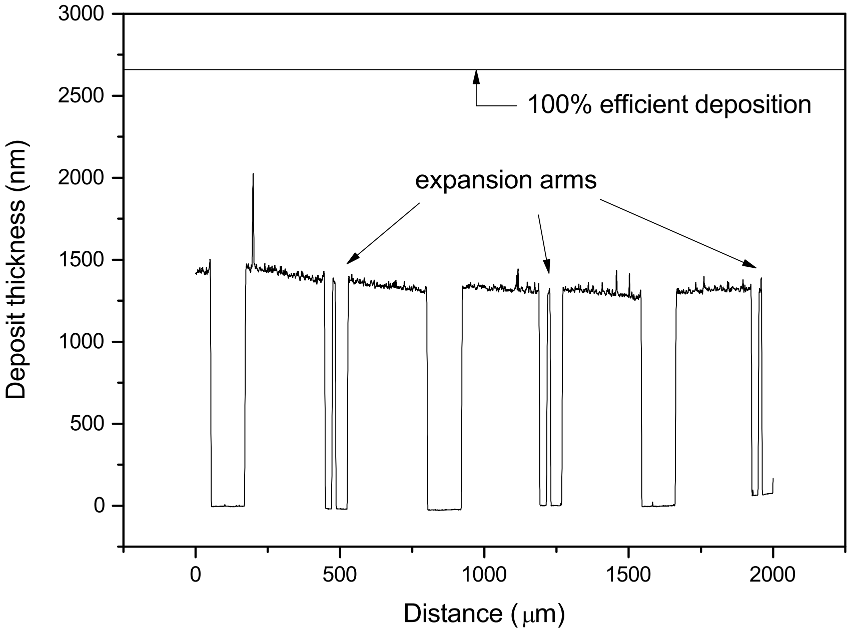

Figure 5.6: Surface profile of a film deposited at 60 °C with agitation displaying a high surface roughness and poor efficiency. The solid line indicates the predicted film thickness for a nickel deposited with 100 % coulombic efficiency.

Figure 5.7 shows the film composition and the film thickness, both measured using XRF, across different iron (II) concentrations. It was found that the iron content in the films increased linearly with concentration until 25 mM Fe (II). At this concentration the film thickness decreased and iron content of the deposits increased. This corresponds with an increase in surface roughness of the deposit visually observed by a darkening of the metal deposits.

For a nickel film, *i.e.* [Fe] = 0 mM, the target film thickness is 2.45 μm. The measured thickness for this film was found to be 2.75 μm. This is obviously larger than what can be expected but could be due to bias in the measurement points (more measurements are taken near the edges of the electrode) or that the density of the electrodeposited, polycrystalline, film is less than for bulk nickel. If this thickness were taken to represent approximately 100 % efficient plating then the films deposited with an increased iron concentration are approximately 60–65 % efficient. If this decrease in efficiency was solely due to the decreasing nickel plating efficiency the deposited would reduce in thickness by 16 % (nickel content × decrease in expected nickel content = 0.8 × 0.2) or 0.44 μm.

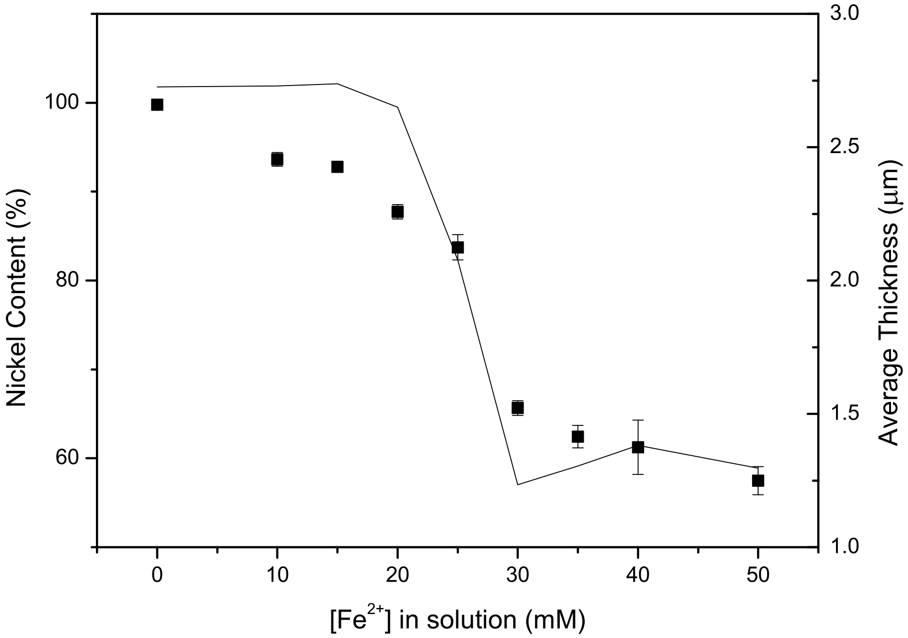

Figure 5.7: Nickel content (points) and measured thickness (line) for increasing Fe (II) concentration in solution.

This is not a large enough decrease to reduce the film thickness to 1.25 µm so the efficiency of iron deposition must also be reduced.

The open circuit potentials after deposition of the films indicate a change in the deposited material at the electrode. At concentrations up to 25 mM Fe (II) the OCP was found to be -0.279 ± 4 mV. At the higher concentrations of Fe (II) (30 to 50 mM) the OCP was found to shift further negative at -0.365 ± 13 mV. With increasing iron content in the bath a more inert electrode may be produced during deposition due to the formation of iron oxides or hydroxides, as discussed by Vaes [109]. Once this layer is formed an increased potential would be required to drive a reaction and the HER could become more favorable resulting in the decreased film thickness observed.

Varying the iron chloride concentration in the deposition bath is one method for determining the composition of the nickel-iron deposit. For the current bath, the film quality and efficiency is lost as the $Ni_{80}Fe_{20}$ composition is approached. To obtain the desired composition, alternative methods of changing the film composition without the formation of troublesome iron species were sought.

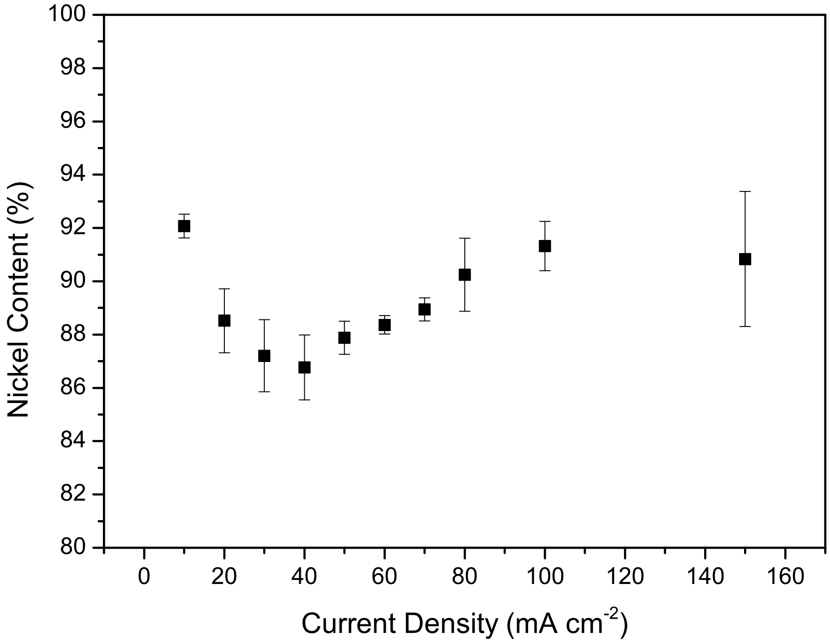

Figure 5.8: Measured composition of NiFe deposit. Deposits were made from a citric bath containing 20 mM Fe^{2+}at 60 °C with agitation from a magnetic stirrer.

5.6 Current Density

An alternative method to control the deposit properties is to vary the current density. Changes in current density will change, among other properties, the composition of the deposits as well as the grain size (or roughness), hardness and efficiency [151, 28, 103].

Using a 20 mM Fe^{2+} bath, deposits were made between 10 and 150 mA cm^{-2} at 60 °C with agitation. All deposits appeared bright and the composition was measured as shown in Figure 5.8. For this bath the increase in iron content peaked at 40 mA cm^{-2} after which the nickel composition increases to approximately 91 %. At the highest current densities bubbles were visible after formation on the electrode. This type of curve has been demonstrated previously in boric acid based baths [152] and demonstrates that the same composition of film can be deposited from two different plating regimes.

Similarly, the effect of current density on baths with increased concentrations of Fe(II) was measured (Figure 5.9). Iron concentrations of 25 and 30 mM showed similar trends to that of the 20 mM bath. However, at higher current densities the film showed a decrease in nickel content as well as

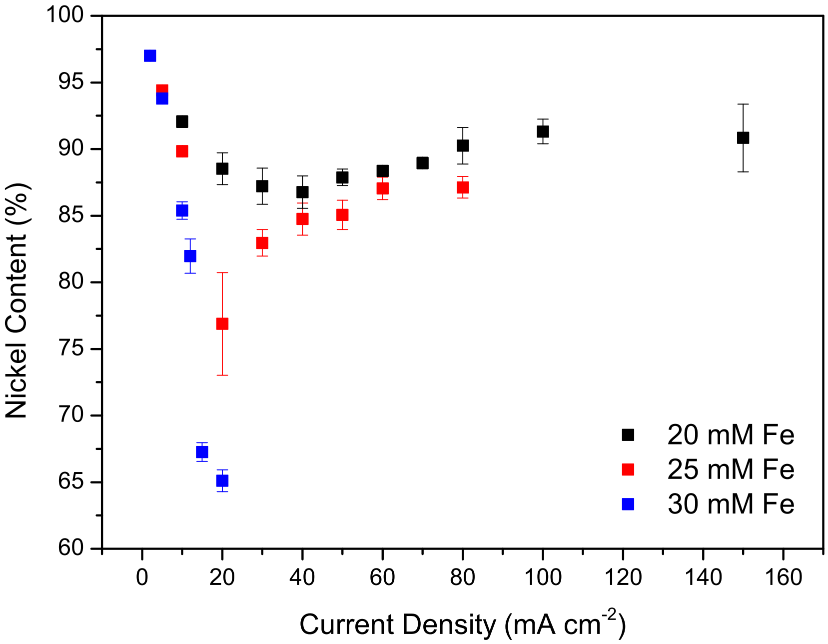

Figure 5.9: Composition of nickel-iron films deposited at varying current densities and iron (II) chloride concentration.

increased surface roughness. Images of test structures deposited at 20 mA cm^{-2} (Figure 5.10) show the gradual darkening of the deposited film as the Fe(II) concentration is increased.

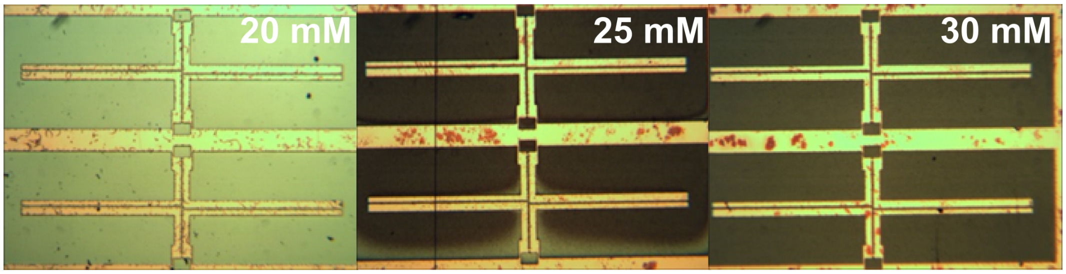

Figure 5.10: Images of NiFe films deposited at 20 mA cm^{-2} from solutions with varying Fe (II) content.

It was apparent that to obtain a reasonable deposit with a composition of $Ni_{80}Fe_{20}$ varying the iron composition or current density would not achieve the desired deposits. Additional changes to the bath chemistry would be required to obtain a suitable film. The main parameters which were yet to be taken into account with an increased bath temperature were the additive concentration, which remained the same as for the boric bath at 25 °C, and the pH of the bath. Without adjustment the pH of the bath varies with temperature and may require further optimisation for deposition at 60 °C.

5.7 Effects of Saccharin Concentration

The saccharin content of the bath was increased to see if an improvement in the film properties could be obtained. The saccharin concentration was increased between 2 g L^{-1} and 5 g L^{-1} with deposits made at 20 mA cm^{-2}. Figure 5.11 shows images of deposit made with different concentrations of sodium saccharin. At a concentration of 2 g L^{-1} the films appear dark and rough. The film composition was measured as 39.85 ± 2.44 % iron. At a concentration of 3 g L^{-1} dark and more reflective areas were observed across the electrode. The dark area had a higher proportion of iron in the film than the brighter areas. The average composition across the test structure electrode was 32.18 ± 6.33 % Fe with the larger standard deviation in composition across the electrode being due to the varying composition of these areas. At a saccharin concentration of 5 g L^{-1} a bright reflective film was deposited. The composition across the electrode was measured as 20.44 ± 1.01 % Fe.

To ensure deposits remained bright and reflective with increasing iron content additional iron chloride was added to the bath which contained 5 g L^{-1} sodium saccharin. Deposited films visually remained of similar quality throughout. The composition of the films was measured and the iron content of the film was found to increase linearly with the concentration of Fe (II) in solution (Figure 5.12).

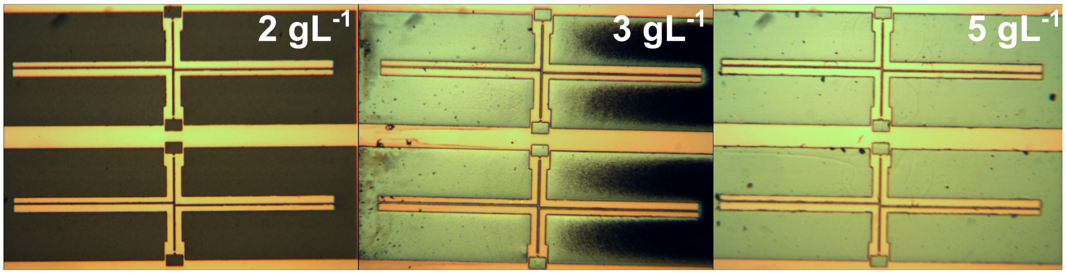

Figure 5.11: Micrographs of test structures deposited with increasing concentration of sodium saccharin.

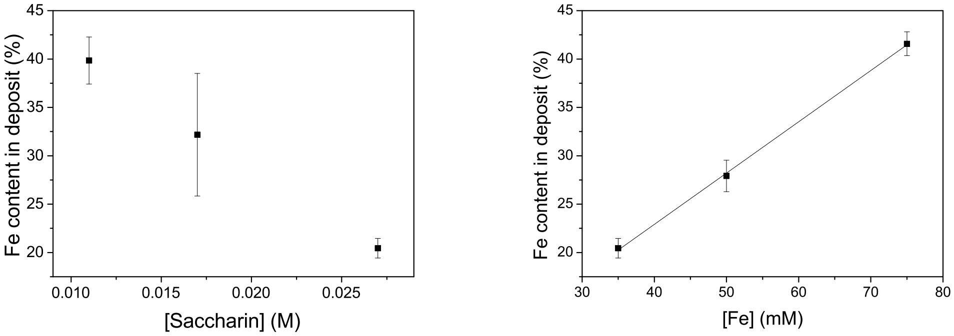

Figure 5.12: Iron content in deposited films of nickel-iron. left: varying saccharin concentration. Right: varying Fe (II) concentration in solution.

Using the increased saccharin concentration in the bath these experiments show that nickel-iron films with iron content of up to 40 % Fe can be deposited. At these compositions these films appeared to remain of uniform quality and thickness. These deposits demonstrated the conditions required for suitable deposits from the citric bath.

5.7.1 Procedure for Saccharin Quantification

It has been demonstrated that the concentration of saccharin in the plating solution changes the properties of the deposited films. In an industrial environment it would be necessary to maintain the bath under optimal conditions. To this end, a procedure for the quantification of the saccharin content in the bath was developed. The following describes a procedure for the quantitative analysis of sodium saccharin in the citric acid based nickel-iron deposition bath as detailed in Table 5.2.

The method is based upon the extraction of sodium saccharin to an organic solvent before titration against a standard solution of NaOH. The method first requires the construction of a calibration curve using standards with known concentrations of sodium saccharin.

Chemical	Concentration (g L^{-1})	Concentration (M)
$NiCl_2.6H_2O$	110	0.46
$FeCl_2.4H_2O$	7	0.035
$Na_3Cit.2H_2O$	30	0.10
Sodium Saccharin	5	0.027
SDS	0.1	0.0035

Table 5.2: Citric acid based plating bath for the deposition of nickel iron. To achieve the composition $Ni_{80}Fe_{20}$ deposits were made at a current density of 20 mA cm^{-2}and a temperature of 60 °C with agitation from a magnetic stirrer. Prior to deposition the bath is adjusted to pH 2.8 with 10 % v/v HCl.

To create a range of standards with a fixed background solution and vary concentration of sodium saccharin the following procedure was used. For use as a background solution for the nickel-iron citric bath the contents of Table 5.3 was dissolved in 250 cm^3 of D.I. water.

Standard solutions, with a total volume of 50 cm^3, were made using 40 cm^3 of the background solution (Table 5.3). This was then added to a sodium saccharin solution (1.25 g in 25 cm^3), where 1 cm^3 gives 1 g L^{-1}, sodium saccharin in 25 cm^3. This was repeated to give a range of sodium saccharin concentrations. Each standard solution was then titrated using the following procedure to construct a calibration curve (Figure 5.13).

The analysis for determining the saccharin concentration was performed *via* extraction then titration. 2 cm^3 of 10 % v/v HCl was added to a 50 cm^3 aliquot of the plating solution. This was then washed with ethyl acetate (3 x 25 cm^3) and the organic layers were then combined. To the organic layer 10 cm^3 methanol and 5 cm^3 of Bromocresol Purple indicator (0.04 % aqueous solution) were added. Ethyl acetate was added to the organic layer to make the organic layer up to 100 cm^3.

Chemical	Quantity / g
$NiCl_2.6H_2O$	34.38
$FeCl_2.4H_2O$	2.19
$Na_3Cit.2H_2O$	9.38
SDS	0.031

Table 5.3: Contents of background solution used to make calibration standards. The contents were dissolved in 250 cm^3 of D.I. water. To make the calibration standards, 40 cm^{3}of this background solution was added to a saccharin solution of known concentration and made up to 50 cm^3.

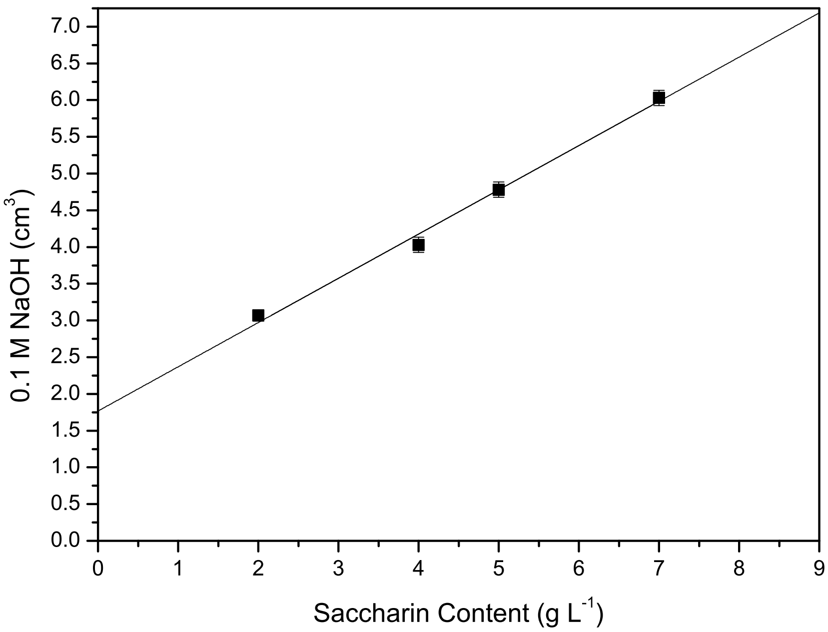

Figure 5.13: Calibration curve constructed from standard solutions with known concentrations of sodium saccharin.

20 cm^3 portions were then titrated against a standard solution of 0.01 M NaOH. The endpoint is a colour change of yellow to purple.

This procedure demonstrates the ability to measure the saccharin concentration in the citric bath. This could prove a useful analytical tool for to keep the bath under the optimal conditions in applications where larger volume baths are required and it is impractical to make fresh solutions. This analytical technique could also be applied to measure the rate of additive consumption in the bath over prolonged periods of plating.

5.8 Bath Optimisation

With the knowledge obtained from previous experiments a revised bath was then used to test for the optimal temperature. In order to maintain a constant pH at the different temperatures used to deposit the film a different approach to "buffering" the solution was used. In this case tri-sodium citrate was added to the bath in a concentration of 0.1 M. The pH was then adjusted to 2.8 using 10 % HCl.

Deposits were made onto test structure electrodes using the bath described in Table 5.2. A current density of 20 mA cm^{-2} was passed for 360 s to deposit a film. The temperature was varied from 70 to 25 °C with agitation at 750 rpm. The pH was adjusted to 2.8 with 10 % HCl prior to deposition.

The surface profiles (Figure 5.14) and the composition of the deposited films (Figure 5.15) were measured. The flattest deposits were found at elevated temperatures of 50 and 60 °C. At lower temperatures non-level, dome-like, films were deposited and at 70 °C deposits showed an increase in thickness at the edge of the structures. At 40 °C there was found to be tall protrusions around the expansion arms. The non-uniform nature of the deposits at the lower temperatures are thought to arise from the the generation and then the formation of hydrogen bubbles on the electrode surface. At increased temperatures the efficiency of the deposition process increases resulting in flatter, more uniform deposits.

The composition of the films deposited was measured and was shown to vary greatly with changing temperature. Above 30 °C the fraction of nickel deposited was found to increase with increasing temperature from 58 to 83 % Ni. The plating potential was measured and was shown to become more positive at higher temperatures.

Changes in the deposition potential will affect the ratio of Ni:Fe:H produced, as reflected in the alloy composition. The deposition of nickel is a kinetically controlled process and with an increase in temperature the rate for this reaction can increase greatly. The reduction of iron, at a far smaller concentration, is under mass transport control. The changing temperature may have little effect on the rate of deposition for iron. For hydrogen evolution the rate may be expected to increase with an increased temperature; however, the rate of this reaction may be reduced due to the lower potential required to pass the specified current.

Figure 5.16 shows a before and after example of deposition from the citric bath onto the test structure electrodes. The deposits were made in a bath at 60 °C at a pH of 2.8. Agitation was provided from a magnetic stirrer at 750 rpm. Preparation of the seed layer is an important step to produce a even film. Blemishes seen in the copper seed layer (this image is taken before oxide removal in H_2SO_4) were carried through onto the nickel-iron film. It was apparent that under these conditions films appeared to be deposited in an adequate manner for use in the microfabrication of MEMS devices. Level and bright films were deposited across the electrode at a compositions close to $Ni_{80}Fe_{20}$ as desired.

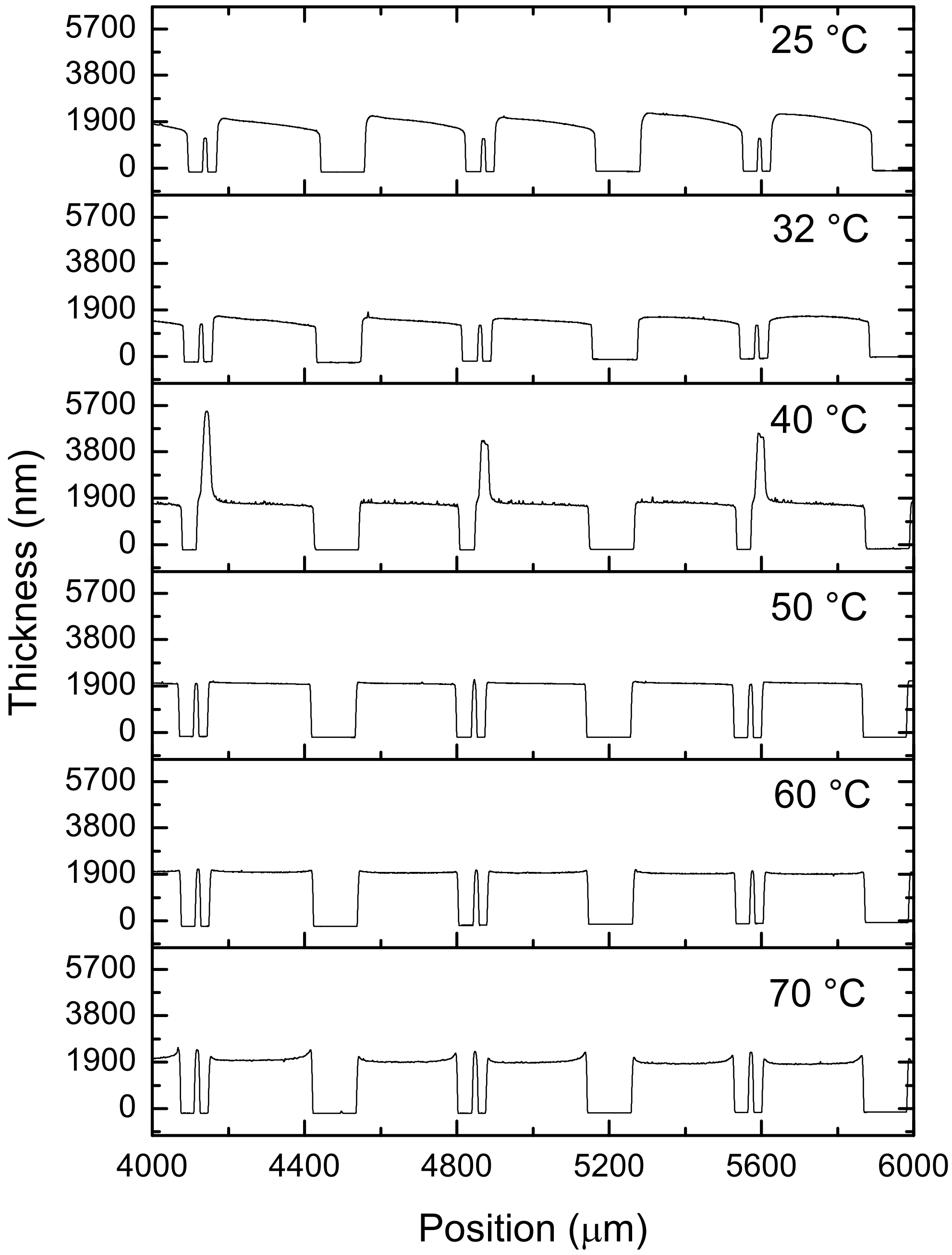

Figure 5.14: Surface profilometry performed on test structure electrodes. Deposits of nickel-iron were made from the bath described in Table 5.2 at varying temperatures.

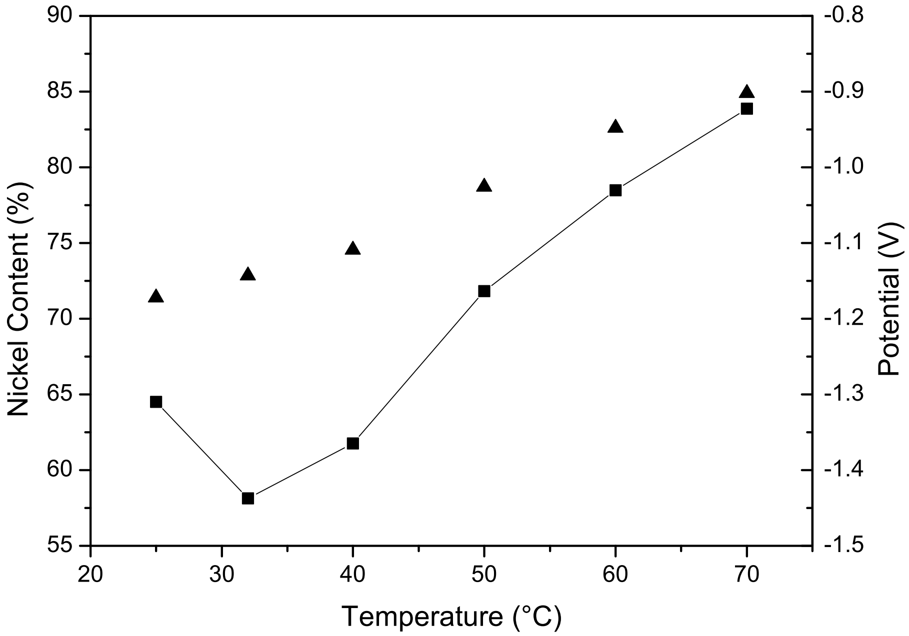

Figure 5.15: Nickel content (■) of electrodeposited nickel-iron films and steady state potential during deposition (▲) at varying temperatures.

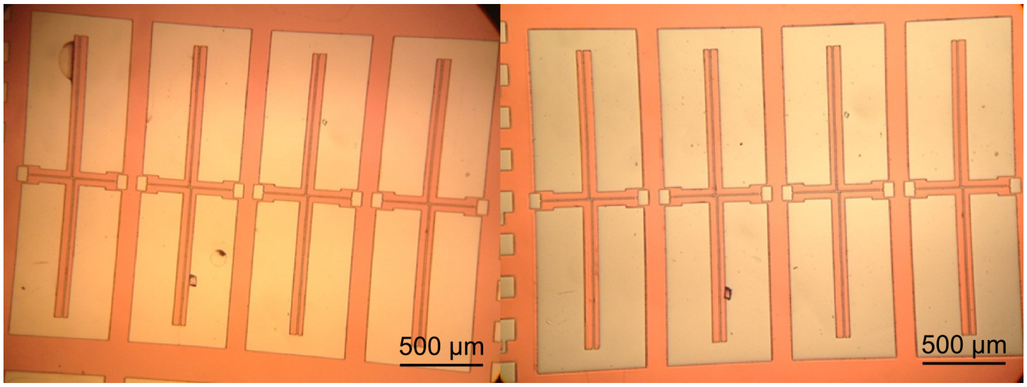

Figure 5.16: Before (left) and after (right) of NiFe electrodeposition onto test structure electrodes. The nickel-iron film was deposited from the citric bath at 60 °C with 750 rpm agitation.

5.9 Conclusions

In this chapter a nickel-iron deposition bath which contains no boric acid has been developed. The potential for this bath to produce bright, level and uniform deposits was demonstrated. To confirm the suitability of these films for use in MEMS and the ability to use this bath as a direct replacement for boric acid based baths further investigation is required. To this end comparisons of films deposited from a boric acid bath and a citric bath are detailed in Chapter 8.

During the process of development it was demonstrated that the composition of the deposited film can be tuned by varying parameters such as current density, the concentration of iron and temperature. It is also apparent that the hydrogen evolution reaction continues to play a significant role during the deposition of nickel-iron from the citric bath. To fundamentally understand the processes occurring in the citric bath further work is required.

Chapter 6

Electrodeposition of Nickel from a Citric Bath

6.1 Motivation

In the previous chapter a citric acid based electrodeposition bath for depositing nickel-iron has been developed. The aim of this chapter is to examine the fundamental electrochemistry of this bath. To do so first the system was simplified to a nickel only bath. Voltammetry and EQCM were then used to investigate the electrochemical behavior of nickel-citrate baths.

As discussed in Section 1.2.3 the hydrogen evolution reaction has a significant role in the mechanism of nickel and nickel-iron alloy deposition from boric acid based baths. Similarly the role of hydrogen in citric based baths can be probed using a variety of techniques. Cyclic voltammetry can give an overview of when hydrogen is likely to be evolved and when combined with EQCM measurements the quantity of H_2 gas evolved can be confirmed. The pH of the plating solution has influence on the HER and the properties of deposited films [83, 82]. In a nickel bath the role of citrate and the effects of pH was examined during galvanostatic and potentiostatic deposition using EQCM to obtain information about the coulombic efficiency of the deposition process. This provides insight into the optimal conditions for deposition of nickel and the influence of the HER.

To obtain uniform and bright deposits the addition of further additives are required. Work described in Chapter 5 demonstrated that an increased concentration of saccharin is required in the citric

Chemical	Concentration (g L^{-1})	Concentration (M)
$NiCl_2.6H_2O$	110	0.46
$Na_3Cit.2H_2O$	30	0.10
Sodium Saccharin	5	0.027
SDS	0.1	0.0035

Table 6.1: Citric based plating bath for the deposition of nickel. Prior to deposition the bath is adjusted to pH 2.8 with 10 % v/v HCl.

bath. Understanding of the cooperative effects of additives aids the understanding of how the metal deposits in this bath and also facilitates bath optimisation.

The nickel-iron plating bath performed optimally at elevated temperatures (Section 5.8). The temperature of the bath affects a wide range of properties including composition, efficiency and film uniformity. The effects of temperature on the deposition therefore were investigated to understand the benefits of these higher temperatures and why they are required to obtain uniform deposits.

6.2 Cyclic Voltammetry on Pt Disc Electrodes

Cyclic voltammetry was performed on the optimized citric bath at 60 °C (Table 6.1) on a platinum disc electrode and is shown in Figure 6.1. Three main features were found in the voltammetry, attributed to hydrogen reduction (a), nickel deposition (b) and nickel stripping (c). There is a wide separation of the deposition and stripping peaks. This separation can be attributed to the slow kinetics of nickel reduction and oxidation resulting in the large over-potential.

The hydrogen reduction peak (a) is identified by comparison to voltammetry performed in the background electrolyte (see Figure 6.2). In both the background and nickel-containing voltammetry the peak current begins to grow at -0.38 V. In the nickel containing CV the peak current is proportional to the square root of the scan rate indicating the reaction is mass transport limited. The nickel stripping peak showed a sharp decrease in the current as the nickel metal was completely removed exposing the platinum surface.

A Tafel plot for the voltammetry is shown in Figure 6.3. By examining the Tafel plot the mechanism of the nickel reduction and oxidation can be examined [153]. Linear regions ($R^2 > 0.999$) corresponding to the reduction and oxidation of nickel are shown to have gradients of (124 mV)$^{-1}$ and (71 mV)$^{-1}$ respectively. In terms of electron transfer there are three types of mechanism which

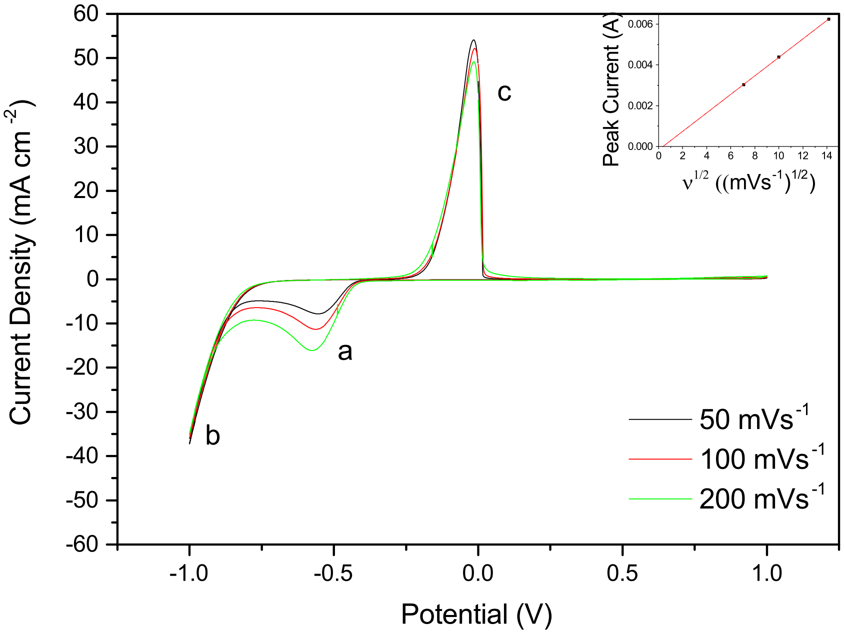

Figure 6.1: Cyclic voltammetry of nickel deposition from the citric bath (Table 6.1). Inset: peak current vs. scan rate$^{1/2}$ for peak a. The starting potential was 1.0 V, the potential was then swept between 1.0 and -1.0 V. The 5th scan is shown. Voltammetry was performed at 60 °C.

can be considered for the reduction and oxidation of nickel. The first is a direct two electron transfer. The others are two-step mechanisms where either the first or second electron transfer can be the RDS.

The mechanism of deposition/reduction can be probed with the gradients of these slopes of the Tafel plot as described by the equation

$$\log j = \log j_0 + \frac{n\alpha F}{2.3RT}\eta \tag{6.1}$$

From the measured Tafel gradients the value of $n\alpha$ can be determined. For nickel deposition and stripping $n = 2$ therefore a value for α can be calculated. If $\alpha < 0.5$ then the RDS is the first electron transfer, if $\alpha > 0.5$ then the RDS would be the second electron transfer. If $\alpha = 0.5$ this implies the reaction undergoes a reaction with a single two electron reduction or oxidation.

For the deposition of nickel the Tafel slope was (124 mV)$^{-1}$, using Equation 6.1, $n\alpha$ was calculated to be 0.52 and hence $\alpha = 0.26$. This shows the first electron transfer is the RDS in the deposition

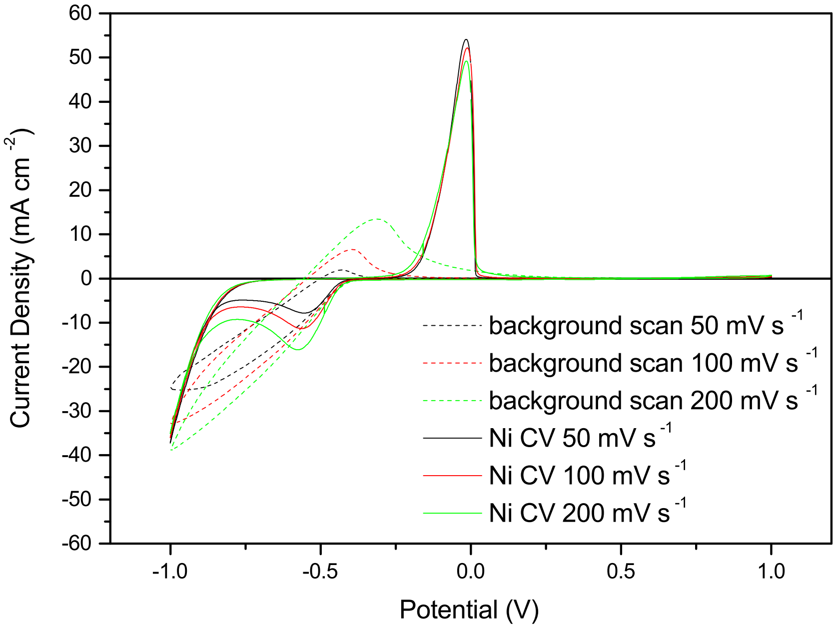

Figure 6.2: Overlays of the background electrolyte containing sodium citrate (0.10 M), sodium saccharin (0.027 M) and SDS (0.0035 M) (dashed lines) on the nickel CV (solid lines) as shown and described in Figure 6.1.

of nickel. For the stripping of nickel the Tafel slope was (71 mV)$^{-1}$ and $n\alpha$ was calculated to be 0.93 and hence $\alpha = 0.47$. This indicates that that during stripping the Ni(I) species is in a high energy state and rapidly undergoes the second electron transfer.

The plating and stripping mechanisms in this bath are therefore demonstrated to be different. This can be expected as the stripping is performed from bulk nickel whereas deposition forms an ad-atom on the electrode. Furthermore, with the use of a complexing agent like the citrate anion, deposition occurs from a species in complex and when stripped it is not directly stripped into the complexed form.

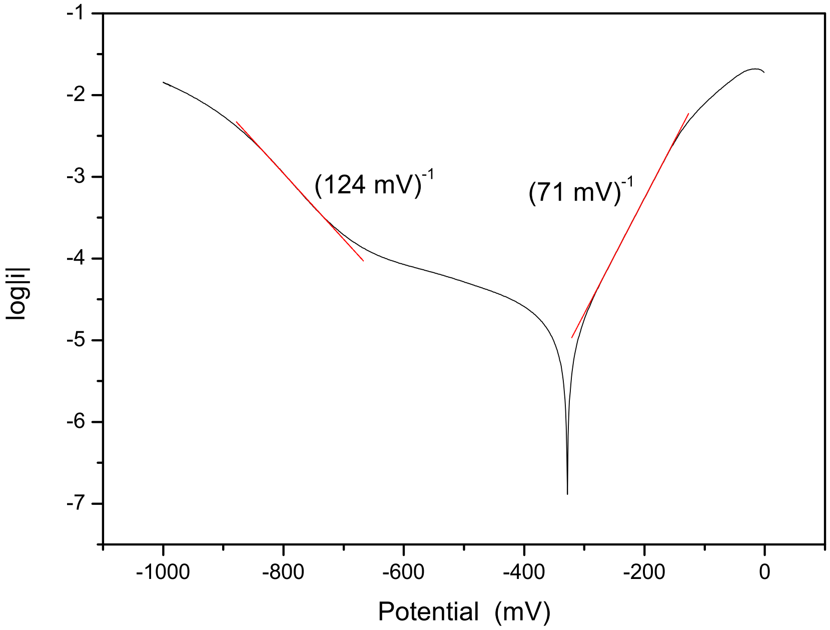

Figure 6.3: Tafel plot constructed from voltammetry in Figure 6.1. The reverse scan (from -1 to +1 V) at a sweep rate of 50 mV s^{-1} was used.

6.2.1 Citrate Electrochemistry

Cyclic voltammetry of 0.1 M tri-sodium citrate is shown in Figure 6.4. Previous studies by Berkh *et al.* have studied the electrochemical behavior of citrate on a platinum electrode [80, 154]. In the work of Berkh *et al.* they identified the peaks observed in the voltammetry and studied the effects of prolonged electrolysis. Features in the voltammetry can be with attributed to PtO reduction (-0.25 V), adsorption (-0.7, -0.8 V) and desorption (-0.6, -0.4 V) of atomic hydrogen, and the formation of an oxide layer (+0.4 V). Additionally, they speculate the hydrogen desorption peaks are shifted positive due to citrate adsorption. The adsorption of citrate on to a platinum electrode is thought to occur through the reaction, $C_6H_8O_7 \rightleftharpoons 3H^+ + (C_6H_5O_7)^{3-}_{ad}$ [146].

6.2.2 Influence of Additives

The importance of the additives in the bath cannot be understated. To obtain uniform and bright deposits all components of the bath must be present. Voltammetry performed on a bath of nickel chloride and sodium citrate aptly demonstrates this. Figure 6.5 shows voltammetry performed on

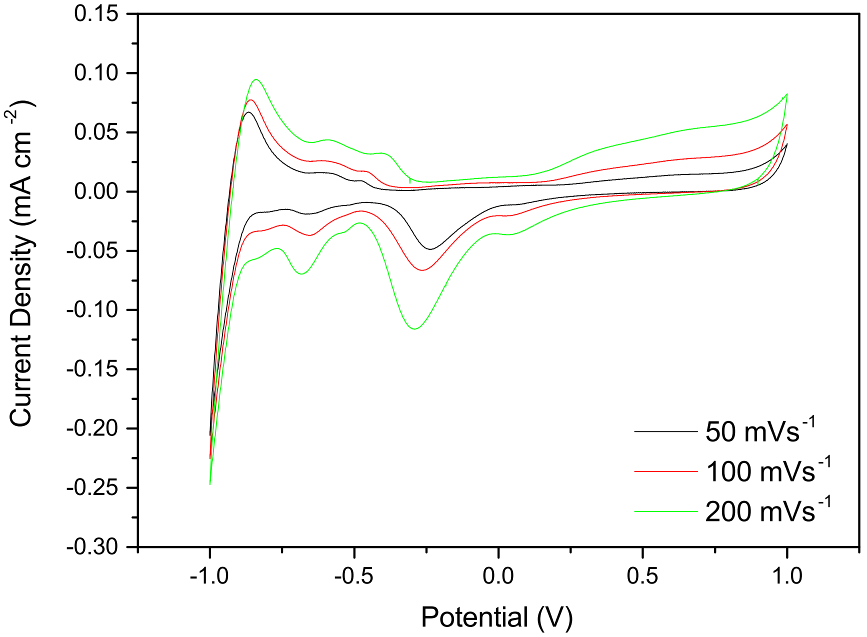

Figure 6.4: Cyclic voltammetry of 0.1 M tri-sodium citrate on a Pt electrode. The potential was swept between 1.0 and -1.0 V *vs.* SCE.

a bath containing 110 g L^{-1} $NiCl_2.6H_2O$ and 30 g L^{-1} $Na_3Cit.4H_2O$ which was pH adjusted to 2.8 with HCl. Similar behavior was found regardless of whether the solution had been purged with argon.

With the absence of saccharin and SDS in the bath the voltammetry becomes more complicated and contains additional features. The anodic sweep remains similar to the that for the full bath; a peak was observed for the HER followed by an increasingly negative current. Unlike the full citric bath, a single nickel stripping peak is not observed. Instead, there are multiple oxidation peaks. At faster scan rates oxidation occurs at a more negative potential than for nickel stripping and may be associated with hydrogen oxidation. As the scan progressed further positive, a peak which aligns with the potential for nickel stripping is observed. This peak grows larger with decreasing scan rates. Further, unassigned, oxidation peaks with drawn out tails were then observed, this may indicate the difficulty of removing any remaining material on the electrode. For the 50 mV s^{-1} scan rate a peak was seen at 0.7 V, although difficult to assign this peak may be related to nickel hydroxide species on the electrode caused by precipitation due to an increased magnitude of the local pH change at the slower scan rate.

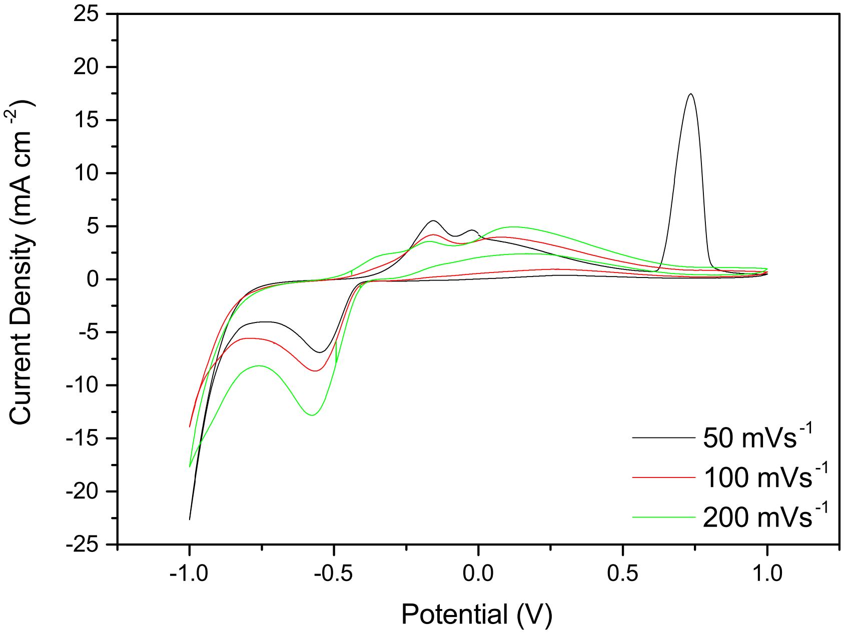

Figure 6.5: Voltammetry of nickel chloride and sodium citrate under the same conditions as Figure 6.1 (T = 60 °C, pH 2.8). The 5th scan at each scan rate is shown.

The influence of saccharin was investigated by varying the concentration in the citric bath (Table 6.1). Cyclic voltammetry was performed as shown in Figure 6.6. An unusual peak shape is observed due to the current limits of the potentiostat, therefore the peak shape cannot be analysed. However, the change in peak potential and size gives insight into the electrochemistry. The largest influence observed in the electrochemistry occurred with the introduction of saccharin into the bath. With no saccharin in the bath the hydrogen reduction peak (at -0.5 V) was found to be much larger and the potential at which nickel is deposited was seen to become more negative. This may be due to the adsorption of saccharin on the surface of the electrode selectively reducing the extent the HER. Also with no saccharin in the bath there was an additional oxidation peak which begins at + 0.52 V similar to the oxidation peak seen in the bath with no additives (Figure 6.5).

In saccharin containing baths the positive and negative charge passed remains consistent (see Table 6.2). The average positive charge passed is 39.5 ± 0.8 mC and the average negative charge passed is 72.9 ± 1.0 mC. When compared to the scan where the bath contained no saccharin the overall charge passed negative is slightly smaller (70.6 mC). The overall positive charge passed is higher (50.9 mC) but divided under two peaks. The first peak occurs at a more negative potential than

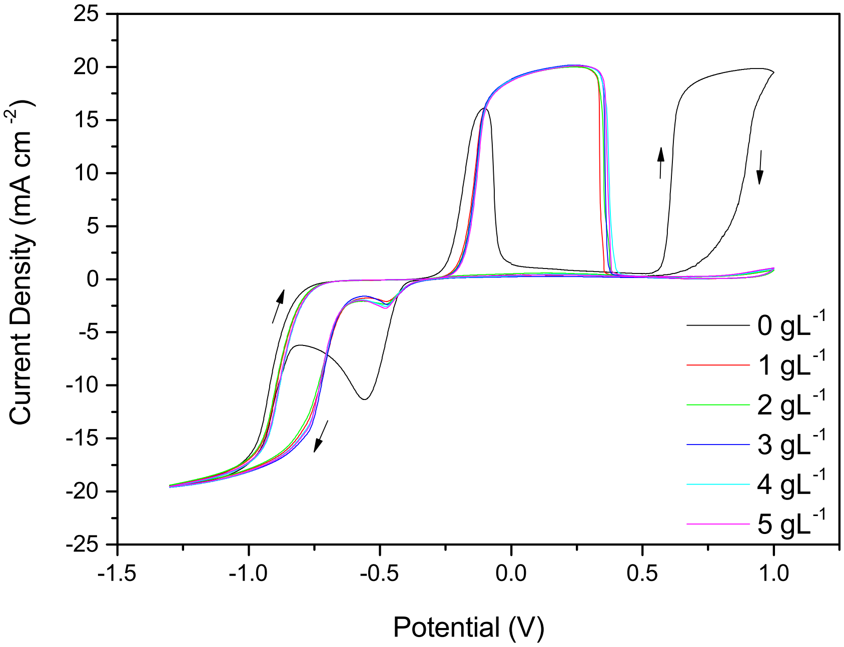

Figure 6.6: Voltammetry of nickel deposition bath (Table 6.1) with varying concentration of saccharin. Scans were performed at scan rate 100 mV s^{-1} with a starting potential of 1.0 V, the potential was then swept between 1.0 and -1.3 V. The 5th scan at each concentration of saccharin is shown. Voltammetry was performed at a pH of 2.8 at 60 °C. Note: during this experiment the peak shape is distorted due to the limitations in the current range of the potentiostat. The unusual shapes of these peaks were confirmed through additional experiments displaying similar effects and is believed to be due to equipment limitations. Therefore the peak shape can not be analysied in the usual manner due to the limited current range. However, the change in position and size of these peaks on addition of saccharin yields useful information.

nickel stripping in the saccharin containing baths and results in 11.0 mC of charge. The second peak had a charge of 39.9 mC. Clearly in the absence of saccharin nickel deposition is not favoured, this may be associated with the increase in the peak for the HER. The peak at + 0.52 V may be associated with the formation of hydroxide species which is further discussed in Sections 6.3.3 and 6.3.4.

[saccharin] (g L^{-1})	Q+ (mC)	Q- (mC)
0	50.9*	70.6
1	38.3	72.2
2	39.5	71.5
3	39.3	73.9
4	40.3	73.6
5	39.9	73.4

Table 6.2: Charge passed during cyclic voltammetry (Figure 6.6). * of which 39.9 mC is the second oxidation.

6.2.3 Voltammetry with Varying Nickel Concentration

In the full citric bath there is a large concentration of nickel due to the desire not to be limited by mass transport control of Ni^{2+} and also to ensure the concentration of nickel does not vary significantly after long periods of deposition. However, to examine the fundamental electrochemistry of the bath it is limiting to use such a large concentration as the deposition of nickel dominates the electrochemisrty. By examining the electrochemisrty at reduced concentrations of nickel in the bath insight into the extent of inhibition for the HER by nickel or related species can be examined.

Voltammetry of the background electrolyte containing sodium citrate, sodium saccharin and SDS at 60 °C and a pH of 3.0 is shown in Figure 6.7. On the anodic scan, hydrogen evolution is observed from a potential of approximately -0.4 V. This is comparable to the value calculated thermodynamically from the Nernst equation of -0.440 V *vs.* SCE. There is a peak in the current at approximately -1.0 V. The current then increases slightly again near -1.2 V. On the reverse scan a single peak is observed due to hydrogen oxidation on the platinum electrode.

Figure 6.8 shows the addition of $NiCl_2$ in increasing concentrations between 10 and 100 mM. At a concentration of 10 mM Ni^{2+} the voltammetry is broadly similar to the background scans. In the cathodic scan the peaks are shifted to a more positive potential, possibly due to the presence of nickel. There is an additional peak in the anodic scan due to the stripping of nickel, which is removed form the electrode before the potential for hydrogen oxidation is reached. At 25 mM Ni^{2+} large quantities of hydrogen are still evolved and additional nickel is deposited.

At 50 mM concentrations of nickel the extent of the HER was suppressed. This may be due to a sufficient nickel coverage on the electrode preventing the catalytic evolution of hydrogen on the platinum electrode. At slower scan rates a stripping peak for Ni is observed, albeit at very low

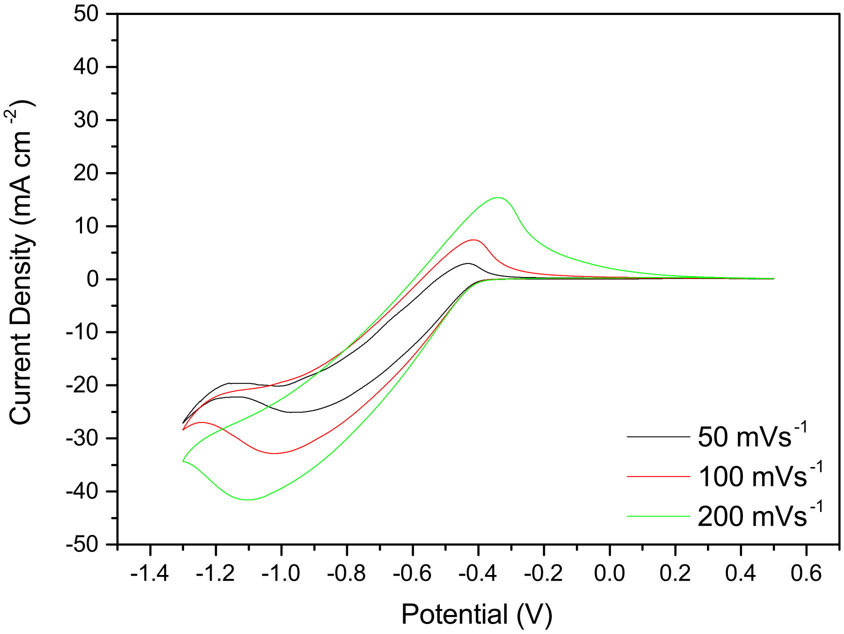

Figure 6.7: CV of background electrolyte containing sodium citrate (0.1 M), sodium saccharin (0.027 M) and SDS (0.0035 M) at pH 3.0. With an initial potential of 0.5 V scans were performed between 0.5 and -1.0 V. The scans were performed at 60 °C and at a pH of 3.0 using a SCE reference.

coulombic efficiency. At 100 mM Ni^{2+}, where all the citrate should be complexed with nickel (see speciation diagram in Figure 6.23), the size of hydrogen peak is significantly reduced (i_{peak} $\approx$ 1 mA cm^{-2}), and more defined plating peaks are observed. In the reverse scan larger stripping peaks indicate the degree to which nickel deposition has improved in efficiency.

It is possible that either the nickel species located on the electrode inhibit the HER or that with no nickel present there is 0.1 M of free citric acid. When nickel is introduced this complexes with the citrate (to mainly form NiH_2Cit^+ and NiHCit) preventing the evolution of hydrogen from citric acid.

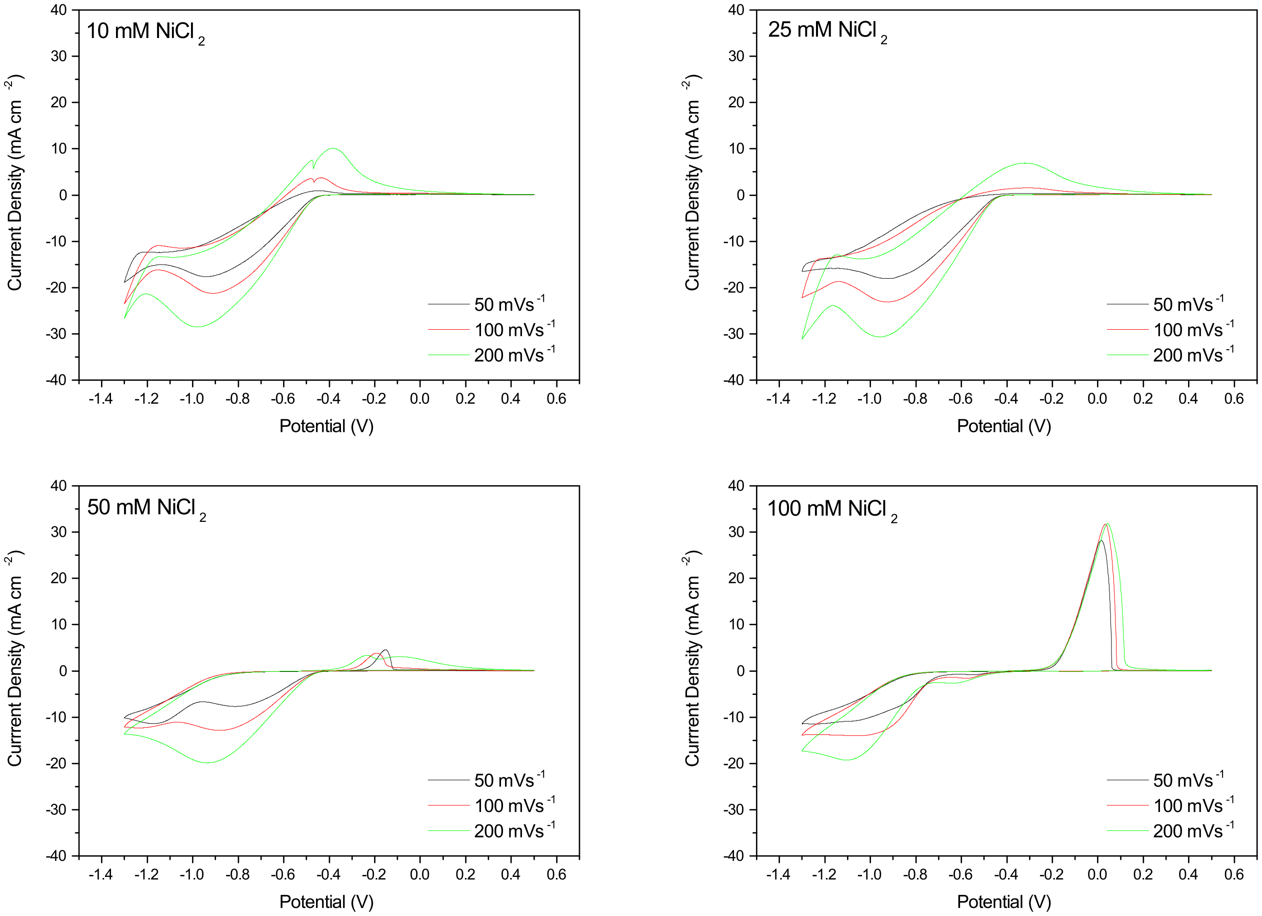

Figure 6.8: Cyclic voltammetry for nickel-citrate baths as described in Table 6.1 with varying concentrations of Ni (II). With an initial potential of 0.5 V scans were performed between 0.5 and -1.0 V. The scans were performed at 60 °C and at a pH of 3.0 using a SCE reference.

6.3 EQCM

The electrochemical quartz crystal microbalance is an effective tool to monitor the rate of deposition of the deposited film separately from the evolution of gas or other solution based reactions. This can provide a useful insight into the deposition mechanism and a 'real time' measurement of efficiency. A description of the system used and the calibration procedures are found in Section 3.3.2. Comparisons can also be made to the similar experiments performed on the boric acid bath shown in Section 4.2.2. The EQCM provides a particularly useful service for examining the deposition of nickel by distinguishing the deposition of material on the electrode from hydrogen evolution.

6.3.1 Cyclic Voltammetry

To distinguish between depositing solid material on the electrode and the generation of hydrogen cyclic voltammetry was performed on the Pt EQCM. The voltammetry was performed at room temperature (17 °C) using the citric bath (Table 6.1) at a pH of 3.0.

Plots for the change in frequency with the voltammetry are seen in Figure 6.9 at scan rates of 50, 100 and 200 mV s^{-1}. It was observed that the slower scan rates result in a larger change in frequency as expected due to the increased charge passed. It was also observed that each scan results in the frequency returning to zero implying all deposited material is completely removed with each scan.

Figure 6.10 shows the differentiated frequency change and compares this with the voltammogram. df/dt shows the rate at which mass is deposited or removed enabling a more direct comparison with current in the voltammetry. The plating and stripping regions for nickel are clearly shown and the additional peak in the voltammogram at -0.6 V can now confidently be associated with hydrogen evolution. The HER is shown to occur before any significant nickel deposition. During stripping it was observed that all material is removed from the electrode before the end of the stripping peak despite the fact there is a non-zero current.

Insight into the mechanism of Ni deposition can be gained by examining the plot of charge against frequency during the cathodic sweep (Figure 6.11). In this nickel plating bath two different regimes are observed. The first region corresponds to potentials where hydrogen is produced at the electrode in comparatively large amounts. Here a low coulombic efficiency was observed. At further negative

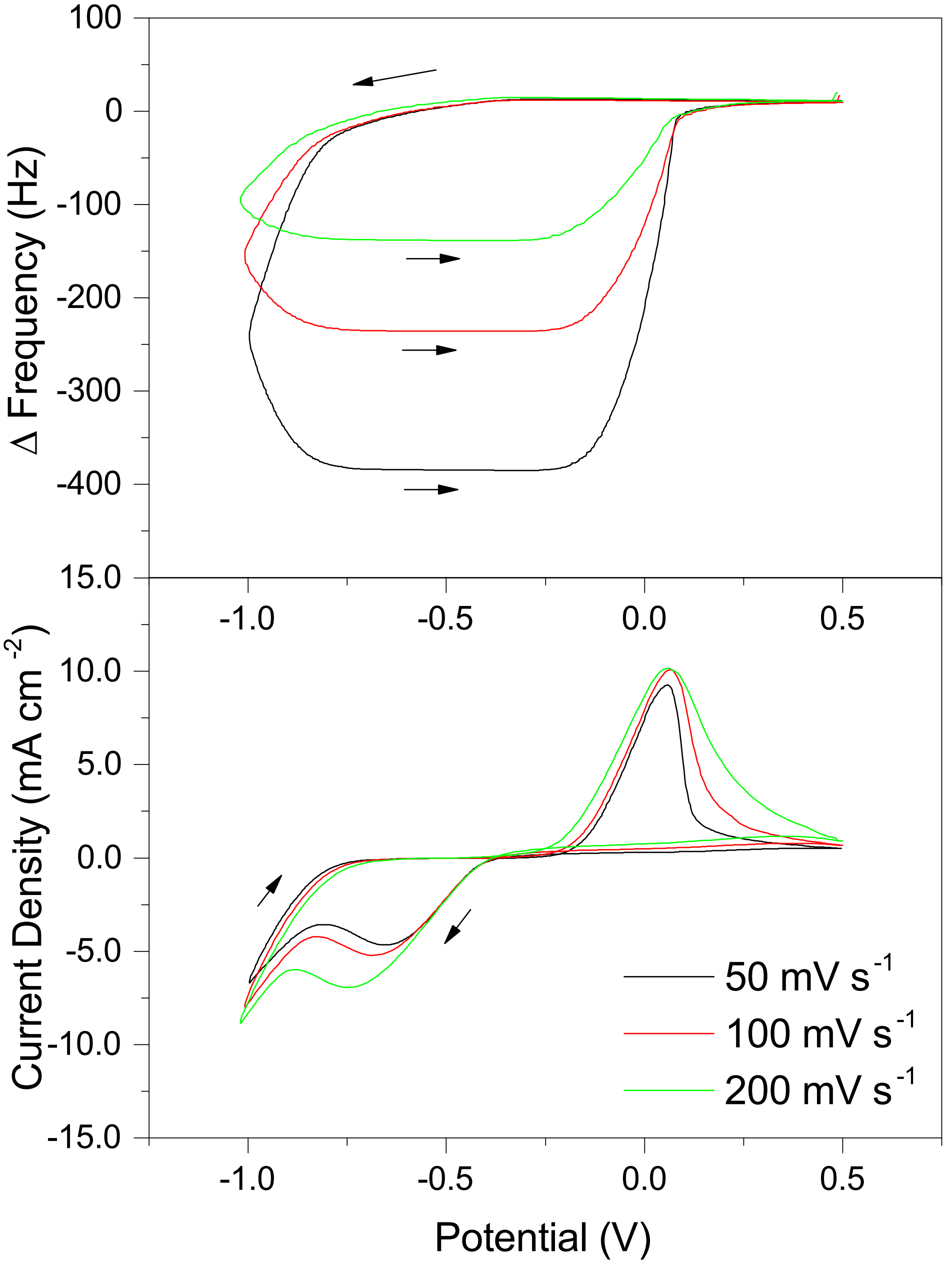

Figure 6.9: The change in frequency and voltammetry during nickel plating and stripping from the citric bath (Table 6.1). With a starting potential of 0.5 V The potential was swept between 0.5 and -1.0 V. The 5th scan is shown. Voltammetry was performed at a pH of 3.0 at room temperature using a SCE electrode.

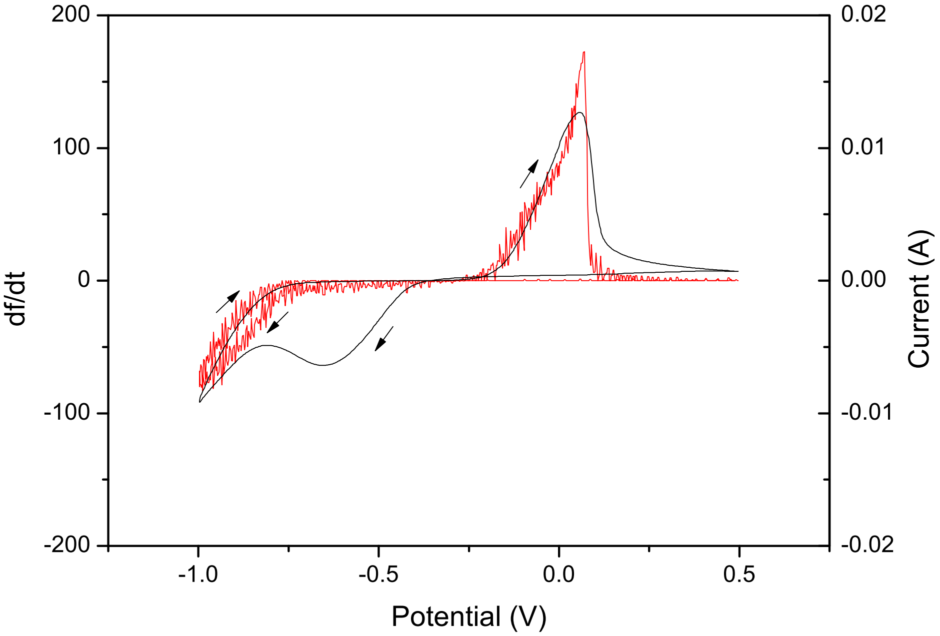

Figure 6.10: The rate of change of frequency w.r.t. time (df/dt) during a cyclic voltammogram at 50 mVs^{-1}. Voltammetry was performed with a starting potential of 0.5 V The potential was swept between 0.5 and -1.0 V. The 5th scan is shown.

potentials a second plating regime occurs with a much larger coulombic efficiency. Table 6.3 shows the measured coulombic efficiency in these regions at these different scan rates.

Initially the coulombic efficiency is linear (gradient = 0.204, R^2 = 0.9999) against the square root of the scan rate. This indicates the reaction in this region is diffusion controlled but the line does not go through the origin (intercept = -0.684 Hz mC^{-1}). This change in mechanism could be attributed to the electrode surface going from platinum to nickel. A monolayer coverage of nickel can be calculated to be 158 ng cm^{-2} or a frequency change of 9.9 Hz. The transition point is independent of the charge passed but occurs where there is a frequency change of approximately 30-40 Hz (corresponds to approximately 470-630 ng cm^{-2}). This gives approximately 3 to 4 layers of nickel on the surface of the electrode before a change in mechanism is observed. It is conceivable that this quantity of nickel is required to be deposited before the reaction can be said to take place on a homogenous nickel surface.

This behavior contrasts that of the boric acid bath, where no transition from low to high efficiency was observed (see 4.2.2). It could be that boric acid is more effective at suppressing the HER on the

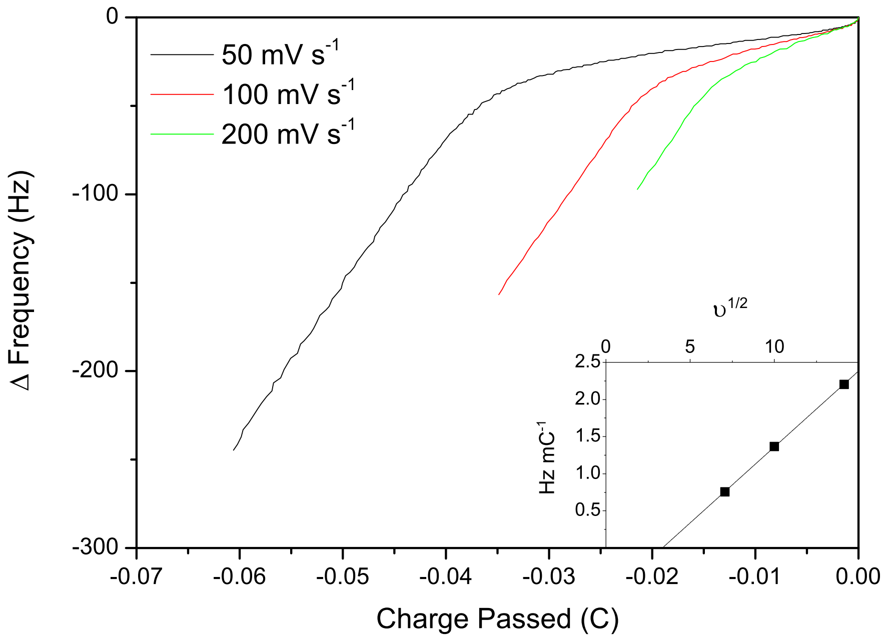

Figure 6.11: Change in frequency on the outward scan. Inset: gradient against the square root of scan rate during the initial plating region.

Scan rate (mV s^{-1})	C.E. 1	C.E. 2
50	2.9 % (757 Hz C^{-1})	32.8 % (8557 Hz C^{-1})
100	5.2 % (1368 Hz C^{-1})	31.6 % (8256 Hz C^{-1})
200	8.4 % (2204 Hz C^{-1})	32.6 % (8506 Hz C^{-1})

Table 6.3: Coulombic efficiency measured from the gradients (shown in brackets) at the various scan rates for the initial low efficiency region (C.E. 1) and higher efficiency region (C.E. 2).

platinum surface. This is also supported by the larger hydrogen peaks found in the voltammetry of the citric bath. Once larger overpotentials are reached and the surface becomes covered with nickel the rate of HER is reduced sufficiently to enable the effective deposition of nickel. This shows the influence of the underlying substrate during the initial stages of deposition.

To study the deposition of larger deposits, nickel was deposited on the EQCM by cyclic voltammetry at varying scan rates between 2 and 50 mV s^{-1}. C_f measured for this EQCM crystal was 0.056 Hz ng^{-1} cm^{2}. The slowest scan rate was performed first with each scan rate repeated 3 times. The frequency change and current passed was measured and is shown in Figure 6.12. During cyclic voltammetry it was found that there is a small positive drift (approximately 0.03 Hz s^{-1}) in the

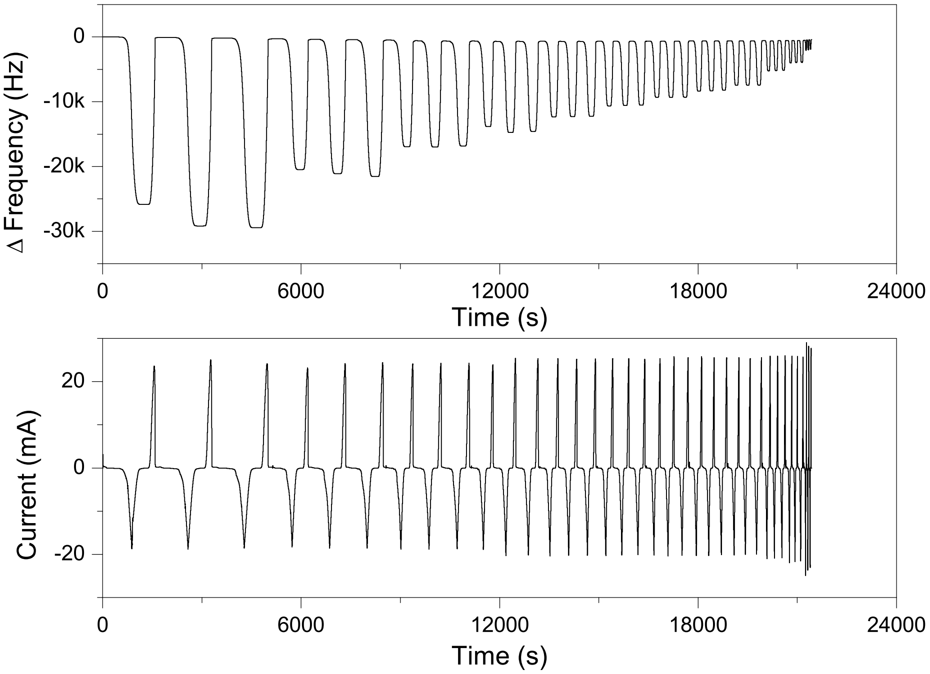

Figure 6.12: Change in frequency and current during cyclic voltammetry in the nickel citrate bath (Table 6.1).

frequency across the scans. Essentially the change in frequency returns to zero with each scan implying all the deposited material is removed in the reverse scan.

The current was integrated to obtain the charge passed during plating and stripping. In each scan it was observed that the charge passed during plating exceeds that of the stripping charge as expected due to the evolution of hydrogen during deposition.

Each scan rate deposits a different quantity of metal therefore the overall coulombic efficiency of deposition and stripping across the voltammogram can be calculated from a plot of the total charge passed against change in frequency. Figure 6.13 shows a linear relationship between charge passed and the change in frequency across these scans. The gradient of the fitted line for deposition was 8.16 ± 0.09 Hz mC^{-1} and for stripping was 11.25 ± 0.03 Hz mC^{-1}. From the gradients of the fitted lines and using a Sauerbrey coefficient of 0.056 Hz ng^{-1} cm^{2} the efficiency of plating was calculated to be 65.6 ± 0.7 % and 90.5 ± 0.2 % for stripping (given 100 % efficient deposition would result in a gradient of 12433 Hz C^{-1}). The stripping efficiency was similar to that for the boric acid bath and the plating efficiency was found to be lower (C.E. for boric acid bath = 83.9 ± 0.2 %). The plating

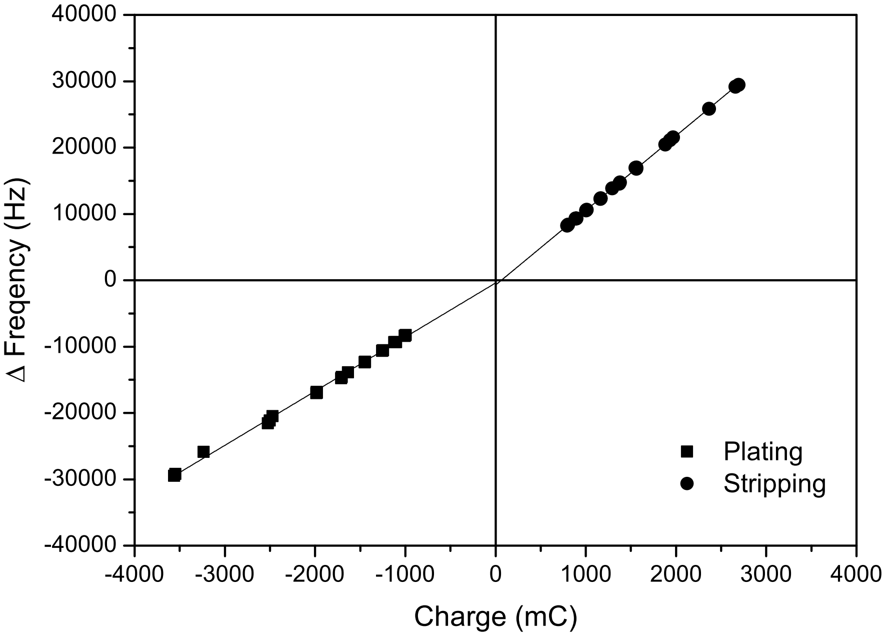

Figure 6.13: Charge passed *vs.* total frequency change for nickel deposition and stripping shown in Figure 6.12.

efficiency of nickel from the citric bath appears quite low in comparison due to a more pronounced H_2 peak.

6.3.2 Galvanostatic Deposition

Industrially, films of nickel and nickel-iron are commomly deposited galvanostatically. When depositing material galvanostatically it would be expected that material is deposited at a constant rate, according to the current density and the deposition efficiency. The EQCM can determine the mass of the material deposited onto the electrode and hence a plot of frequency against time should appear as linear allowing the efficiency of deposition calculated.

6.3.2.1 Nickel Deposition on Nickel

To measure the efficiency of the citric bath at different current densities deposits were made galvanostatically on the EQCM. To remove the influence of the underlying Pt electrode a nickel layer was first deposited at 20 mA for 100 s. On this layer deposits were made at currents between

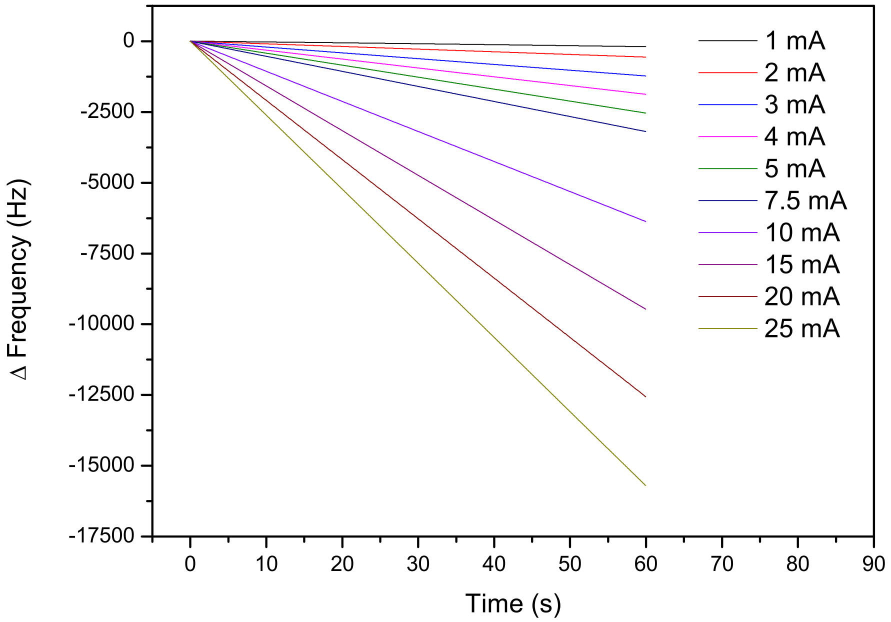

Figure 6.14: Frequency response for the deposition of nickel from the citric bath (Table 6.1) for a range of applied currents. A pre-deposited layer of nickel was applied to the electrode to remove the effects of the under lying Pt and reduce changes in stress and surface roughness.

0.5 and 25 mA. Deposits were made at room temperature with a pH of 3.0 under no agitation. A linear response was observed at all the applied currents with $R^2 > 0.999$ as shown in Figure 6.14. From the frequency-time plots the gradient was measured and efficiency readily calculated using the measured Sauerbrey coefficient of 0.0514 ± 0.0006 Hz ng^{-1} cm^{-2} for this EQCM crystal (see Section 3.3.3.2).

Figure 6.15 shows the resulting efficiencies measured at different currents. It is apparent that the most efficient plating occurs at higher current densities. This could be a result of the HER becoming mass transport limited and no longer capable of passing as much current. In this case the current is then supplied by depositing a larger fraction of nickel resulting in an increased deposition efficiency. Compared to the boric acid bath the measured efficiencies are lower (see Section 4.2.2). The maximum value of efficiency for the citric bath under these conditions is 80 % compared to 95 % for the boric acid bath. The measured efficiency also increases more rapidly for the boric acid bath this suggests that at room temperature boric acid prevents the HER more readily.

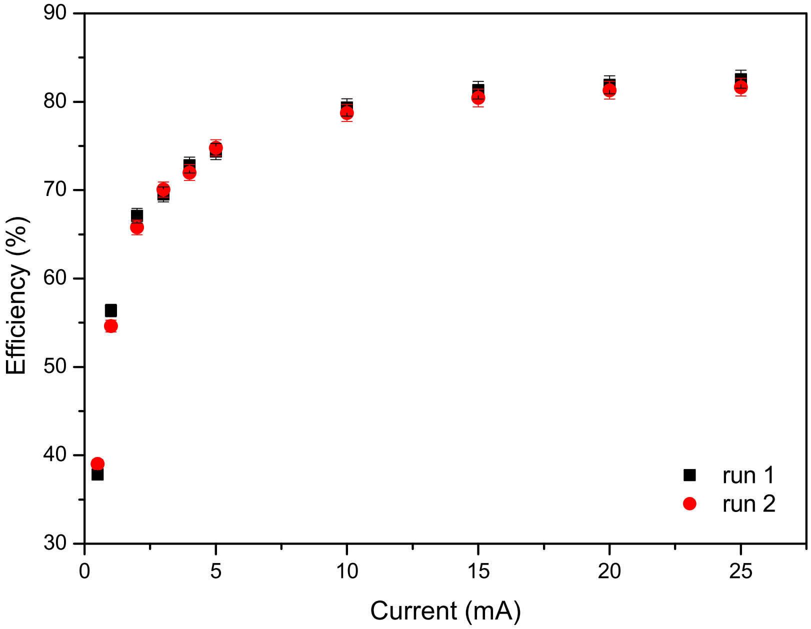

Figure 6.15: Measured efficiencies for galvanostatic nickel deposition from the citric bath (Table 6.1) at room temperature. The errors shown are propagated from the standard deviation in the measure value of C_f for the EQCM crystal used.

6.3.2.2 Nickel Deposition on Platinum

The deposition of nickel onto the platinum surface was also investigated . Using the citric bath at room temperature nickel was deposited at between 1 and 25 mA onto a bare Pt EQCM electrode. Plots for the change in frequency against charge and the change in potential against time are shown in Figures 6.16 and 6.17 respectively.

The response for nickel deposition on a platinum electrode is more complex than for nickel deposition on nickel shown previously (Figure 6.14). Initially the change in frequency follows a common curve independent of the current applied (see inset in Figure 6.16). This common, linear curve is followed to a frequency change of approximately -200 Hz with a charge passed of 38 mC. This represents a change in frequency corresponding to approximately 20 layers of nickel coverage. In this region the gradient is -5.8 Hz mC^{-1}corresponding to an efficiency of 47 %. During this stage the efficiency is lower due to an increased proportion of hydrogen evolution. This contrasts the deposition of nickel from the boric acid bath where high efficiencies (85 %) were measured in this initial region (see Section 4.2.2).

Following the initial common curve the frequency response diverges with the smaller currents resulting in a more positive deviation. This is associated with a negative change in potential after 38 mC of charge was passed as shown in Figure 6.17. The deviation in frequency may be due to the film evolving different levels of stress or surface roughness during deposition at the varying currents. As the deposited films become thicker the gradient increases and becomes linear with gradients approximately -9 Hz mC^{-1} or an efficiency around 70 %. This portion better resembles the deposition of nickel on bulk nickel with little change in stress or the surface roughness.

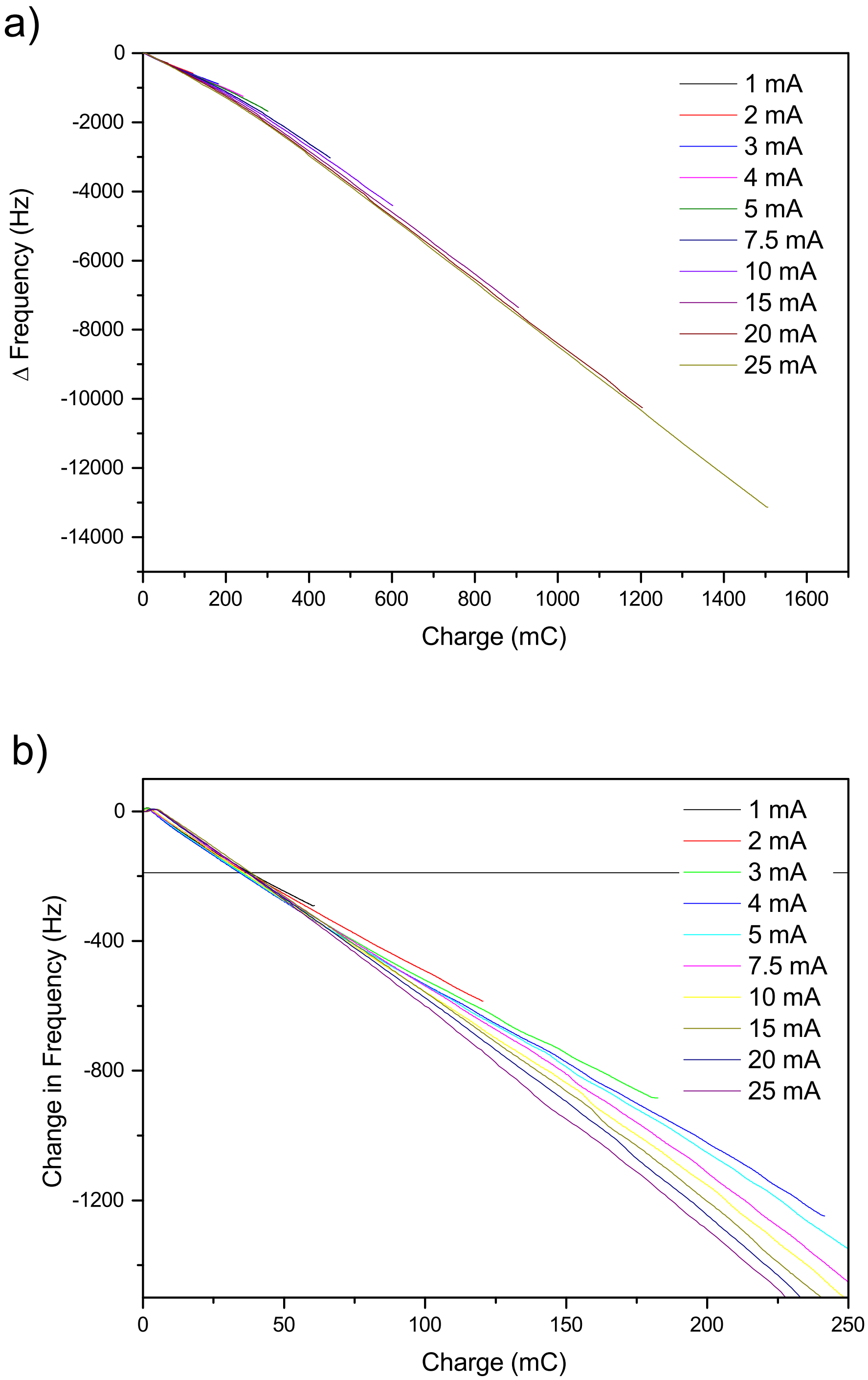

Figure 6.16: Change in frequency during the galvanostatic deposition of nickel. a) Over the entire duration of plating. b) Shows the early stages of deposition where a common curve is followed until a frequency of approximately -330 Hz.

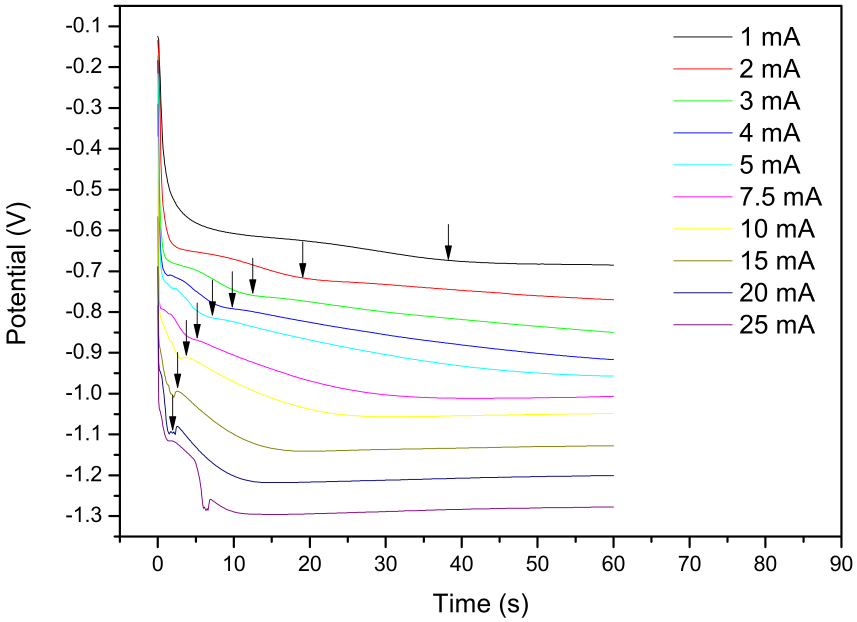

Figure 6.17: Potential-time transients for the deposition of nickel on Pt electrodes. The arrows indicate the time at which 38 mC of charge passed which corresponds to the initial linear response of the EQCM in Figure 6.16.

For the film deposited at 10 mA the change in frequency (a) and potential (c) over time is shown in Figure 6.18. In addition a calculated line (b) was added as a guide to the eye. This line represents 69 % efficient nickel deposition to match that which is measured in the linear region of the plot. The three regions described previously are shown. The first linear region, I, is shown to align with a plateau in the changing potential after 38 mC of charge was passed. The region is defined by less efficient deposition and the morphology of the deposits being dominated by the platinum electrode. In region II there is a non-linear frequency response and a negatively shifting potential. The offset in the frequency may be due to the changing film properties (stress and surface roughness) as growth occurs. Once the film grows thicker there is a linear response (region III). At this stage the film properties remain constant so a mass response is observed.

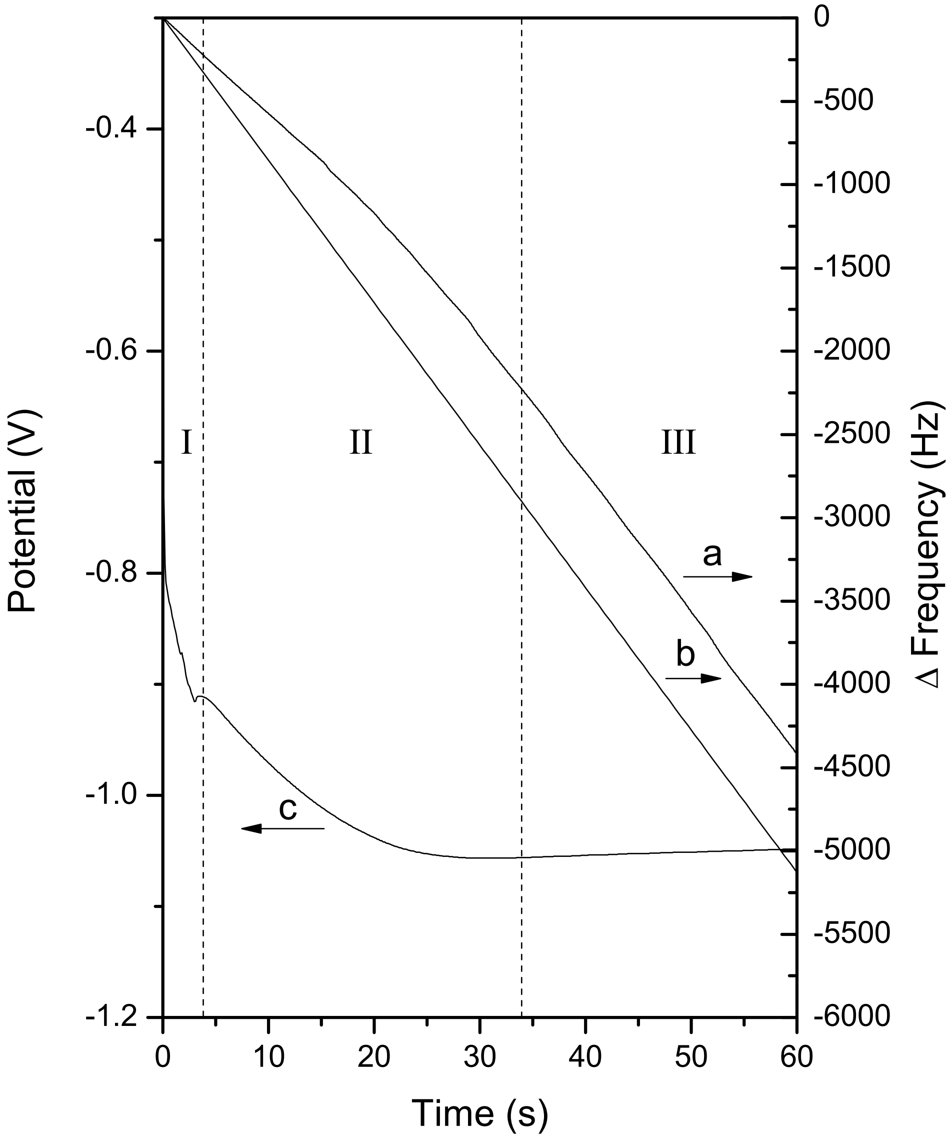

Figure 6.18: Deposition of nickel from the citric bath (Table 6.1) at a current of 10 mA over 60 s showing: (a) the change in frequency measured experimentally; (b) the calculated change in frequency expected for 69 % efficient deposition; (c) the electrode potential.

6.3.3 Additives

There are a wide range of additives used in electrodeposition. These can be categorised in differing ways according to their chemical properties or the effects on the deposit. Classifications include the chemical nature of the additive (organic, inorganic), the effect on the interface (surfactants), the dimension of particles (molecular solutions, colloids), the mechanisms of adsorption on the cathode (rapid adsorption/desorption, specific adsorption) or the effect on the deposit (levelers or brighteners). In addition there are additives generally used in high enough concentrations that they are no longer considered additives. They tend to be some sort of complexing agent (boric acid, citric acid, *etc.*) but there role in the mechanism of electrodeposition is not straight forward and could be multifaceted (see Section 1.2.2).

In this section the effect of additives in the nickel plating bath is examined systematically using the electrochemical quartz crystal microbalance. The intent was to measure changes in efficiency and the deposition potential due to the presence of any given additive in the bath. This may give insight into the role or mechanism of the additives in the citric nickel deposition bath.

Eight solutions were made up as described in Table 6.4 where each solution contains $NiCl_2$ with specific combinations of the additives. The pH of each solution was then adjusted to 3.0 with 10 % HCl. Deposits were made galvanostatically at 20 mA cm^{-2} for 100 s. The potential and change in resonant frequency were measured.

Potential-time transients and the change in frequency observed are shown in figures 6.19 and 6.20 respectively. Differences in the potential were found between baths with citrate and those without. Citrate containing baths deposit at a more positive potential than -1.5 V and those without deposit

Chemical	Concentration (g L^{-1})	Solution Number							
		1	2	3	4	5	6	7	8
$NiCl_2.6H_2O$	110	✓	✓	✓	✓	✓	✓	✓	✓
$Na_3Cit.2H_2O$	30	✗	✓	✓	✓	✓	✗	✗	✗
sodium saccharin	5	✗	✗	✓	✓	✗	✓	✗	✓
SDS	0.1	✗	✗	✗	✓	✓	✓	✓	✗

Table 6.4: Solution contents used during deposition experiments (see figures 6.19 and 6.20). ✓ - indicates the presence of that species in the solution. ✗ - indicates species is not present in the solution.

lower than -1.5 V. Spikes are observed as bubbles are formed and leave the electrode surface the effect of which is also observed with variations in potential (for example later in solution 7).

Figure 6.20 shows the change in frequency of the EQCM before, during and after the current was applied. Four solutions (those containing sodium citrate) show deposition where the change in frequency is linearly proportional to the charge passed as would follow from Faraday's law and the Sauerbrey equation. The remaining four give a non-linear response. From the bath with nickel only there was prominent hydrogen evolution and layers of material were removed from the electrode during deposition and after the current ceased to be passed. The removal of the material is observed as the rising frequency. Solutions 6, 7 and 8 showed a small drop in frequency after the current was stopped. The films made from baths containing no sodium citrate were soluble in weak acid.

According to the Sauerbrey equation, nickel deposited at 100 % coulombic efficiency at 20 mA cm^{-2} would result in a change in frequency of -34070 Hz or a gradient of 340.66 Hz s^{-1}. For baths not containing sodium citrate the change in frequency is greater than the calculated value for nickel only. In the citric free baths the film deposited may not be nickel metal. If the film deposited was nickel hydroxide (which is soluble in acid) the change in frequency would be -55 kHz this is comparable to the observed frequency changes of -45 to -55 kHz.

The four baths which display linear type plots all contain sodium citrate demonstrating its presence is required for the efficient deposition of nickel. Table 6.5 shows the average efficiency measured from the gradient of the Δ frequency vs. charge plots assuming the film is nickel metal. It is seen from the standard deviations (n = 3) that there is no significant change in efficiency from the addition of the additives.

The role of citrate is obviously highly significant. There are a range of suggested mechanisms for additives such as citrate. A general explanation is the metal ions form complexes reducing the concentration of bare metal ions, shifting the reduction potential. Other complexing mechanisms suggest induced absorption or ion bridging to enhance the rate of reduction [155]. Induced adsorption is suggested as complexing agents tend to readily absorb onto metal surfaces and hence the metal complex may also more readily absorb than the unbound ion. The increase in adsorption of metal ions would then increase the rate of reaction at the electrode. Ion bridging is a mechanism where the complexing agent acts as an electron bridge to the metal ion. As it has been suggested that boric acid acts as an electron bridge [57] it is possible that citrate may act in a similar manner.

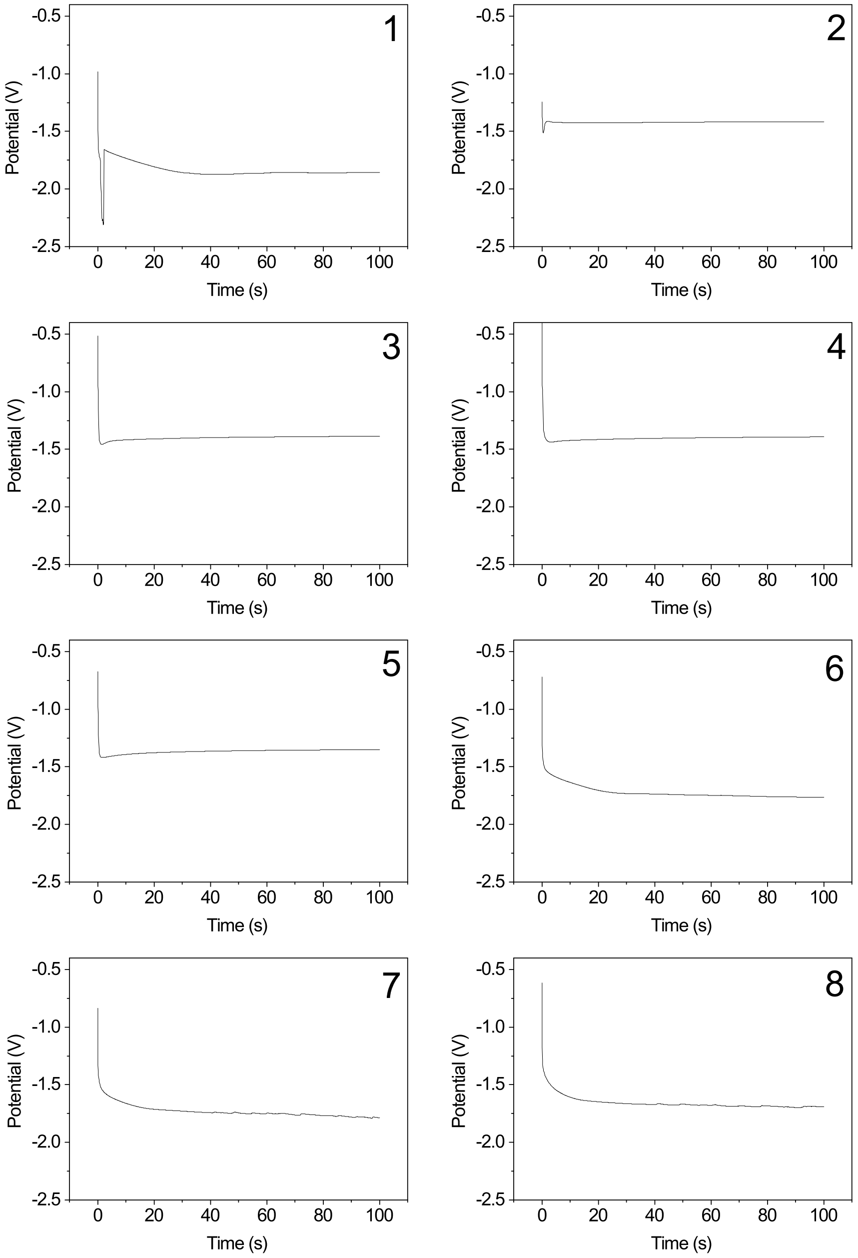

Figure 6.19: Potential-time transients for deposition from different solutions at 20 mA cm^{-2}. From top left: 1) Ni; 2) Ni + Cit; 3) Ni +Cit + Sac; 4) Ni + Cit + Sac + SDS; 5) Ni +Cit + SDS; 6) Ni + Sac; 7) Ni + Sac + SDS; 8) Ni + SDS.

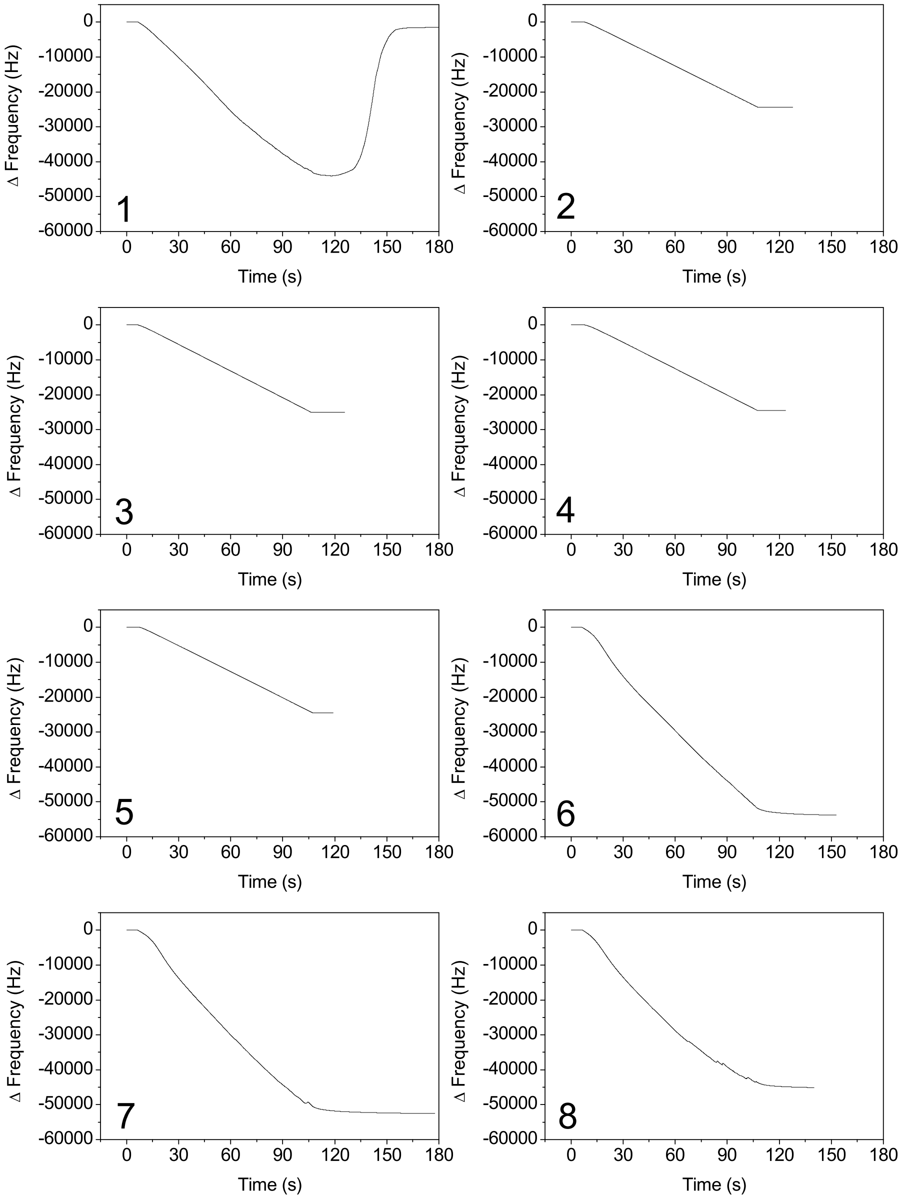

Figure 6.20: Changes in frequency for deposition from different solutions at 20 mA cm^{-2}. From top left: 1) Ni; 2) Ni + Cit; 3) Ni +Cit + Sac; 4) Ni + Cit + Sac + SDS; 5) Ni +Cit + SDS; 6) Ni + Sac; 7) Ni + Sac + SDS; 8) Ni + SDS.

Bath Contents	Average efficiency / %
Ni + Cit	73.2 ± 1.5
Ni + Cit + Sac	75.5 ± 0.7
Ni + Cit + Sac + SDS	75.4 ± 1.3
Ni + Cit + SDS	74.0 ± 1.1

Table 6.5: Efficiency of nickel deposition from solutions containing different additives. The efficiency was calculated from the gradient of Δ Frequency *vs.* time plots.

6.3.4 pH

The effect of pH on the coulombic efficiency is of interest as well as any effect on the nature of the deposited film. Deposits were made from the nickel-citrate bath (including saccharin and SDS) at 20 mA for 100 s on the EQCM and the change in frequency recorded. The pH was varied with the addition of 10 % vol HCl. The resulting frequency-time plots are shown in Figure 6.21. The deposition potential remained constant across the range of pH at -1.39 V

At pH 4.74 (unadjusted bath) there were large fluctuations in frequency indicating the erratic nature of the deposition. The resulting film was found to readily dissolved in 0.1 M H_2SO_4. This is consistent with the formation of $Ni(OH)_2$ which may be formed due to the higher bath pH. The pH of the bath was decreased using HCl and further deposits were made. The films produced at a reduced pH no longer dissolved in H_2SO_4 or in a solution of $NiCl_2$ adjusted to pH 3.0 (as for the films deposited for solution 1 in Figure 6.20). The coulombic efficiency of plating is plotted against pH in Figure 6.22. The efficiency was highest at a pH of 3.87 as the pH was lowered the HER becomes more important and the efficiency for nickel deposition decreases. It is suggested that any change in efficiency in previous experiments is dominated by the variation in pH.

It is of use when performing pH based experiments to examine the speciation in the solution. A speciation diagram was computed using Visual MINTEQ [156] to include 0.5 M $NiCl_2$ and 0.1 M citrate, similar to that within the plating bath. In the specation diagram (Figure 6.23) there is an excess of nickel, when compared to citrate, which remains as Ni^{2+}in much larger concentration across this range of pH. The highest efficiency for nickel deposition was measured at pH 3.87. This pH corresponds to the region where the $NiHCit \rightleftharpoons NiCit^{-} + H^{+}$ reaction buffers the solution. In addition there is a small proportion of free H^{+} present.

Figure 6.24 shows further investigation of films deposited at a higher pH from a bath consisting of

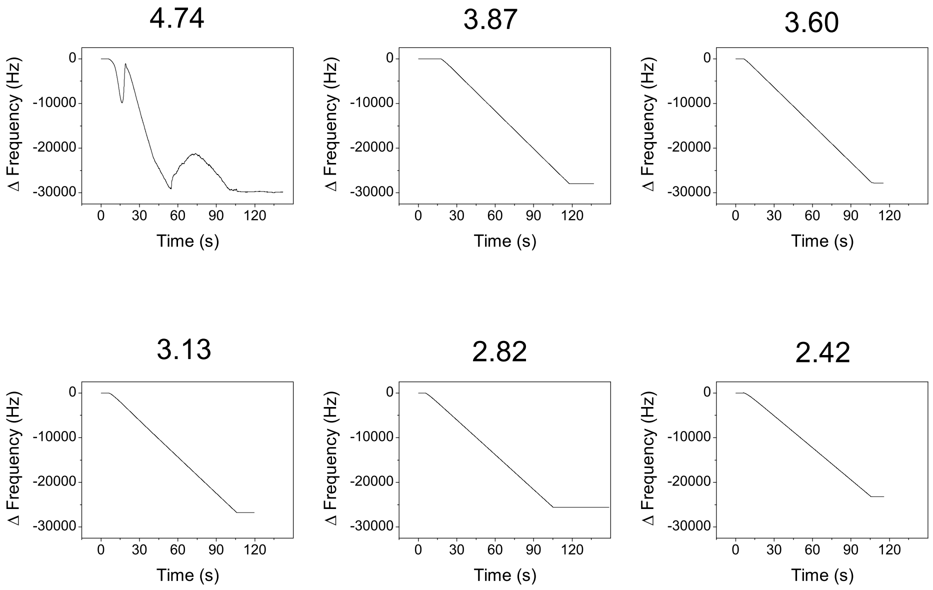

Figure 6.21: Change in frequency during deposition from the nickel-citrate bath at 20 mA cm^{-1} at the stated pH.

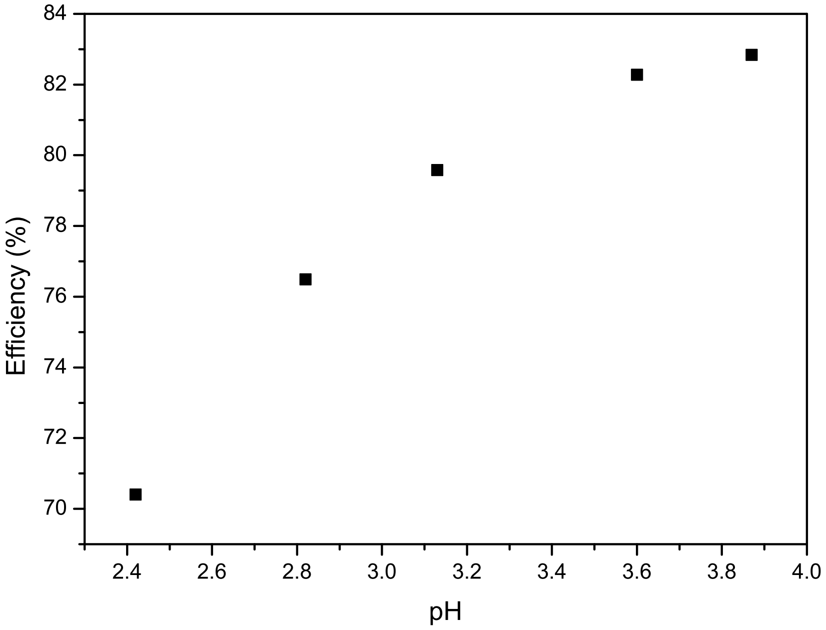

Figure 6.22: Efficiency of nickel deposition from the citric bath at 20 mA cm^{-2} with varying pH.

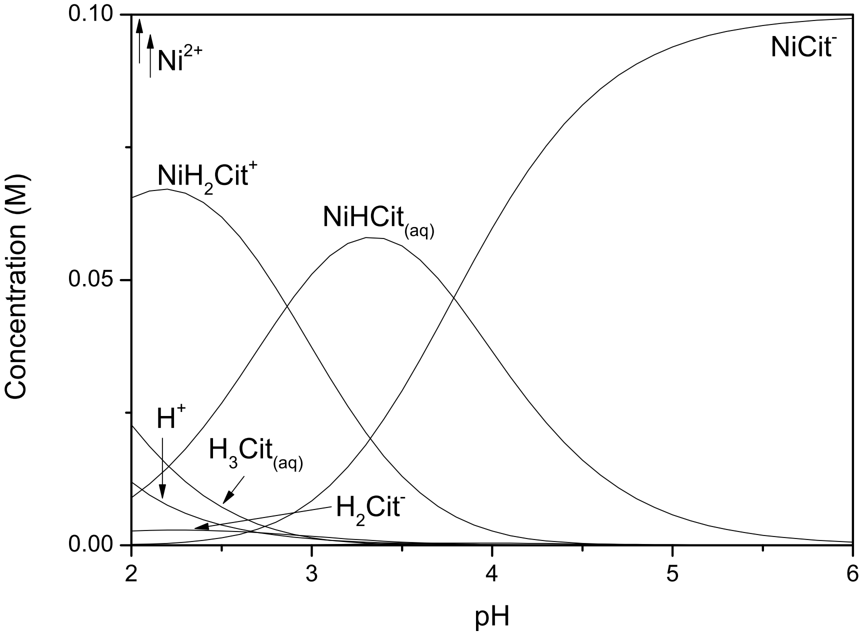

Figure 6.23: Speciation diagram showing Ni and citrate species calculated using Visual MINTEQ. Initial [$NiCl_2$] = 0.5 M, initial [Cit^{3-}] = 0.1 M at 25 °C.

Species	logK
$HCit^{2-}$	6.396
H_2Cit^-	11.157
H_3Cit	14.285
$Ni(Cit)_2{}^{4-}$	9
$NiCit^-$	6.64
$Ni(OH)_2$	-18.994
$Ni(OH)_3{}^-$	-29.991
$NiH(Cit)_2{}^{3-}$	15
NiHCit	10.63
NiH_2Cit^+	13.29
$NiOH^+$	-9.897

Table 6.6: logK values for species used to calculate speciation diagram from NIST thermodynamic database [55].

$NiCl_2$ with no citrate buffer or additives. A solution of 0.5 M $NiCl_2$ was adjusted to a pH of 3 with a small volume (compared to the citric baths as there is no buffer) of HCl. A current of 20 mA was passed for 100 s to deposit a film on the electrode. The film formed under these conditions results in a large change in frequency (-57 kHz). The working electrode was then transferred in to 0.1 M H_2SO_4. The change in frequency shows the film is not stable and is chemically removed. The same experiment was repeated but this time with a larger volume of HCl being added to lower the pH to 0.7. The resulting film gives a frequency change of -16 kHz and when transferred to 0.1 M H_2SO_4 is shown to be stable.

The maximum change in frequency expected for nickel deposition is 34 kHz for the charge passed. The film deposited at pH 3 has a much larger change in frequency and therefore can not be due to the deposition of nickel on its own. The deposited film must either contain large quantities of trapped solvent or more likely be a film with a greater mass, for example nickel hydroxide which would have an expected frequency change of approximately -55 kHz. Also displayed in Figure 6.24 is the resistance of the motional branch of the EQCM (see Figure 2.5). At high pH the resistance is higher than for the film deposited at low pH which is consistent with the formation of nickel hydroxide.

When there is no ‘buffer’ or reservoir of protons the local pH at the electrode is depleted sufficiently as to not deposit nickel, similar to the high pH full bath. In addition when a film was deposited from a deoxygenated bath at pH 3.0 the resulting film remains soluble in acid. It is suggested that the soluble films deposited are $Ni(OH)_2$ which is deposited *via* two steps (Equations 6.2 and 6.3) or NiOOH. The first step is an electrochemical reaction which creates hydroxyl ions at the electrode. Then a chemical reaction occurs which precipitates nickel hydroxide on to the electrode [157].

$$2H_2O + 2e^- \rightarrow H_2 + 2OH^- \tag{6.2}$$

$$Ni^{2+} + 2OH^- \rightleftharpoons Ni(OH)_2 \tag{6.3}$$

It is obvious that the surface pH at the electrode is highly important. The ability to prevent the creation of OH^- or reduce its rate of formation sufficiently is a key factor in producing a nickel film. At a pH of 3.0 the majority of the citrate anion is protonated (at least to some degree) and can act

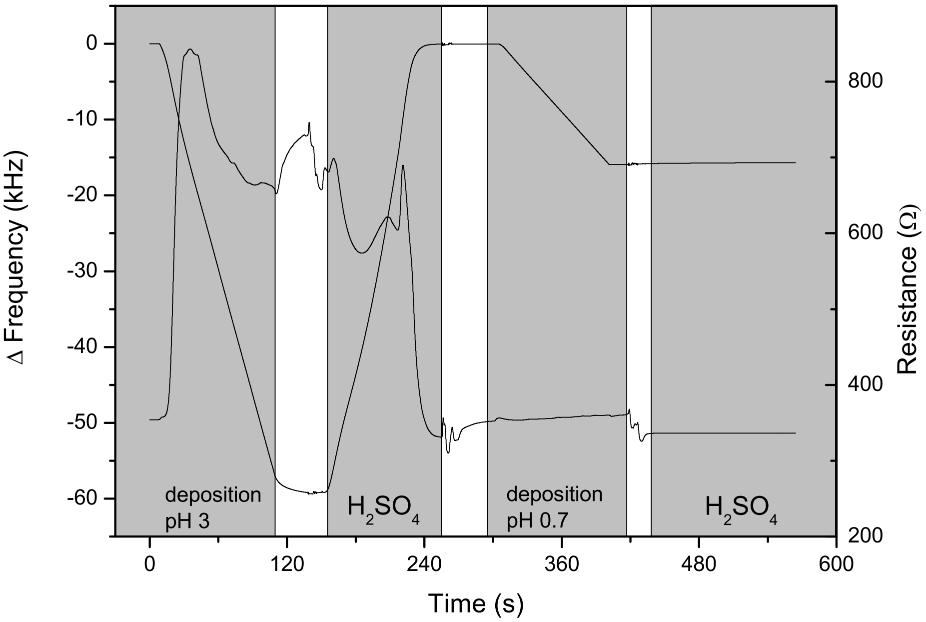

Figure 6.24: Change in frequency and resistance measured on the EQCM for the deposition of films from a 0.5 M solution of $NiCl_2$. The areas marked H_2SO_4 are where the stability of the film was tested in a 0.1 M solution of sulfuric acid. Shaded areas indicate time when the electrode is in a solution. Spiking in the resistance is observed when the electrode was rinsed in DI water.

as a source of protons. The buffering action of citrate may help reduce the depletion of H^+ at the electrode surface sufficiently during nickel deposition.

Ni $^{2+}$ on its own is difficult to deposit, however with a large excess of Ni^{2+} in solution it is proposed that nickel could be deposited from the NiHCit species which is then regenerated.

$$NiHCit + 2e^- \rightarrow Ni(s) + HCit^{2-} \tag{6.4}$$

$$HCit^{2-} + Ni^{2+} \rightarrow NiHCit \tag{6.5}$$

The voltammetry in Section 6.2.3 demonstrated the deposition of nickel in a bath with equal concentrations of nickel and citrate and therefore no excess Ni^{2+}. A nickel plating peak and the large nickel stripping peak demonstrated the successful deposition of nickel in this bath demonstrating that free nickel is not required. When excess nickel is introduced the current in the CV no longer peaks for nickel plating and the current continues to increase. This could be due to the replenishment of the NiHCit species.

6.3.5 Effects of Temperature

In the previous chapter it was shown that temperature has a significant effect on the deposition of nickel and nickel iron films. To examine these effects investigations were made on the EQCM. Care must be taken when performing temperature studies on the EQCM due to changes in the resonant frequency. In this work an AT-cut quartz crystal was used which has a turn around point at 25 °C *(i.e.* there is minimal resonant frequency change with temperature close to 25 °C). Section 3.3.2 details the effects of temperature on the the EQCM showing that at temperatures up to 60 °C there is minimal change in the resonant frequency of the quartz crystal and C_f.

6.3.5.1 Galvaonstatic Experiments

Galvanostatic measurements were made to measure the change in efficiency with temperature. A current density of 20 mA cm^{-2} was applied for 100 s with the potential and change in frequency measured. This was performed over a temperature range between 20 and 60 °C. The electrodes were cleaned between each deposition in 0.1 M H_2SO_4 by cyclic voltammetry.

Typical potential-time plots for galvanostatic deposition of nickel at different temperatures are shown in Figure 6.25. The potential required to drive the reaction at this rate is shown to decrease with increasing temperature. When rearranged the Butler-Volmer equation shows the over potential is related to the temperature at a fixed current density, j.

$$\eta = \ln\left(\frac{j}{j_o}\right)\frac{R}{\alpha n F}T \tag{6.6}$$

However E° and the exchange current density, j_o, also vary with temperature resulting in the slight curve observed in the temperature *vs.* potential plot (inset in Figure 6.25).

The overall efficiency at each temperature was calculated from the total charge passed and the total change in frequency over the 100 s of deposition (Figure 6.26). There is a slight increase seen in efficiency at higher temperatures with a minimum observed at around 30 °C as at lower temperatures the efficiency is found to increase again. This matches with experiments performed depositing

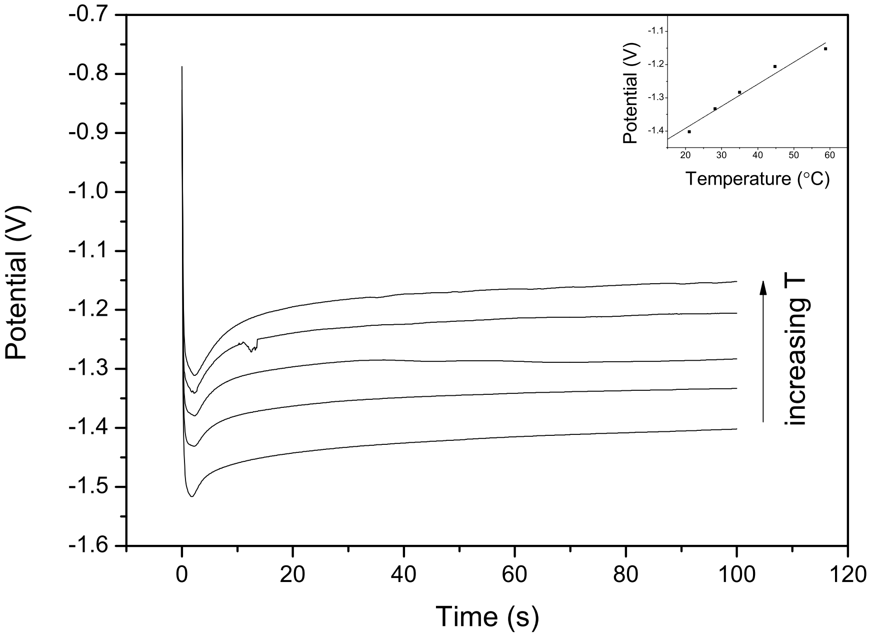

Figure 6.25: Potential-time plots for the galvanostatic deposition of nickel at 20 mA cm^{-2} from the citrate bath (Table 6.1) performed at temperatures of 21.0, 28.2, 25.0, 44.8, and 58.8 °C. The pH was adjusted to be 2.8 ± 0.1 at each temperature using 10 % HCl.

nickel-iron films where the Ni content of the films varies in the same way with temperature (Section 5.15).

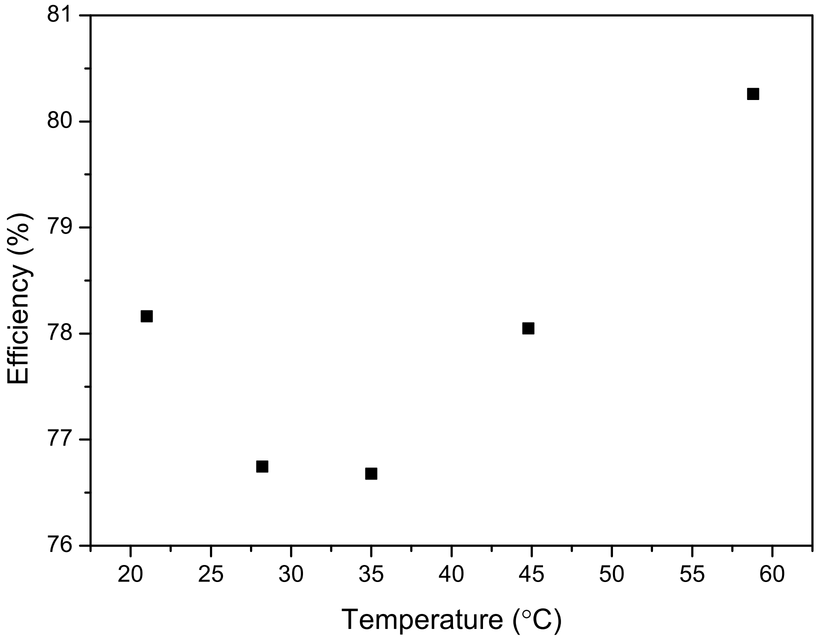

Figure 6.26: Efficiency of nickel deposition across varying temperatures measured from EQCM data for films deposited at 20 mA cm^{-2}.

6.3.5.2 Potentiostatic Experiments

In potentiostatic experiments deposits of nickel were made using the citric bath using a fixed potential of -1.0 V *vs.* SCE for 100 s on the EQCM. Given the increased observed efficiency at 60 °C, the bath was heated to 60 °C and adjusted to a pH of 3.0 ± 0.1 with HCl prior to deposition. The electrodes were cleaned thoroughly between each deposition in H_2SO_4.

The current-time transients for nickel deposition at varying temperatures are shown in Figure 6.27. The currents observed were seen to increase with higher temperatures. At lower temperatures hydrogen evolution is more prominent (51 % of the current). At the higher temperatures the nickel deposition reaction becomes more significant (up to 59 % of the current). The nickel deposition reaction remains under electrochemical (kinetic) control and has a greater effect on the current-time response.

The efficiency for nickel deposition was calculated from the change in frequency at the different temperatures used (Figure 6.28). As the temperature increased that measured efficiency for deposition increased steadily until a temperature of 50 °C. Using the efficiency measurements the fraction of current used to deposit nickel can be calculated. If the deposition of nickel is under kinetic control then it should display Arrhenius behavior. Figure 6.29 shows a plot of of $\ln|i_{Ni}|$ against $1/T$. The gradient of this plot can then be used to estimate the activation energy for the nickel deposition reaction as $dln|i|/d(1/T) = -E_a/R$. The gradient is -2747 ± 171 giving an estimate for the activation energy of 22.8 ± 1.4 kJ mol^{-1}.

Figure 6.30 shows the rate of change of frequency measured during the experiment. It is apparent that there is an initial phase where a large proportion of the current is not depositing material on the electrode. There is a sharp initial spike in the current caused by the charging of the double layer. The current then begins to level during a phase which does not match the changing frequency. A large amount of hydrogen production on the Pt electrode surface could be responsible. There is another change in the current occurring between 7 and 20 s, depending on temperature, after which the df/dt appears to match the current presumably where deposition of nickel dominates the electrochemical processes. At higher temperatures it requires a shorter timescale to achieve the dominant nickel plating regime implying that less hydrogen is evolved. The effects of hydrogen evolution on the initial phase of deposition are apparently suppressed at higher temperature.

6.3.5.3 Potential Step Experiments

To investigate the properties of the deposited Ni films potential step experiments were performed to examine the stripping of films deposited from the bath. This can bring to light more information about how the film is deposited and the nature of the films. Deposits were made at -1.0 V over increasing deposition time (10, 20, 30, 40 and 60 s). A potential step was performed to strip the film at at 0.0 V. The experiments were performed at room temperature (Figure 6.31) and at 60 °C (Figure 6.32).

In the initial stages of the deposition the current and df/dt were found to match much closer, unlike the previous experiment. As these experiments were performed sequentially without cleaning the electrode in H_2SO_4 between deposits the electrode surface does not have the same level of cleanliness as before. It is thought that on the clean Pt surface it will be easier to produce hydrogen which continues until a layer or layers of nickel cover the electrode. On a dirtier surface the catalytic generation of hydrogen is hindered and it is favorable to deposit nickel.

The rate of stripping for the final part of the film (which is deposited first) was found to vary between the two temperatures. At room temperature there is an increase in df/dt which then falls

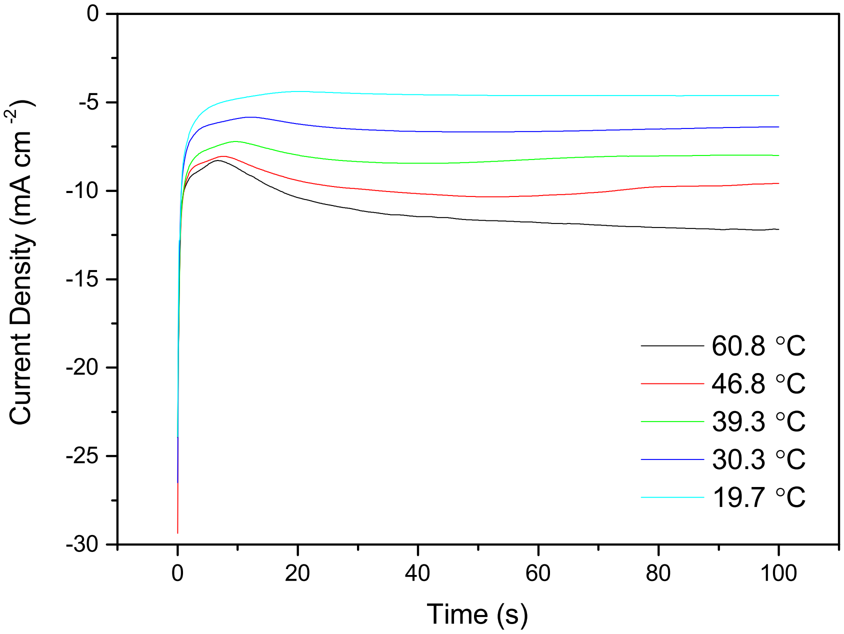

Figure 6.27: Current-time plots for the deposition of nickel at -1.0 V on the EQCM for the citric bath (Table 6.1). At the varying temperatures the pH was adjusted to 3.0 ± 0.1 using 10 % HCl.

to zero simultaneously with the current. This increase may be due to a decrease in the surface roughness as the platinum electrode is exposed after removal of the electroplated nickel.

At 60 °C there is no increase in rate and df/dt returns to zero before the current. This implies material is removed from the electrode until a point where oxidation occurs with no significant mass change. It is speculated this could be due to the oxidation of the platinum surface or oxidation of any trapped hydrogen.

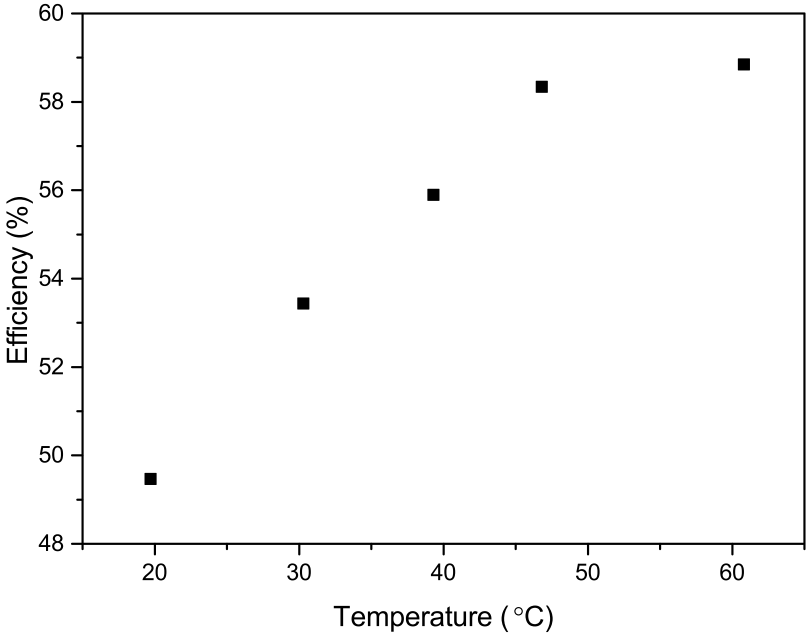

Figure 6.28: Measured efficiency from the EQCM data for nickel deposition from the citric bath. Deposits were made potentiostatically at -1.0 V as for Figure 6.27.

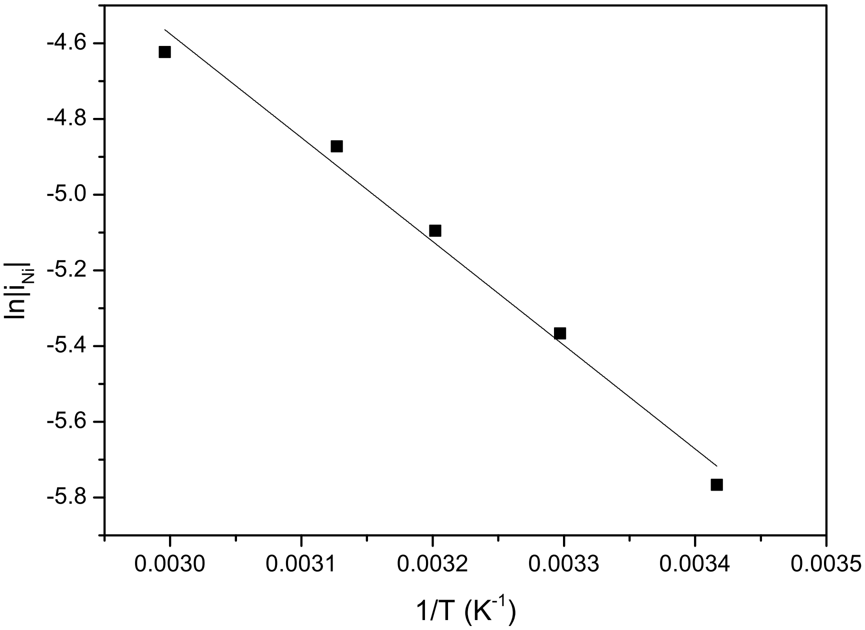

Figure 6.29: Arrhenius type plot for the potentiostatic deposition of nickel from the citric bath.

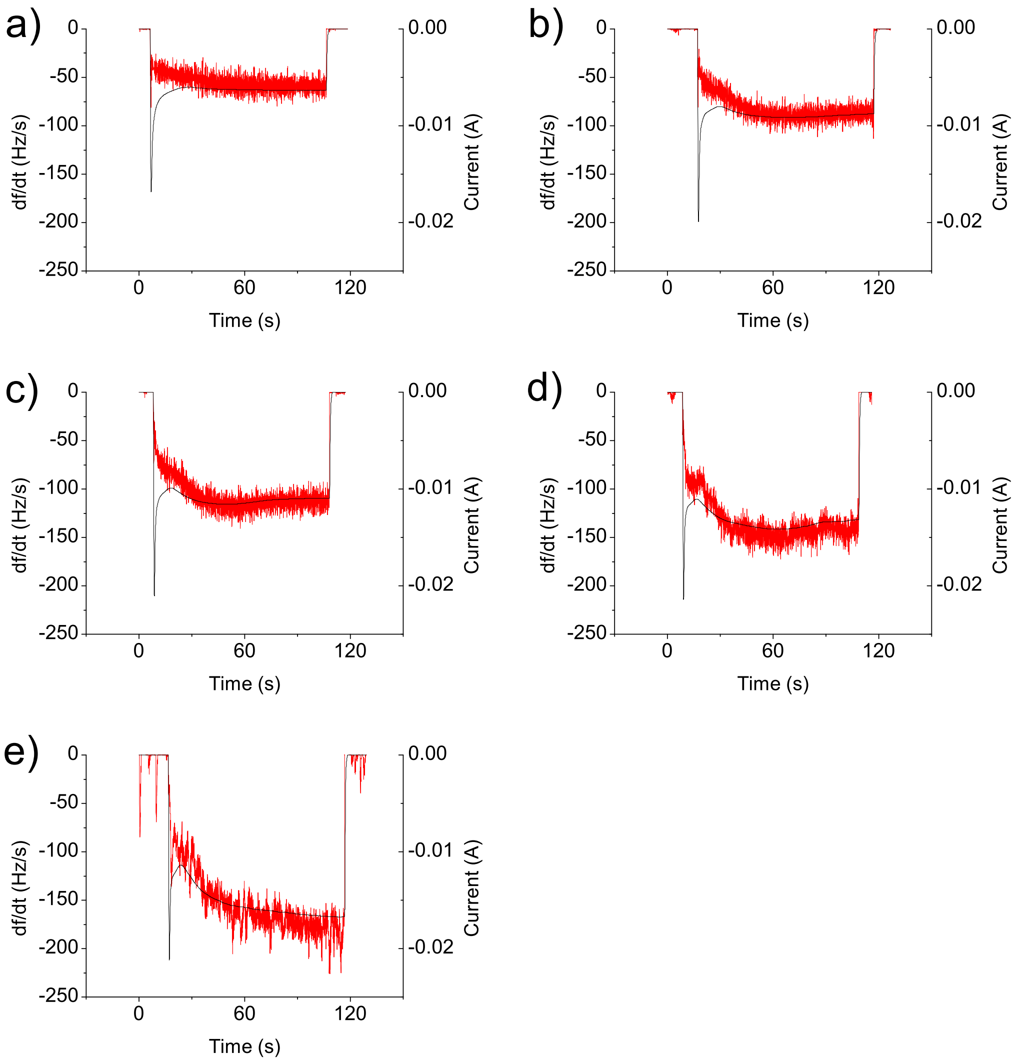

Figure 6.30: *df/dt* and current for the potentiostatic deposition of nickel at 20 mA cm^{-2} from the citric bath. Deposition was performed at the temperatures a) 20 °C, b) 28 °C, c) 38 °C, d) 45 °C, e) 60 °C.

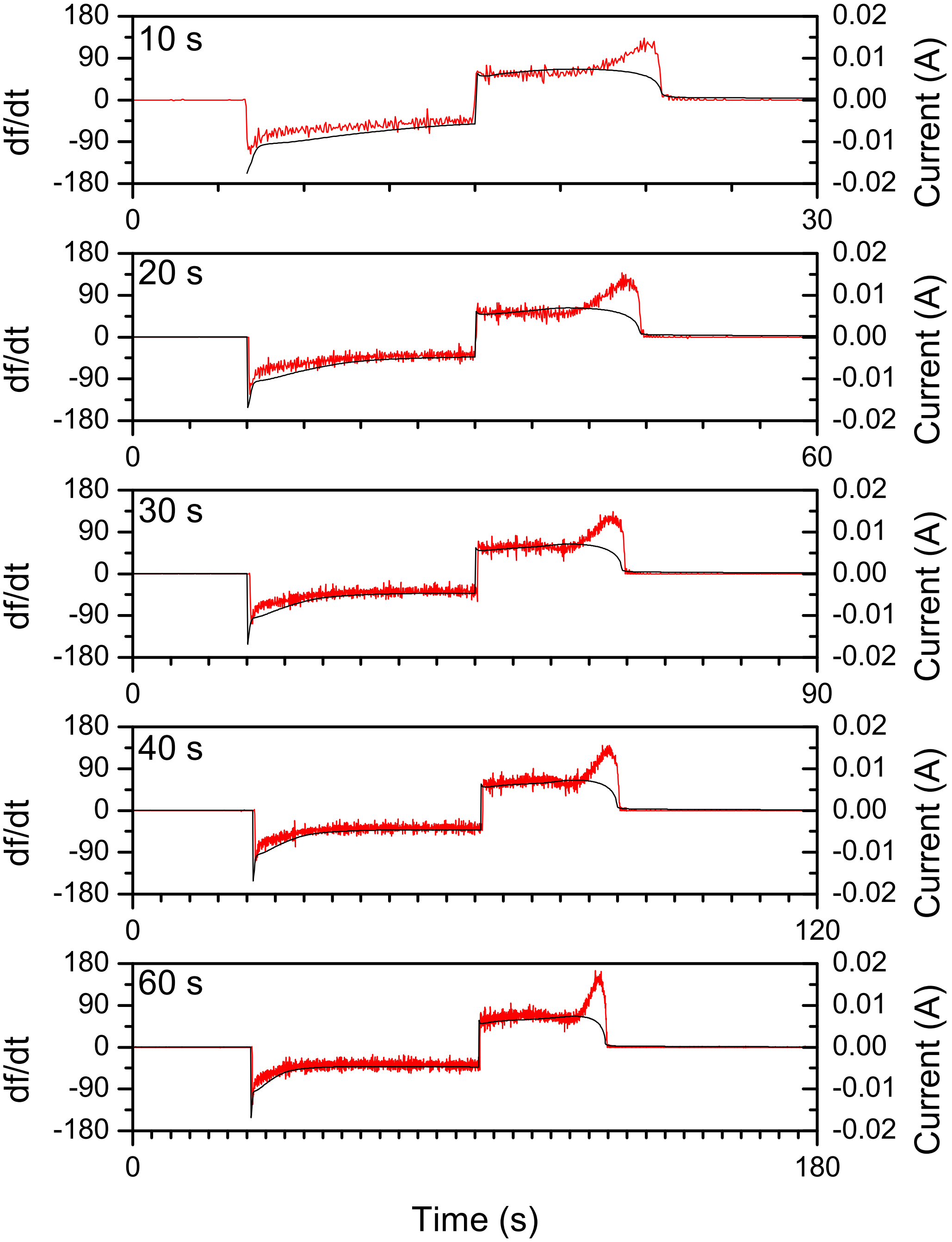

Figure 6.31: Potential step experiments showing df/dt (red) and current (black) at room temperature. Each division in the time axis is 5 s.

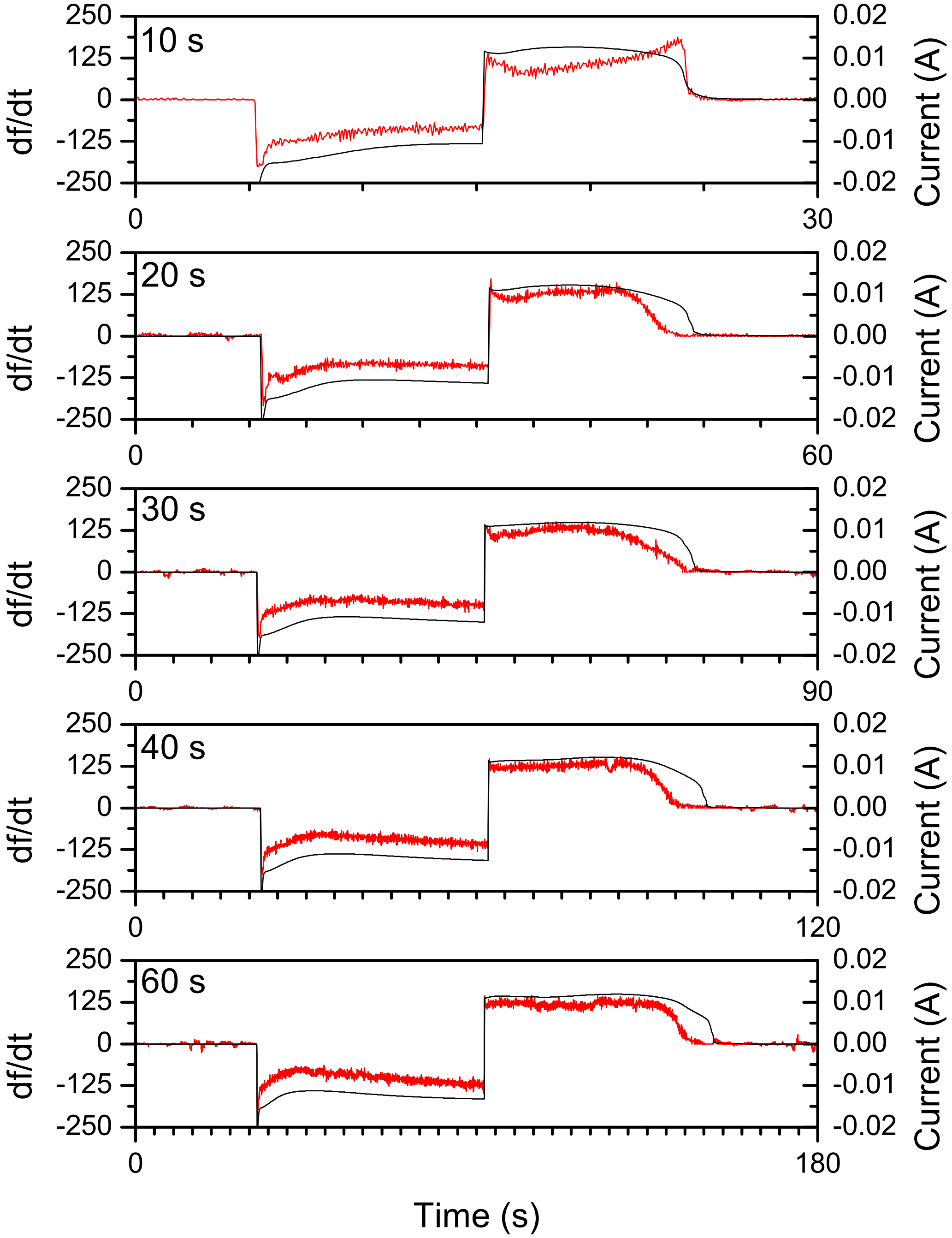

Figure 6.32: Potential step experiments showing df/dt (red) and current (black) at 60 °C. Each division in the time axis is 5 s.

6.4 Conclusions

The citrate anion has been shown to enhance the deposition of nickel in a similar manner to boric acid. Controlling the hydrogen evolution reaction remains of high importance in the nickel-citrate bath as this dictates the nature of the deposits and the deposition efficiency. It is clear that the control of the hydrogen evolution reaction is key for the deposition of nickel . During the deposition of nickel on platinum it appears, mechanisticly, that there are two plating regimes for the deposition of nickel from the citric bath. A first regime where there is a low efficiency and hydrogen evolution is prevalent and a second regime where nickel deposition dominates over the HER.

This chapter demonstrates how the HER can be limited during deposition. pH control is important as increased efficiency of the deposition on lowering pH was shown to rapidly lead to an enhanced rate of the hydrogen evolution reaction due to the further increase in the H^+ concentration. The HER can also be limited using the optimal current densities to deposit films. It was shown that in the range up to 18 mA cm^{-2} a increased current reduces the extent of the hydrogen evolution reaction.

An additional issue in the deposition of nickel films is the formation of $Ni(OH)_2$. Citrate helps to prevent the formation of $Ni(OH)_2$ which passivates the electrode. It may perform this role due to an ability to provide acid and prevent changes in the local pH near the electrode through the equilibrium $NiHCit \rightleftharpoons NiCit^- + H^+$.

Chapter 7

Electrodeposition of Nickel-Iron Films from a Citric Bath

7.1 Motivation

Having performed an analysis for the deposition of nickel from the citric bath the system was then be made more complex with the addition of iron species to deposit magnetic alloys. Characterisation of the electrochemical behavior of this binary system was performed. Examination of the deposition of the nickel-ion alloy from an alternative bath (not containing boric acid) was performed to make a REACH compatible bath and to give further insight into the anomalous deposition behavior of the nickel-iron system.

Voltammetry was first performed on the nickel-iron citric bath to examine the basic electrochemistry. Comparisons were then made to the behavior of the boric acid based bath.

It is important to be able to distinguish between the deposition of nickel and iron in order to separate their individual effects. The EQCM does not provide a suitable method to identify the two metals and separate their effects as the mass and valency of nickel and iron means that the depsoition/charge masses are almost identical. It is known that agitation has a significant effect on the deposit properties, to this end experiments were performed on the rotating ring disc electrode (RRDE). This technique has the advantage of controllable hydrodynamic behavior, an important factor in determining alloy composition and deposition efficiency. From this work the optimal conditions for NiFe deposition from this bath were determined.

7.2 Cyclic Voltammetry

7.2.1 Voltammetry of the Iron-Citrate Bath

To examine the behavior of iron in the citric bath voltammetry was performed on an iron bath containing iron chloride, sodium citrate, sodium saccharin and SDS. Cyclic voltammetry was performed at 60 °C using a platinum disc electrode with area 0.387 cm^2. The potential was swept between 1.0 V and -1.3 V over a range of scan rates.

Using the speciation diagram shown in Figure 7.1 the initial composition of the bath can be approximated for a pH of 3.0. The speciation of iron is split equally between free Fe^{2+} and the citrate bound FeHCit complex. In this bath there is an excess of the citrate anion at pH 3.

Figure 7.2 shows voltammetry for the iron bath. Peaks in the scan related to hydrogen can be identified by comparison to the CV of the background electrolyte (Figure 6.7) where hydrogen gas oxidation and hydrogen ion reduction on the platinum electrode occurs at around -0.4 V. This compares well to peaks (b) and (e) in the iron-citrate bath.

Two peaks are observed for the oxidation of Fe(II) to Fe(III) around 0.2 V and 0.5 V (c and d). Peak (d) is consistent with the oxidation of Fe^{2+} to Fe^{3+} seen in the boric acid electrodeposition bath (Figure 4.10). The presence of peak (c) is consistent with an additional complexed iron (II) species (FeHCit) as shown in the speciation diagram. For the reverse scan there are no major corresponding back peaks, possibly due to the strength of the iron (III) citrate complex and excess of the citrate anion.

A further peak is observed in the cathodic scan at -1.2 V (peak f) before the current rapidly increases. On the reverse scan there is an associated stripping peak (a) most likely due to the oxidation of iron. Further positive of this peak the current becomes negative once again. This occurs due to the platinum surface of the electrode being revealed at a potential were hydrogen evolution can occur. As the potential is increased further, hydrogen oxidation then results in peak (b).

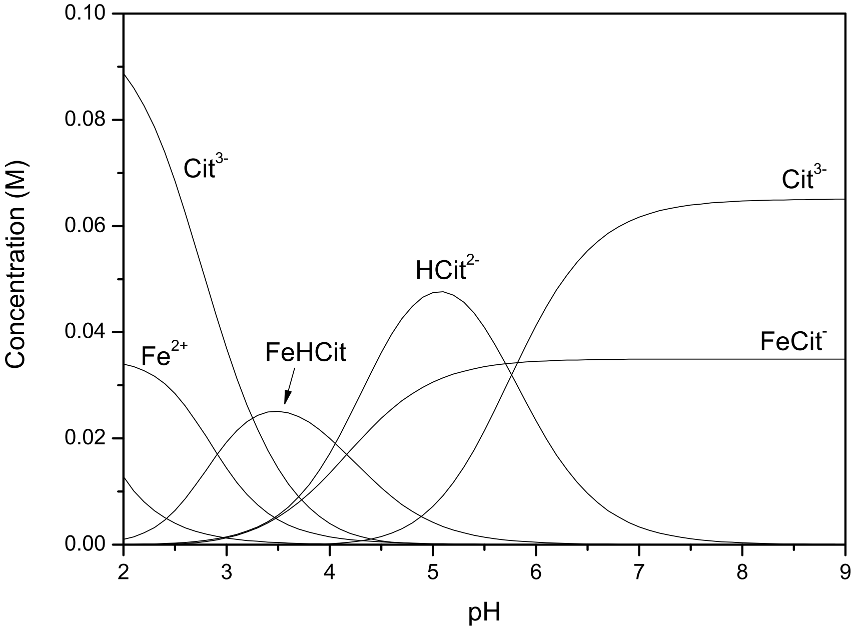

Figure 7.1: Speciation diagram showing Fe and Citrate species calculated using Visual MINTEQ. Initial [Cit^{3-}] = 0.1 M, initial [Fe^{2+}] = 0.035 M at 60 °C. Calculated from data included in tables 6.6 and 7.1.

Species	logK
Fe(III) citrate	13.13
Fe(II) H citrate	10.17
Fe(II) citrate $^{-}$	5.89

Table 7.1: Stability constants for iron citrate species from NIST database reference [55]

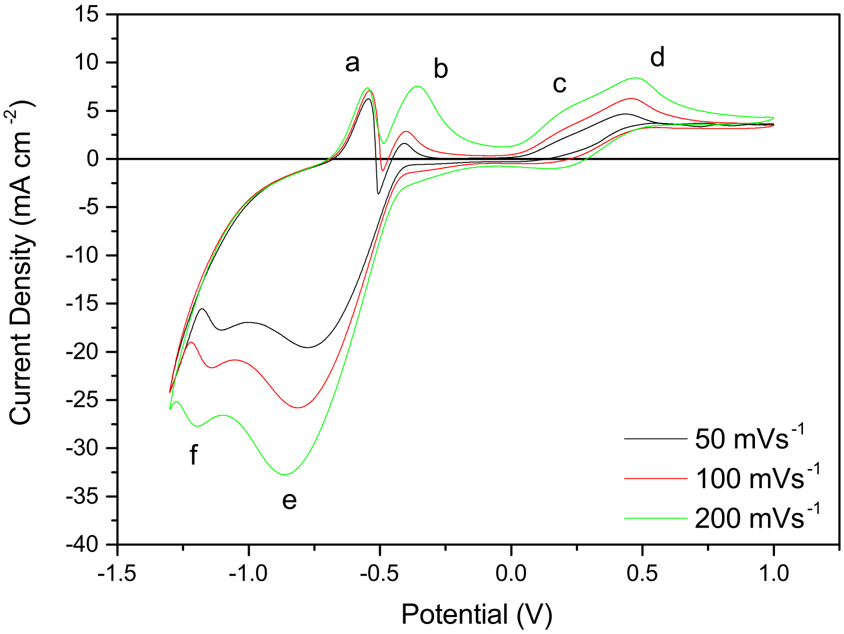

Figure 7.2: Cyclic voltammetry of an iron-citrate bath with [$FeCl_2$] = 0.035 M, [Na_3Cit^{3-}] = 0.1 M, [sodium saccharin] = 0.027 M, [SDS] = 0.0035 M. The pH was 3.0 at 60 °C. The potential was swept positive from a starting potential of 0.00 V and scanned between 1.0 V and -1.3 V. The 5th scan for each scan rate is shown.

7.2.2 Voltammetry of the Nickel-Iron-Citrate-Bath

Cyclic voltammetry was then performed on the nickel-iron citric bath (as described in Table 5.2) at 60 °C using a platinum disc electrode with area 0.387 cm^2. The potential was swept between 1.0 V and -1.0 V over a range of scan rates to avoid the deposition of nickel dominating the response. The resulting voltammagrams are shown in Figure 7.3.

To identify the main species in solution a speciation diagram was constructed and is presented in Figure 7.4. The nickel species present in the bath are largely similar to the nickel-citrate bath as described in Section 6.2. There is a large excess of Ni^{2+} and the major nickel citrate species present at pH 3 are NiHCit and NiH_2Cit^+. In this bath there is a single dominant iron (II) species of unbound Fe^{2+}.

In the voltammetry the potential was swept positive from 0.0 V. In this direction there is a single oxidation peak at 0.4 V this corresponds to the potential for the oxidation of Fe^{2+}as seen for the iron-citrate bath (Section7.2.1) and the nickel-iron-boric acid bath (Section 4.2.1). When compared to the iron-citrate bath only one peak is observed as unbound iron is now the dominant iron species in solution.

On the reverse scan a reduction peak is observed at -0.2 V. It is suggested that this peak is due the the reduction of an iron (III) citrate complex which is formed following the oxidation of the bare iron (II) species. A quantitative prediction for the shift in potential due to the formation of an iron citrate complex can be made using the thermodynamic cycle shown in Figure 7.5 and the stability constants for iron citrate species (Table 7.1).

The stability constants for iron citrate species represent the following reactions:

$$Fe(III) + Citrate \overset{K_3}{\rightleftharpoons} Fe(III)Citrate \tag{7.1}$$

$$Fe(II) + Citrate \overset{K_4}{\rightleftharpoons} Fe(II)Citrate^- \tag{7.2}$$

For these reactions the Gibbs free energy can be calculated as $\Delta G = -RT \ln K$. Using the thermodynamic cycle in Figure 7.5 it follows that

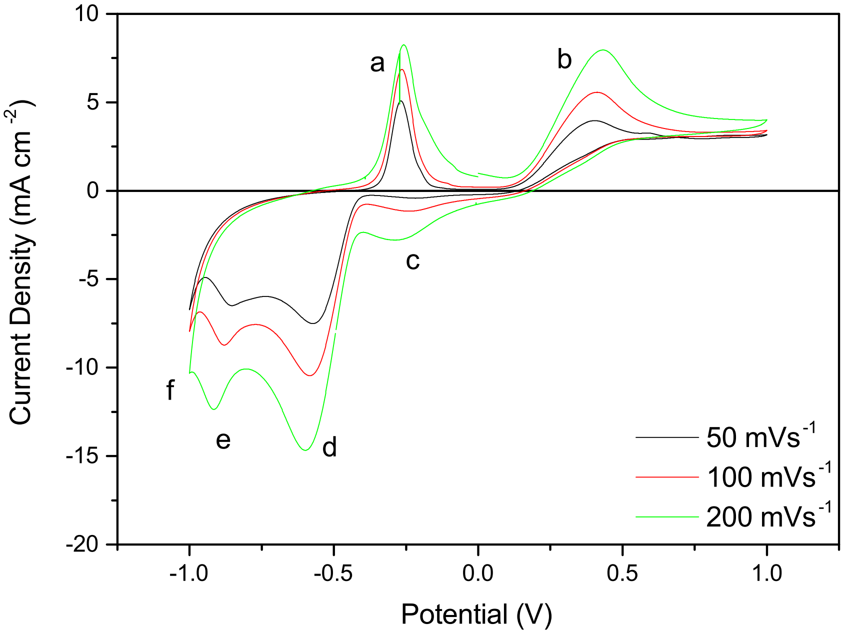

Figure 7.3: Cyclic voltammetry for the nickel-iron citric bath as detailed in Table 5.2. [NiCl$_2$] = 0.5 M [FeCl$_2$] = 0.035 M, [Na$_3$Cit^{3-}] = 0.1 M, [sodium saccharin] = 0.027 M, [SDS] = 0.0035 M. A starting potential of 0.0 V was used. The potential was then swept to 1.0 V and then to -1.0 V. The 5th scan is shown.

$$\Delta G_1^{\ominus} + \Delta G_4^{\ominus} = \Delta G_3^{\ominus} + \Delta G_2^{\ominus} \tag{7.3}$$

$$-nFE_1^{\ominus} - RT\ln K_4 = -RT\ln K_3 - nFE_2^{\ominus} \tag{7.4}$$

$$E_2^{\ominus} - E_1^{\ominus} = \frac{RT}{nF}\ln\frac{K_4}{K_3} \tag{7.5}$$

From this the change in redox potential due to the formation of a complexed iron species can be calculated using the stability constants given in Table 7.1. At 60 °C the expected shift in potential is $(5.89 - 13.13) \times 66\,\mathrm{mV} = -0.478\,\mathrm{V}$. This is in reasonable agreement with the observed shift in potential for the iron oxidation and reduction peaks. The formation of Fe(II)Citrate$^-$ species is not stable in the bath under these conditions. It is expected that iron then dissociates, predominatly to Fe^{2+}.

As the sweep progresses further negative in Figure 7.3, a peak consistent with hydrogen ion

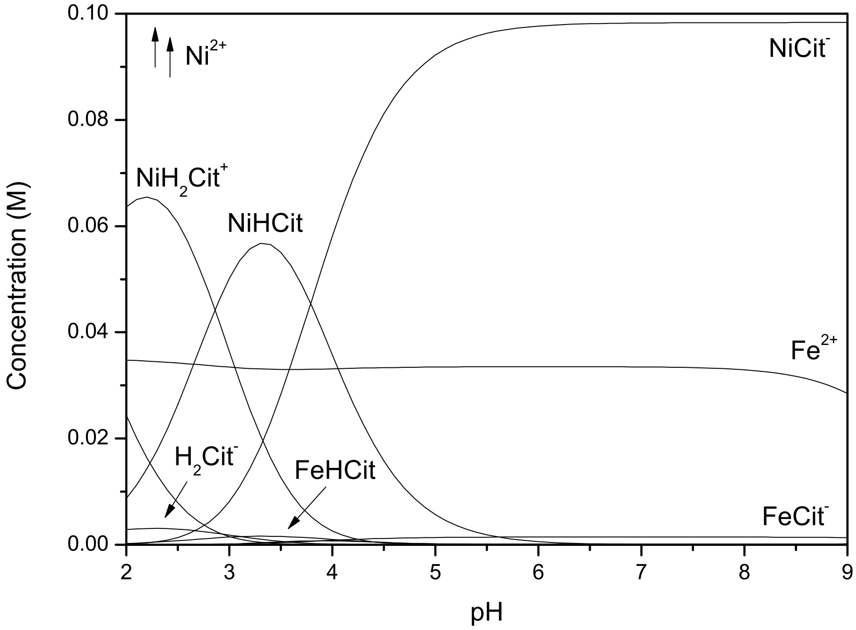

Figure 7.4: Speciation diagram showing Ni, Fe and citrate species calculated using Visual MINTEQ. Initial [Ni^{2+}] = 0.5 M, initial [Cit^{3-}] = 0.1 M, initial [Fe^{2+}] = 0.035 M at 60 °C. Calculated from data included in tables 6.6 and 7.1.

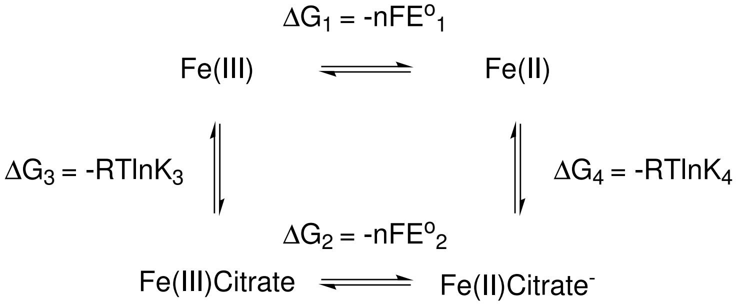

Figure 7.5: Thermodynamic cycle for iron and citrate.

reduction occurs similar to the that seen for the iron-citrate bath (Section 7.2.1) and the nickel-citrate bath (Section 6.2). A further peak is observed at -0.9 V. As the scan approaches -1.0 V nickel begins to deposit (f) before the return scan. During the scans there is little metal deposited on the electrode which results in any stripping peaks being swamped by the hydrogen oxidation peak (a) seen at -0.26 V.

As the sweep progresses further negative a peak consistent with hydrogen ion reduction occurs similar to that seen for the iron-citrate bath (Section 7.2.1) and the nickel-citrate bath (Section 6.2). A further peak is observed at -0.9 V. As the scan approaches -1.0 V nickel begins to deposit (f) before the return scan. During the scans there is little metal deposited on the electrode which results in any stripping peaks being swamped by the hydrogen oxidation peak (a) seen at -0.26 V.

The potential window of the scan was extended to see the plating and stripping of the nickel-iron films. Figure 7.6 shows the extended scan for the the nickel-iron bath and compares it to the nickel bath under the same conditions. Large plating currents are observed and a single stripping peak shows the removal of the film.

For comparison the equivalent scan for Ni only (solid lines) is shown. Larger currents were found during plating in the nickel only bath showing the currents are not simply cumulative. This demonstrates that iron has an inhibiting effect on nickel during electrodeposition.

7.2.2.1 Effects of Ni(II) Concentration in the Nickel-Iron Bath

To examine the influence of nickel concentration and bridge the gap between voltammetry of the iron bath and full nickel iron bath voltammetry was performed with intermediate concentrations of nickel. These experiments link the change in the voltammetry and enable evaluation of the interaction between nickel, iron and hydrogen. Figure 7.7 shows voltammetry performed on citric-based baths containing 10, 25, 50 and 100 mM $NiCl_2$.

At low concentrations of Ni(II) (10 mM) there is little change to the voltammetry from the iron citrate bath seen in Figure 7.2. When the Ni(II) concentration was increased to 25 and 50 mM the stripping peak at -0.5 V was found to increase in magnitude indicating the increased quantities of metal deposited.

At a concentration of 100 mM the onset of what could be considered bulk NiFe deposition was observed, particularly at the slow scan rate of 50 mV s^{-1}. The potential of the stripping peak was

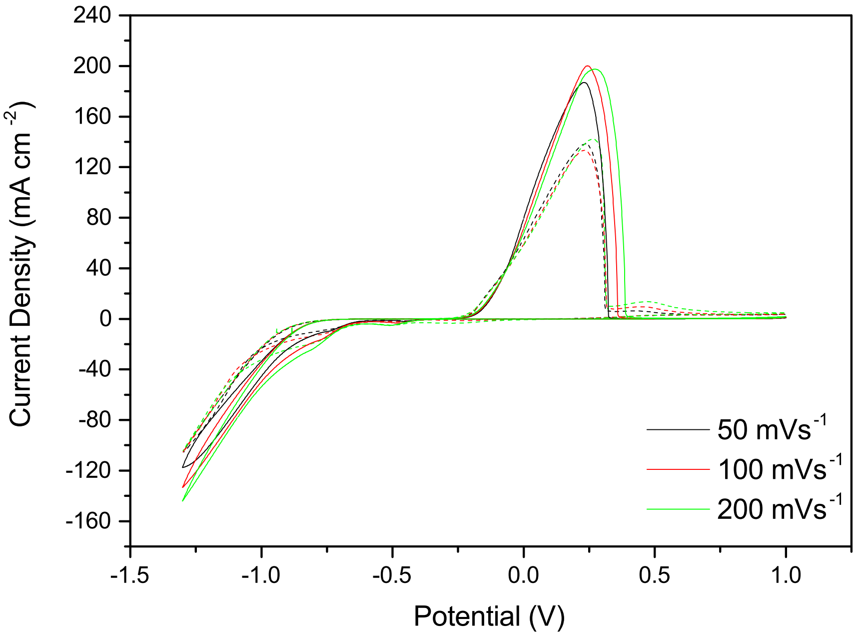

Figure 7.6: Comparison of cyclic voltammetry for the nickel (solid lines) and nickel-iron (dashed lines) citric bath. CVs were made over the extended potential window between -1.3 and 1.0 V

found to become more positive possible due to an increasing nickel content in the deposited film. Additionally, the hydrogen oxidation peak at -0.2 V became less prominent.

These experiments indicate how the reduction of hydrogen on the platinum electrode can dominate the system. In this system the deposition of both nickel and iron occurs beyond the potential at which hydrogen evolves.

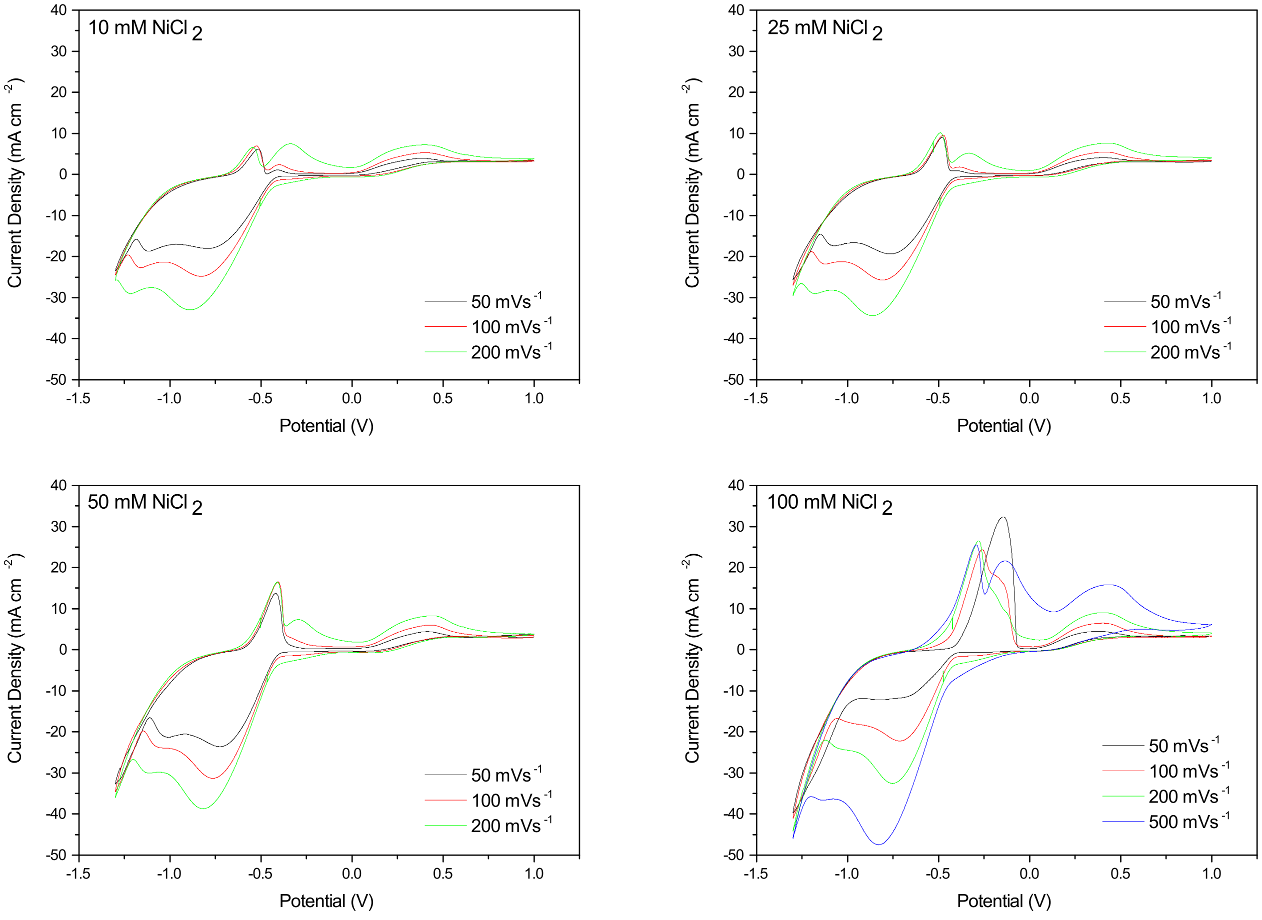

Figure 7.7: Cyclic voltammetry of nickel-iron citric bath with varying nickel concentration.

7.3 Hydrodynamic Measurements of Nickel and Nickel-Iron Films

The effects of mass transport play a significant role in the deposition of nickel-iron. Varying the hydrodynamic conditions (through agitation or under a controlled flow) can lead to changes in film composition and deposition efficiency. The RDE offers a controllable and quantifiable manner to investigate the effects of varying the plating conditions. Furthermore, the RRDE may conveniently be used to measure the composition and efficiency across a range of rotational frequencies. For an industrial setting it is important to understand the effects of flow at the electrode to enable the optimisation of the deposition parameters and to aid with troubleshooting.

In principle the RRDE can be used to determine the quantities of nickel, iron and hydrogen which are produced during the deposition process. In a simple experiment, the volume of hydrogen produced can be calculated. Nickel or nickel-iron is first deposited on to the electrode passing a known quantity of charge. The deposited film can be removed and, by measuring the amount of charge required to do so, the quantity of hydrogen evolved during deposition can be calculated. In this section, a series of experiments evaluates this method for determining film composition and deposition efficiency. Following this evaluation, the extent of the HER and film composition was examined at various rotational rates under otherwise fixed galvanostatic conditions, as would be used in a simple industrial cell.

Previous studies in boric acid based baths have demonstrated that agitation affects film composition and deposition efficiency. Rotating disc studies demonstrated that with increasing rotational frequencies the coulombic efficiency decreased. In addition it was shown that iron deposition occurred largely under mass transport control at higher current densities (20 and 30 mA cm^{-2}) and at the lower range of rotational frequencies used (100 rpm to 400 rpm) [106]. Additional studies have demonstrated that increased rotational frequencies enhance the mass transport of H^+ to the electrode and hence decrease the deposition efficiency [104, 158]. The effect on alloy composition is more complex. At low current densities there is a decrease in the iron percentage, whereas at higher current densities ($>$ 10 mA cm^{-2}), there is an increase [106]. It is also suggested that under high current densities and low rotation rates the iron deposition reaction occurs under mass transport control.

The range of rotation rates studied on the RDE was chosen to be between the rotational frequency required to maintain controlled hydrodynamic conditions and the upper, practical, limit where fast rotation rates introduced noise into the response. The Levich equations break down when the size of the hydrodynamic boundary layer approaches the disk radius. A lower limit for the rotation rate can be obtained from the condition that $\omega = 10\nu/r^2$, where ω is the rotational speed (rad s^{-1}), ν is the kinematic velocity and r is the electrode radius [111]. For an RDE with r = 0.35 cm and ν = 0.01 cm^2 s^{-1} this condition is met when the rotational frequency is 1.5 Hz. To ensure hydrodynamic control, with relevant rotational frequencies for industry frequencies between 1 and 16 Hz were used for the RDE.

7.3.1 Hydrodynamic Behavior of Nickel Deposition

Using a citric bath nickel deposits were made at room temperature (23 °C) with a current density of 20 mA cm^{-2}, to match with the optimal conditions of the NiFe bath. Plating was performed for 200 s so that the total charge passed, Q_t, was 1548 mC. Deposits were made with a rotational frequency, W, of the RDE at 1, 2, 4, 9 and 16 Hz to represent differing degrees of flow of the electrolyte. The deposits were then rinsed with de-ionised water and stripped in a solution of 0.5 M NaCl and 0.2 M HCl at 0.00 V and a fixed rotational frequency of 16 Hz to determine the efficiency of deposition.

The potential time transients for deposits at varying rotational frequencies are shown in Figure 7.8. The steady state deposition for deposition is more positive when the rotational frequency is increased indicating it is easier to deposit nickel. At 16 Hz, it is seen that the potential takes significantly longer, around 30 s, to reach this steady potential, possible due to the slow rotational frequency. To measure the fraction of charge resulting in nickel deposition and hydrogen evolution, deposits were stripped in the HCl:NaCl electrolyte and the current measured for each deposit. The charge required for stripping the entire nickel film was measured *via* integration of the *i*-t curve.

Figure 7.9 shows the charge required to remove the deposit against the rotational frequency used during deposition. Given that a known quantity of charge was used during deposition of the films (1548 mC) the remaining charge which has not been used to deposit nickel was calculated. This charge was attributed to the hydrogen evolution reaction; however, it may contain a contribution due to the formation of soluble products during deposition.

A plot of the stripping charge against the square root of the rotational frequency used during deposition is shown in Figure 7.9. The plot demonstrates a linear relationship between the quantity

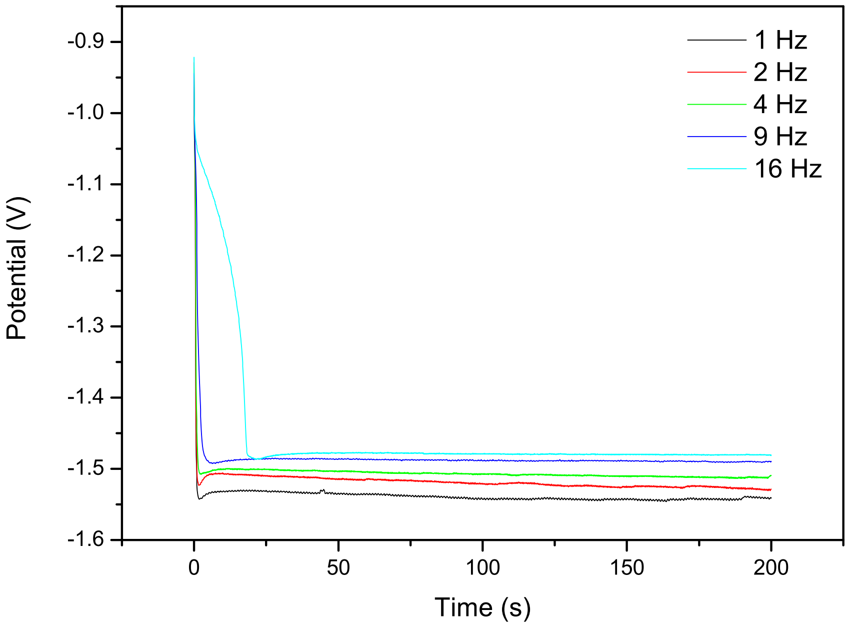

Figure 7.8: Potential-time plots for deposition of nickel from the citric bath (Table 5.2 with [$FeCl_2$] = 0 mM) at 20 mA cm^{-2} on the RDE with varying rotation frequency. Potentials were measure *vs.* SCE.

of hydrogen produced and $W^{1/2}$. This shows that, similar to the boric acid bath, increased rotational frequency enhances the mass transport of H^+ influencing the extent of the HER and decreasing the efficiency. The remaining current which cannot be supplied from the HER results in the deposition of nickel. This aptly demonstrates how the rotational frequency, or flow of species to the electrode, can affect the deposition efficiency.

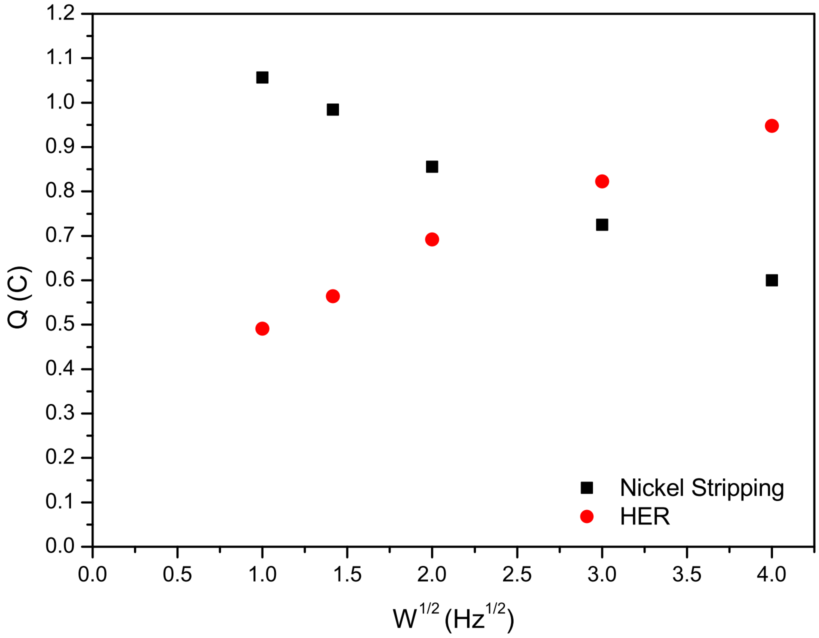

Figure 7.9: Stripping analysis for nickel films deposited at varying rotational rates (see Figure 7.8). The charge require to strip the nickel film was measured in a NaCl:HCl electrolyte at rotating at 16 Hz. Stripping was performed at 0.00 V. The stripping charge, Q, is plotted against the rotation frequency, $W^{1/2}$, used during deposition of the nickel film.

7.3.2 Detection of Iron from Nickel-Iron Films Using the RRDE

With nickel-iron films this can be taken a step further using a rotating ring disc electrode by detecting the iron removed during stripping of the electrodeposited film on the ring. Using the measured collection efficiency the quantity of iron in the deposited film can be determined. The quantity of each of these species at varying rotational frequencies can then be determined. To ensure quantitative information was obtained the behavior of the RRDE must first be assessed. A series of experiments were performed to test any potential dependance relating to the collection efficiency for iron and to ensure the minimal effects of any background currents.

On the RRDE a NiFe film deposited on the disc electrode can be oxidised to the Ni(II) and Fe(II) cations at a potential, V_1 (Equations 7.6 and 7.7) .

$$Ni_{(s)} \rightarrow Ni^{2+}_{(aq)} + 2e^- \tag{7.6}$$

$$Fe_{(s)} \rightarrow Fe^{2+}_{(aq)} + 2e^- \tag{7.7}$$

If the ring is held at a potential, V_2, where the oxidation of Fe(II) to Fe(III) (Equation 7.8) occurs then the composition of the film can be measured provided the collection efficiency is known and any other reactions are insignificant.

$$Fe^{2+}_{(aq)} \rightarrow Fe^{3+}_{(aq)} + e^{-} \tag{7.8}$$

In the following experiments nickel-iron films were deposited on to the disc of a RRDE using the citric bath (Table 5.2) at room temperature. The deposited films were then stripped in the HCl:NaCl (0.5 M NaCl and 0.2 M HCl) electrolyte. By controlling the potential the ring was used to detect iron. This was used to determine a suitable detecting potential for Fe^{2+} .

NiFe was deposited on the disc electrode at 20 mA cm^{-2} with 4 Hz rotation speed for 400 s. The solution was then swapped to the HCl:NaCl stripping solution. A background scan of the electrolyte was first performed on the platinum ring a CV was taken between 0.1 and 1.0 V on the Pt ring without stripping the deposited film. The rotation frequency was 4 Hz and a scan rate of 10 mV s^{-1} was used. The potential of the disc was then set to 0.00 V, to strip the deposited NiFe, and a CV was performed on the ring under the same conditions as described for the background scan.

Figure 7.10 shows the stripping current measured from the disc and the voltammetry performed on the ring. The stripping current was found to be consistent throughout the experiment. On the ring electrode a wave was observed between 0.1 V and 1.0 V. This wave is constant with the reaction of Fe(II) to Fe(III) ($E^{\ominus} = 0.529$ V *vs.* SCE) [129]. The background currents observed were low (10 µA) with the main feature being a wave at 0.48 V. This is most likely due to oxide formation on the platinum electrode. The currents observed during the detection of iron were found to be 25 times larger than the background. This demonstrates the mass transport limited detection of Fe^{2+} on the disc at a potential of 0.8 V and no detection of Fe^{2+} at 0.3 V.

With detecting and non-detecting potentials for Fe^{2+} established further potential step experiments were performed to confirm the detection of Fe^{2+} using a constant potential of 0.8 V. During the stripping of a nickel-iron film the ring potential was stepped between detecting (0.8 V) and non-detecting (0.3 V) potentials and is shown in Figure 7.11.

There was a large change in the ring current between the detecting and non-detecting potentials. This is consistent with detection of Fe^{2+} from the film dissolution. At the non-detecting potential there is a small background current approximately 10 % of the magnitude of the detecting current.

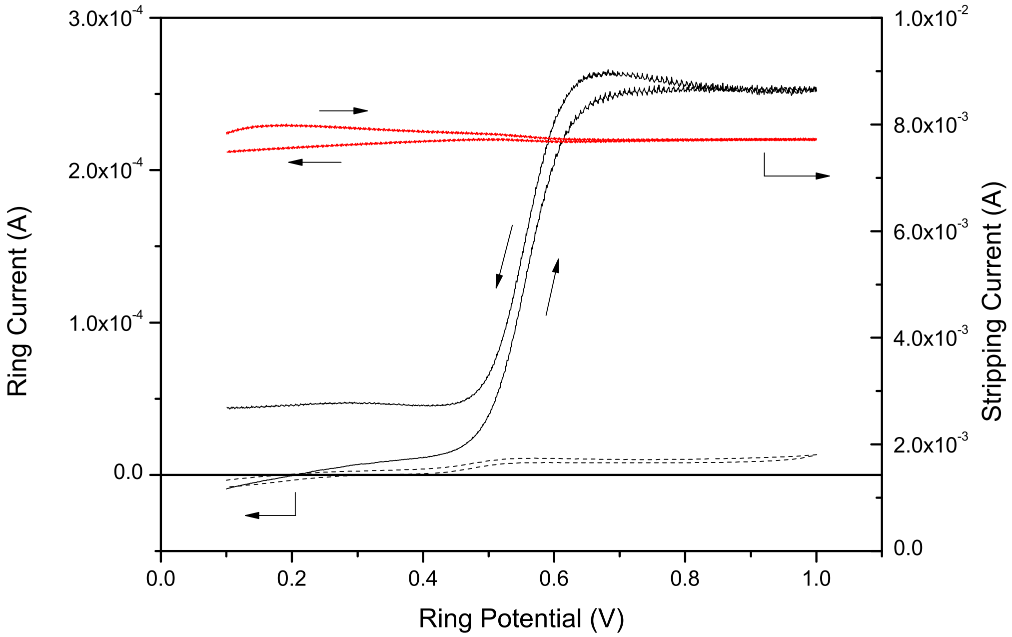

Figure 7.10: Cyclic voltammetry performed between 0.1 V and 1.0 V on the ring of an RRDE (solid black line) while stripping NiFe from the disc at 0.0 V (solid red line). A background scan of the NaCl:HCl stripping electrolyte on the ring is shown as the black dashed line. Scan rate = 10 mV s^{-1}, rotational frequency 4 Hz. Potentials were measure *vs.* SCE.

To ensure there was no bias in the detection of iron due to the stripping potential used on the disc the NiFe film was stripped during cyclic voltammetry. After the deposition of a nickel-iron film on the disc of a RRDE (400 s at 20 mA cm^{-2}, 4 Hz) the electrode was placed in the stripping solution where a CV was performed on the disc (10 mV s^{-1}, -0.5 to 0.5 V) and the ring was held at either 0.8 V (detecting) or 0.3 V (non-detecting). Figure 7.12 shows an experiment where the ring is held at a non-detecting potential. Note the scale for the ring current, i_{ring}, is 100 times smaller than for the disc current, i_{disc}. The current is essentially a baseline at 0 mA which demonstrates no background current.

Figure 7.13 shows when the ring was held at a detecting potential. An increase in current at the disc due to stripping closely resembles the increased current at the ring until the film is nearly stripped off.

The collection efficiency of the ring electrode was measured as 0.203 (see Section 3.3.1.2) therefore the composition of the film can be calculated. The current at the disc due to iron dissolution, $i_{D,Fe}$

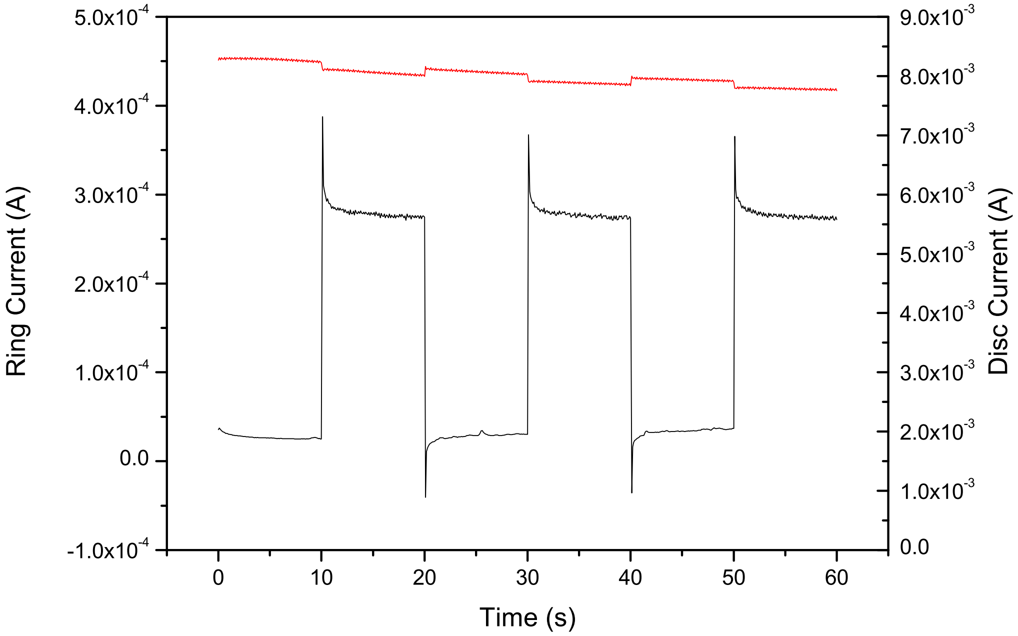

Figure 7.11: Pulsing on ring (black) between 0.3 V *vs.* SCE and 0.8 V while stripping NiFe at 0.0 V (red). Rotation frequency 4 Hz.

can be calculated taking into account the collection efficiency, N, and the number of electrons required for each reaction. As the reaction of Ni and Fe to Ni(II) and Fe(II) at the disc involves a two electron transfer and Fe(II) to Fe(III) a one electron transfer $i_{D,Fe}$ can be calculated using Equation 7.9.

$$i_{D,Fe} = (i_{ring}/N) \times 2 \tag{7.9}$$

$i_{D,Fe}$ can then be used to calculate the film composition by dividing $i_{D,Fe}$ by i_{disc} . The measured fraction of iron in the nickel-iron film is plotted against the disc potential in Figure 7.14 essentially giving a plot of film composition against thickness.

The fraction of iron in the film is measured to be approximately 0.5 ± 0.1 with a higher iron content in the upper portion of the deposited film. The initial stages of the stripping voltammetry are non-representative of the film due to the transit time it takes for species to flow to the ring electrode. For this RRDE and a rotation frequency of 4 Hz the transit time should be approximately 1-2 s.

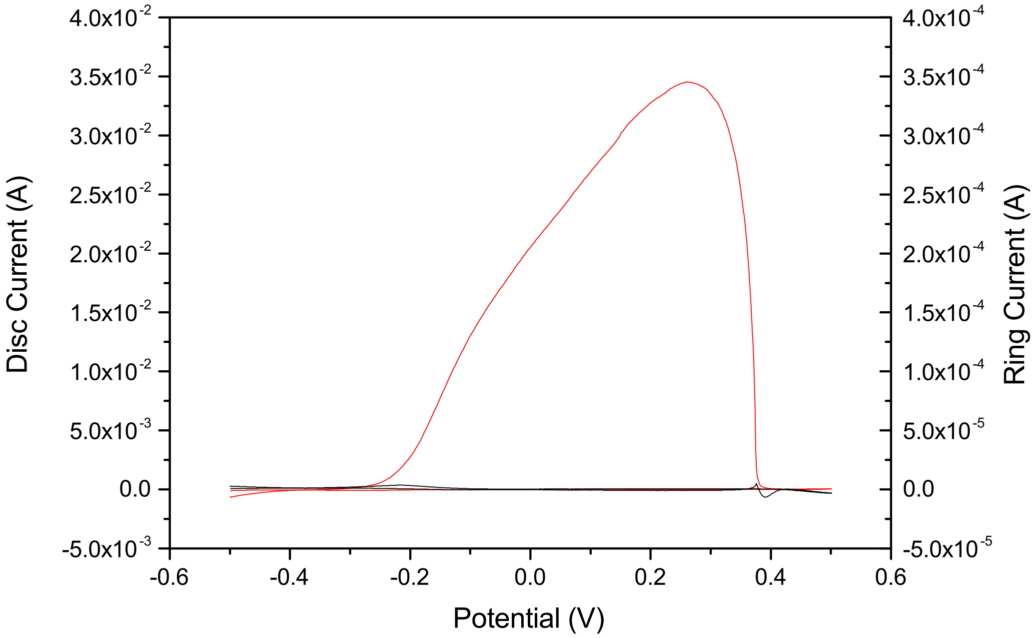

Figure 7.12: CV on disc (red) while detecting at 0.3 V *vs.* SCE at the ring (black). Scan rate = 10 mV s^{-1}, rotation frequency 4 Hz.

Additionally $i_{D,Fe}$ and i_{disc} are small at these potentials resulting in measurement artifacts and erroneous composition measurements.

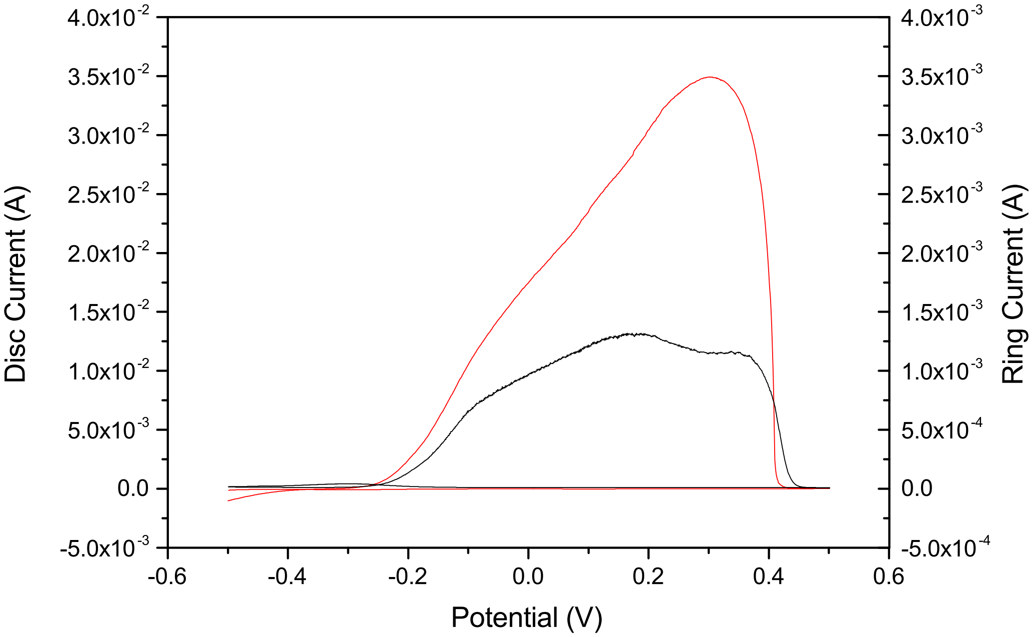

Figure 7.13: CV on disc (red) while detecting Fe(II) at 0.8 V *vs.* SCE at the ring (black). Scan rate = 10 mV s^{-1}, rotational frequency 4 Hz.

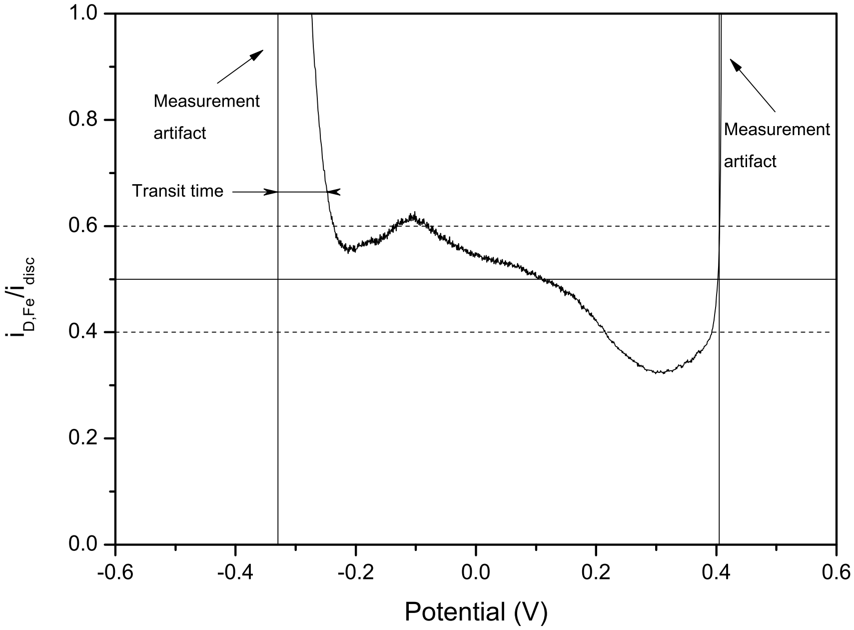

Figure 7.14: Calculated film composition from $i_{D,Fe}/i_{disc}$ during stripping voltammetry of a NiFe film. Scan rate = 10 mV s^{-1}, rotational frequency 4 Hz.

7.3.3 Measurements of Film Composition on the RDE Using XRF

To confirm the electrochemical analysis of the nickel-iron films an XRF analysis was performed on films deposited on the disc. Measurements were taken to spatially investigate the thickness and composition of the alloy deposited. In addition measurements were made at elevated temperature where optimal plating performance has been demonstrated (see Section 5.8).

In this series of experiments films were deposited at 20 mA cm^{-2} for 200 s from the citric bath described in Table 5.2. The plating temperature was varied between 25 and 60 °C in a stagnant solution and also under rotation of 4 Hz. XRF was used to determine the composition and thickness at points from the center of the disc to the outside at intervals of 30 mils (1 mils = 1/1000 inch). The spot size for the X-ray beam was 2 mils and the collection time was 60 s. Figures 7.15 and 7.16 show the variation in thickness and composition across the films measured with XRF. The overall composition of the films was calculated from the composition and thickness measurements taking into account the radial distribution of the deposits. The average for thickness and composition across the electrode is shown in Table 7.2. Faraday's law predicts a thickness for a $Ni_{80}Fe_{20}$ film deposited for 200 s at 20 mA cm^{-2} as 1.76 μm.

Most of the films (with the exception of 60 °C, 0 Hz) show an increase in thickness towards the outside of the disc. The film thickness and hence the efficiency at 60 °C is greater than that at 25 °C. There are also changes in the composition across the film particularly in the 4 Hz at 25 °C and 0 Hz at 60 °C. Having conditions with no rotation and hence no flow of electrolyte across the solution may result in the local depletion of reactive species at the electrode affecting the composition. Having rotation and hence a laminar flow across the electrode may remove or displace reactive intermediates from where they are generated.

It is reassuring that the composition of the nickel iron film deposited at 25 °C and 4 Hz is similar to that measured using the RRDE. Using XRF the composition is measured as 50.2 % Fe. For the RRDE the iron content was largely in the range of 40 to 60 % iron (see Figure 7.14).

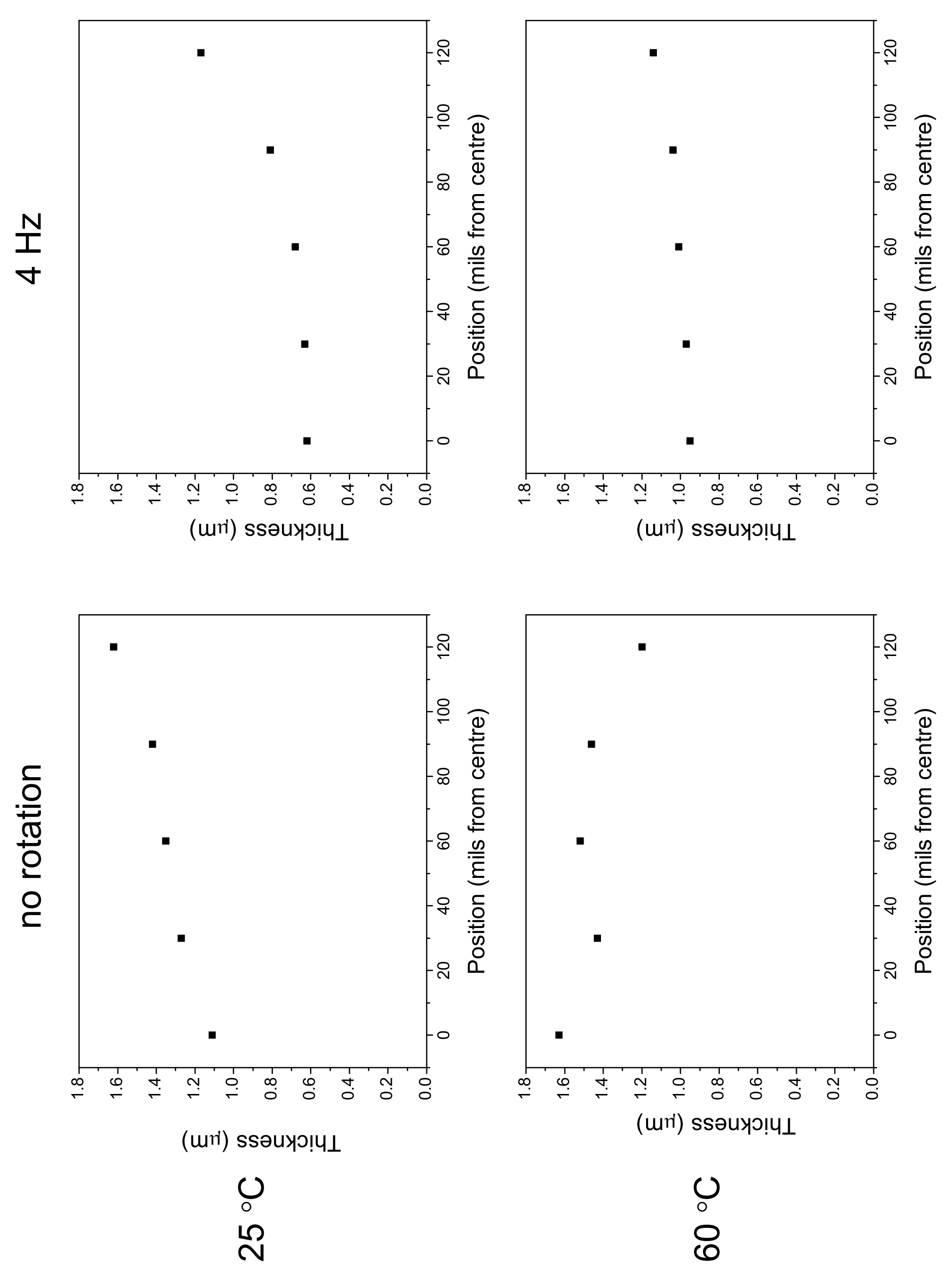

Figure 7.15: Thickness of NiFe films measure by XRF under no rotation (left) 4 Hz rotation (right) and at 25 °C (upper) and 60 °C (lower).

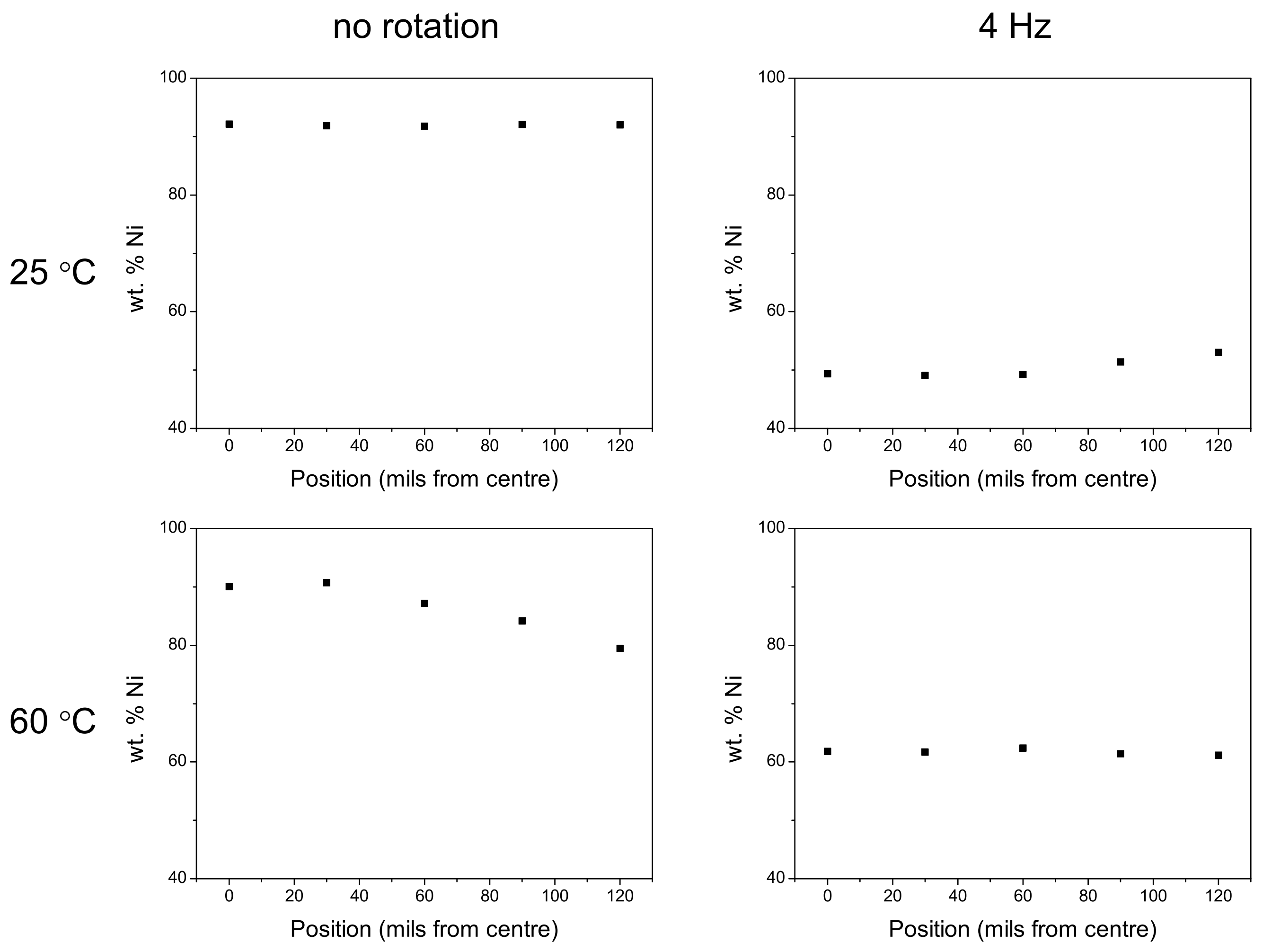

Figure 7.16: Composition of NiFe films measure by XRF under no rotation (left) 4 Hz rotation (right) and at 25 °C (upper) and 60 °C (lower).

Deposition Conditions	Average Thickness / µm	Average Composition / % Ni	Efficiency / %
no rotation, 25 °C	1.35	91.9	77
4 Hz, 25 °C	0.75	50.2	43
no rotation, 60 °C	1.46	86.7	83
4 Hz, 60 °C	1.01	61.7	57

Table 7.2: Summary of film thickness and composition measured from varying conditions.

7.3.4 Hydrodynamic Behavior of Nickel-Iron Deposition

The experiments so far demonstrate that quantitative information can be obtained using the RRDE. It was also shown that there is minimal influence from background currents when detecting iron from the deposits. It follows that this technique is appropriate to study the influence of rotational frequency on the deposition of NiFe films from the citric bath. Using the controlled hydrodynamic conditions provided from the RRDE the quantity of nickel, iron and hydrogen generated during deposition of the films can be measured.

NiFe films were deposited on the disc of a RRDE from the citric bath detailed in Table 5.2. Deposits were made at room temperature passing a current density of 20 mA cm^{-2} for 200 s ($Q_t = 1548\ mC$) using a range of rotational frequencies. The deposited films were then stripped at a potential of 0.1 V in the HCl:NaCl electrolyte. The ring electrode was set at a potential of 0.8 V to detect the presence of Fe^{2+}as the deposited NiFe film was removed.

The total charge required to remove the film from the electrode, Q_{disc}, was measured by the integration of i_{disc} against time. Using i_{ring} and Equation 7.9 the proportion of charge require to remove iron in the film, $Q_{d,Fe}$ was also calculated. The quantity of nickel and iron in the film was calculated from Q_{disc} and $Q_{d,Fe}$. The remaining charge passed ($Q_t - Q_{disc}$) was attributed to the HER. Figure 7.17 shows the fraction of nickel, iron and hydrogen produced during deposition of the alloy at different rotational frequencies.

Across these rotational frequencies the HER was found to dictate the overall efficiency of nickel-iron deposition. The close to linear type response to $W^{1/2}$ for the HER indicates that it is somewhat under conditions of mass transport control. At low rotational frequencies the deposition of nickel is favoured in contrast with the HER. At increased rotational frequencies the film composition tends toward a constant ratio approximately 60 % iron. (Section 7.3.3).

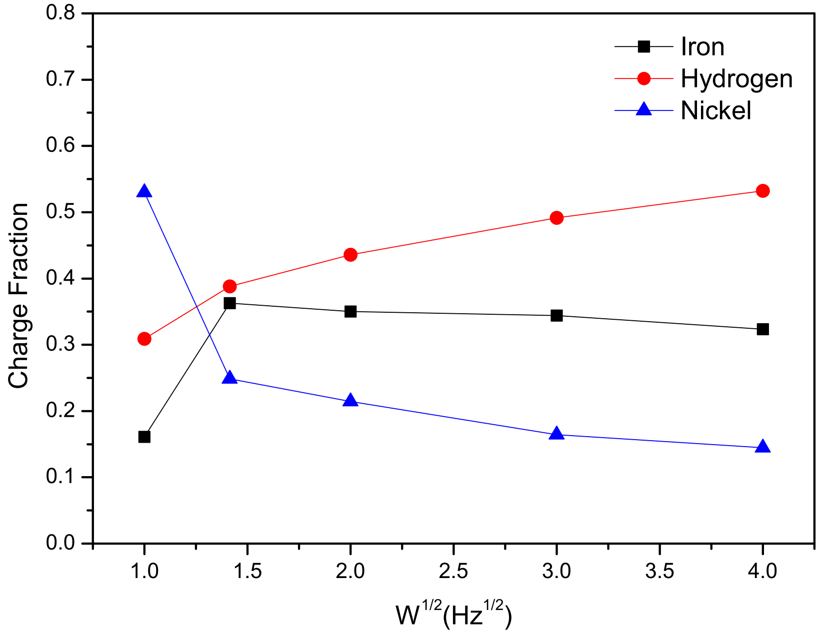

Figure 7.17: Calculated fraction of the charge passed for nickel, iron and hydrogen during the deposition of nickel-iron films. The NiFe films were deposited from the citric bath detailed in Table 5.2 at a pH of 2.8 at room temperature for 200 s using rotation frequencies of 1, 2, 4, and 9 and 16 Hz.

In principle this type of experimental method could be used to systematically assess the efficiency and film composition against a range of variables. For example, by using a fixed rotational frequency the effects of temperature, pH or iron concentration could be examined.

7.4 Films on Copper Electrodes

So far in this chapter nickel-iron films have been deposited on platinum electrodes. In practical applications the films are deposited on an alternative material as a seed layer. A common seed layer used for electrodeposition in microfabrication is copper. In this section therefore nickel-iron films were deposited onto copper 1 cm × 1 cm square electrodes to examine the behavior on this seed layer.

Blanket films were deposited galvanostically from the citric bath (Table 5.2) at currents between 10 and 50 mA cm^{-2}, passing an overall charge of 7200 mC. The temperature of the bath during

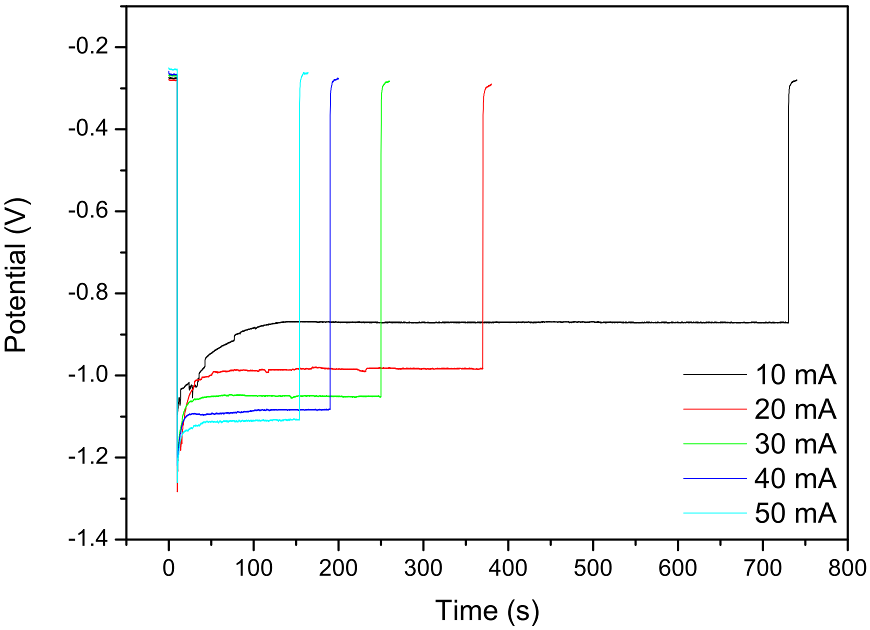

Figure 7.18: Potential-time plots for deposition of NiFe films from the citric bath on Cu electrodes.

deposition was 60 °C and agitation was provided using a magnetic stirrer rotating at 750 rpm. The composition of the deposits was measured using XRF across 5 locations on the film.

Potential-time plots are shown for the deposition of the nickel-iron films in Figure 7.18. An increased reducing potential is required to deposit at the same current density for the citric bath when compared to the boric bath. At larger current densities an increasingly negative potential is required as expected. A plot of the $|\ln|(i)$ against the potential gives a linear plot ($R^2 = 0.99$) with a gradient of -6.36 ± 0.32 V^{-1}. This is comparable with the equivalent experiment depositing from the boric acid bath where the gradient was found to be -6.87 ± 0.46 V^{-1}.

The nickel content was measured as a function of the current density applied. Figure 7.19 shows the the average iron content is at a maximum between 20 and 30 mA cm^{-1}. This maximum coincides with the desired composition for a Permalloy film ($Ni_{80}Fe_{20}$) The error bars show the standard deviation of the composition across the electrode therefore indicating the variation of composition across the square. With increasing currents the variation in composition increases.

Additionally, films were deposited on the copper electrodes at a current density of 20 mA cm^{-2} for times from 60 to 480 s. The thickness of the films at the edge of the electrode was measured

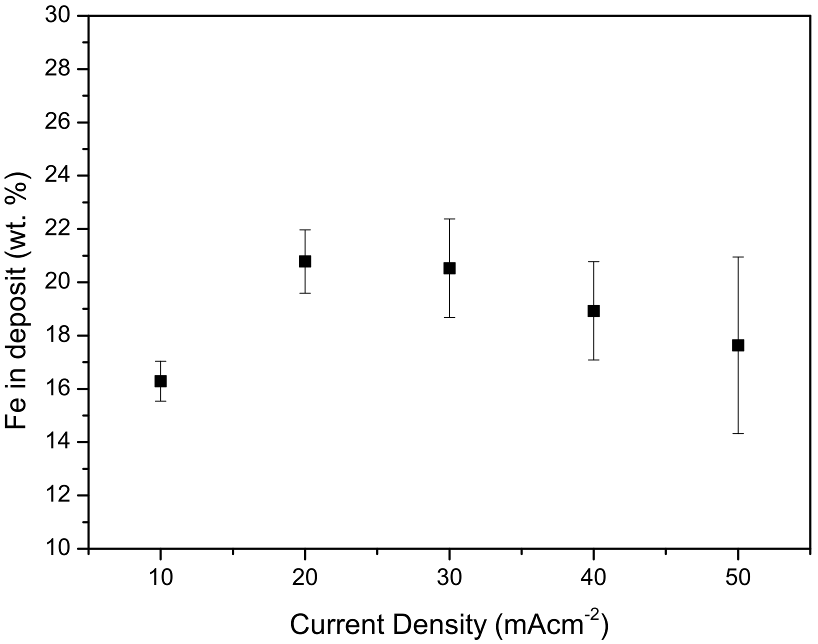

Figure 7.19: Iron content in nickel-iron deposits on to copper square electrodes from the citric bath.

using a Dektak surface profiler. The edge step height is seen to increase linearly with the charge passed as shown in Figure 7.20. The linear nature of this plot indicates there is no variation in the efficiency with the duration of deposition, ideal for deposition of thick films. The deposition rate for nickel-iron, assuming 100 % efficiency, was calculated as 356 nm C^{-1} cm^{-2} or 427 nm min^{-1} using Equation 3.7 ($\rho_{\mathrm{Ni_{80}Fe_{20}}} = 8.447$ g cm^{-3}) [130]. The observed deposition rate for these films was 442 ± 9 nm C^{-1} or 529 ± 11 nm min^{-1}. Edge effects were found to be prominent resulting in a thicker film at the edge of the electrode. This may be due to the additional diffusion of material to the edge of the electrode. Furthermore the density of the film may be less than for bulk nickel-iron due to its polycrystalline nature and the presence of trapped voids in the film.

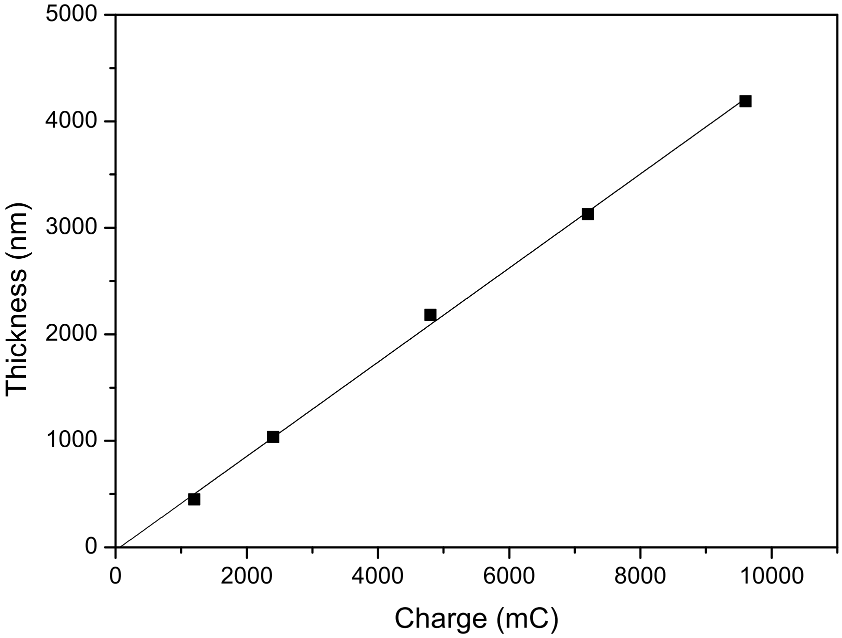

Figure 7.20: Variation of thickness for NiFe deposit with magnitude of charge passed during deposition

To confirm this SEM images were taken of the deposited NiFe films to examine the surface structure. Figure 7.21 shows images of films deposited at different current densities. On the right hand side of the micrographs is the electrodeposited nickel-iron film, on the left hand side is the sputtered titanium layer deposited as part of the Ti-Cu-Ti seed layer in these devices. The nickel-iron film appears in general to have a smooth, flat surface. Image (d) shows the a film at a greater magnification where some surface texture is apparent.

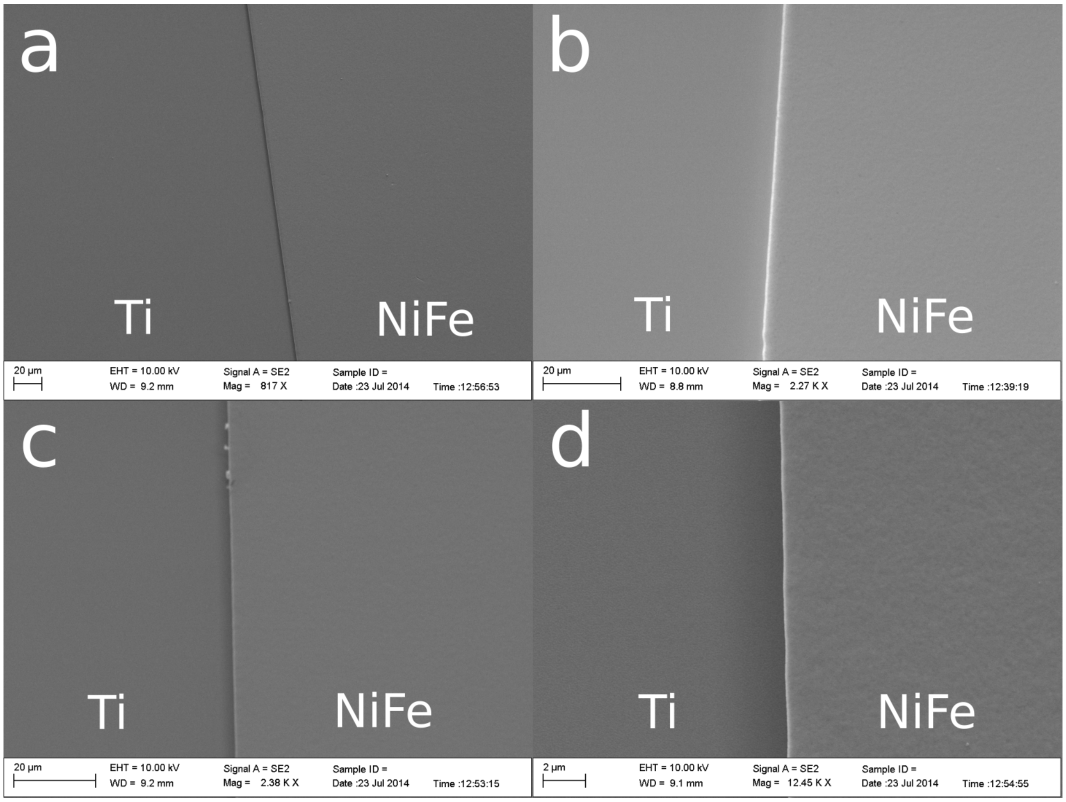

Figure 7.21: SEM images of NiFe films (right hand side of images) deposited at (a) 10 mA, (b) 20 mA, (c) 50 mA, (d) 50 mA (increased magnification).

7.4.1 Fe(III) as a Contaminant in Nickel-Iron Deposition Baths

The potential air oxidation of iron (II) to iron (III) is of concern in the deposition bath for nickel-iron alloys. Additionally, commercial Fe(II) salts may contain significant amounts of Fe(III). Also, Fe(III) may be produced during plating by reaction at the counter electrode. The presence of iron (III) compromises the stability of the bath due to the formation and precipitation of iron (III) hydroxide [33]. It is therefore interesting to probe the effects of Fe(III) in the bath.

Previously complexing agents such as 5-SSA and citric acid have been added to a boric acid based deposition bath to inhibit precipitation of the oxidised iron (III) species [74, 75, 77]. Citrate is a well-known chelator for iron (II) and (III). With it's high stability constant (see Table 7.1) iron (III) is expected to be present as the 1:1 iron-citrate complex Fe(III)Cit.

To test the stability of the citric NiFe plating bath deposits were made on 1 cm^2 square copper electrodes. Using both the boric and citric baths for comparison (as described in Table 8.1) volumes of 0.1 M $FeCl_3$ were added to increase the concentration of Fe(III) in the bath. Galvanostatic deposition was performed at a current density of 20 mA cm^{-2} for 360 s at a pH of 2.8 and a temperature of 60 °C. Agitation was provided by a magnetic stirrer at 750 rpm.

Figure 7.22 shows the potential-time plots measured at different Fe(III) concentrations. As expected, the open-circuit potential measured before and after plating becomes less negative with increasing Fe(III) content for both baths but the range of deposition potentials is much narrower from the citric bath when compared to the boric bath. This shows that Fe(III) has a smaller effect on the citric bath than the boric bath. It was observed that a brown/orange precipitate, assumed to be iron oxide, was present in significant quantities after deposition from the boric bath, whereas no precipitate was seen in the citric bath.

Images of the deposits were taken to observe the surface after deposition (Figure 7.23 and 7.24). For the boric bath it was found that the quality of the surface deteriorated rapidly with an increase in Fe(III) content. The appearance of deposits from the citric bath were found to be dependent on the quality of the underlying seed layer. The appearance of circular type artifacts in deposits from the boric bath suggests the production of hydrogen bubbles on the surface during deposition.

This demonstrates a benefit of the citric bath. The increased stability of the citric bath to the presence of iron (III) may result in a longer lived deposition bath therefore requiring less frequent replacement.

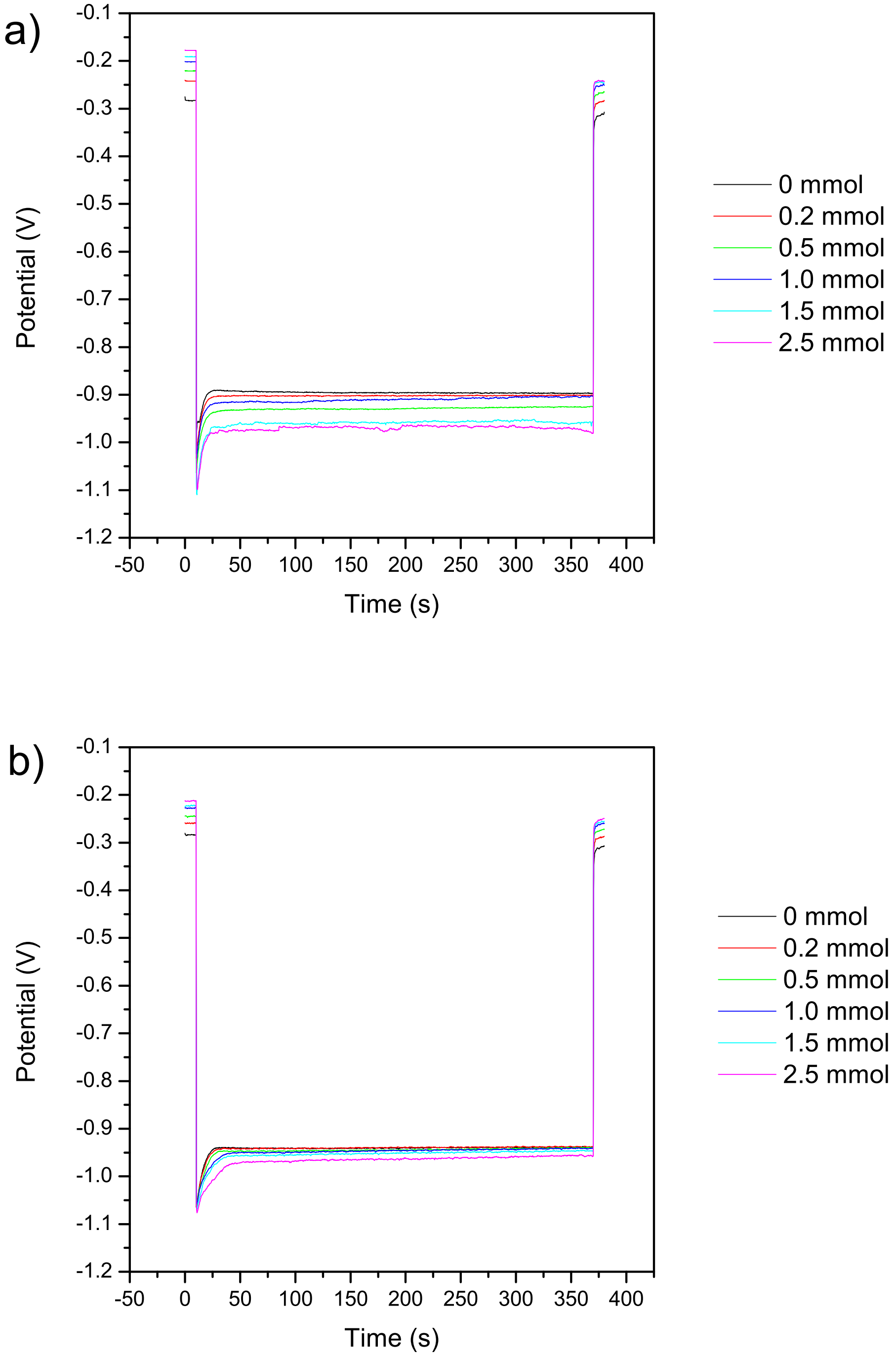

Figure 7.22: Potential-time plots for the galvanostatic deposition of nickel-iron films from a) a boric acid bath and b) a citric bath, both described in Table 8.1. The concentration of $FeCl_3$ in each bath was increased as shown. Deposits were made at a current density of -20 mA cm^{-2} for 360 s at a pH of 2.8 and a temperature of 60 °C. Agitation was provided by a magnetic stirrer at 750 rpm.

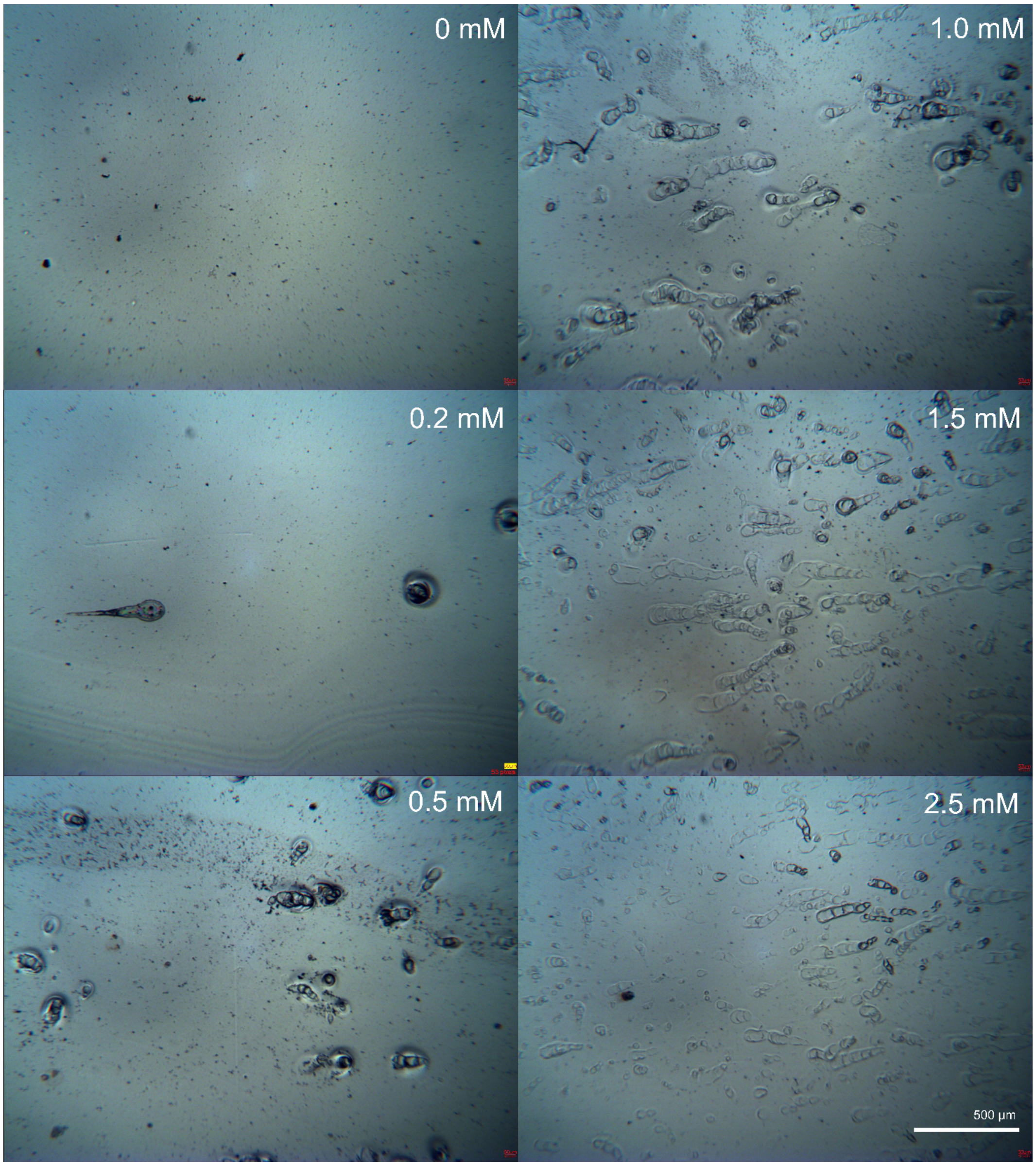

Figure 7.23: Optical images for films deposited for the boric acid based nickel-iron bath in Figure 7.22 (a) containing the stated concentrations of $FeCl_3$.

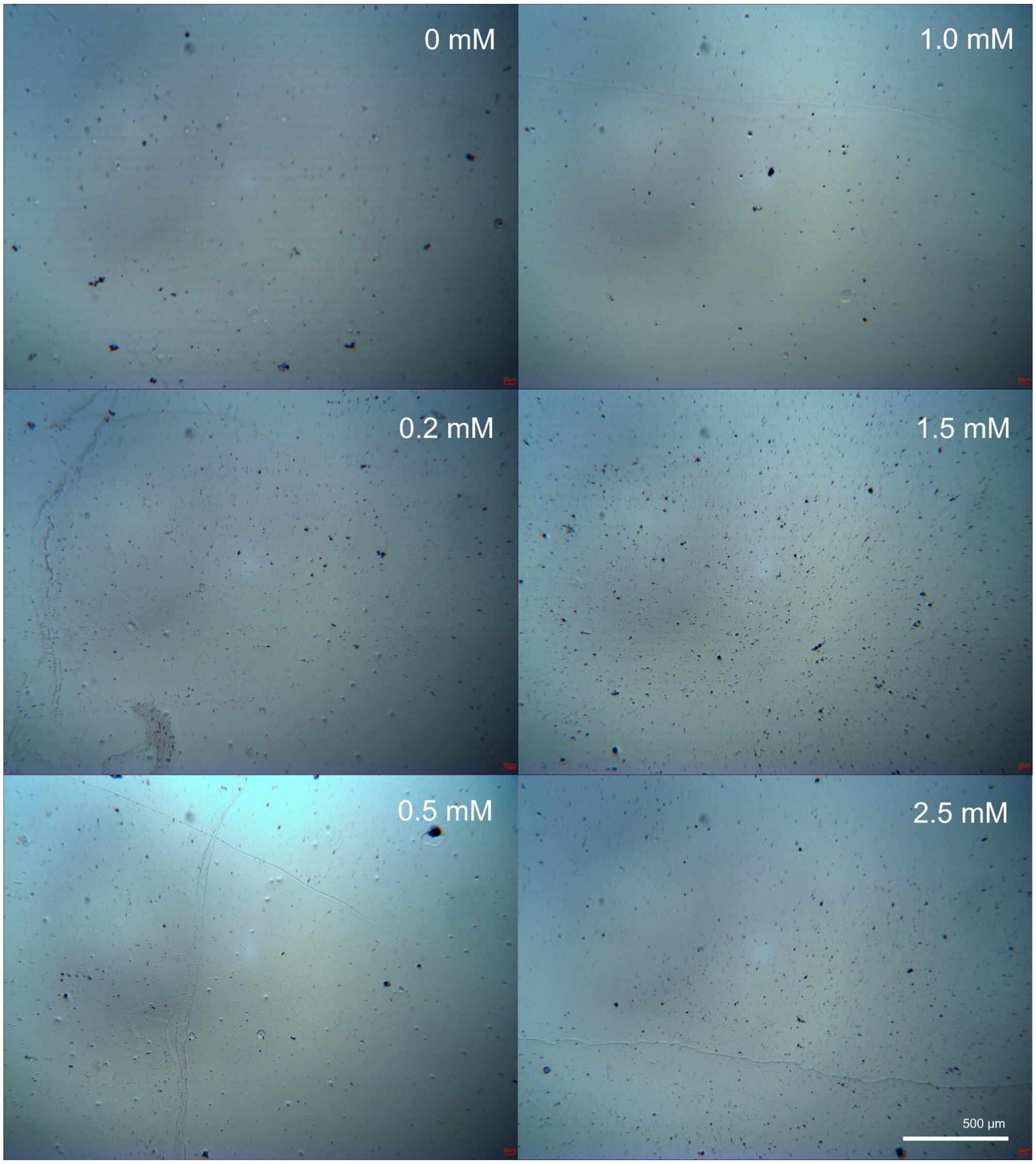

Figure 7.24: Optical images for films deposited for the citric based nickel-iron bath in Figure 7.22 (b) containing the stated concentrations of $FeCl_3$.

7.5 Conclusions

The behavior of the citric based nickel-iron bath has been investigated using cyclic voltammetry. The importance of speciation for nickel and iron to interpret the voltammetry was demonstrated. It was shown that due to the large excess of nickel (II) ions in the citric bath iron (II) is present unbound from citrate. Additionally the role of citrate as chelator for iron (III) was illustrated in the voltammetry. This role was then demonstrated to increase the bath tolerance to additional iron (III) species which may be present in commercial baths due to air oxidation or contamination.

The RRDE was shown to be an effective tool for measuring the efficiency and composition of electrodeposited nickel-iron films. This tool may be used to assess a range of variables present in the deposition of nickel-iron films. In this work the effects of rotational frequency on nickel and nickel-iron deposition was assessed. Using the RRDE it was found that the hydrogen evolution reaction seems to play a significant role in determining the alloy composition and deposition efficiency. For the deposition of nickel it was shown that the generation of hydrogen is under mass transport control. For the deposition of nickel-iron the effects of mass transport dominate the extent of the hydrogen evolution reaction and hence the overall efficiency of nickel-iron deposition.

Nickel-iron films were deposited from the citric bath onto copper electrodes to replicate blanket deposition as used in MEMS devices. With control of the temperature and agitation NiFe films were deposited at various current densities showing control of the deposit composition. Thick (up to 5 μm) films were deposited, only limited by the photoresist thickness, and the relationship to charge passed shown to be linear, constant with Faraday's law. A deposition rate of 529 ± 11 nm min^{-1} was measured for deposits made at current densities of 20 mA cm^{-2} which successfully produced the Permalloy composition.

Chapter 8

Nickel-Iron Films from Boric Acid and Citric Acid Baths

8.1 Motivation

In previous chapters the electrochemistry of a citric based nickel-iron electrodeposition bath was investigated and with this knowledge the deposition conditions were optimised. With a view to replace boric acid based baths for the deposition of NiFe films it is important to characterise and compare key properties of the electrodeposited films. In this chapter comparisons are made between deposits made from the established boric acid based bath and the optimised citric bath from this work developed in Chapter 5.

One of the main properties focused on in this work is the alloy composition. A change in composition produces a major effect on the physical properties of the film. Importantly, the magnetic properties (*e.g.* permeability, magnetostriction, thermal expansion coefficient, *etc.*) are particularly dependent on the film composition. For example, the composition with the highest relative permeability and where there is zero magnetostriction is approximately $Ni_{80}Fe_{20}$, whereas the lowest thermal expansion coefficient is found for the Invar composition ($Ni_{36}Fe_{64}$) [20]. It follows that the uniformity of the deposit composition is important for device manufacture. Little variation in the composition or thickness across the deposits is also desired to ensure reproducibility in the film behavior.

As a magnetic alloy, arguably the most important properties are the magnetic behavior of the films.

A B-H hysteresis looper was used to measure these bulk magnetic properties of the film including the saturation magnetisation, permeability and coercivity. Comparisons were made between the films deposited from the two types of plating bath.

For use in power applications, for example as an inductor, the electrical resistance of the deposits is also of great importance as it affects the behavior and design of any working device. Ensuring the resistance of films deposited from the new bath is similar to that of films deposited from the boric bath is important if citrate is to be used as a direct replacement. This has also been measured using test structures.

8.2 Deposition onto Test Structure Electrodes

To replicate bottom up filling of lithographically patterned devices, test structure chips were fabricated (as detailed in Section 3.2.4) and used to characterise the deposition of nickel-iron films. The composition of the films was measured spatially across these electrodes and the surface profile was also measured to give an indication of the variation across the deposit. In addition, these electrodes enabled the evaluation of the strain in the film (using the rotating arm test structures) and the measurement of sheet resistance (using the Greek cross test structures).

These experiments show a comparison of two different plating baths, an established boric acid bath and the optimised citric bath. The baths used throughout this chapter to deposit nickel-iron films are described in Table 8.1. Deposits were made with agitation from a magnetic stirrer (at 750 rpm) and at a temperature of 60 °C. The bath pH was adjusted with HCl to obtain a pH of 2.8 at 60 °C.

Prior to deposition on the test structure electrodes the copper surface was immersed in 5 % sulfuric acid to remove the native oxide. The current density used to deposit the films was 20 mA cm^{-2} for 360 s. This current density provided a target thickness of 2.56 µm assuming 100 % coulombic efficiency and uniform deposition.

Potential-time plots for deposition from the citric and boric baths are shown in Figure 8.1. The spikes in potential are associated with hydrogen evolution and the agitation from the magnetic stirrer. For the citric bath a steady potential is reached of approximately -0.95 V *vs.* SCE. The OCP after deposition is observed to be lower than prior to deposition this is indicative of a change in metal surface, *i.e.* going from electrodeposition on the copper seed layer to a nickel-iron alloy. For the boric acid bath, similar behavior was observed. The steady state deposition potential was

Chemical	Concentration / g L^{-1}	
	Citric Bath	Boric Bath
$NiCl_2.6H_2O$	110	110
$FeCl_2.4H_2O$	7	9
$Na_3Cit.2H_2O$	30	-
H_3BO_3	-	25
Sodium Saccharin	5	2
SDS	0.01	0.01

Table 8.1: Comparison of boric acid based and citric based electrodeposition baths for nickel-iron.

measured at a less negative potential, -0.88 V. There also appears to be a shorter transition time to achieve this potential. All deposits appeared bright and reflective to the eye.

8.3 Composition and Uniformity

The composition of the deposited samples was measured using X-ray fluorescence. Uniformity between individual electrodes and consistency between deposits is important to demonstrate reproducibility. The composition across the electrode was measured at 5 points to assess the variation. Figure 8.2 shows the composition of the nickel-iron film deposited onto the test structure electrodes from the citric bath. The average composition across the five citric samples was $Ni_{78.1}Fe_{21.9}$ (with a standard deviation of 1.4 %). The average composition of films from the boric bath was measured as $Ni_{80.2}Fe_{19.8}$ (with a standard deviation of 1.0 %).

The photoresist was removed and the surface profile across the second row of structures (as shown in Figure 8.3) was measured to examine the thickness and uniformity of deposits across the structures. An even and level fill is required for use in microfabrication. Low roughness on the surface is also favourable to reduce the time required for post-deposition polishing which may be required before subsequent processing steps.

Figure 8.4 shows the surface profile across the structures for deposits from the citric bath. The thickness of the deposits was measured to be around 2200 nm which corresponds to an efficiency of approximately 86 % for $Ni_{80}Fe_{20}$. The pointer arms were the same height as the bulk material, showing there is no preferable deposition to smaller trenches or to large areas. The deposits were

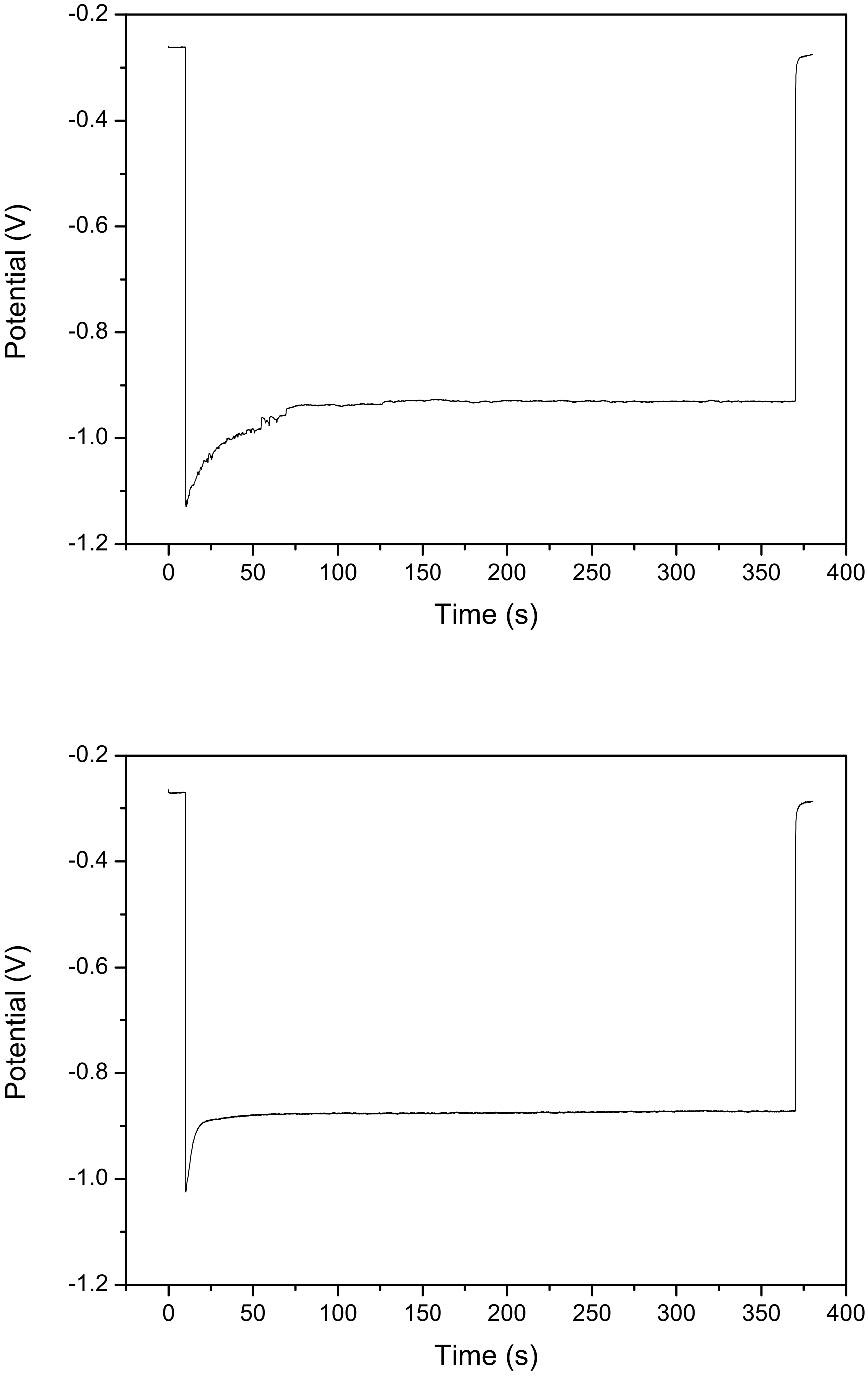

Figure 8.1: Typical examples for potential-time plots of depositing NiFe from the citric bath (top) and the boric acid bath (bottom).

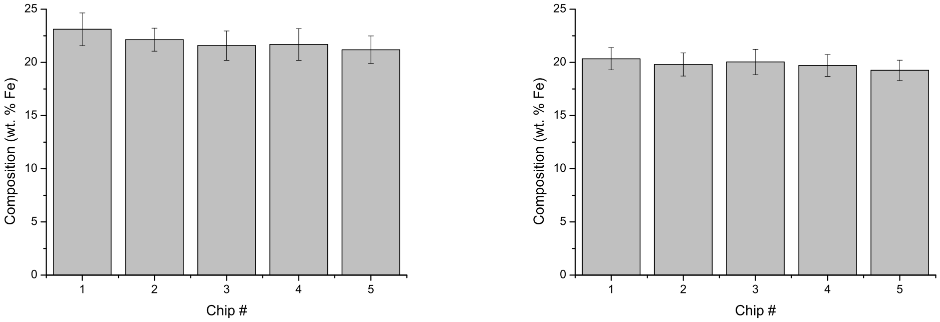

Figure 8.2: Composition of NiFe films deposited from the citric bath (left) and the boric acid bath (right). Error bars shown are calculated from the standard deviation of the composition from a single test structure electrode.

reasonably level, even where there may be enhanced diffusion of species to the edges, which could increase the deposit thickness. Thicknesses were seen to be consistent across the multiple samples.

The general shape of the deposits is as desired. Figure 8.5 shows the equivalent surface profiles of deposits from the boric acid bath. For the deposit from the boric bath an anomalous protrusion was found on one of the test structures. This may be due to dirt on the electrode. The RMS roughness of the deposits was measured to be 4.2 ±0.8 nm from the citric bath and 7.5 ±1.9 nm from the boric bath. Otherwise there is no major recognisable difference between deposits from the two baths. The thickness of the films throughout remain 2200 nm indicating the same efficiency for the boric and citric bath.

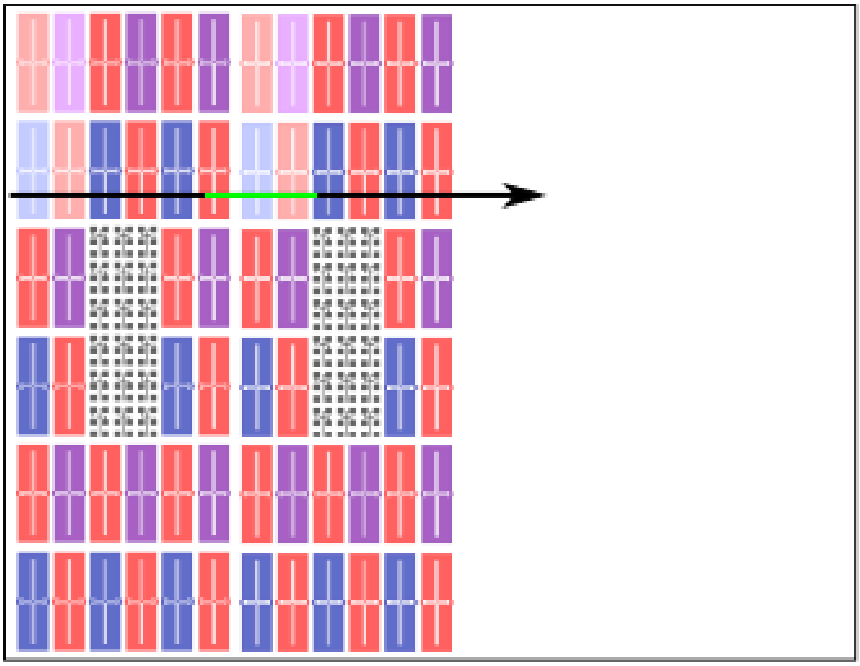

Figure 8.3: Location of surface profile measurements made on the test structure chips. Measurements were made in the direction of the arrow. The green portion of the line indicates the location of the structures portrayed in figures 8.4 and 8.5.

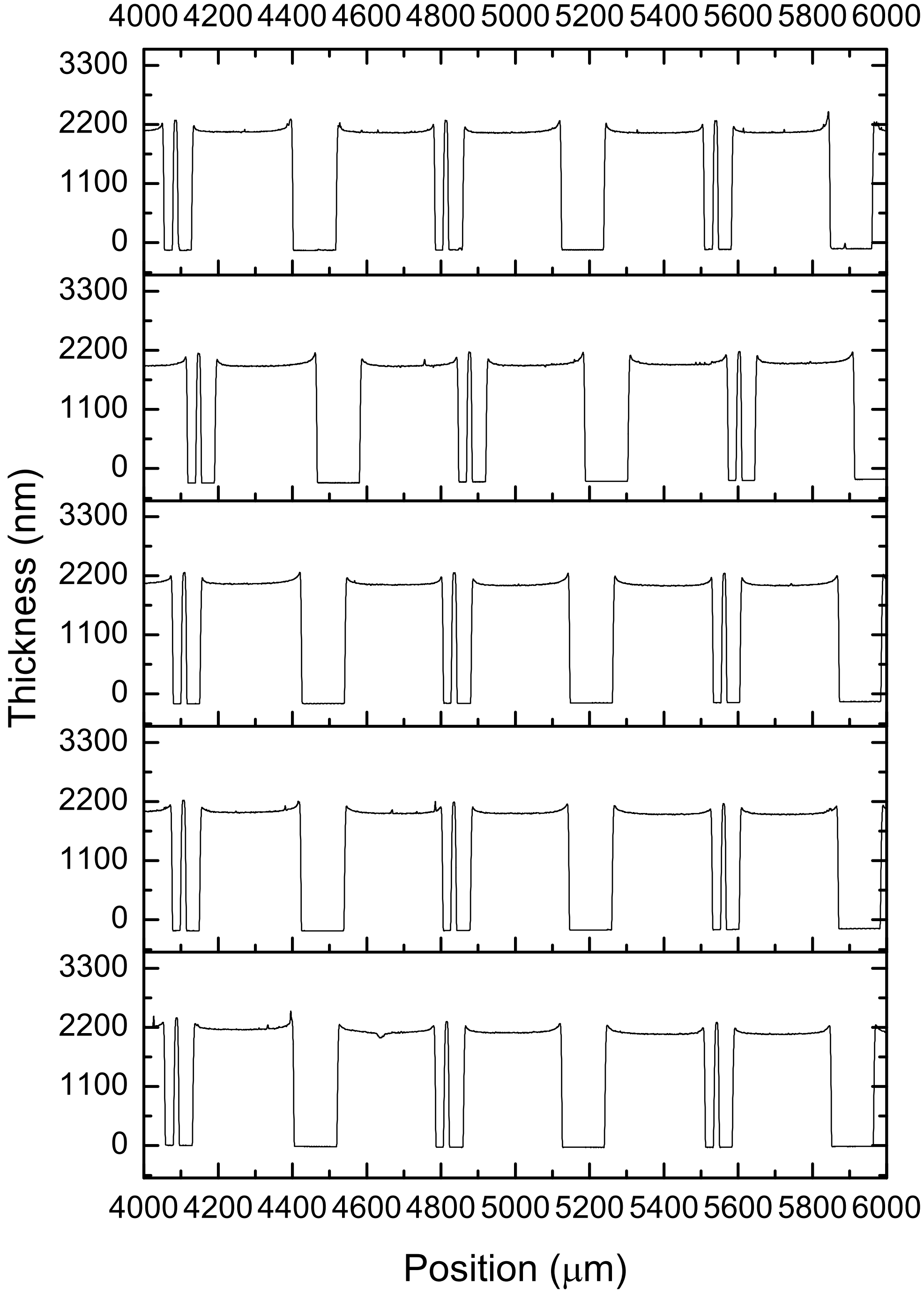

Figure 8.4: Surface profilometry of rotating arm structures deposited from the citric bath. The location of the measurements are shown in Figure 8.3. Note that the pointer arms for each test structure are located at 4100, 4800 and 5520 μm.

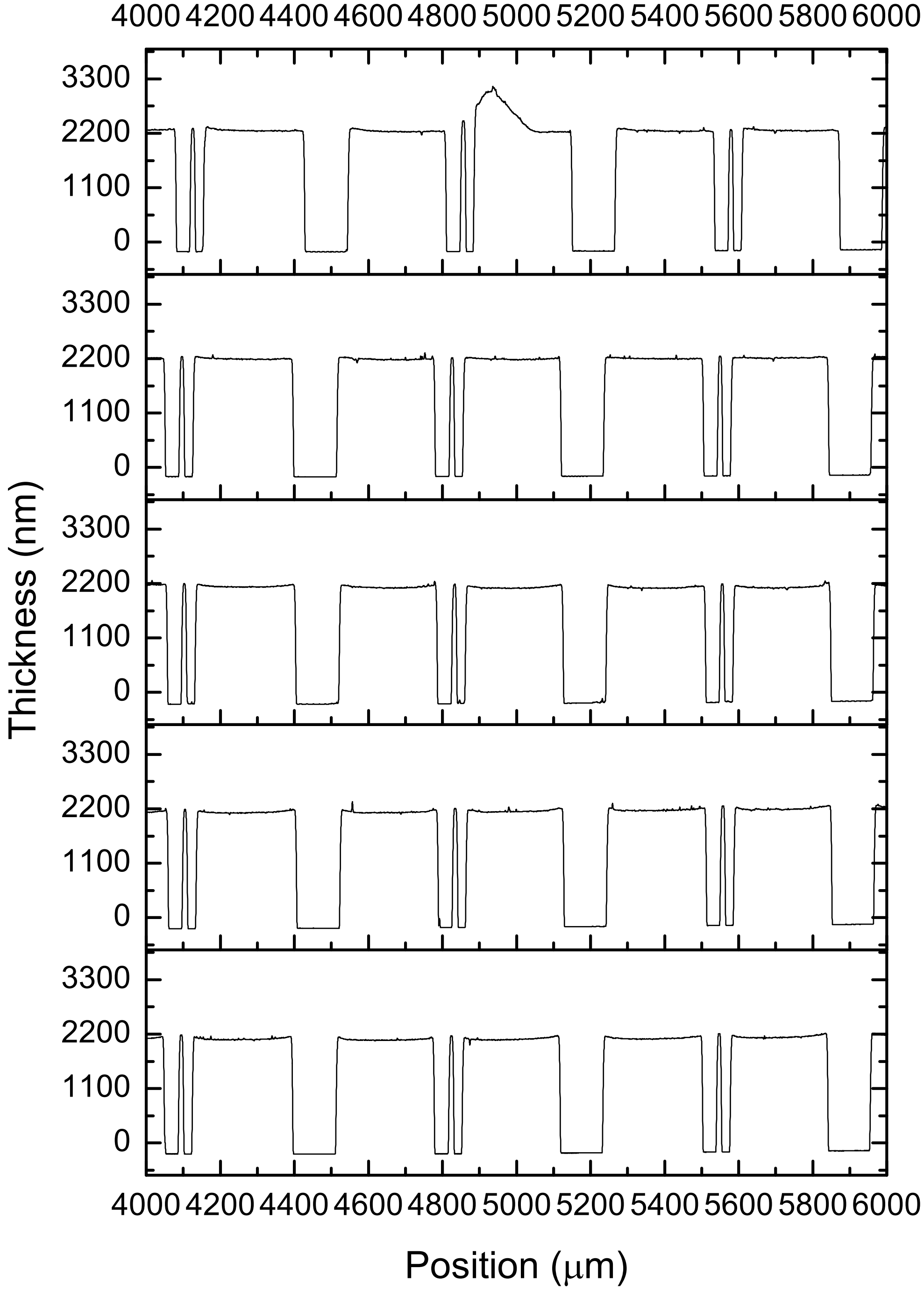

Figure 8.5: Surface profilometry of rotating arm structures deposited from the boric bath.The location of the measurements are shown in Figure 8.3. Note that the pointer arms for each test structure are located at 4100, 4800 and 5520 μm.

8.4 Test Structure Measurements

8.4.1 Sheet Resistance

The test structure chips enable measurements of electrical resistance from the Greek cross structures and the strain in the deposit can be measured for the angle of rotation of the rotating arm structures. Before either measurement is possible the copper seed layer must be removed, first as it is electrically conductive, and secondly as the removal of the seed layer also releases the pointer arms from the underling layer suspending the structure, so the arms are free to rotate. The seed layer was removed using a wet etch (procedure 3.2.6) which undercuts and releases the structures.

The electrical sheet resistance for the films was measured using 4-point resistance measurements on the Greek cross structures. The use of a semi-automatic prober enabled the rapid measurement of the 32 Greek cross structures on each test structure electrode. Section 3.4.3 gives a detailed procedure for this measurement method. For this method the magnitude of the current to be forced is important, as heating of the structure, which can result in a change in the resistance, should be avoided. Conversely, if too little current is passed sensitivity of the voltmeter becomes an issue, which limits the accuracy and precision of the measurement.

Figure 8.6 details the extracted sheet resistance as a function of the applied current for a nickel-iron film of thickness 2.2 µm. The extracted sheet resistance was found to vary significantly with the current applied during the sheet resistance measurement. Below 5 mA of applied current the apparent sheet resistance increases at a rapid rate. This occurs due to the resolution of the voltmeter being too low to accurately measure the voltage. As the forced current was increased beyond 15 mA there was a slow rise in the apparent sheet resistance being measured. This is due to the current heating the metal. As the temperature of the metal increases the resistance also increases. As the current was increased further, past 30 mA, the structure melted and failed. A largely constant linear region was found between 7 mA and 15 mA. Therefore a current of 10 mA was applied to measure sheet resistance for these films.

The sheet resistance was measured for each test structure using the 4-point probe method. After discounting measurements for failed structures the average sheet resistance was calculated for each device. The average sheet resistance measured for the films deposited from the citric bath was 0.090 ± 0.006 Ω/square (N = 131) compared to 0.078 ± 0.004 Ω/square (N = 131) for the films deposited from the boric bath. Table 8.2 shows the average sheet resistance for each device.

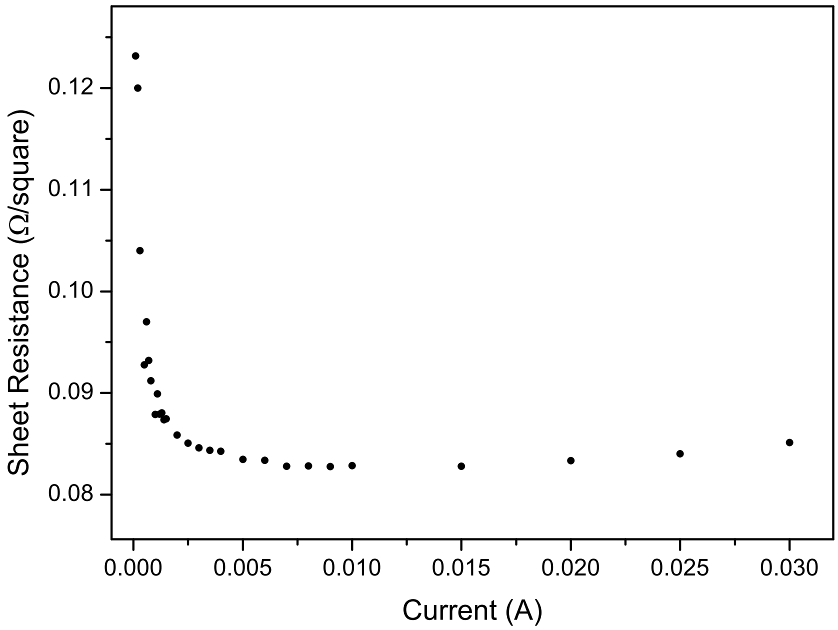

Figure 8.6: Relationship between the current forced and the sheet resistance extracted using a Greek cross.

Between the two types of bath there was a measured difference in the sheet resistance which is significant at the 99.9 % level (two tailed t-test, t-statistic = 19.67, 280 d.o.f.). This difference may be attributed to a change in grain size between the deposits from the different baths. For an inductor a higher resistance is beneficial as it reduces energy losses due to eddy currents in the core, especially for high frequency applications.

Chip #	Sheet Resistance (Ω/square)	
	Citric Bath	Boric Bath
1	-	0.0769 ± 0.0051
2	0.0886 ± 0.0036	0.0813 ± 0.0007
3	0.0907 ± 0.0059	0.0786 ± 0.0053
4	0.0891 ± 0.0056	0.0785 ± 0.0034
5	0.0907 ± 0.0066	0.0783 ± 0.0029

Table 8.2: Measured sheet resistance for 2.2 µm NiFe films (Ω/square).

8.4.2 Strain

To compare the strain in the nickel-iron films deposited from the different baths the angle of rotation for the rotating arm test structures were measured (strain is related to the angle of rotation through Equation 3.20). Images of the pointer arms were taken and, using pattern recognition software, the angle of rotation extracted (as detailed in Section 3.4.3). The rotating arm structures have 3 different arm offsets ($\Delta Y/W = 1.5$, 1.75 and 2.0). For identical films each offset ratio would provide a different angle of rotation. Each chip has 64 structures consisting of 28 with a 1.75 ratio and 14 each of the 1.5 and 2.0 offset ratios.

Figure 8.7 shows the distribution of angles measured for the structures with an offset ratio of 1.75. Rotation was clockwise for all measurements indicating the films were under compressive stress. A comparison between the boric acid and citric baths was then made. The solid lines represent normal distributions which best fit the two sets of data. A two-tailed t-test demonstrates there is no significant difference in the mean rotation angle (t-statistic = 1.40, 234 d.o.f.). The measured angle for deposits from the boric acid bath was 2.86 ± 0.44° compared to 2.95 ± 0.54° from the citric bath.

Table 8.3 gives the average angle of rotation for the test structure with an offset ratio of 1.75 for each chip. There was no significant difference found between the angle of rotation between chips deposited from the boric bath or the citric baths. This indicates the strain in both sets of deposits is comparable.

Figure 8.8 compares the angle of rotation at each location, and across all offset ratios, on the test structure electrodes between the citric and boric bath. The standard deviation for the rotation angle is given as the error bar for each point. The angles of rotation were grouped between 2.5 and

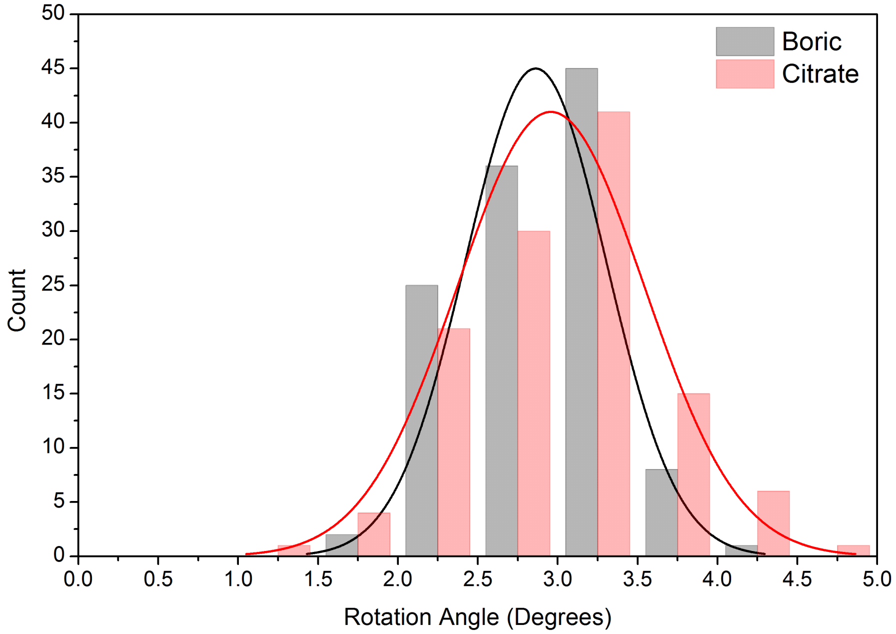

Figure 8.7: Distribution of measured pointer arm angles (1.75 offset ratio) deposited from the boric acid (black) and citric (red) baths. The solid line indicates a fitted normal distribution for the data sets.

3.5 degrees for the majority of test structures. There does not appear to be any location dependent trends as the variation at any location is as much as the variation across the entire electrode. If there were systematic location dependence a 45° line through zero would be apparent in this plot.

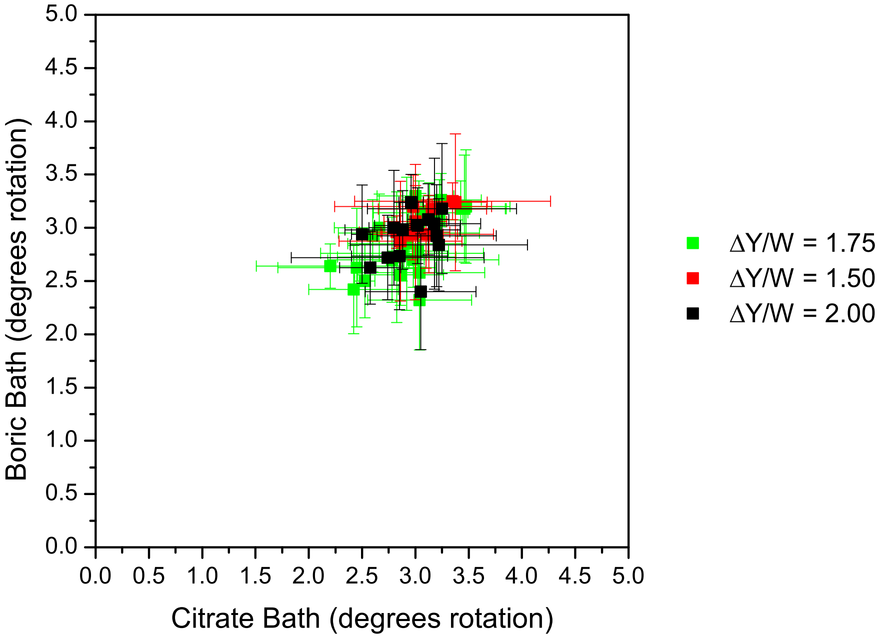

Figure 8.8: Comparison of rotation angle between films deposited from the citric and boric bath.

Chip #	Boric Bath	Citric Bath
1	2.8 ± 0.8	3.2 ± 0.8
2	3.1 ± 0.4	2.9 ± 0.4
3	3.0 ± 0.5	3.0 ± 0.5
4	2.7 ± 0.4	2.9 ± 0.5
5	2.7 ± 0.4	2.9 ± 0.5

Table 8.3: The average angle of rotation for rotating arm structures with an offset ratio of 1.75 for each device. Rotation was clockwise indicating compressive stress.

8.5 Magnetic Characterisation

The main reasons for using nickel-iron films in MEMS devices are for their favourable magnetic properties as discussed in Section 1.1.2. Particular importance is given to the coercivity (H_c), relative permeability (μ_r) and the magnetic saturation (M_s). These key properties can be extracted from the B-H hysteresis loops of the deposited films.

For the magnetic characterisation of nickel-iron films deposits were made on to circular electrodes (see Section 3.2.5 for fabrication details). Deposits were made simultaneously on the four circular electrodes of the device and, when diced, produced 4 replicate samples. Films were deposited from the each of the boric acid and the citric baths as previously detailed in this chapter. The current density applied to deposit the films was again 20 mA cm^{-2} and the thickness of the deposits was varied systematically using the different deposition times of 20, 100, 360 and 800 s. These deposition times correspond to target thicknesses of 0.14, 0.71, 2.57 and 5.70 µm. Samples were identified by bath (boric or citric), time deposited (in seconds) and position (1-4) on the electrode, for example B3603 refers to a film deposited from a boric acid bath for 360 s at position 3.

Samples with a deposition time of 20 s did not provide a magnetic response large enough to overcome the noise on the B-H looper, most likely due to the small sample volume. These samples were therefore discarded from further analysis as magnetic results were not obtainable.

Non-magnetic characterization of the films was performed to determine the composition and thicknesses of the deposited films. Surface profile measurements were performed to approximate the thickness for each circle by taking the average of the edge heights. Typical examples of the surface profile measurements are shown in Figure 8.9. Bowing of the chip was observed due to the stress in the films. The composition of the films was measured using a single spot at the center of each circle using XRF. The measured thickness and composition of all films are included in Table 8.5 at the end of this chapter.

After the initial characterisation the electrodes were diced to separate the 4 samples from each electrode. Half of the films (positions 1 and 3) were then subjected to an 'annealing' step to simulate later processing, soldering for example, which may occur during subsequent packaging. At the temperature used (200 °C) there should be no true alloy annealing as this is far below the melting point of the alloy (1450 °C) but it is more likely to give a true representation of performance in a working device. Annealing was performed in a nitrogen atmosphere with the temperature increased

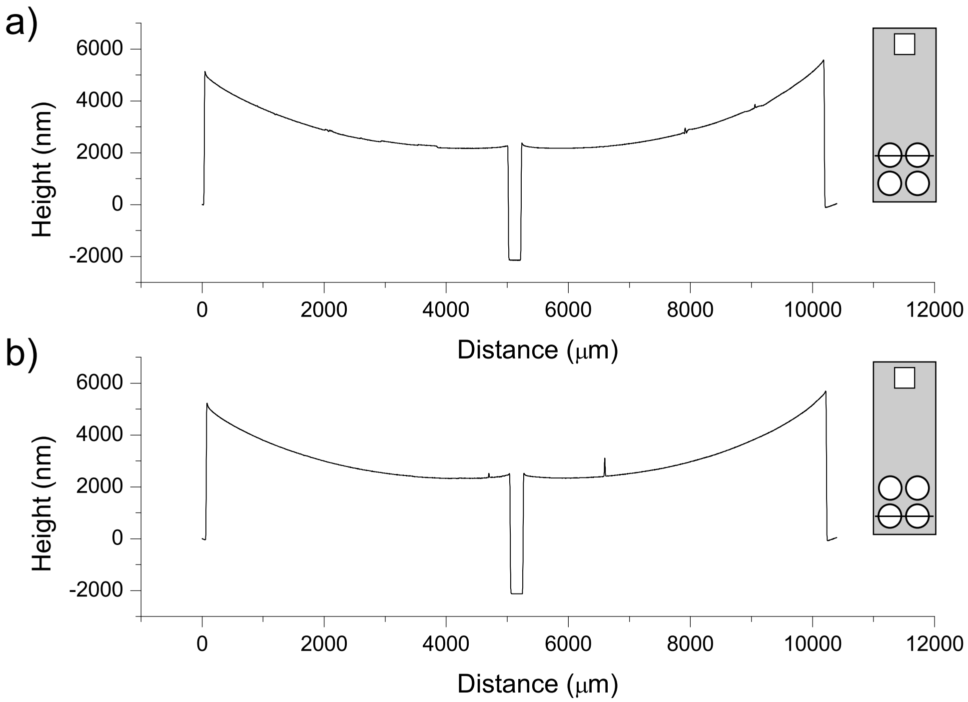

Figure 8.9: Typical surface profile measurements for a deposited nickel-iron film on circular electrodes. a) is the measurement taken across the top two circular electrodes on the chip. b) is the measurement taken across the bottom two circular electrodes on the chip.

at a rate of 5 °C / min from 25 °C up to 200 °C then held for 60 minutes before cooling at 1°C / min down to 25 °C.

8.5.1 Saturation Magnetisation

SQUID measurements (Section 3.5) were performed on four samples to enable the determination of M_s from the B-H loop measurements. M_s was determined for the samples B8004, C8004, B3604 and C3604. As the volume of the samples are identical for both types of measurement a conversion factor, independent of volume, can be calculated to relate the measured pickup flux (measured in nWb) in the B-H loops to a value of magnetisation (emu cm^3 cm^{-3}) through the equation $M_s = A \times Flux$. M_s measured from the SQUID, the flux measured from the B-H loop and the conversion factor, A, for each sample is shown in Table 8.4. The average conversion factor for the four samples was 0.0193 emu nWb^{-1} with a standard deviation of 0.0014 emu nWb^{-1}. This value can then be used to relate the pickup flux measured to the magnetisation of any sample.

Sample ID	SQUID M_s / emu cm^3 cm^{-3}	B-H loop Flux / nWb	A / emu nWb^{-1}
B8004	0.0840	4.57	0.0184
C8004	0.0873	4.67	0.0187
C3604	0.0379	1.77	0.0214
B3604	0.0368	1.93	0.0191

Table 8.4: Conversion factors for the calibration of hysteresis loops.

In-plane B-H hysteresis loops were measured for the samples through a range of angles at 0, 45, 90, 135 and 180° using a frequency of 10 Hz. Examples of the B-H loops measured at different angles are shown in Figure 8.10. Films showed minimal anisotropy in this plane, as demonstrated by the minimal change in the response with measurement angle. This indicates there is no predominant hard or easy axis in this plane.

The B-H loops for different thicknesses of films were also measured and compared. Figure 8.11 shows typical hysteresis loops for NiFe films deposited from both boric acid and citric deposition baths. There was no significant difference between annealed and non-annealed samples.

The total magnetisation of a material is volume (or mass) dependent. For identical materials under the same conditions, i.e. magnetic saturation, a sample double the volume would have double the magnetisation. Using the B-H loop data the saturation magnetisation per unit volume was calculated for each sample using the thickness acquired from the surface profiling, this is detailed in Table 8.5.

The saturation magnetisation of the samples is compared to the thickness of the sample in Figure 8.12. The average values for M_s measured in these films was 895 ± 66 and 923 ± 111 emu cm^{-3} for deposits made from the boric acid bath and citric bath respectively. M_s for $\mathrm{Ni_{80}Fe_{20}}$ has been reported as 800 emu cm^{-3} at 290 K [159] in reasonable agreement with this work.

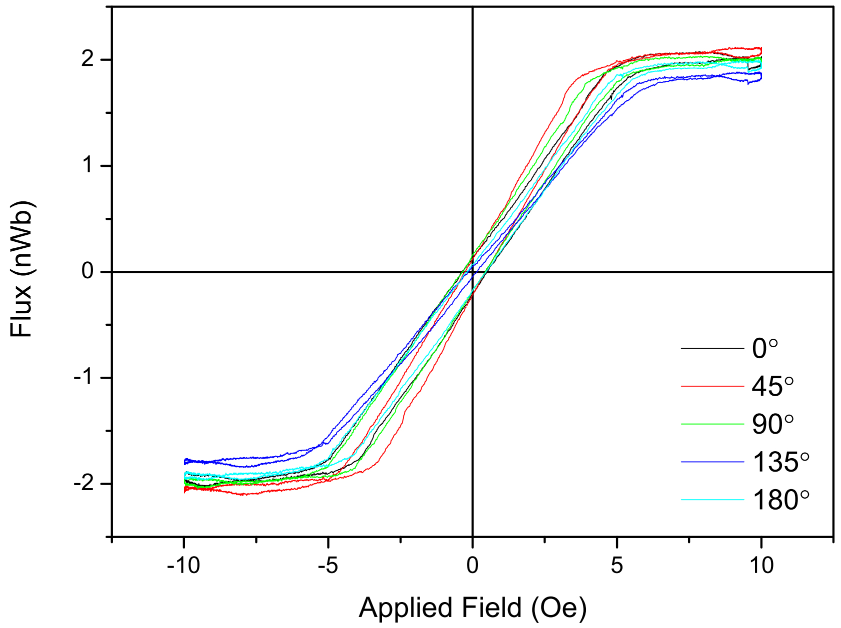

Figure 8.10: Hysteresis loops for a NiFe film measured at different angles (sample C3603).

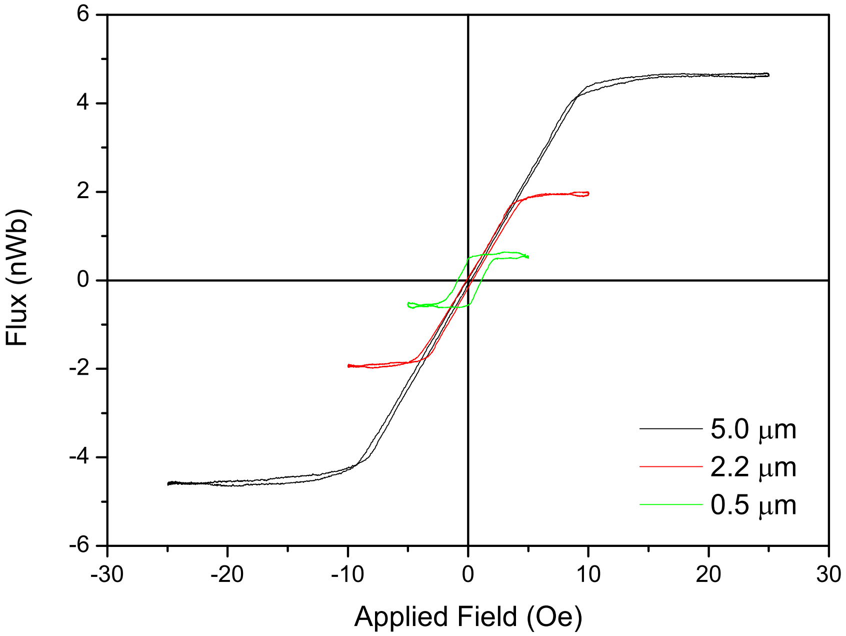

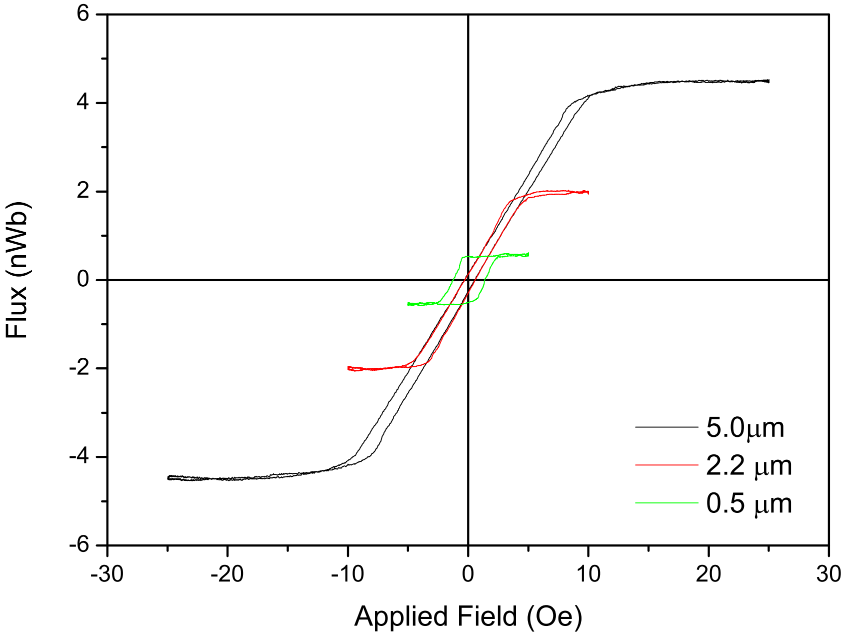

Figure 8.11: In-plane hysteresis loops for NiFe films of varying thickness. Top: deposited from the boric bath. Bottom: deposited from the citric bath.

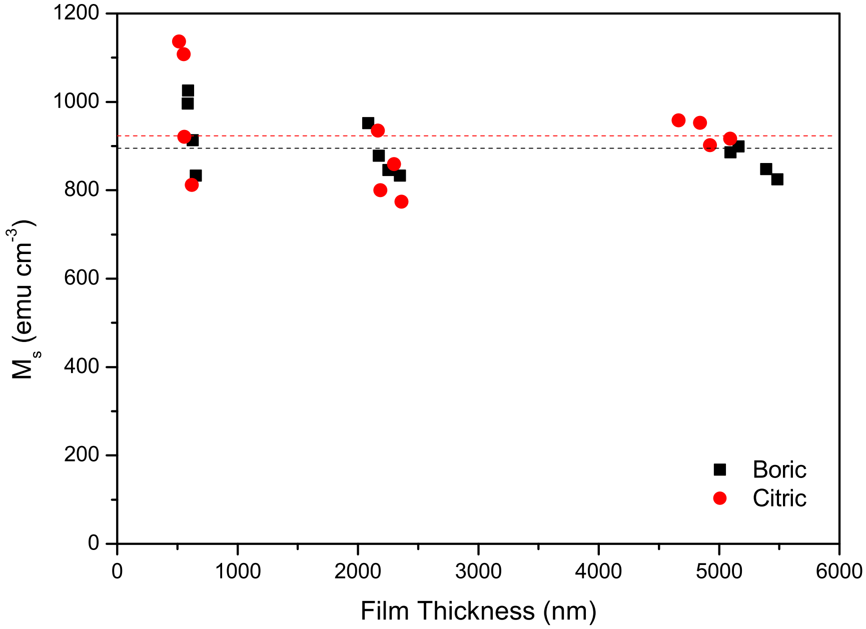

Figure 8.12: Saturation magnetisation of deposited nickel-iron films compared to the thickness. The dashed lines show the average value for M_s for deposits made from the boric bath (black) and the citric bath (red).

8.5.2 Coercivity

The coercivity has a large impact in determining the energy lost during magnetisation and demagnetisation as required for use in inductors. A smaller coercivity results in less energy loss which is represented by the area enclosed in the B-H loop.

The coercivity of the films was extracted from the B-H loops. Low coercivity (<1.5 Oe) was measured across all the films. An increase in the coercivity, H_c, is observed with a decrease in thickness, t. Qualitatively this can be explained due to a transition from a Bloch to a Néel wall [13]. In a Bloch wall, the transition between magnetic domains occurs perpendicular to the axis of magnetisation, whereas in a Néel wall this transition occurs in plane (Figure 8.13). The energy of Bloch and Néel walls between magnetic domains is dependent on the thickness of the film. When the thickness of the film becomes less than the thickness of the wall thickness a Néel wall becomes energetically favourable.

Zhao *et al.* have proposed a model to describe the change in coercivity caused by the effects of the demagnetising field on domain wall movement including surface roughness [160]. In this model the change in coercivity of a magnetic film due to domain wall movement is proportional to the inverse of the film thickness, $H_c^{mov} \propto t^{-1}$, as defined by Equation 8.1.

$$H_c^{mov} = \frac{1}{J_s}\left(\frac{A\pi^2}{Dt} + \frac{KD}{2t} + \frac{Dt + 2D^2}{(t+D)^2}\pi J_s^2\right)\rho_{rms} \tag{8.1}$$

where $J_s = \mu_0 M_s$, t is the film thickness, A is the exchange constant, ρ_{rms} is the root mean square for the local slope (a dimensionless parameter), D is the domain wall thickness and K is the in-plane volume anisotropy constant. The exchange constant, A, and anisotropy constant K, remain constant for a given material at a fixed temperature. $A = (JS^2)/a$, where J is the exchange integral, S is the spin and a is the interatomic spacing. For Permalloy films A is in the order of 1×10^{-11} J m^{-1}[161] and K $\approx 10^4$ J m^{-3}[162]. In this model the contribution of a perfectly flat film is zero. For ease of fitting the final term can be neglected as it represents a second order correction [163].

The total coercivity for the film can be approximated from the sum of the anisotropic contribution, H_c^{anis}, and the contribution due to domain wall movement, H_c^{mov}.

$$H_c = H_c^{anis} + H_c^{mov} \tag{8.2}$$

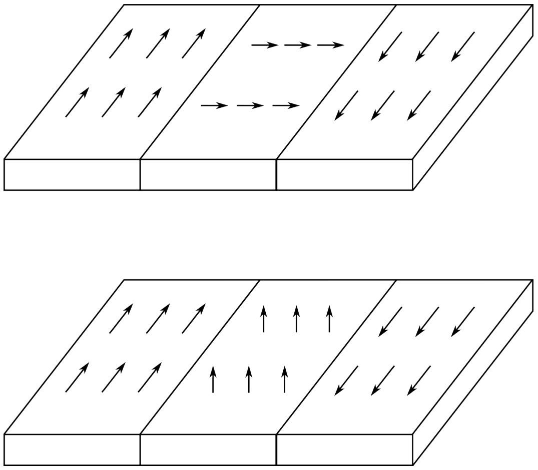

Figure 8.13: Néel (top) and Bloch (bottom) wall type structures.

The measured coercivity data (Figure 8.14) is fitted to to the function $H_c = \alpha t^{-1} + c$. The constant, c, represents H_c^{anis} and the term αt^{-1} represents the contribution to the coercivity from domain wall movement and it's dependance on the film thickness. The fitted equations for deposits yield $H_c = 4.24 \times 10^{-5} t^{-1} + 11$ from the boric acid bath and $H_c = 4.18 \times 10^{-5} t^{-1} + 32$ from the citric bath.

Although the measured coercivity is low for films deposited from both baths there is a small increase in the coercivity for the films deposited from the citric bath compared to the boric bath. For nanocrystaline films the coercivity due to anisotropy in the film can be approximated using the Equation 8.3 [164].

$$H_c^{anis} \approx \frac{p_c K^4 D^6}{M_s A^3} \tag{8.3}$$

where p_c is the particle shape prefactor (0.64 for randomly orientated cubic particles), K is the anisotropy constant, D is the grain size (typically 10 to 100 nm), M_s is the saturation magnetisation (1.01 T) and A the exchange constant. Using typical values of $K \approx 10^4$ J m^{-3}, D = 10 nm, M_s = 1.01 T and $A \approx 1 \times 10^{-11}$ J m^{-1} H_c^{anis} is calculated to be in the order of 10^1, similar to the experimentally measured values.

The small difference in the measured coercivities may be due to a change in the grains size. This however opposes evidence from the electric measurements made previously in Section 8.4.1 on similar films which suggest films from the citric bath have a smaller grain size. It is also likely that any variation in the film composition or microstructure may also influence the measured coercivity.

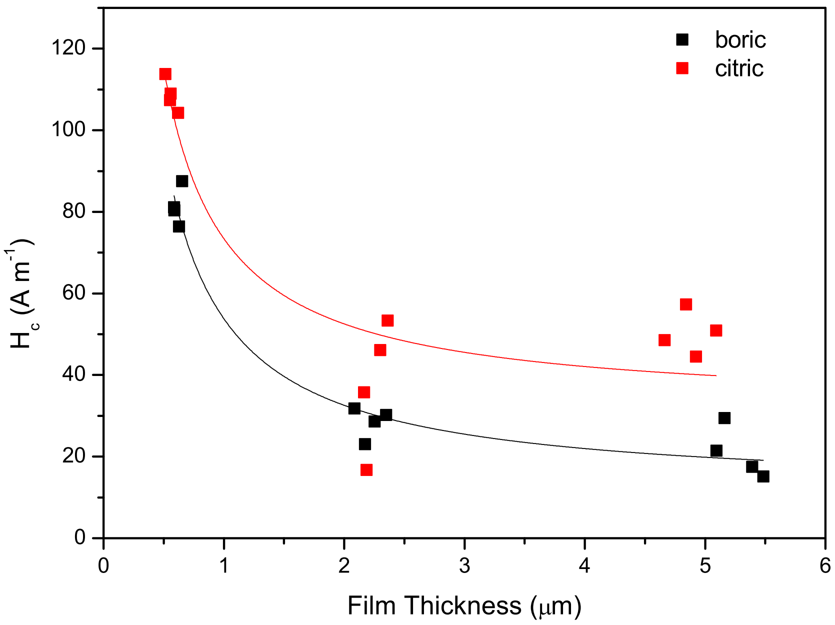

Figure 8.14: Measured coercivity for deposited NiFe films from the boric acid bath and the citric bath.

8.5.3 Permeability

The relative permeability, μ_r, of the films is another important property. For use as a soft magnetic core in an inductor the permeability is directly related to the inductance, L, through the equation $L = \mu_0 \mu_r N^2 l A$, where the permeability of free space $\mu_0 = 4\pi \times 10^{-7}$ H m^{-1}, N is the number of turns in the coil, l is the length of the coil and A is the cross sectional area.

The relative permeability of the deposited films was calculated from the B-H loops as described in Section 2.3. Using calibrated values for B the values for the maximum relative permeability were calculated. Figure 8.15 shows there is a clear thickness dependance on the permeability. It is apparent that the type of deposition bath used has little effect on the permeability of these films.

Similar behavior for nickel-iron films has been described by O'Donnell *et al.* [165] and Feldmann and Buttenbach [166]. It is suggested that this behavior may be due to the Villari effect. This can be thought of as inverse magnetostriction, where there is a volume change due to a magnetic field, which causes a strain in the film. The converse effect, where a mechanical strain in the film causes a change in the easy axis and hence a change in permeability is known as the Villari effect [13].

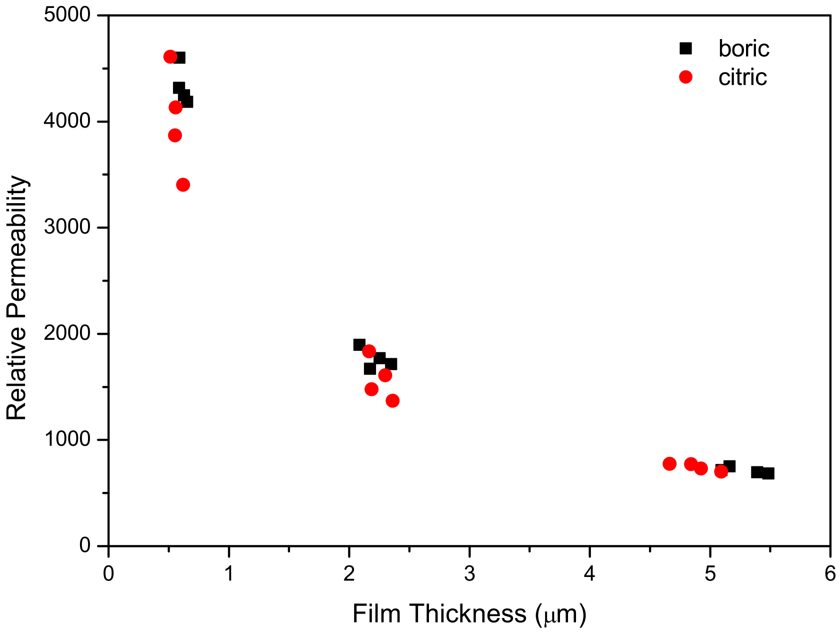

Figure 8.15: Relative permeability, μ_r, measured from in-plane B-H loops for NiFe films.

8.6 Conclusions

The properties of electrodeposited NiFe films from a new citric based electroplating bath and a boric acid based bath were compared. Similar properties for films deposited from the boric acid bath and the citric bath were observed.

Comparison of the strains in the films were made using pointer arm test structures. There was no discernible difference between deposits made for the boric or citric bath. Using electrical test structures the sheet resistance was measured for deposits from the different baths. The sheet resistance for 2.2 μm thick films from the citric bath were measured as 0.0898 ± 0.0056 Ω/square, slightly higher than those from the boric bath at 0.0784 ± 0.0041 Ω/square.

The magnetic properties of the films were also assessed using B-H measurements. The volume magnetic saturation was measured as 895 ± 66 and 923 ± 111 emu cm^{-3} for the boric acid bath and citric bath respectively, demonstrating no significant difference. The coercivity was measured and shown to be a function of thickness. The citric bath was shown to give a higher coercivity, due to a larger anisotropic contribution. The in-plane relative permeability was shown to be the same within error for both sets of films and to be dependent on the film thickness.

Overall the physical behavior of nickel-iron films deposited from the citric bath were shown to be similar. This suggests the new citric based bath is suitable as a direct replacement of the boric bath. To confirm the suitability further work should focus on the up-scaling of this deposition bath to deposit films on a full wafer scale.

Deposition Time / s	Bath	Position	Flux / nWb	H_s / Oe	H_c / Oe	Thickness / nm	M_s / emu cm^{-3}	μ_r
800	Boric	1	4.58	15.1	0.19	5485	825	686
800	Boric	2	4.63	15.3	0.22	5390	848	697
800	Boric	3	4.70	15.0	0.37	5162.5	899	753
800	Boric	4	4.57	15.5	0.27	5095	886	718
360	Boric	1	1.93	6.0	0.36	2252.5	846	1773
360	Boric	2	1.98	6.1	0.38	2347.5	833	1716
360	Boric	3	2.01	6.3	0.40	2086	952	1898
360	Boric	4	1.93	6.6	0.29	2172	878	1671
100	Boric	1	0.55	2.5	1.10	652.5	833	4185
100	Boric	2	0.58	2.7	0.96	627.5	913	4249
100	Boric	3	0.61	2.8	1.01	587.5	1026	4603
100	Boric	4	0.59	2.9	1.02	585	996	4317
800	Citric	1	4.50	15.5	0.56	4925	902	732
800	Citric	2	4.73	16.4	0.64	5092.5	917	703
800	Citric	3	4.52	15.5	0.61	4662.5	958	776
800	Citric	4	4.67	15.5	0.72	4842.5	953	772
360	Citric	1	2.00	6.7	0.58	2300	859	1611
360	Citric	2	1.85	7.1	0.67	2360	774	1370
360	Citric	3	2.05	6.4	0.45	2165	935	1836
360	Citric	4	1.77	6.8	0.21	2185	800	1479
100	Citric	1	0.52	2.8	1.37	557.5	921	4135
100	Citric	2	0.51	2.8	1.31	620	812	3403
100	Citric	3	0.59	3.1	1.43	512.5	1137	4609
100	Citric	4	0.62	3.6	1.35	552.5	1108	3869

Table 8.5: Summary of extracted data from B-H loops measured on NiFe deposits. Note: 1 Oe = $10^3/4\pi$ A m^{-1}.

Chapter 9

Conclusions and Future Work

This thesis set out to develop and demonstrate the use of an environmentally benign alternative to boric acid in the nickel and nickel-iron electrodeposition baths. Boric acid is currently a key component in electrodeposition baths as it increases the quality and adherence of nickel films. Through EU legislation the use of boric acid is likely to come under more stringent regulation therefore environmentally benign alternatives must be sought. There are numerous suggestions for the role of boric acid in these electrodeposition baths (see Section 1.2.2) . These suggested roles include the suppression of the hydrogen evolution reaction (HER), action as a catalyst, action as a buffering agent and reduction of passive film formation. From the examination of the behaviour of an alternative bath insight was gained into the primary roles of boric acid. Once an alternative bath was developed an assessment for the suitability of the film for use in industrial microfabrication was made.

Initial work was performed in Chapter 4 to benchmark the existing boric acid based electroplating baths used to deposit nickel and nickel-iron. This allowed the assessment of the electrochemical behaviour of the bath.

The evaluation of the nickel bath was performed using cyclic voltammetry, along with the electrochemical quartz crystal microbalance (EQCM) to simultaneously measure film mass. This demonstrated the key role of the hydrogen evolution reaction in determining the overall deposition efficiency during electrodeposition. Using the EQCM, efficiencies of up to 93 % were calculated for the deposition of nickel from the established boric bath. The use of boric acid in this bath was shown to control the extent of the HER and increase efficiency. Any suitable replacement must also therefore at least perform this function.

Nickel-iron films were also deposited from the boric bath on to copper electrodes deposited to establish the benchmark behavior of this electroplating bath. The effects of current density, iron (II) chloride content and temperature on the composition of the deposited films were examined. The iron content of the film was demonstrated to be linearly proportional to the Fe(II) concentration at a fixed current density. Film composition was also confirmed to vary with the applied current density and maximum iron content was measured at current densities of 20 mA cm^{-2}. Increasing the temperature was also shown to increase the fraction of nickel present in the resulting films. This demonstrated the controllable and tunable deposition of nickel-iron from the boric bath, and established the benchmark behavior to which a new bath could be compared.

Citric acid was previously identified as a potential alternative to boric acid. Its applicability was postulated as being due to its ability to buffer at a suitable pH and the potential ability to reduce the extent of the HER. In order to investigate this an iterative approach was undertaken to improve the performance of a citric based electrolyte. By depositing films on a small scale using test structure electrodes the quality of deposited films under different conditions could be rapidly assessed. Through varying the component concentrations and deposition parameters bright, level, uniform thick films of $Ni_{80}Fe_{20}$ were successfully deposited from this new citric based electrodeposition bath. There was particular difficulty in achieving the desired $Ni_{80}Fe_{20}$ composition while maintaining a reasonable efficiency and low surface roughness. Importantly, elevated temperatures (60 °C) were required to obtain acceptable film morphology, unlike boric baths which can perform at room temperature. Under these conditions controllable and tunable deposition of nickel-iron was achieved. This approach to developing a new electrodeposition bath was shown to firstly help provide fundamental insight into the behavior of the bath, and secondly provides a rapid technique to develop a new plating bath as required by industry.

To further investigate the fundamental behavior of the citric bath, deposition of nickel only films was performed from the new bath in Chapter 6. From this work, initial comparisons for the behaviour of citric based baths were made with boric baths. Using cyclic voltammetry and EQCM the deposition of nickel was investigated and the importance of the HER verified. It was also demonstrated that the importance of the HER was increased by increased mass transport and hence increased agitation produced a less efficient deposition process. From EQCM measurements the efficiency of deposition was measured and found to be highest (upwards of 80 %) at current densities of 25 mA cm^{-2} in stagnant solutions. This again demonstrated that the optimal conditions for electrodeposition of nickel are when the HER is minimised.

pH is a critical parameter in the deposition of nickel and nickel-iron films from boric baths. It was shown that this remains the case for citric baths. In this work it was demonstrated that a pH above 4 should be avoided due to the formation of nickel hydroxide during deposition. It was apparent that, like boric acid, the use of citric acid inhibits the formation of hydroxide species. As the pH was decreased the efficiency of nickel deposition was shown to decrease accordingly. The maximum efficiency for nickel deposition was found where the speciation of citrate in solution was predominately NiHCit and NiCit$^-$. This is a region where the solution provides a buffering action to maintain the local pH at the electrode. As others have previously pointed out, boric acid cannot strictly buffer around pH 3 due to its pKa of 9.23, but it is still able to dissociate and provide protons reducing any pH change. This demonstrates the importance of considering the speciation of the buffering species which are present in determining the response.

The importance of additives in the deposition bath was also demonstrated using EQCM measurements. The use of citric acid in the bath was demonstrated to be essential in forming a coherent nickel film. Further additives (sodium saccharin and sodium dodecyl sulfate) were demonstrated not to influence the coulombic efficiency but rather enhance the morphological properties of the deposit. This showed a significant effect, but the precise mechanism remains to be determined

The deposition of nickel-iron alloys from the citrate bath was studied in Chapter 7. In contrast to the boric bath, evidence for the presence of a stable iron (III) citrate complex was provided in the cyclic voltammetry. This was shown to enhance the stability of the bath, particularly with respect to the presence of Fe (III) species. The citric bath was also examined with added Fe (III) and shown to be more stable than the boric bath under these conditions. This is important as it indicates the potential for insensitivity to oxidation of Fe(II) and hence an extended bath lifetime reducing the maintenance schedule. This is consistent with previous studies, but unlike others completely removes the use of boric acid.

The effect of agitation for the citric bath was investigated using the RRDE. Agitation has a strong effect on efficiency and film composition. With increasing convective mass transport the efficiency of the deposition was shown to decrease. In the nickel-iron bath the rate of the HER was shown to increase with mass transport particularly at lower rotation frequencies.

Importantly, both boric and citric acid reduce the extent of the hydrogen evolution reaction. In this work it was found that boric acid was more effective at suppressing the HER. However, with efficiencies > 80 % the citrate bath is suitable for use in industrial applications as film morphology is unaffected. It is apparent that both boric and citric acid help to prevent passive film formation (insoluble hydroxides) through buffering. The buffering action can help prevent an increase in local pH at the electrode and the formation of insoluble species. This demonstrates that the required properties for the deposition of nickel are not exclusive to boric acid and that citric acid can be beneficial alternative. This work demonstrates for the first time the development of an all citric bath able to efficiently plate nickel-iron.

In Chapter 8 direct comparisons were made of the films made from boric acid and citric acid nickel-iron plating baths to assess the suitability of the bath as a direct replacement. Using test structure electrodes containing rotating arm structures and Greek cross test structures comparisons of the strain and sheet resistance for the electrodeposited films were made. Using rotating arm structures and measuring the angle of rotation it was shown that films from both the citric bath and the boric bath exhibit a similar degree of strain. Resistance measurements were performed on the Greek cross structures. For films 2.2 μm thick the sheet resistance was measured as 0.090 ± 0.006 Ω/square for deposits from the citric bath and 0.078 ± 0.004 Ω/square for deposits from the boric bath. This demonstrates a small but statistically significant (through the T-test) increase in the sheet resistance for the films deposited from the citric bath and suggest citric films may be better. It is suggested that further work would be required by others to confirm this difference. The use of test structures on small electrodes provides a useful platform to evaluate key properties of deposited films such as strain and resistivity.

The magnetic properties of the films were measured using a B-H looper. The saturation magnetisation was measured as 895 ± 66 and 923 ± 111 emu cm^{-3} for films from the boric bath and citric bath respectively the same within experimental error. Similar values for the relative permeability of the films were found between the films deposited from both baths with values up to $\mu_{\mathrm{r}} = 4600$. A slightly larger coercivity for the films was measured for deposits made from the citric bath compared to the boric bath.

In summary a new citric acid based electrodeposition bath was developed to replace existing boric baths. This new bath was demonstrated to deposit nickel and nickel-iron. In general electrodeposition from the two baths is similar and the resulting deposits are comparable. There are still, however some minor difference between them. The coulombic efficiency of the citrate bath is slightly lower implying citrate does not inhibit the HER to the same extent as boric acid. The nickel-iron citrate bath requires elevated temperatures, approximately 60 °C, to avoid low efficiencies and rough deposits. For the deposited films the measured sheet resistance and coercivity were measured to have minor differences. Despite these differences it is apparent that the citrate bath developed is suitable for the deposition of nickel and nickel-iron films in microfabrication.

There are two major avenues along which further work can be pursued. The first area is predominantly chemistry based, to continue to investigate the fundamental aspects of electrochemical deposition. With regards to the nickel and nickel-iron systems, determining the surface species is critical to identifying and understanding these mechanisms. Progression to other electrochemical systems similar in nature to nickel and nickel-iron would also be beneficial to enhance the physical properties of the films and understand the nature of deposition in these systems. The second area for further work is predominantly engineering based. The the citrate based nickel-iron bath developed in this thesis requires development on the larger, wafer scale. This will undoubtedly require work to develop the process to ensure high quality films are deposited reliably and repeatably on this scale. This should occur in conjunction with the development of monitoring processes to assess the quality of the films and longevity of the bath. It follows that various devices would be fabricated and tested during this work.

The deposition of nickel and nickel-iron can be further studied using various electrochemical methods. In terms of understanding the mechanism of anomalous deposition work can be pursued developing the models suggested in the literature [104, 105, 106, 110]. The robustness of these models can be tested using both citric acid and boric acid based baths for the nickel-iron system. The variation between these systems in the aqueous chemistry (*e.g.* stability constants, speciation) could provide a rigorous test for these models. This work would involve include additional rotating disc studies and pursuing electrochemical impedance spectroscopy (EIS) to test these mathematical models against experiment. EIS would also provide an alternative technique which may bring further insight into the surface chemistry during deposition.

There is a substantial array of literature with regards to functional magnetic materials. Nickel-iron is only one of the iron group alloys that is used for its favourable magnetic properties. Development of plating baths for alternative binary, ternary and quaternary alloys could be pursued. Superior magnetic properties are present in cobalt containing alloys such as CoFe, NiCo, FeCo, FeCoB and

NiFeCo [167, 168, 101]. Many of these materials are more commonly sputtered but many can also be deposited electrochemically. Systematic evaluation of the magnetic properties (magnetic saturation, coercivity), electrical resistivity and strain in these films would provide comparisons between the alloys and nickel-iron, aid material selection to enhance the performance of MEMS devices, and add to fundamental understanding.

Extreme control of the magnetic properties can also be achieved through the introduction of nanostructure (multilayers, wire type). Yahalom and Zadok have previously demonstrated controlled electrodeposition for nano-layers of nickel and copper from the same electroplating bath [169]. With suitable dimensions these multilayered films can exhibit giant magnetoresistance (GMR) [170] making them of use as magnetic field sensors. Furthermore, this principle could be applied to other systems to create multilayer structures with novel magnetic properties.

In terms of the development of the citric acid based nickel-iron electrodeposition bath, the next major challenge is to demonstrate its viability on the larger, wafer scale. It is anticipated that the bath can be prepared using standard methods. The presence of Fe(III) in commercial salts can be reduced through dummying the bath at a low pH. Organic contaminants can be removed by adsorption on activated carbon. To prolong the use of the bath it should be operated under an argon or nitrogen blanket to minimise Fe(II) oxidation, additionally, if the bath is not under use the anodes should be removed. During use, carful monitoring of the pH will be required. Hydrogen evolution during plating will cause a pH rise with prolonged use, which is associated with the formation of hydroxides.

An assessment of the long term stability of the bath is an important step in determining the lifetime of the bath. Work in this thesis indicates that the citrate bath could be more tolerant to oxidation. Given the importance of additives, the rate of additive depletion (if any) could also affect the lifetime of the bath. Having developed a method for determining the saccharin concentration through extraction and titration (Section 5.7.1) it would be worth measuring the saccharin concentration as a function of time during plating to determine its sensitivity, and assess whether monitoring is required. Using the method of extractive titration developed in this thesis the saccharin content of the bath can be monitored over the baths lifetime. If saccharin were depleted an alternative is to measure the sulfur content of the deposits through inductively coupled plasma methods (*e.g.* ICP-AES). The sulfur content can then be related to the rate of additive depletion and the corrosion characteristics of the deposited films.

During scale up there may be a number of engineering challenges. These include adequate temperature control to avoid variation in the deposit composition. In addition controlling the electrolyte flow across the wafer is a critical parameter in terms of efficiency and deposit composition. On a larger scale the optimisation of cell geometry may be required to ensure consistent and uniform plating. The characterization of films deposited at the wafer scale could then be performed using similar methods used in this thesis to assess the composition, thickness, roughness, strain and sheet resistance to ensure consistency across the wafer. The measurements in this thesis enable the design of such an industrial bath.

It naturally follows that this bath should then be used to produce MEMS devices, such as inductors or actuators, and their performance tested. At this stage it is anticipated that a standard plating procedure will be established and the deposition of nickel-iron from the citric acid bath can be applied as a fabrication step to produce various devices. The performance of these devices should then be compared to devices fabricated with Permalloy films from existing boric acid based baths and comparisons can be made.

In summary, this thesis has demonstrated the development of a new citric acid based nickel and nickel-iron electrodeposition bath, suitable for use in the microfabrication industry. The electrochemical behavior of the bath was investigated and deposit properties evaluated. In the future, this work can be used as a basis for further understanding of anomalous co-deposition and the new bath used as a safer alternative for the deposition of nickel-iron alloys.

Bibliography

[1] Feynman, R. P. *Microelectromechanical Systems, Journal of* **1992**, *1*, 60–66.

[2] Liu, C.-H.; Kenny, T. W. *Microelectromechanical Systems, Journal of* **2001**, *10*, 425–433.

[3] Seshia, A. A.; Palaniapan, M.; Roessig, T. A.; Howe, R. T.; Gooch, R. W.; Schimert, T. R.; Montague, S. *Journal of Microelectromechanical Systems* **2002**, *11*, 784–793; cited By 142.

[4] Alper, S. E.; Akin, T. *Microelectromechanical Systems, Journal of* **2005**, *14*, 707–717.

[5] Xie, H.; Fedder, G. K. *Sensors Journal, IEEE* **2003**, *3*, 622–631.

[6] Eaton, W. P.; Smith, J. H.; pp 30–41. `http://dx.doi.org/10.1117/12.276606`.

[7] Zhou, J.; Dasgupta, S.; Kobayashi, H.; Wolff, J. M.; Jackson, H. E.; Boyd, J. T. *Optical Engineering* **2001**, *40*, 598–604.

[8] Sadler, D. J.; Zhang, W.; Ahn, C. H.; Kim, H. J.; Han, S. H. *Magnetics, IEEE Transactions on* **1997**, *33*, 3319–3321.

[9] Ahn, C. H.; Allen, M. G. *Industrial Electronics, IEEE Transactions on* **1998**, *45*, 866–876.

[10] Oshiro, O.; Tsujimoto, H.; Shirae, K. *Magnetics, IEEE Transactions on* **1987**, *23*, 3759–3761.

[11] Sullivan, C. R.; Sanders, S. R. *Power Electronics, IEEE Transactions on* **1996**, *11*, 228–238.

[12] Jiles, D. *Introduction to Magnetism and Magnetic Materials*; Chapman & Hall: London, UK, 1990.

[13] Coey, J. M. D. *Magnetism and magnetic materials*; Cambridge University Press: Cambridge, UK, 2010.

[14] Mason, B. H. *Principles of geochemistry*; John Wiley & Sons, Inc.: New York, 1952.

[15] Arnold, H. D.; Elmen, G. W. *Bell System Technical Journal* **1923**, *2*, 101–111.

[16] Kajiwara, G.; Harakawa, K.; Ogata, H.; Kado, H. *Magnetics, IEEE Transactions on* **1996**, *32*, 2582–2585.

[17] Kamiya, J.; Ogiwara, N.; Nishikawa, M.; Hikichi, Y.; Yanagibashi, T.; Kinsho, M. *Vacuum* **2013**, *98*, 12–17.

[18] Moser, A.; Takano, K.; Margulies, D. T.; Albrecht, M.; Sonobe, Y.; Ikeda, Y.; Sun, S.; Fullerton, E. E. *Journal of Physics D: Applied Physics* **2002**, *35*, R157+.

[19] Ross, C. A. *Annual Review of Materials Research* **2001**, *31*, 203–235.

[20] Davis, J. R. *ASM Speciality Handbook: Nickel, Cobalt, and Their Alloys*; ASM International, 2000.

[21] Li, H.; Ebrahimi, F. *Materials Science and Engineering: A* **2003**, *347*, 93–101.

[22] Ebrahimi, F.; Ahmed, Z.; Li, H. Q. *Materials and Manufacturing Processes* **2006**, *21*, 687–693.

[23] Franssila, S. *Introduction to microfabrication.*; John Wiley & Sons: Chichester, 2004.

[24] Zhang, Y.-h.; Ding, G.-f.; Cai, Y.-l.; Wang, H.; Cai, B. *Materials Characterization* **2006**, *57*, 121–126.

[25] Eftekhari, A. *Journal of Physics D: Applied Physics* **2003**, *36*, 1183+.

[26] EerNisse, E. P. *Journal of Applied Physics* **1972**, *43*, 1330–1337.

[27] Rouya, E.; Stafford, G. R.; Beauchamp, C.; Floro, J. A.; Kelly, R. G.; Reed, M. L.; Zangari, G. *Electrochemical and Solid-State Letters* **2010**, *13*, D87–D90.

[28] Luo, J. K.; Pritschow, M.; Flewitt, A. J.; Spearing, S. M.; Fleck, N. A.; Milne, W. I. *Journal of The Electrochemical Society* **2006**, *153*, D155–D161.

[29] Cho, H. J.; Oh, K. W.; Ahn, C. H.; Boolchand, P.; Nam, T.-C. *Magnetics, IEEE Transactions on* **2001**, *37*, 2749–2751.

[30] Murray, J.; Schiavone, G.; Smith, S.; Terry, J.; Mount, A. R.; Walton, A. J. In *Microelectronic Test Structures (ICMTS), 2011 IEEE International Conference on*; IEEE; pp 63–68. `http://dx.doi.org/10.1109/icmts.2011.5976861`.

[31] Smith, S.; Brockie, N. L.; Murray, J.; Wilson, C. J.; Horsfall, A. B.; Terry, J. G.; Stevenson, J. T. M.; Mount, A. R.; Walton, A. J. In *Microelectronic Test Structures (ICMTS), 2010 IEEE International Conference on*; IEEE; pp 80–85. `http://dx.doi.org/10.1109/icmts.2010.5466852`.

[32] Smith, S.; Brockie, N. L.; Murray, J.; Wilson, C. J.; Horsfall, A. B.; Terry, J. G.; Stevenson, J. T. M.; Mount, A. R.; Walton, A. J. In *Microelectronic Test Structures (ICMTS), 2010 IEEE International Conference on*; IEEE; pp 8–13. `http://dx.doi.org/10.1109/icmts.2010.5466870`.

[33] Schlesinger, M.; Paunovic, M. *Modern electroplating*, 5th ed.; John Wiley & Sons, Inc: Hoboken, New Jersey, 2010.

[34] *http://sinlist.chemsec.org/*; Acessed May 2015.

[35] Weir, R. J.; Fisher, R. S. *Toxicology and Applied Pharmacology* **1972**, *23*, 351–364.

[36] Moore, J. A.; Committee, E. S. *Reproductive Toxicology* **1997**, *11*, 123–160.

[37] Fail, P. A.; Chapin, R. E.; Price, C. J.; Heindel, J. J. *Reproductive Toxicology* **1998**, *12*, 1–18.

[38] Heindel, J. *Fundamental and Applied Toxicology* **1992**, *18*, 266–277.

[39] Robbins, W. A.; Xun, L.; Jia, J.; Kennedy, N.; Elashoff, D. A.; Ping, L. *Reproductive Toxicology* **2010**, *29*, 184–190.

[40] Scialli, A. R.; Bonde, J. P.; Brüske-Hohlfeld, I.; Culver, B. D.; Li, Y.; Sullivan, F. M. *Reproductive Toxicology* **2010**, *29*, 10–24.

[41] *Member State Committee Draft Support Document For Identification of Boric Acid as a Substance of Very high Concern Because of its CMR Properties*; European Chemicals Agency, 2010.

[42] *Nickel Plating Handbook*; The Nickel Institute: Brussels, Belgium, 2014; www.nickelinstitute.org.

[43] Bird, G. *Philosophical Transactions of the Royal Society of London* **1837**, *127*, 37–45.

[44] Bottger, R. *Erdmann's J. Praktishe Chemie* **1843**, *30*, 267+.

[45] Adams, I.; *Improvement in the Electro-deposition of Nickel, Patent No. 93157*; 1869; Patent No. 93157.

[46] Watts, O. P. *Transactions of the American Electrochemical Society* **1916**, *29*, 395–403.

[47] Cupery, M. E.; *Electrodeposition, Patent No. 2,318,592*; 1943; US Patent 2,318,592. `http://www.google.us/patents/US2318592`.

[48] DiBari, G. A. *Metal Finishing* **2002**, *100*, 34–49.

[49] Sahari, A.; Azizi, A.; Schmerber, G.; Dinia, A. *Surface Review & Letters* **2008**, *15*, 717–725.

[50] Vicenzo, A.; Cavallotti, P. L. *Russian Journal of Electrochemistry* **2008**, *44*, 716–727.

[51] Abdel-Hamid, Z. *Materials Chemistry and Physics* **1998**, *53*, 235–238.

[52] Ji, J.; Cooper, W. C.; Dreisinger, D. B.; Peters, E. *Journal of Applied Electrochemistry* **1995**, *25*, 642–650.

[53] Tilak, B. V.; Gendron, A. S.; Mosoiu, M. A. *Journal of Applied Electrochemistry* **1977**, *7*, 495–500.

[54] Horkans, J. *Journal of The Electrochemical Society* **1979**, *126*, 1861–1867.

[55] Martell, A. E.; Smith, R. M. *NIST Standard Reference Database 46 Version 8.0: NIST Critically Selected Stability Constants of Metal Complexes.*

[56] Hoare, J. P. *Journal of The Electrochemical Society* **1987**, *134*, 3102–3103.

[57] Hoare, J. P. *Journal of The Electrochemical Society* **1986**, *133*, 2491–2494.

[58] Tsuru, Y.; Nomura, M.; Foulkes, F. R. *Journal of Applied Electrochemistry* **2002**, *32*, 629–634.

[59] Yin, K. *Surface and Coatings Technology* **1996**, *78*, 205–210.

[60] Popov, B. N.; Yin, K. M.; White, R. E. *Journal of The Electrochemical Society* **1993**, *140*, 1321–1330.

[61] Wiart, R. *Electrochimica Acta* **1990**, *35*, 1587–1593.

[62] Epelboin, I.; Joussellin, M.; Wiart, R. *Journal of Electroanalytical Chemistry and Interfacial Electrochemistry* **1981**, *119*, 61–71.

[63] Oriňáková, R.; Turoňová, A.; Kladeková, D.; Gálová, M.; Smith, R.; Oriňáková, R.; Turoňová, A.; Kladeková, D.; Gálová, M.; Smith, R. M. *Journal of Applied Electrochemistry* **2006**, *36*, 957–972.

[64] Saraby-Reintjes, A.; Fleischmann, M. *Electrochimica Acta* **1984**, *29*, 557–566.

[65] Oriňáková, R.; Strečková, M.; Trnková, L.; Rozik, R.; Gálová, M. *Journal of Electroanalytical Chemistry* **2006**, *594*, 152–159.

[66] Cui, C. Q.; Lee, J. Y. *Electrochimica Acta* **1995**, *40*, 1653–1662.

[67] Gómez, E.; Muller, C.; Proud, W. G.; Vallés, E. **1992**, *22*, 872–876.

[68] Gómez, E.; Pollina, R.; Vallés, E. *Journal of Electroanalytical Chemistry* **1995**, *386*, 45–56.

[69] Isabel, A.; Díaz, S. L.; Barcia, O. E.; Mattos, O. R. *Journal of The Electrochemical Society* **2009**, *156*, D331–D335.

[70] Vazquez-Arenas, J.; Pritzker, M. *Journal of The Electrochemical Society* **2010**, *157*, D283+.

[71] Marikkannu, K. R.; Kalaignan, G. P.; Vasudevan, T. *Journal of Alloys and Compounds* **2007**, *438*, 332–336.

[72] Takahashi, K.; MacDougall, B.; Graham, M. J. *Journal of The Electrochemical Society* **1990**, *137*, 3023–3029.

[73] Gilman, S. *Electrochimica Acta* **2012**, *65*, 141–148.

[74] Zhou, X. S.; Liu, Q.; Ivey, D. G. In *Nanoelectronics Conference, 2008. INEC 2008. 2nd IEEE International*; IEEE; pp 474–479. `http://dx.doi.org/10.1109/inec.2008.4585531`.

[75] Freitag, W. O.; Mathias, J. S. *Journal of The Electrochemical Society* **1965**, *112*, 64–67.

[76] Ghorbani, M.; Dolati, A. G.; Afshar, A. *Russian Journal of Electrochemistry* **2002**, *38*, 1173–1177.

[77] Zhang, Y.; Ivey, D. G. *Chem. Mater.* **2004**, *16*, 1189–1194.

[78] Donten, M.; Osteryoung, J. *Journal of Applied Electrochemistry* **1991**, *21*, 496–503.

[79] Trettenhahn, G.; Köberl, A. *Electrochimica Acta* **2007**, *52*, 2716–2722.

[80] Berkh, O.; Burstein, L.; Diamand, Y. S.; Gileadi, E. *Journal of The Electrochemical Society* **2011**, *158*, F85–F91.

[81] Doi, T.; Mizumoto, K.; Tanaka, S.; Yamashita, T. *Metal Finishing* **2004**, *102*, 26–35.

[82] Doi, T.; Mizumoto, K.; Tanaka, S.; Yamashita, T. *Metal Finishing* **2004**, *102*, 104–111.

[83] Li, C.; Li, X.; Wang, Z.; Guo, H. *Transactions of Nonferrous Metals Society of China* **2007**, *17*, 1300–1306.

[84] Shimokawa, T.; Yanai, T.; Takahashi, K.; Nakano, M.; Suzuki, K.; Fukunaga, H. *Magnetics, IEEE Transactions on* **2012**, *48*, 2907–2909.

[85] Oniciu, L.; Mureşan, L. *Journal of Applied Electrochemistry* **1991**, *21*, 565–574.

[86] Weil, R.; Paquin, R. *Journal of The Electrochemical Society* **1960**, *107*, 87–91.

[87] Cui, X.; Chen, W. *Journal of The Electrochemical Society* **2008**, *155*, K133–K139.

[88] Rashidi, A. M.; Amadeh, A. *Surface and Coatings Technology* **2009**, *204*, 353–358.

[89] Matsui, I.; Takigawa, Y.; Uesugi, T.; Higashi, K. *Materials Letters* **2011**, *65*, 2351–2353.

[90] El-Sherik, A. M.; Erb, U.; El-Sherik, A. M.; Erb, U. *Journal of Materials Science* **1995**, *30*, 5743–5749.

[91] Mockute, D.; Bernotiene, G. *Surface and Coatings Technology* **2000**, *135*, 42–47.

[92] Mockute, D.; Bernotiene, G.; Vilkaite, R. *Surface and Coatings Technology* **2002**, *160*, 152–157.

[93] Bhandari, A.; Hearne, S. J.; Sheldon, B. W.; Soni, S. K. *Journal of The Electrochemical Society* **2009**, *156*, D279–D282.

[94] Marcus, P.; Talah, H. *Corrosion Science* **1989**, *29*, 455–459.

[95] Beacom, S. E.; Riley, B. J. *Journal of The Electrochemical Society* **1959**, *106*, 309–314.

[96] Osaka, T.; Sawaguchi, T.; Mizutani, F.; Yokoshima, T.; Takai, M.; Okinaka, Y. *Journal of The Electrochemical Society* **1999**, *146*, 3295–3299.

[97] Cheng, C.; West, A. C. *Journal of The Electrochemical Society* **1997**, *144*, 3050–3056.

[98] Higashi, K.; Fukushima, H.; Urakawa, T.; Adaniya, T.; Matsudo, K. *Journal of The Electrochemical Society* **1981**, *128*, 2081–2085.

[99] Roventi, G.; Fratesi, R.; Guardia; Barucca, G. *Journal of Applied Electrochemistry* **2000**, *30*, 173–179.

[100] Hu, C.-C.; Bai, A. *Journal of The Electrochemical Society* **2002**, *149*, C615–C622.

[101] Osaka, T.; Takai, M.; Hayashi, K.; Ohashi, K.; Saito, M.; Yamada, K. *Nature* **1998**, *392*, 796–798.

[102] Dahms, H.; Croll, I. M. *Journal of The Electrochemical Society* **1965**, *112*, 771–775.

[103] Horkans, J. *Journal of The Electrochemical Society* **1981**, *128*, 45–49.

[104] Hessami, S.; Tobias, C. W. *Journal of The Electrochemical Society* **1989**, *136*, 3611–3616.

[105] Matlosz, M. *Journal of The Electrochemical Society* **1993**, *140*, 2272–2279.

[106] Andricacos, P. C.; Arana, C.; Tabib, J.; Dukovic, J.; Romankiw, L. T. *Journal of The Electrochemical Society* **1989**, *136*, 1336–1340.

[107] Zech, N.; Podlaha, E. J.; Landolt, D. *Journal of The Electrochemical Society* **1999**, *146*, 2892–2900.

[108] Zech, N.; Landolt, D. *Electrochimica Acta* **2000**, *45*, 3461–3471.

[109] Vaes, J.; Fransaer, J.; Celis, J. P. *Journal of The Electrochemical Society* **2000**, *147*, 3718–3724.

[110] Larson, R. S. *Journal of The Electrochemical Society* **2007**, *154*, D427–D434.

[111] Bard, A. J.; Faulkner, L. R. *Electrochemical methods : fundamentals and applications*, 2nd ed.; John Wiley & Sons, Inc: Hoboken, New Jersey, 2001.

[112] Sand, H. J. S. *Philosophical Magazine Series 6* **1901**, *1*, 45–79.

[113] Bhatt, A. I.; Bond, A. M.; MacFarlane, D. R.; Zhang, J.; Scott, J. L.; Strauss, C. R.; Iotov, P. I.; Kalcheva, S. V. *Green Chem.* **2006**, *8*, 161–171.

[114] Sauerbrey, G. *Zeitschrift für Physik A Hadrons and Nuclei* **1959**, *155*, 206–222.

[115] Bard, A. J.; Rubinstein, I. *Electroanalytic chemistry: a series of advances*; CRC Press: New York, USA, 2003; Vol. 22.

[116] Vatankhah, G. *Electrochimica Acta* **2003**, *48*, 1613–1622.

[117] Cassiède, M.; Daridon, J. L.; Paillol, J. H.; Pauly, J. *Journal of Applied Physics* **2010**, *108*, 034505+.

[118] Wang, D.; Mousavi, P.; Hauser, P. J.; Oxenham, W.; Grant, C. S. *Colloids and Surfaces A: Physicochemical and Engineering Aspects* **2005**, *268*, 30–39.

[119] Gileadi, E.; Tsionsky, V. *Journal of The Electrochemical Society* **2000**, *147*, 567–574.

[120] Bund, A.; Schneider, O.; Dehnke, V. *Phys. Chem. Chem. Phys.* **2002**, *4*, 3552–3554.

[121] Wieckowski, A. *Interfacial Electrochemistry: Theory: Experiment, and Applications*; Taylor & Francis, 1999.

[122] Bertotti, G. *Hysteresis in Magnetism: For Physicists, Material Scientists, and Engineers*; Academic Press Limited: London, UK, 1998.

[123] Maxtek, Inc.; Santa Fe Springs, CA; *Operation and Service Manual RQCM Research Quartz Crystal Microbalance*; 2nd ed.; 2004.

[124] Murray, J.; Ph.D. thesis; University of Edinburgh; 2014.

[125] Snook, G. A.; Ph.D. thesis; Monash University; Melbourne, Austrlia; 2000.

[126] Nasirpouri, F.; Nasirpouri, F. *Ionics* **2011**, *17*, 331–337.

[127] Jeffrey, C. A.; Storr, W. M.; Harrington, D. A. *Journal of Electroanalytical Chemistry* **2004**, *569*, 61–70.

[128] Bechmann, R. *Proceedings of the IRE* **1956**, *44*, 1600–1607.

[129] Lide, D. R. *CRC Handbook of Chemistry and Physics*; CRC Press: Boca Raton, FL, 2005.

[130] McKeehan, L. *Physical Review* **1923**, *21*, 402–407.

[131] Elam, W. T.; Ravel, B. D.; Sieber, J. R. *Radiation Physics and Chemistry* **2002**, *63*, 121–128.

[132] Carver, G. P.; Mattis, R. L.; Buehler, M. G.; *Design considerations for the cross-bridge sheet resistor*; Tech. Rep.; 1982. `https://archive.org/details/designconsiderat8225carv`.

[133] Enderling, S.; Brown, C. L.; Smith, S.; Dicks, M. H.; Stevenson, J.; Mitkova, M.; Kozicki, M. N.; Walton, A. J. *Semiconductor Manufacturing, IEEE Transactions on* **2006**, *19*, 2–9.

[134] Buehler, M. G.; Grant, S. D.; Thurber, W. R. *Journal of The Electrochemical Society* **1978**, *125*, 650–654.

[135] Buehler, M. G.; Thurber, W. R. *Journal of The Electrochemical Society* **1978**, *125*, 645–650.

[136] Grujicic, D.; Pesic, B. *Electrochimica Acta* **2005**, *50*, 4405–4418.

[137] Ji, J.; Cooper *Electrochimica Acta* **1996**, *41*, 1549–1560.

[138] Díaz, S. L.; Calderón, J. A.; Barcia, O. E.; Mattos, O. R. *Electrochimica Acta* **2008**, *53*, 7426–7435.

[139] Rasmussen, A. A.; Møller, P.; Somers, M. A. J. *Surface and Coatings Technology* **2006**, *200*, 6037–6046.

[140] Motoyama, M.; Fukunaka, Y.; Sakka, T.; Ogata, Y. H. *Journal of The Electrochemical Society* **2006**, *153*, C502–C508.

[141] Amadelli, R.; Ferro, S.; Barison, S.; Kötz, R.; Schnyder, B.; Velichenko, A. B. *Electrocatalysis* **2013**, *4*, 329–337.

[142] Erlebacher, J.; Aziz, M. J.; Karma, A.; Dimitrov, N.; Sieradzki, K. *Nature* **2001**, *410*, 450–453.

[143] Pickering, H. W.; Wagner, C. *Journal of The Electrochemical Society* **1967**, *114*, 698–706.

[144] Fritz, J. D.; Pickering, H. W. *Journal of The Electrochemical Society* **1991**, *138*, 3209–3218.

[145] Sun, L.; Chien, C.-L.; Searson, P. C. *Chem. Mater.* **2004**, *16*, 3125–3129.

[146] González-Peña, O. I.; Chapman, T. W.; Vong, Y. M.; Antaño López, R. *Electrochimica Acta* **2008**, *53*, 5549–5554.

[147] Mehrizi, S.; Sohi, M. H.; Seyyed Ebrahimi, S. A. *Surface and Coatings Technology* **2011**, *205*, 4757–4763.

[148] Kieling, V. C. *Surface and Coatings Technology* **1997**, *96*, 135–139.

[149] Vazquez-Arenas, J.; Cruz, R.; Mendoza-Huizar, L. H. *Electrochimica Acta* **2006**, *52*, 892–903.

[150] Gómez, E.; Pollina, R.; Vallés, E. *Journal of Electroanalytical Chemistry* **1995**, *397*, 111–118.

[151] Rashidi, A.; Amadeh, A. *Surface and Coatings Technology* **2008**, *202*, 3772–3776.

[152] Fricoteaux, P.; Rousse, C. *Journal of Electroanalytical Chemistry* **2008**, *612*, 9–14.

[153] Pletcher, D. *A First Course in Electrode Processes*, 2nd ed.; The Royal Society of Chemistry: Cambridge, UK, 2009.

[154] Chen, D.; Ye, J.; Xu, C.; Li, X.; Li, J.; Zhen, C.; Tian, N.; Zhou, Z.; Sun, S. *Science China Chemistry* **2012**, *55*, 2353–2358.

[155] Franklin, T. C. *Surface and Coatings Technology* **1987**, *30*, 415–428.

[156] Gustafsson, J. P.; *Visual MINTEQ (version 3.1)*; Available Online from http://vminteq.lwr.kth.se/; 2014.

[157] Jayashree, R. S.; Kamath *Journal of Power Sources* **2001**, *93*, 273–278.

[158] Zech, N.; Podlaha, E. J.; Landolt, D. *Journal of The Electrochemical Society* **1999**, *146*, 2886–2891.

[159] O'Handley, R. C. *Modern Magnetic Materials: Principles and Applications*; J W Wiley & Sons: New York.

[160] Zhao, Y. P.; Gamache, R. M.; Wang, G. C.; Lu, T. M.; Palasantzas, G.; Th *Journal of Applied Physics* **2001**, *89*, 1325–1330.

[161] Smith, N.; Markham, D.; LaTourette, D. *Journal of Applied Physics* **1989**, *65*, 4362–4365.

[162] Encinas-Oropesa, A.; Nguyen Van Dau, F. *Journal of Magnetism and Magnetic Materials* **2003**, *256*, 301–305.

[163] Rhen, F. M. F.; Roy, S. *Journal of Applied Physics* **2008**, *103*, 103901+.

[164] Herzer, G. *Magnetics, IEEE Transactions on* **1990**, *26*, 1397–1402.

[165] O'Donnell, T.; Wang, N.; Kulkarni, S.; Meere, R.; Rhen, F. M. F.; Roy, S.; O'Mathuna, S. C. *Journal of Magnetism and Magnetic Materials* **2010**, *322*, 1690–1693.

[166] Feldmann, M.; Buttgenbach, S. *Magnetics, IEEE Transactions on* **2007**, *43*, 2567–2569.

[167] Ciureanu, M.; Beron, F.; Clime, L.; Ciureanu, P.; Yelon, A.; Ovari, T. A.; Cochrane, R. W.; Normandin, F.; Veres, T. *Electrochimica Acta* **2005**, *50*, 4487–4497.

[168] Myung, N. V.; Nobe, K. *Journal of The Electrochemical Society* **2001**, *148*, C136–C144.

[169] Yahalom, J.; Zadok, O. *Journal of Materials Science* **1987**, *22*, 499–503.

[170] Alper, M.; Baykul, M. C.; Péter, L.; Tóth, J.; Bakonyİ, I. *Journal of Applied Electrochemistry* **2004**, *34*, 841–848.